Coherent ϕ-meson photoproducion from helium-4 with linearly polarized photon beam

Toshihiko Hiraiwa

A Dissertation Submitted in Partial Fulfillment of
the Requirements for the Degree of Doctor of Science

Department of Physics
Kyoto University

Sep 2018

Abstract

The multi-gluon exchange is a fundamental process and dominates high-energy hadron-hadron scattering processes at forward scattering angles, known as the Pomeron exchange in Regge theory. The Pomeron is a gluon-rich non-perturbative object and is universal for all high-energy hadronic processes. However, very little is known about its fundamental properties, and its physical nature is not fully understood within Quantum Chromo Dynamics. In general, it is difficult to study the Pomeron and multi-gluon exchange processes at low energies because the contribution from meson exchange processes becomes significant and masks the contribution from the Pomeron and multi-gluon exchange processes. Coherent ϕ-meson photoproduction from helium-4 ($\gamma^4\mathrm{He} \rightarrow \phi^4\mathrm{He}$) provides a unique and clean way of investigating such gluonic interactions at low energies because unnatural-parity exchange processes are absent owing to the target with spin-parity $J^P = 0^+$, and thus the natural-parity Pomeron and multi-gluon exchanges are much enhanced.

We have measured the differential cross sections and $\phi \rightarrow K^+K^-$ decay angular distributions for coherent ϕ-meson photoproduction from helium-4 at forward angles ($-t < 0.2$ GeV^2) using linearly polarized photons in the energy range of $E_\gamma = 1.685$–2.385 GeV. This measurement provides the first-ever data for this reaction. The experiment was carried out at the SPring-8/LEPS facility. The measurement of the decay angular distributions demonstrates the strong dominance ($> 94\%$) of the natural-parity Pomeron exchange, and also indicates strongly the presence of double helicity-flip transitions from the incident photon to the produced ϕ-meson ($\lambda_\gamma = \pm 1 \rightarrow \lambda_\phi = -\lambda_\gamma$). The latter suggests that the Pomeron exchange can be considered as an effective tensor exchange. To evaluate the Pomeron contribution to the forward cross section ($\theta = 0°$) for the elementary $\gamma p \rightarrow \phi p$ reaction as well as other possible natural-parity contribution, the energy dependence of the forward cross section ($\theta = 0°$) for the $\gamma^4\mathrm{He} \rightarrow \phi^4\mathrm{He}$ reaction was analyzed. The comparison to available low-energy data for the $\gamma p \rightarrow \phi p$ reaction suggests the presence of additional natural-parity exchange processes beyond the Pomeron exchange such as the daughter Pomeron exchange in ϕ-photoproduction and/or the need to modify a conventional Pomeron exchange model.

Acknowledgement

First of all, many people have helped and supported me to carry out and complete this work at different stages. I would like to thank all of them.

I would like to express my sincere gratitude to my supervisor Prof. Masaru Yosoi for the continuous support of my Ph.D study and related research. His guidance helped me in all the time of research and writing of this thesis. I could not have imagined having a better supervisor for my Ph.D study.

Besides my supervisor, I would like to thank Prof. Takashi Nakano for his insightful comments and encouragement, but also for the hard question which incented me to widen my research from various perspectives.

My sincere thanks also go to Dr. Masayuki Niiyama, who provided me an opportunity to join the LEPS experiment and gave me a lot of valuable advice throughout my Ph.D study. Without his precious support, it would not be possible to conduct this research.

I would like to express my special appreciation and thanks to Prof. Tomofumi Nagae, who was my supervisor when I was a graduate student of Kyoto University. I would like to thank you for encouraging my research and allowing me to grow as a research scientist. Your advice on both research as well as on my career have been priceless.

I would also like to express my gratitude to Prof. Masahiko Iwasaki, who was my supervisor at RIKEN and provided me an opportunity to join the J-PARC E15 experiment. I would like to thank you for always having time to discuss a lot of things about physics and data analysis and for always having my back.

I am also grateful to Prof. Megumi Naruki for her devoted contribution in reviewing my dissertation and making correction to improve and finalize it.

Many thanks go to all of my colleagues of the LEPS Collaboration. I am especially grateful to Dr. Mizuki Sumihama, Dr. Yuhei Morino and Dr Yohei Nakatsugawa for taking care of my data analysis and providing a lot of advice. Special thanks also go to Dr. Hideki Kohri and Dr. Yuji Ohashi for their valuable advice and comments, and also for encouraging me at the stage of writing a paper. I would like to thank Prof. Eugene A. Strokovsky and Prof. Wen-Chen Chang for reading the paper carefully and providing a lot of comments and advice.

I owe a special thanks to my fellow lab-mates in Nuclear and Hadronic Physics Laboratory of Kyoto University; especially, Dr. Atsushi Tokiyasu,

Contents

1 Introduction

1.1 Photon interaction with hadron

It is one of our most important missions in hadron physics today to understand the internal structures of hadrons from Quantum Chromo Dynamics (QCD). Electromagnetic interactions of hadrons are widely used as a probe for this purpose: for example, the nucleon structure has been intensively studied via electron scattering off proton, or a bound neutron in a deuteron target. The MIT-SLAC experiment concerning deep inelastic scattering of electrons off protons [1] revealed that the proton is made of extremely small and hard particles, later called quarks. Taylor, Friedman and Kendall were awarded the Nobel Prize in 1990 for this discovery [2].

It is well known that electromagnetic interactions are mediated by photons. If a photon has a hadronic component, i.e, a photon state $|\gamma\rangle$ is a superposition of a "bare" state $|\gamma\rangle^{\text{bare}}$ and a hadron state $|q\bar{q}\rangle$:

$$|\gamma\rangle = a\,|\gamma\rangle^{\text{bare}} + b\,|q\bar{q}\rangle \quad (|a|^2 + |b|^2 = 1), \tag{1.1}$$

then the charge distribution of protons measured by elastic electron scattering, for example, is different from that expected from the bare photon state $|\gamma\rangle^{\text{bare}}$. Such a speculation was first made by Nambu [3], who suggested that the charge distribution of protons and neutrons, as determined by electron scattering, could be accounted for by introducing an isoscalar vector ($I = 0, J^P = 1^-$) meson, now known as ω-meson. A similar attempt was made by Frazer and Fulco [4] to explain the nucleon form factors by considering a $\pi\pi$ resonance with $I = 1, J^P = 1^-$ around a total energy of ~ 770 MeV, now called ρ-meson.

On the other hand, experimental data on the total γp cross section as well as vector meson photoproduction at high energies also support the "hadronic structure" of photons, which is discussed in the next section.

1.2 Vector meson photoproduction

High-energy photo-reactions with a hadron have been discussed on the basis of "Vector Meson Dominance" (VMD) [5]. Since neutral vector mesons have the same quantum numbers as those of photons, namely $J^{PC} = 1^{--}$, Heisenberg's uncertainty principle allows a photon to fluctuate into a $q\bar{q}$ pair, forming a virtual vector meson for a short time before interactions. The

VMD picture relates the photoproduction amplitude for vector mesons ($\equiv \mathcal{M}_{\gamma N \to VN}$) to the amplitude of the $VN' \to VN$ transition ($\equiv \mathcal{M}_{V'N \to VN}$), so that

$$\mathcal{M}_{\gamma N \to VN} = \sum_{V'} \sqrt{\frac{\alpha}{4} \cdot \frac{4\pi}{\gamma_{V'}^2}} \mathcal{M}_{V'N \to VN}, \qquad (1.2)$$

where the summation runs over possible vector meson states V', α is the fine structure constant and $4\pi/\gamma_V^2$ measures a photon coupling to a vector meson V. A constant γ_V can be evaluated from the decay of a vector meson into a lepton pair [6]. Since the $VN \to V'N$ ($V \neq V'$) amplitudes cannot be measured, it is unknown whether or not the right-hand side of Eq. (1.2) is diagonal (i.e., $\mathcal{M}_{V'N \to VN} = 0$ for $V' \neq V$). Commonly, the off-diagonal amplitudes are assumed to be negligible compared to the diagonal ones. In such case, Eq. (1.2) becomes

$$\mathcal{M}_{\gamma N \to VN} = \sqrt{\frac{\alpha}{4} \cdot \frac{4\pi}{\gamma_V^2}} \mathcal{M}_{VN \to VN}. \qquad (1.3)$$

Thus, in the context of VMD, vector meson photoproduction from nucleons can be regarded as elastic scattering of a vector meson off nucleons.

In fact, high-energy photon-hadron collision, including vector meson photoproduction, has common characteristics to high-energy hadron-hadron collision:

- The total cross section rises very slowly as the energy $\sqrt{s}$ increases (Fig. 1.1).

- Differential cross section for elastic hadron-hadron scattering (vector meson photoproduction) exhibits a strong forward-peaking behavior, and the forward peak shrinks with increasing energy[1] (a so-called "shrinkage" mechanism) (Fig. 1.2).

These characteristics can be well understood by the t-channel exchange of "Pomeron trajectory" in the framework of VMD.

---

[1]These phenomena resemble those of the diffraction of light on a black disk. Therefore, the term "*diffraction*" is often used in high-energy scattering.
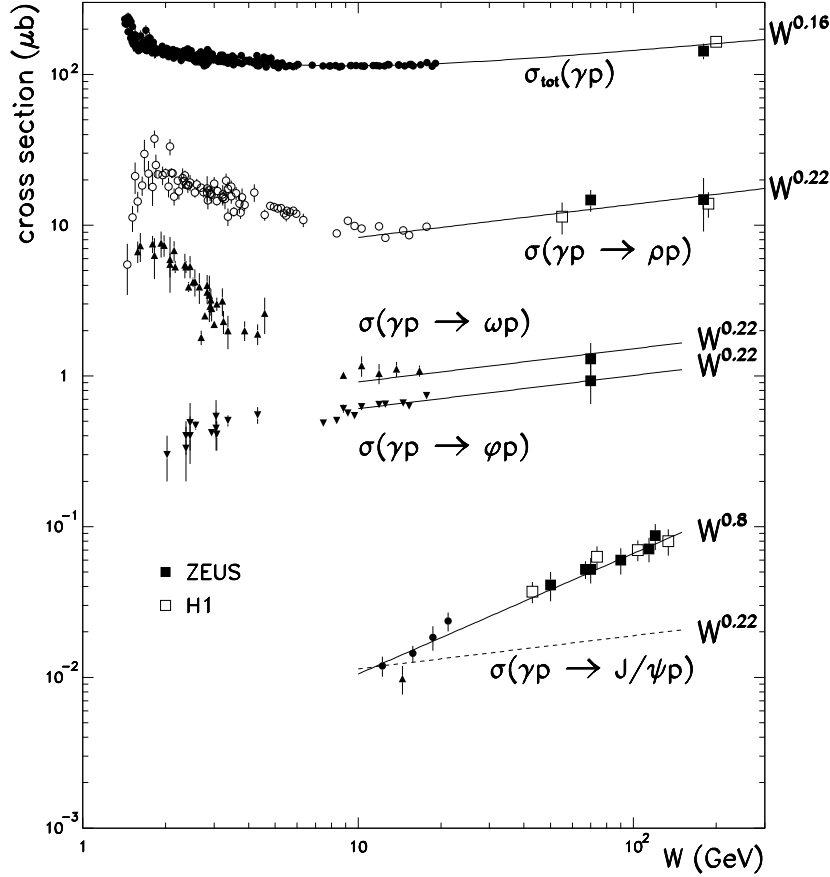
Figure 1.1:   Total photon-proton hadronic cross section, together with the total (integrated) cross sections for the elastic vector meson (ρ, ω, ϕ, J/ψ) photoproduction off protons, as a function of the total energy $W = \sqrt{s}$. The solid curves for $\sigma_{\text{tot}}(\gamma p)$, $\sigma(\gamma p \to \rho p)$, $\sigma(\gamma p \to \omega p)$ and $\sigma(\gamma p \to \phi p)$ and the dashed curve for $\sigma(\gamma p \to J/\psi p)$ correspond to predictions from a "Pomeron" exchange model (see Sect. 1.3 and Appendix A for Pomeron), whereas the solid curve for $\sigma(\gamma p \to J/\psi p)$ corresponds to a prediction from perturbative QCD models. The figure is taken from Ref. [7].
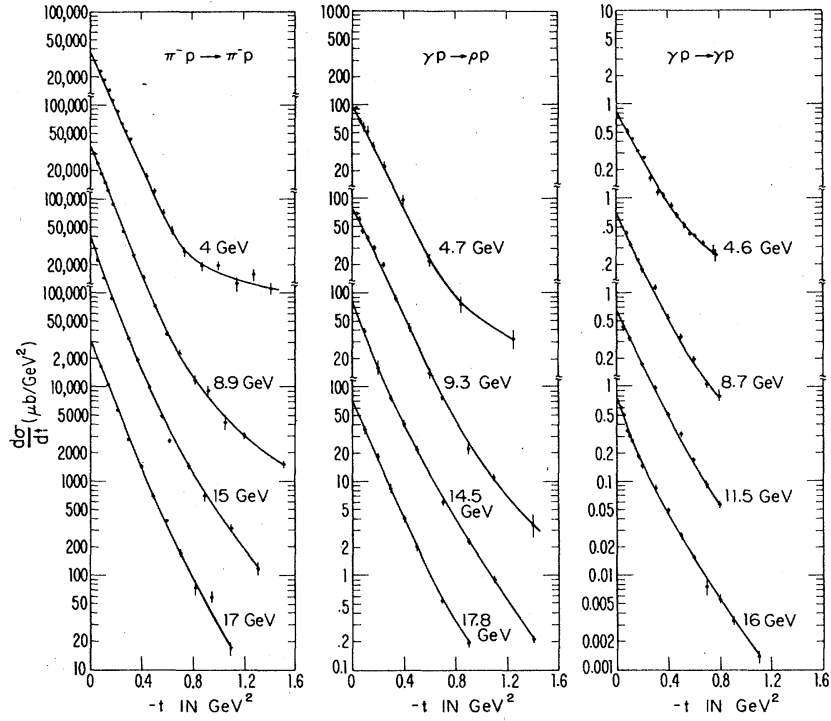
Figure 1.2:   Differential cross sections as a function of momentum transfer $-t$ for the $\pi^- p \to \pi^- p$ reaction (left figure), the $\gamma p \to \rho p$ reaction (middle figure) and the $\gamma p \to \gamma p$ reaction (right figure). The figures are taken from Ref. [5].

1.3 Introduction to Pomeron

An introduction to "Pomeron"[2] is presented here. The details about Pomeron and related topics are described in Appendix A.

Before the advent of QCD, Regge theory [9] was developed and successfully described high-energy hadron-hadron scattering. Since Regge theory is based on the general properties of scattering amplitudes (i.e., Lorentz invariance, unitary and analyticity), even nowadays it is an effective tool for describing high-energy soft processes[3], where perturbation theory is inapplicable.

In Regge theory, a strong interaction is described by the exchange of a family of particles characterized by the quantum numbers other than spin. Chew and Frautschi [10, 11] found that such a family of particles exchanged in a scattering process falls along a straight line by plotting their spins (J) against their squared masses (m^2) (see for example Fig. A.1); namely

$$J = \alpha(m^2) = \alpha(0) + \alpha' \cdot m^2. \tag{1.4}$$

This is a so-called "Regge trajectory". In the above equation, $\alpha(0)$ and α' are the intercept and slope, respectively, of a Regge trajectory. All the experimentally established hadrons (both mesons and baryons) belong to a Regge trajectory with an intercept of $\alpha(0) \lesssim 0.5$ and a "universal slope" of $\alpha' \approx 0.9~\mathrm{GeV}^{-2}$.

Historically, a linear relation of Eq. (1.4) for meson trajectories has been explained by a string model [12], in which a meson is regarded as a rotating open string or a massless quark-anti-quark pair connected by a string with a constant tension σ_q, which is responsible for the "confinement" property of quarks. In this picture, the angular momentum excitations of such an open string are given by

$$J = \frac{1}{2\pi\sigma_q} m^2. \tag{1.5}$$

This mimics a linear behavior of Eq. (1.4). Comparing Eqs. (1.4) and (1.5),

---

[2]We should distinguish two pomerons (soft and hard ones) [8]. In this thesis, "Pomeron", where the first letter is capitalized, refers to the soft one.

[3]A soft process means a process in which the momentum transferred between two colliding particles is small enough compared to the QCD scale $\Lambda_{\mathrm{QCD}} \simeq 210$ MeV.
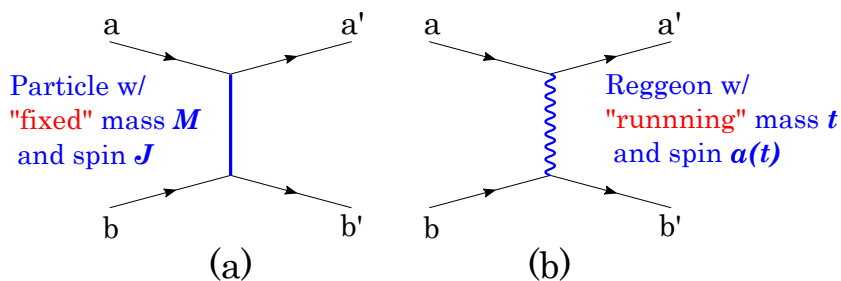
Figure 1.3: Schematic diagrams (a) for the t-channel exchange of a particle with fixed mass M and spin J and (b) for the t-channel exchange of a Reggeon $[\alpha(t)]$.

one finds a relation between the Regge slope and the string tension:

$$\alpha' = \frac{1}{2\pi\sigma_q}. \tag{1.6}$$

The string tension σ_q calculated by this equation with a universal slope $\alpha' \approx 0.9 \text{ GeV}^{-2}$ is in excellent agreement with the values obtained from quarkonium[4] spectroscopy [13].

According to Regge theory, the amplitude for a two-particle to two-particle scattering process (i.e., $a + b \rightarrow a' + b'$) at high energies and at small scattering angles is approximately expressed as

$$\mathcal{A}(s,t) \sim i\beta(t)s^{\alpha(t)}, \tag{1.7}$$

where s is the total energy, t is the 4-momentum transferred in the process, $\alpha(t)$ is the leading Regge trajectory for the process written in terms of t [i.e., $\alpha(t) = \alpha(0) + \alpha't$], and $\beta(t)$ is a residue function.

The term $s^{\alpha(t)}$ in Eq. (1.7) can be viewed as the t-channel exchange of a particle with spin equal to $\alpha(t)$. In the language of Regge theory, this particle-like object is called a "Reggeon". The t-channel exchange of a Reggeon corresponds to the exchange of all possible particles in t-channel (Fig. 1.3).

By means of the optical theorem, which relates the forward elastic scattering amplitude to the total cross section, one can deduce the high-energy be-

---

[4]A quarkonium refers to a flavorless meson consisting of a heavy quark and its own antiquark ($c\bar{c}$ or $b\bar{b}$). Note that a quarkonium made of a top quark and an anti-top quark does not exist due to the quite large mass of the top quark.

havior of the total cross section for hadron-hadron scattering from Eq. (1.7):

$$\sigma_{\text{tot}} = \frac{1}{s}\text{Im}\mathcal{A}(s, t = 0) \sim s^{\alpha(0)-1}. \tag{1.8}$$

Since all the known mesonic trajectories have an intercept of $\alpha(0) \lesssim 0.5$, one expects total hadron-hadron cross sections to fall down with increasing energy $\sqrt{s}$. However, the total cross sections for pp and $\bar{p}p$ scattering, for example, exhibit a slow growth at $\sqrt{s} > 10$ GeV (see Fig A.2). Pomeron trajectory is a hypothetical object that were introduced to account for slowly-rising total hadron-hadron cross sections at high energies [14].

Pomeron trajectory has an intercept nearly equal to but slightly greater than unity, and is known to carry the quantum numbers of the vacuum [15, 16]. The intercept $\alpha_{\mathbb{P}}(0)$ and slope $\alpha_{\mathbb{P}}'$ of Pomeron trajectory were determined in detail from total hadron-hadron and photon-hadron cross section data and from elastic pp and $\bar{p}p$ scattering data, respectively, as [17, 18]:

$$\begin{aligned}
\alpha_{\mathbb{P}}(t) &= \alpha_{\mathbb{P}}(0) + \alpha_{\mathbb{P}}'t, \\
\alpha_{\mathbb{P}}(0) &= 1.08, \quad \alpha_{\mathbb{P}}' = 0.25 \text{ GeV}^{-2}.
\end{aligned} \tag{1.9}$$

The physical particles lying on Pomeron trajectory have not been identified yet, but there has been a long-standing speculation that the physical particles responsible for Pomeron trajectory might be glueballs, i.e., bound states of gluons [19–21] (see also Appendix A.3) because all the known hadronic states fall on Regge trajectories with slopes close to 0.9 GeV^{-2} but different intercepts ($\lesssim 0.5$). In fact, experimental data on deep inelastic ep scattering [22] and on diffractive $\bar{p}p$ collision [23, 24] have revealed that a substantial fraction of the Pomeron momentum is carried by "hard" gluons, i.e. constituent gluons.

Experimentally, the t-channel exchange of such an object with the vacuum quantum numbers is characterized by a region in the rapidity[5] space devoid of particles, i.e. a so-called "rapidity gap", in pp or $\bar{p}p$ diffraction dissociation

---

[5]In collider physics, "rapidity", y, is often used for representing the angle of a particle momentum relative to the beam axis (z), and is defined as

$$y = \frac{1}{2}\ln\frac{E + p_z}{E - p_z}, \tag{1.10}$$

where E and p_z are the energy and the z-component of the momentum, respectively, of a particle. Practically, "pseudo-rapidity" is used instead of rapidity. A pseudo-rapidity η is
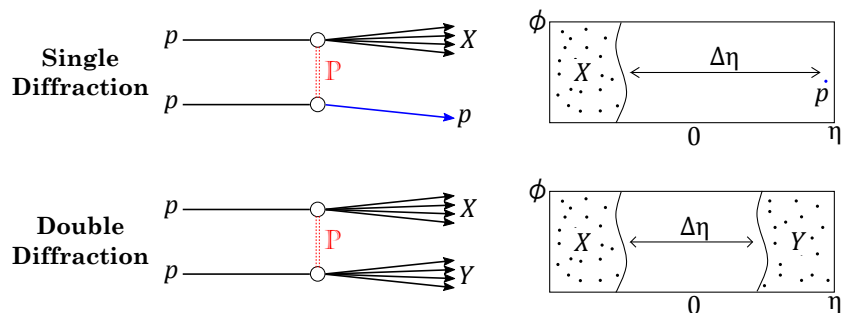
Figure 1.4: (Left figures) illustrations for single (top) and double (bottom) diffraction dissociation with the Pomeron ($\mathbb{P}$) exchange. (Right figures) corresponding event patterns in a two-dimensional plot for pseudo-rapidity η versus azimuthal angle ϕ. $\Delta\eta$ stands for a "rapidity gap".

at high energies; see e.g. Refs. [25, 26]. In diffraction dissociation, one of the colliding hadrons emits a Pomeron, loosing a very small fraction of its energy, and then dissociates into a system with a small invariant mass, i.e. a bundle of hadrons with small relative momenta. The other colliding hadron, on the other hand, is scattered off by the Pomeron, remaining intact (called "single diffraction dissociation"), or absorbs the Pomeron, dissociating into a low-mass system (called "double diffraction dissociation"). In both cases, we see a characteristic event pattern in a two-dimensional angular plot as in Fig. 1.4: a forward (backward) region or both of forward and backward regions are filled with particles from hadron dissociation whereas the rest is empty. This empty space is thought to be an experimental signature of the exchange of a colorless object, i.e. a Pomeron[6], between the two hadrons. Diffraction dissociation is explained well by phenomenological models based on Regge

---

given by

$$\eta = \frac{1}{2} \ln \frac{|\boldsymbol{p}| + p_z}{|\boldsymbol{p}| + p_z} = -\ln\left(\tan\frac{\theta}{2}\right), \tag{1.11}$$

where $|\boldsymbol{p}|$ is the magnitude of a particle momentum, and θ is the angle of a particle momentum relative to the beam axis. From Eqs. (1.10) and (1.11), pseudo-rapidity corresponds to rapidity in the limit where the velocity of a particle is close to the speed of light, or equivalently the mass of a particle is negligible. Note that we often refer to η just as rapidity, not as pseudo-rapidity.

[6]The exchange of secondary Reggeons such as ρ and ω trajectories, which are also colorless objects, could make a rapidity gap. However, the contribution from secondary Reggeon exchanges is small at high energies, as is expected from the Regge phenomenology.

theory [27–32], although new data from Large Hadron Collider (LHC) call for a significant modification of the current models (see Ref. [33]).

The Pomeron exchange is often described in terms of the two-gluon exchange, which was first proposed individually by Low [34] and Nussinov [35, 36]. In fact, even the simplest QCD diagram involving the exchange of two gluons can reproduce some properties inherent in the Pomeron exchange such as the constancy of the total cross sections at high energies [37], although the full understanding of the Pomeron exchange in terms of the QCD degree of freedom, i.e. quarks and gluons, remains a challenge due to the inapplicability of perturbation theory. Nevertheless, the Pomeron hypothesis is regarded as an effective description for soft gluonic interactions between hadrons, especially at high energies.

The simplest and basic diagram in QCD is the one-gluon exchange between quarks. At the level of hadrons, such a process, i.e. the one-gluon exchange between hadrons, is forbidden because hadrons are in total colorless whereas a gluon has intrinsic color charge. Thus, in a sense, the exchange of two gluons in the color-singlet configuration between hadrons, which mimics the Pomeron exchange, is one of the most fundamental processes in hadron-hadron interactions. In general, for example, in elastic scattering between hadrons with common flavors, meson (quark) exchanges play a significant role at low energies and mask the contribution from the Pomeron (multi-gluon) exchange. Thereby, the applicability of "the concept of the Pomeron exchange" to the low-energy regime is not completely clear (see e.g. Refs. [38, 39]).

1.4   Low-energy ϕ-photoproduction off nucleon

1.4.1   Overview

As already discussed in Sect. 1.2, at high energies, vector meson photoproduction can be well described by the t-channel Pomeron exchange in the VMD framework. Among light vector meson (ρ, ω, ϕ) photoproduction, ϕ-meson photoproduction off nucleons is of particular interest. Since the $\phi(1020)$-meson is a vector meson ($J^{PC} = 1^{--}$) mostly consisting of a strange quark (s) and an anti-strange quark ($\bar{s}$), which are hidden in the sea of nucleons, meson and baryon (quark) exchange processes are suppressed by the Okubo-Zweig-Iizuka (OZI) rule [40–42] [see also Fig. 1.5(a)]. Consequently, the multi-gluon exchange (or the Pomeron exchange) is expected to be dom-
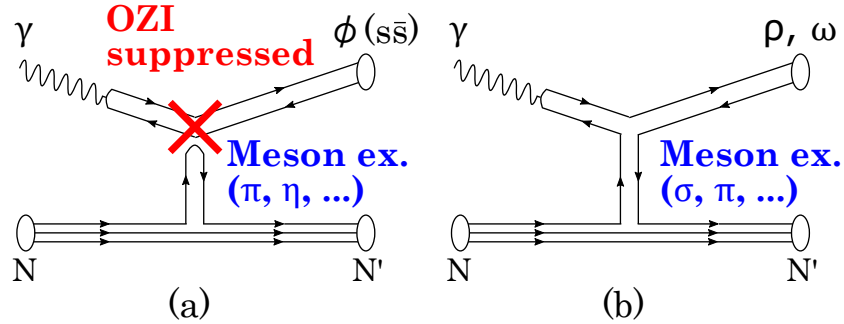
Figure 1.5:   Feynman diagrams for (a) φ-photoproduction from nucleons via meson-exchange processes and (b) ρ and ω-photoproduction from nucleons via meson-exchange processes. In the diagram (a), quark lines are disconnected at the upper vertex. Thereby, such processes are suppressed (the OZI rule).

inant even at low energies. This is not the case for other light vector meson (ρ, ω) photoproduction [Fig. 1.5(b)], in which meson-exchange processes have a significant contribution at low energies [see the low-energy enhancements of $\sigma(\gamma p \to \rho p)$ and $\sigma(\gamma p \to \omega p)$ in Fig. 1.1]. Therefore, φ-photoproduction off nucleons is a clean system for investigating gluonic interactions at low energies. Traditionally, this reaction has been considered as a tool for the direct study of the Pomeron exchange at low energies [43], and there has also been a speculation that low-energy φ-photoproduction will give access to an exotic gluonic interaction [44] (see also Sect. 1.4.3), although the π and η exchanges are now known to have a non-negligible contribution near the production threshold [38, 39].

1.4.2   Theoretical models for conventional Pomeron, π and η exchanges

As mentioned above, φ-photoproduction off protons predominantly proceeds via the multi-gluon exchange even at low energies. Since there is no reliable model for describing soft gluon exchange processes in this energy regime ($W = \sqrt{s} \lesssim 5$ GeV), a Pomeron exchange model, which is well established at high energies, is conventionally used to describe such processes. Besides the Pomeron exchange, at low energies, the pseudoscalar π and η-meson exchanges play a non-negligible role [38, 39], which can be, though,

considered as a small correction to the production mechanism.

The Pomeron exchange is usually described based on the Donnachie-Landshoff (DL) Pomeron model (see Appendix A.2), together with a modification to consider the Pomeron exchange as the non-perturbative two-gluon exchange (hereafter, this model is referred to as the modified DL model) [37, 45, 46]. In Ref. [47], the Lorentz-invariant amplitude for the Pomeron exchange in the $\gamma p \to \phi p$ reaction is given by

$$
\begin{aligned}
T_{fi}^{\mathbb{P}} &= -M_{\mathbb{P}}(s,t)\Gamma_{fi}^{\mathbb{P}}, \\
\Gamma_{fi}^{\mathbb{P}} &= \varepsilon_{\mu}^{*}(\lambda_{\phi})\bar{u}_f h_{\mathbb{P}}^{\mu\nu} u_i \varepsilon_{\nu}(\lambda_{\gamma}),
\end{aligned}
\tag{1.12}
$$

where $\varepsilon_{\mu}(\lambda_{\phi})$ $[\varepsilon_{\nu}(\lambda_{\gamma})]$ is the polarization vector of the outgoing ϕ-meson (the incoming photon), and $u_i \equiv u_{m_i}(p)$ $[u_f \equiv u_{m_f}(p')]$ is the Dirac spinor of the proton with four-momentum p (p') and its spin projection m_i (m_f). A scalar function $M_{\mathbb{P}}(s,t)$ takes an ordinary Regge form:

$$
M_{\mathbb{P}}(s,t) = C_{\mathbb{P}} F_1(t) F_{\phi}(t) \frac{1}{s} \left(\frac{s}{s_{\mathbb{P}}}\right)^{\alpha_{\mathbb{P}}(t)} \exp\left[-\frac{i}{2}\pi\alpha_{\mathbb{P}}(t)\right],
\tag{1.13}
$$

where $F_1(t)$ and $F_{\phi}(t)$ are the form factors for the Pomeron-proton vertex and the Pomeron-ϕ-meson vertex, respectively, which take the following forms:

$$
\begin{aligned}
F_1(t) &= \frac{4M_N^2 - 2.8t}{(4M_N^2 - t)(1 - t/t_0)^2}, \\
F_{\phi}(t) &= \frac{2\mu_0^2}{(1 - t/M_{\phi}^2)(2\mu_0^2 + M_{\phi}^2 - t)},
\end{aligned}
\tag{1.14}
$$

where M_N (M_{ϕ}) is the nucleon (ϕ-meson) mass, $t_0 = 0.7$ GeV^2, and $\mu_0^2 = 1.1$ GeV^2. A Pomeron strength factor $C_{\mathbb{P}}$ in Eq. (1.13), which governs the overall strength, is given by

$$
C_{\mathbb{P}} = \frac{6g^2\sqrt{4\pi\alpha_{\mathrm{em}}}}{\gamma_{\phi}},
\tag{1.15}
$$

where $\alpha_{\mathrm{em}} = e^2/4\pi$, and g^2 is the product of two dimensionless Pomeron-quark coupling constants; $g^2 \equiv g_{\mathbb{P}ss}g_{\mathbb{P}qq} = (\sqrt{s_{\mathbb{P}}}\beta_s)(\sqrt{s_{\mathbb{P}}}\beta_q)$ with $s_{\mathbb{P}} = 4$ GeV^2, $\beta_s = 1.61$ GeV^{-1} and $\beta_q = 2.05$ GeV^{-1}.

A vertex function $\Gamma^{\mathbb{P}}_{fi}$ in Eq. (1.12), which is derived from the analogy between the Pomeron exchange and the non-perturbative two-gluon exchange, is written explicitly as

$$
\begin{aligned}
\Gamma^{\mathbb{P}}_{fi} = &\bar{u}_f \not{k} u_i (\varepsilon^*_{\lambda_\phi} \cdot \varepsilon_{\lambda_\gamma}) - \bar{u}_f \not{\varepsilon}_{\lambda_\gamma} u_i (\varepsilon^*_{\lambda_\phi} \cdot k) \\
&- \bar{u}_f \not{\varepsilon}^*_{\lambda_\phi} u_i \left(\varepsilon_{\lambda_\gamma} \cdot q - \frac{(\varepsilon_{\lambda_\gamma} \cdot \bar{p})(k \cdot q)}{\bar{p} \cdot k} \right),
\end{aligned}
\tag{1.16}
$$

where k (q) denotes the four-momentum of the incoming photon (the outgoing ϕ-meson). $\bar{p}$ is introduced to guarantee the gauge invariance as $\bar{p} \equiv (p + p')/2$, where p (p') is the four-momentum of the initial (final) proton.

The vertex function $\Gamma^{\mathbb{P}}_{fi}$ is responsible for the spin structure of the Pomeron-quark couplings; that is, $\Gamma^{\mathbb{P}}_{fi}$ can be rewritten in the Gottifried-Jackson (GJ) frame (see for the definition Sect. 1.4.4) approximately as

$$
\begin{aligned}
\Gamma^{\mathbb{P}}_{fi} \sim &\delta_{\lambda_\phi \lambda_\gamma} \bar{u}_f \not{k} \bar{u}_i - \delta_{\lambda_\phi 0} k_\gamma \bar{u}_f \not{\varepsilon}_{\lambda_\gamma} u_i \\
&- \sqrt{2} \lambda_\gamma p_x \frac{k \cdot q}{2p \cdot k - k \cdot q} \bar{u}_f \not{\varepsilon}^*_{\lambda_\phi} u_i,
\end{aligned}
\tag{1.17}
$$

where k_γ and p_x are the photon momentum and the x-component of the proton momentum, respectively, and λ_γ (λ_ϕ) is the helicity of the incoming photon (the outgoing ϕ-meson). The first term represents helicity-conserving processes ($\lambda_\phi = \lambda\gamma$), whereas the last two terms represent helicity-flip (helicity-nonconserving) processes ($\lambda_\phi \neq \lambda_\gamma$); that is, the second term is responsible for single helicity-flip transitions from the incident photon to the outgoing ϕ-meson ($\lambda_\gamma = \pm 1 \rightarrow \lambda_\phi = 0$), and the third one for double helicity-flip transitions ($\lambda_\gamma = \pm 1 \rightarrow \lambda_\phi = -\lambda_\gamma$) [47]. At high energies, the first term of Eq. (1.17) dominates over the last two terms, leading to helicity-conservation, but at low energies, the last two terms become significant and give rise to helicity-flips ($\lambda_\phi \neq \lambda_\gamma$).

From the slowly-rising total hadron-hadron cross sections, one infers that the Pomeron will behave like a spin-1 particle. Donnachie and Landshoff [18] postulated that the Pomeron couples to individual quarks like an isoscalar $C = +1$ photon, leading to a vector (γ^μ) coupling as the Pomeron-quark coupling. From this, it follows that the Pomeron does not flip the quark helicity at the vertex [48]. On the other hand, Titov *et al.* [47] deduced the Pomeron-quark couplings from the two-gluon exchange and showed that the Pomeron amplitude contains the helicity-flip terms that are negligible at high

energies but become important at a few GeV of the photon energy. Thus, the difference between these two models (the original and modified DL models) becomes significant at low energies.

The pseudoscalar meson (π, η) exchange amplitudes are often described in terms of a one-boson-exchange model [38, 47, 49]. These amplitudes are purely real [38, 49], whereas the Pomeron amplitude is almost purely imaginary at small $|t|$ [see the phase term[7] in Eq. (1.13)]. This means that the interference effects between the Pomeron and pseudoscalar meson exchanges in the forward cross sections are small. Further, the pseudoscalar meson exchange amplitudes take a simple helicity-conserving form in the GJ frame, i.e. $T_{fi}^{\mathrm{PS}} \propto (\varepsilon_\phi \cdot \varepsilon_\gamma) = \delta_{\lambda_\gamma, \lambda_\phi}$, and thus do not contribute to helicity-flip amplitudes [38, 47, 49]. Accordingly, the presence of helicity-flip processes in ϕ-photoproduction will support the success of the modified DL Pomeron model (i.e., the Pomeron-two-gluon analogy).

1.4.3 Daughter Pomeron trajectory

Thanks to the OZI suppression of meson exchange processes, low-energy ϕ-photoproduction off nucleons offers a possibility of searching for an exotic gluonic interaction, i.e. the exchange of a new glueball-associated trajectory, as suggested by Nakano and Toki [44]

Figure 1.6 shows lattice QCD predictions of the squared masses of scalar $(J^{PC} = 0^{++})$ and tensor (2^{++}) glueballs against their spins [50–56]. The predicted masses for a 2^{++} glueball are populated close to Pomeron trajectory. On the other hand, since a 0^{++} glueball cannot be a physical particle on Pomeron trajectory [, which can be verified by substituting $J = 0$ into Eq. (1.4)], it could be a member of a daughter Pomeron trajectory[8], which is given by

$$\alpha_{0^+}(t) = \alpha_{0^+}(0) + \alpha'_{0^+}t,$$
$$\alpha_{0^+}(0) = -0.75, \quad \alpha'_{0^+} = 0.25 \text{ GeV}^{-2}. \tag{1.18}$$

Since the intercept $\alpha_{0^+}(0)$ is much smaller than unity, the contribution from the daughter Pomeron exchange to the forward cross section $(\theta = 0°)$

---

[7]The phase of the Pomeron amplitude is definitely determined by Regge theory.

[8]A daughter Regge trajectory means a trajectory parallel to the parent one in the M^2–J plane, but with a different intercept.
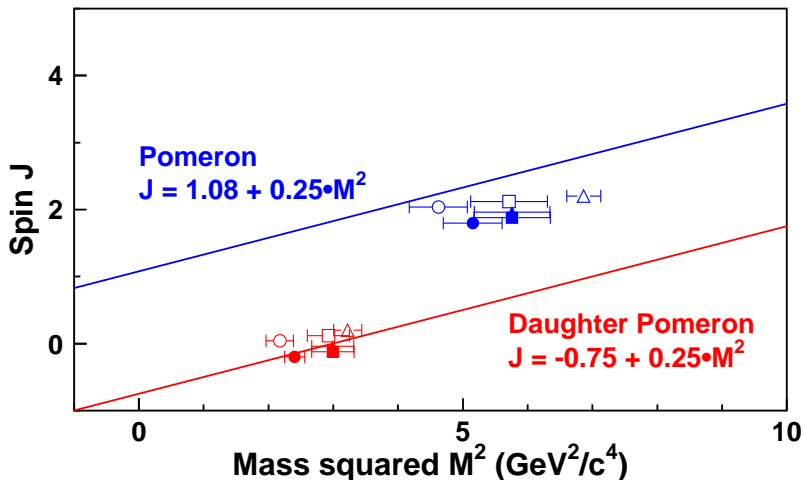
Figure 1.6:   Lattice QCD prediction of the squared masses of a scalar ($J^{PC} = 0^{++}$) glueball (red points) and a tensor (2^{++}) glueball (blue points), against their spins. Data are taken from Refs. [50] (filled circles), [51, 52] (filled squares), [53] (filled triangles), [54] (open circles), [55] (open squares) and [56] (open triangles). For clarity, each data is slightly shifted in the vertical direction. A red line represents a "daughter" Pomeron trajectory whose intercept is determined from the predicted 0^{++} glueball mass, whereas a blue ones represents Pomeron trajectory, whose intercept is determined from total hadron-hadron cross sections (see Appendix A.2).

would become significant near the threshold. Figure 1.7 shows the predicted energy dependence of the forward cross section ($\theta = 0°$) for the $\gamma p \rightarrow \phi p$ reaction. For this plot, the Pomeron contribution was fixed by high-energy light vector meson (ρ, ω, ϕ) photoproduction data [58–82], whereas the daughter Pomeron contribution was determined from the low-energy ϕ-photoproduciton data by the ABBHHM Collaboration (, indicated by an open triangle in Fig. 1.7) [57]. If the daughter Pomeron trajectory really exists, the forward cross section ($\theta = 0°$) would be enhanced near the threshold.

Titov *et al.* [38] pointed out that, as is expected from the Regge phenomenology, the conventional π and η meson exchanges would also enhance the forward cross section near the threshold, and that polarization observables will be helpful for disentangling the daughter Pomeron exchange from
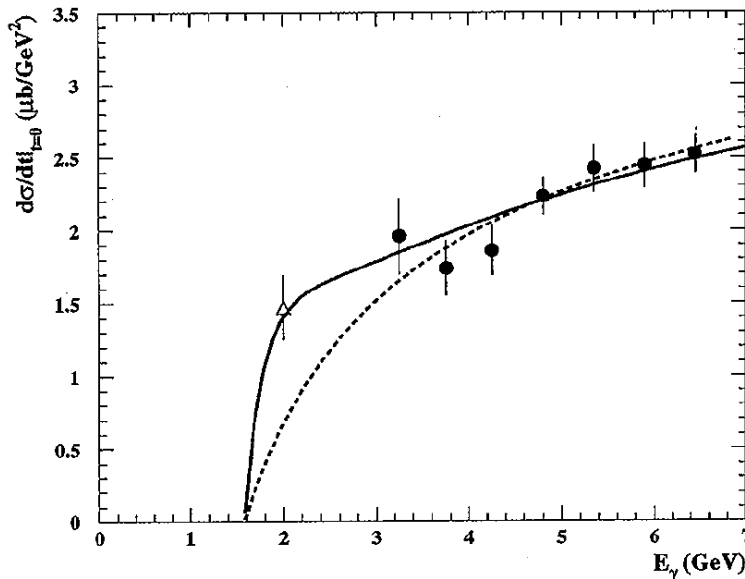
Figure 1.7: Predicted energy dependence of the differential cross section at $t = 0$ ($\theta = 0°$) for ϕ-photoproduction off protons. A solid curve shows the sum of the contribution from the t-channel Pomeron and daughter Pomeron exchanges, whereas a dashed curve shows the contribution from Pomeron exchange. The calculation was made within Regge theory. An open triangle represents the experimental data from the ABBHHM Collaboration [57], while filled circles represent the data from DESY [58]. The figure is taken from Ref. [44].

the conventional π and η exchanges.

1.4.4   Polarization observables with linearly polarized photons

Besides the information on the cross sections, polarization observables, namely spin density matrix elements (SDMEs), with linearly polarized photons provide further insights on the reaction mechanism, specifically on the spin and parity of the particles exchanged in t-channel, and isolate the Pomeron and daughter Pomeron exchanges from the π and η exchanges. The SDMEs describe the distribution of the spin states of the produced ϕ-meson, and are related to the $\phi \to K^+ K^-$ decay angular distributions in
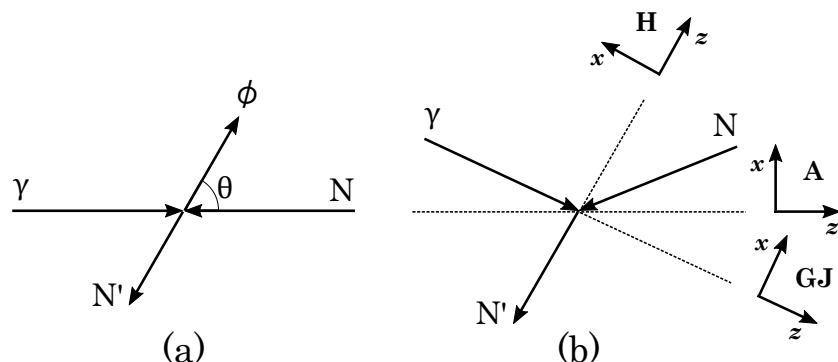
Figure 1.8:   Schematic views of (a) the center-of-mass frame and (b) the Gottifried-Jackson (GJ), Helicity (H) and Adair (A) frames.

the ϕ-meson rest frame. There are several choices of the reference frame to analyze the decay angular distributions; the Gottfried-Jackson (GJ), Helicity and Adiar frames (Figs. 1.8). The difference between these frames is just a choice of the quantization axis of spin (z-axis). Among these frames, the GJ frame is suitable for investigating t-channel exchange processes because some amplitudes take a helicity-conserving form for an arbitrary production angle of the ϕ-meson [38]. Therefore, we chose the GJ frame as a reference one in the present analysis. Note that although the general formalism for the analysis of the ϕ-meson decay is common in all the reference frames, the SDMEs depend on the reference frame.

In the GJ frame, the z-axis is defined in a direction parallel to the photon momentum in the ϕ-meson rest frame, whereas the x and y-axes are defined in such a way that the y-axis is perpendicular to the production plane, and that the x-axis is parallel to the vector product of the y- and z-axes $\hat{y} \times \hat{z}$.

A three-dimensional angular distribution of the $\phi \rightarrow K^+ K^-$ decay, $W(\cos \Theta, \Phi, \Psi)$, as a function of the polar (Θ) and azimuthal (Φ) angles of the K^+ meson in the ϕ-meson rest frame and the azimuthal angle (Ψ) of the photon polarization vector with respect to the production plane, can be parametrized by using nine SDMEs (ρ^0, ρ^1, ρ^2) and the degree of photon polarization (P_γ) [47, 83]:

$$
\begin{aligned}
W(\cos \Theta, \Phi, \Psi) = W^0(\cos \Theta, \Phi) \\
- P_\gamma \left[W^1(\cos \Theta, \Phi) \cos 2\Psi + W^2(\cos \Theta, \Phi) \sin 2\Psi \right],
\end{aligned}
\tag{1.19}
$$

where W^0 is the unpolarized part of the decay angular distribution, whereas

16

W^1 and W^2 are the polarized parts, which can be accessed only by using polarized photons. Here, W^0, W^1 and W^2 are given by

$$
W^0(\cos\Theta, \Phi) = \frac{3}{4\pi} \left[\frac{1}{2}(1 - \rho_{00}^0) + \frac{1}{2}(3\rho_{00}^0 - 1)\cos^2\Theta \right.
$$
$$
- \sqrt{2}\mathrm{Re}\rho_{10}^0 \sin 2\Theta \cos\Phi
$$
$$
\left. - \rho_{1-1}^0 \sin^2\Theta \cos 2\Phi \right], \tag{1.20}
$$
$$
W^1(\cos\Theta, \Phi) = \frac{3}{4\pi} \left[\rho_{11}^1 \sin^2\Theta + \rho_{00}^1 \cos^2\Theta \right.
$$
$$
- \sqrt{2}\mathrm{Re}\rho_{10}^1 \sin 2\Theta \cos\Phi
$$
$$
\left. - \rho_{1-1}^1 \sin^2\Theta \cos 2\Phi \right], \tag{1.21}
$$
$$
W^2(\cos\Theta, \Phi) = \frac{3}{4\pi} \left[\sqrt{2}\mathrm{Re}\rho_{10}^2 \sin 2\Theta \sin\Phi \right.
$$
$$
\left. + \mathrm{Im}\rho_{1-1}^2 \sin^2\Theta \sin 2\Phi \right]. \tag{1.22}
$$

The SDMEs (ρ^0, ρ^1, ρ^2) are defined, in terms of helicity amplitudes $T_{\alpha;\lambda,\lambda_\gamma}$, as

$$
\rho_{\lambda,\lambda'}^0 = \frac{1}{N} \sum_{\alpha,\lambda_\gamma} T_{\alpha;\lambda,\lambda_\gamma} T_{\alpha;\lambda',\lambda_\gamma}^\dagger, \tag{1.23}
$$

$$
\rho_{\lambda,\lambda'}^1 = \frac{1}{N} \sum_{\alpha,\lambda_\gamma} T_{\alpha;\lambda,-\lambda_\gamma} T_{\alpha;\lambda',\lambda_\gamma}^\dagger, \tag{1.24}
$$

$$
\rho_{\lambda,\lambda'}^2 = \frac{i}{N} \sum_{\alpha,\lambda_\gamma} \lambda_\gamma T_{\alpha;\lambda,-\lambda_\gamma} T_{\alpha;\lambda',\lambda_\gamma}^\dagger, \tag{1.25}
$$

where λ_γ and λ (λ') denote the helicities[9] of the incoming photon and the outgoing ϕ-meson, respectively, whereas a symbol α includes the polarizations of the incoming and outgoing baryons (protons). A normalization factor N is given by

$$
N = \sum_{\alpha,\lambda,\lambda_\gamma} T_{\alpha;\lambda,\lambda_\gamma} T_{\alpha;\lambda,\lambda_\gamma}^\dagger. \tag{1.26}
$$

According to Ref. [47], one can obtain five one-dimensional decay angular

---

[9]Here, the definition of the term "helicity" is different from the normal one. Throughout this thesis, the term "helicity" stands for the spin projection onto the z-axis (of the GJ frame), not the spin projection onto the direction of momentum.

distributions by integrating Eq. (1.19) over the remaining variables; i.e.,

$$W(\cos\Theta) = \frac{3}{2}\left[\frac{1}{2}(1-\rho^0_{00})\sin^2\Theta + \rho^0_{00}\cos^2\Theta\right], \qquad (1.27)$$

$$W(\Phi) = \frac{1}{2\pi}(1 - 2\text{Re}\rho^0_{1-1}\cos 2\Phi), \qquad (1.28)$$

$$W(\Phi - \Psi) = \frac{1}{2\pi}\left[1 + 2P_\gamma\bar\rho^1_{1-1}\cos 2(\Phi - \Psi)\right], \qquad (1.29)$$

$$W(\Phi + \Psi) = \frac{1}{2\pi}\left[1 + 2P_\gamma\Delta_{1-1}\cos 2(\Phi + \Psi)\right], \qquad (1.30)$$

$$W(\Psi) = 1 - P_\gamma(2\rho^1_{11} + \rho^1_{00})\cos 2\Psi. \qquad (1.31)$$

Here, we define $\bar\rho^1_{1-1} \equiv (\rho^1_{1-1} - \text{Im}\rho^2_{1-1})/2$ and $\Delta_{1-1} \equiv (\rho^1_{1-1} + \text{Im}\rho^2_{1-1})/2$. Hereafter, we call $\bar\rho^1_{1-1}$ a "decay asymmetry".

When helicity-conservation holds [i.e., $\lambda_\gamma = \lambda$ (λ')], only two SDMEs, ρ^1_{1-1} and $\text{Im}\rho^2_{1-1}$, can take non-zero values, and the others vanish ($= 0$). We also have a relation $\rho^1_{1-1} = -\text{Im}\rho^2_{1-1}$ [83]. Thus, among the five SDMEs in Eqs. (1.27)–(1.31), only $\bar\rho^1_{1-1}$ can take a non-zero value under helicity-conservation.

The decay asymmetry $\bar\rho^1_{1-1}$ has a special meaning: $\bar\rho^1_{1-1}$ can be rewritten in terms of the contribution of natural-parity exchange processes ($\sigma^N = |T^N|^2$) and that of unnatural-parity exchange processes ($\sigma^U = |T^U|^2$) under helicity-conservation [47]:

$$\bar\rho^1_{1-1} = \frac{1}{2}\frac{\sigma^N - \sigma^U}{\sigma^N + \sigma^U}. \qquad (1.32)$$

Thus, $\bar\rho^1_{1-1}$ provides the relative contribution from natural-parity and unnatural-parity exchange processes in t-channel. It gives $+0.5$ for pure natural-parity exchange processes (e.g., Pomeron, daughter Pomeron, multi-gluon and scalar meson exchanges), whereas it gives -0.5 for pure unnatural-parity exchange processes (e.g., pseudoscalar π and η exchanges).

Non-zero values of the SDMEs other than ρ^1_{1-1} and $\text{Im}\rho^2_{1-1}$ indicate the existence of helicity-nonconserving processes. In particular, ρ^0_{00} measures the probability of single helicity-flip transitions from the incident photon to the outgoing ϕ-meson ($\lambda_\gamma = \pm 1 \rightarrow \lambda_\phi = 0$) and is explicitly written from Eq. (1.23) as [64]:

$$\rho^0_{00} = \frac{2}{N}\sum_\alpha |T_{\alpha;01}|^2, \qquad (1.33)$$

18
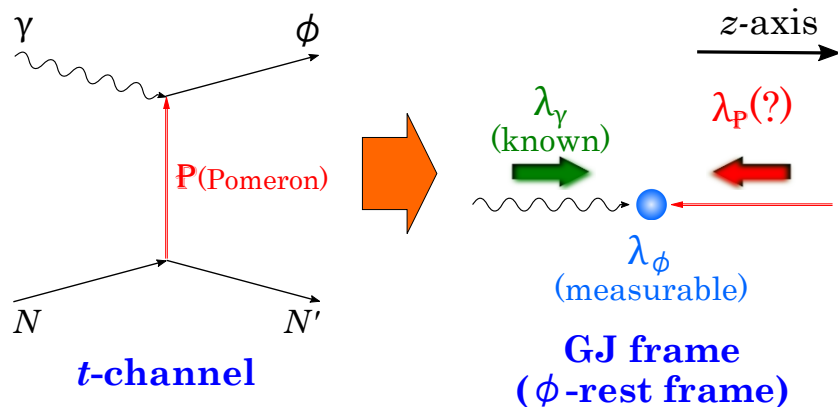
Figure 1.9: (Left figure): Example of t-channel exchange processes. The figure illustrates ϕ-photoproduction off nucleons with the t-channel Pomeron ($\mathbb{P}$) exchange. (Right figure): Illustration of the photon-Pomeron-ϕ vertex viewed in the GJ frame. Simbols λ_γ, λ_ϕ and $\lambda_\mathbb{P}$ stand for the helicities (z-components of spin) of the photon, the ϕ-meson and the Pomeron, respectively.

whereas $\mathrm{Re}\rho^0_{1-1}$ measures the interference of helicity-nonflip ($\lambda_\phi = \lambda_\gamma$) and double helicity-flip ($\lambda_\gamma = \pm 1 \rightarrow \lambda_\phi = -\lambda_\gamma$) amplitudes [64]:

$$\mathrm{Re}\rho^0_{1-1} = \frac{2}{N}\mathrm{Re}\sum_\alpha T_{\alpha;11}T^\dagger_{\alpha;1-1}. \tag{1.34}$$

In the GJ frame, the presence of single helicity-flips indicates that the helicity of the particle exchanged in t-channel is ± 1, whereas the presence of double helicity-flips indicates that the helicity of the exchanged particle is ± 2. This is illustrated in Fig. 1.9. Since the momentum of the exchanged particle is always collinear with the z-axis (the quantization axis of spin), the following equation holds for an arbitrary production angle of the ϕ-meson:

$$\lambda_{t\text{-channel}} = \lambda_\phi - \lambda_\gamma, \tag{1.35}$$

where $\lambda_{t\text{-channel}}$ is the helicity of the particle exchanged in t-channel.

We again emphasize that among the conventional processes (i.e., the Pomeron, π and η exchanges), only the Pomeron exchange can contribute to helicity-flip amplitudes[10] and that the presence of helicity-flips will support the modified DL model (see Sect. 1.4.2).

---

[10]Besides the conventional processes, the scalar meson exchanges [$a_0(980)$, $f_0(980)$, $\sigma =$

1.5   Coherent ϕ-meson photoproduction from helium-4

It has been shown in the previous sections that ϕ-meson photoproduction off nucleons is a good probe for gluonic interactions at low energies owing to the OZI suppression of meson exchanges. In coherent ϕ-meson photoproduction from helium-4 (i.e., $\gamma^4\mathrm{He} \rightarrow \phi^4\mathrm{He}$), the Pomeron and multi-gluon exchange processes are further enhanced thanks to the following reason.

Photoproduction of mesons off nuclei is mostly categorized into two reactions: "coherent" and "incoherent" reactions (Fig. 1.10). In the case of coherent reactions, the incident photon interacts with the whole nucleus, and the nucleus remains intact in the final state. In the case of incoherent reactions, the incident photon interacts with a single nucleon inside the nucleus, and the nucleus breaks up in the final state. Coherent meson photoproduction is of particular interest. With an appropriate choice of the quantum numbers of the target nucleus such as spin and parity, coherent reactions can be used to project out specific parts of the elementary reaction amplitudes (i.e., they act as a "spin and parity filter").

Coherent meson photoproduction off ^{4}He is an interesting channel because the quantum numbers of ^{4}He nuclei filter out unnatural-parity exchange processes such as the π and η exchanges. Here, a natural-parity (unnatural-parity) exchange process means a process where the exchanged particle in t-channel has a natural-parity $P = (-1)^J$ [unnatural-parity $P = -(-1)^J$], where J is the spin of the particle. The above statement can be derived as follows: let us consider a process A $\rightarrow$ A$'$ + B such that a $J^P = 0^+$ particle (A) emits an unnatural-parity particle (B), remaining unchanged in spin and parity, as shown in Fig. 1.11. Let L be the orbital angular momentum of the particle B with respect to the particle A$'$ in the final state. Then the spin of the particle B must be equal to L because both the particles A and A$'$ have spin 0 (spin-conservation). Thus, the parity of the particle B is $P = -(-1)^L$ (unnatural-parity). The total parity of the initial state is $P = +1$, whereas that of the final state is $P = -(-1)^L \times (+1) \times (-1)^L = -(-1)^{2L} = -1$. This violates parity-conservation. Thus, this process (i.e.,

---

$f_0(500)$] and the tensor $f_2'(1525)$ exchange are possible due to their large coupling to the $\bar{K}K$ channel, Among them, the scalar meson exchanges do not contribute to helicity-flip amplitudes, whereas the tensor f_2' exchange can contribute to helicity-flip amplitudes [47]. Note that vector meson exchanges such as the ρ and ω exchanges, which can also contribute to helicity-flip amplitudes, are forbidden in ϕ-photoproduction due to their negative charge conjugation ($C = -1$) [84].

Coherent production

Incoherent production
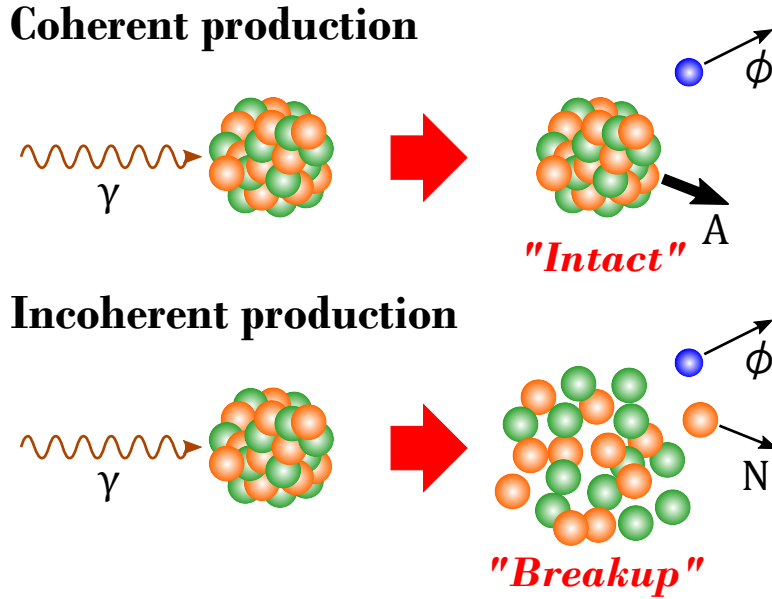
Figure 1.10:   Coherent (top) and incoherent photoproduction (bottom) of ϕ-mesons from nuclei. In coherent production, the nucleus remains intact in the final state, whereas in incoherent production, the nucleus breaks up in the final state (see also the text).
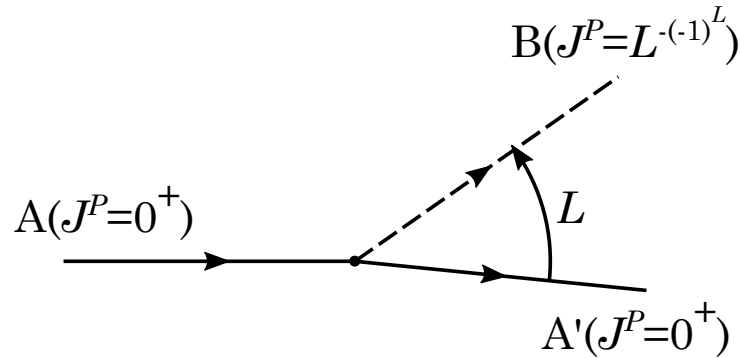
Figure 1.11:   Schematic diagram for a process A $\rightarrow$ A$'$ + B such that a $J^P = 0^+$ particle A emits an unnatural-parity particle B with an orbital angular momentum L with respect to the particle A$'$, remaining unchanged in spin and parity. See the text for the assignments of spin and parity for the particle B.

unnatural-parity exchange processes) is forbidden.

With the elimination of unnatural-parity exchanges as well as the suppression of meson exchanges, coherent ϕ-meson photoproduction off ^{4}He provides an ideal laboratory for investigating gluonic interactions at low energies.

1.6   Experimental status of low-energy ϕ-photoproduction

1.6.1 ϕ-photoproduction off proton

Due to the inherent smallness of the ϕ-photoproduction cross sections, the data on the $\gamma p \to \phi p$ reaction are, in general, sparse with limited statistical precision, and most of them exist in the high-energy regime. The first precise measurement near the production threshold was performed by the LEPS Collaboration [85], who reported that the energy dependence of the forward cross section ($\theta = 0°$) exhibits a localized "bump" around $E_\gamma \sim 2$ GeV, as indicated by blue open circles in Fig. 1.12, whereas a simple Pomeron exchange model predicts a smooth rise from the threshold. Later, the CLAS Collaboration published high-statistics data [86,87] and confirmed this non-monotonic behavior (black open squares in Fig. 1.12), though the data were obtained by extrapolating from rather large scattering-angle regions. More recently, the LEPS Collaboration extended the maximum beam energy from 2.4 to 2.9 GeV and also observed an excess from a model prediction from the Pomeron, π and η exchanges [88] (red filled circles in Fig. 1.12).

The LEPS Collaboration [85,88,89] also measured SDMEs with linearly polarized photons, which help us to understand the production mechanism. Figure 1.13 shows the energy dependence of the SDMEs ρ_{00}^0, $\mathrm{Re}\rho_{1-1}^0$, $\bar{\rho}_{1-1}^1$, Δ_{1-1} and $2\rho_{1-1}^1 + \rho_{00}^1$ in the GJ frame. While ρ_{00}^0 and $\mathrm{Re}\rho_{1-1}^0$ ensure helicity-conservation in t-channel, the decay asymmetry $\bar{\rho}_{1-1}^1$ indicates a sizable 20–30% contribution from unnatural-parity exchange processes[11], decreasing with increasing energy, which is compatible with a theoretical calculation for the Pomeron, π and η exchanges.

There are several interpretations of this non-monotonic behavior: Ozaki *et al.* [90] and Ryu *et al.* [84] conjectured the non-monotonic behavior as coupled-channel effects between the ϕp and $K^+\Lambda(1520)$ channels. Since both channels have the same final state K^+K^-p, they could affect each other. Kiswandhi *et al.* [91,92] made an attempt to attribute the non-monotonic behavior to an excitation of missing nucleon resonances with non-negligible

---

[11]This can be evaluated from Eq. (1.32) under helicity-conservation.
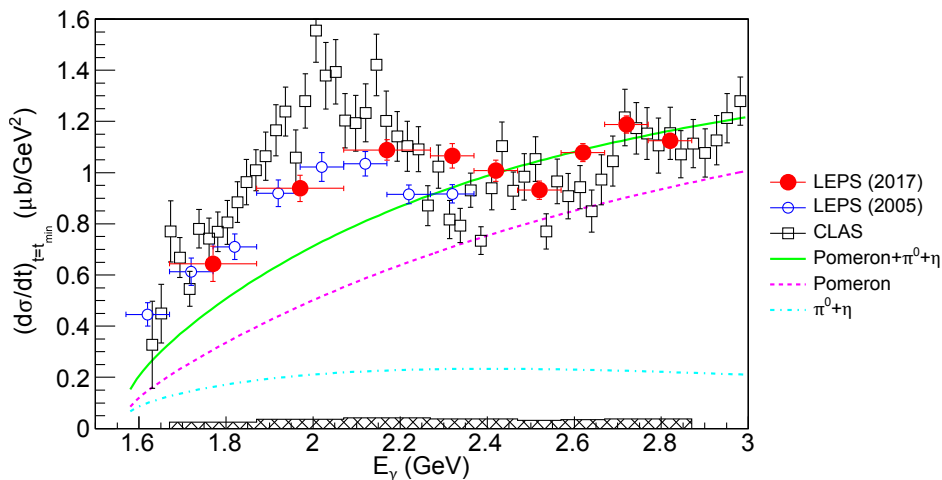
Figure 1.12:   Energy dependence of the forward cross section ($\theta = 0°$). Blue open circles show the first LEPS data [85], whereas red filled circles show the LEPS 2017 data [88]. Black open squares show the CLAS data [86]. A green solid curve shows the sum of theoretical curves for the Pomeron (pink dashed) and ($\pi + \eta$) (blue dash-dotted) exchanges [47]. Note that the overall strength for the Pomeron exchange is adjusted from the LEPS 2017 data and, is different from that in Ref. [47]. The figure is taken from Ref. [88].

amount of $s\bar{s}$ contents. However, this seems to be unlikely because the CLAS data [86,87] show that the non-monotonic behavior appears only at forward production angles. The manifestation of the daughter Pomeron trajectory, which is already discussed in Sect. 1.4.3, could also account for the non-monotonic behavior.

Despite considerable theoretical efforts, a definitive interpretation of the non-monotonic behavior has not been obtained yet. This is mainly because there always exist uncertainties in modeling the Pomeron exchange in the low-energy regime. Therefore, it is important to pin down the low-energy behavior of the Pomeron amplitude experimentally if any.

1.6.2   Coherent ϕ-photoproduction off deuteron

As discussed in Sect. 1.5, coherent meson photoproduction off nuclei can be used as a "filter" to project out specific parts of the elementary reaction amplitudes. Another example for such a reaction is coherent ϕ-meson pho-
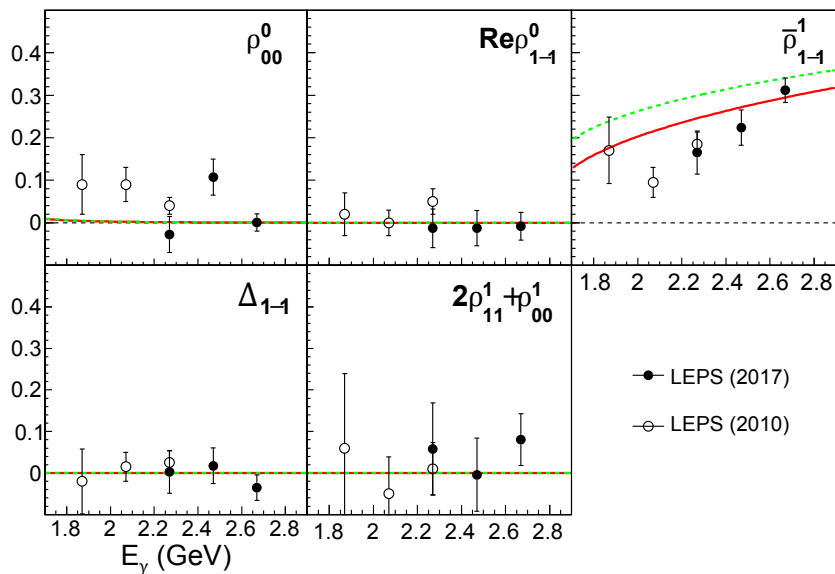
Figure 1.13:   Energy dependence of the SDMEs (ρ_{00}^0, $\mathrm{Re}\rho_{1-1}^0$, $\bar{\rho}_{1-1}^1$, Δ_{1-1} and $2\rho_{1-1}^1 + \rho_{00}^1$) in the GJ frame for the $\gamma p \to \phi p$ reaction. Here, a range for momentum transfer t is restricted to $0 < |t| - |t|_{\min} < 0.05$ GeV^2, where $|t|_{\min}$ is the minimum momentum transfer $|t|$. Filled and open circles show the recent LEPS data (2017) [88] and the previous LEPS data (2009) [89], respectively. A red solid curve shows the same theoretical calculation as that in Fig. 1.12, while a green dashed curve shows the original work by Titov *et al.* [47]. The figures are taken from Ref. [88].

toproduction from deuteron ($\gamma d \to \phi d$). With the use of the isoscalar target, this reaction filters out the isovector part of the ϕ-photoproduction amplitudes (i.e., the π-exchange amplitude). This, in conjunction with negligible contribution from the η exchange[12], enables us to investigate the Pomeron dynamics at low energies [93, 94].

The LEPS Collaboration measured the differential cross section and decay asymmetry for the coherent $\gamma d \to \phi d$ reaction at forward angles near the threshold using linearly polarized photons [95]. In this measurement, the production of ϕ-mesons was identified by detecting K^+K^- pairs from the $\phi \to K^+K^-$ decay with a forward spectrometer, whereas the coherent production events were disentangled from the incoherent ones by looking at

---

[12]This stems from a small value of the ηNN coupling constant $g_{\eta NN}$ [38].
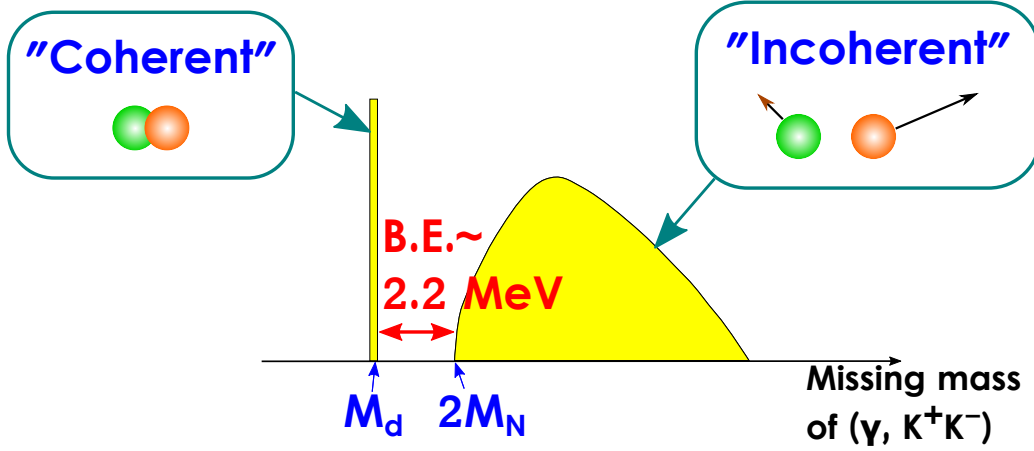
Figure 1.14: Principle of how to identify the coherent production events in a MM(K^+K^-) distribution. The horizontal axis represents the missing mass MM(K^+K^-). M_d and M_N denote the masses of a deuteron and a nucleon, respectively. See the text for the detailed explanation.

the missing mass of the $d(\gamma, K^+K^-)X$ reaction[13] [MM(K^+K^-)]. Figure 1.14 shows the principle of how to identify the coherent events in a MM(K^+K^-) distribution. Since the missing mass MM(K^+K^-) is equivalent to the center-of-mass energy of a pn pair in the final state, the missing mass MM(K^+K^-) corresponds to the deuteron mass (M_d) in the case of the coherent process, whereas in the case of the incoherent process, it is distributed with an end-point of the two-nucleon mass[14] ($= 2M_N$). Ideally, these two distributions are separated by the deuteron binding energy (~ 2.2 MeV), but are practically overlapped due to detector resolutions. Therefore, for the evaluation of the number of the coherent events, MM(K^+K^-) distributions were fitted with Monte-Calro-simulated coherent and incoherent components as shown in Fig. 1.15(a).

Figure 1.15(b) shows the decay asymmetry $\bar{\rho}^1_{1-1}$ in the GJ frame at forward angles, $0 < |t| - |t|_{\min} < 0.1$ GeV^2, as a function of the photon energy. Here, $|t|_{\min}$ is the minimum momentum transfer $|t|$ for the deuteron target. No strong energy dependence of $\bar{\rho}^1_{1-1}$ was found, and the averaged $\bar{\rho}^1_{1-1}$

---

[13]At forward production angles, the momenta of recoil deuterons is too small to detect them directly.

[14]This energy corresponds to the case where the relative momentum of a pn pair is equal to zero.
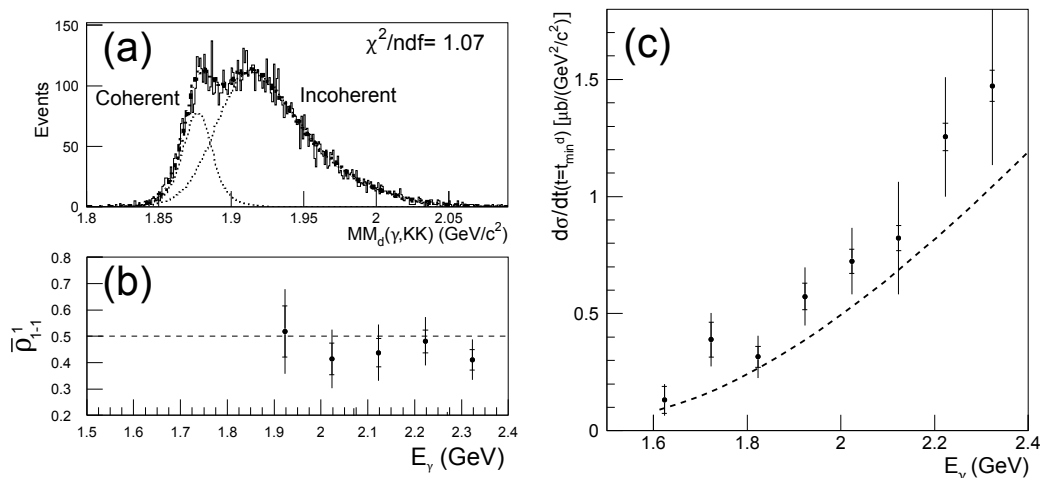
Figure 1.15:   (a) Missing mass spectrum for the $d(\gamma, K^+K^-)X$ reaction. A bold dotted curve represents the fit result with Monte-Carlo-simulated coherent and incoherent components (dashed curves) (b) Decay asymmetry $\bar{\rho}^1_{1-1}$ for the $\gamma d \to \phi d$ reaction in the GJ frame at forward angles ($0 < |t| - |t|_{\min} < 0.1$ GeV^2) as a function of the photon energy. The smaller error bars represent the statistical errors, whereas the larger ones represent the sum of statistical and systematic ones in quadrature. (c) Differential cross section $d\sigma/dt$ at $t = -|t|_{\min}$ for the $\gamma d \to \phi d$ reaction as a function of the photon energy. The meanings of the error bars are the same as those of (b). A dashed curve shows a theoretical calculation for a Pomeron exchange model including a small contribution from the η-exchange [94]. The figures are taken from Ref. [95].

was determined to be $0.48 \pm 0.07(\text{stat}) \pm 0.10(\text{syst})$. This value is consistent with the maximum boundary ($+0.5$), showing a complete dominance of natural-parity exchange processes, or a negligibly small contribution of the unnatural-parity η exchange.

Figure 1.15(c) shows the energy dependence of the differential cross section $d\sigma/dt$ extrapolated to $t = -|t|_{\min}$. A dashed curve shows a model calculation for the Pomeron and η exchanges [94]. Here, large systematic errors were caused by the disentanglement of the coherent production events. This is because, since the separation energy of deuteron is small (~ 2.2 MeV), the coherent production events are not clearly identified in the MM(K^+K^-) spectra [see Fig. 1.15(a)]. Although the precise energy dependence cannot
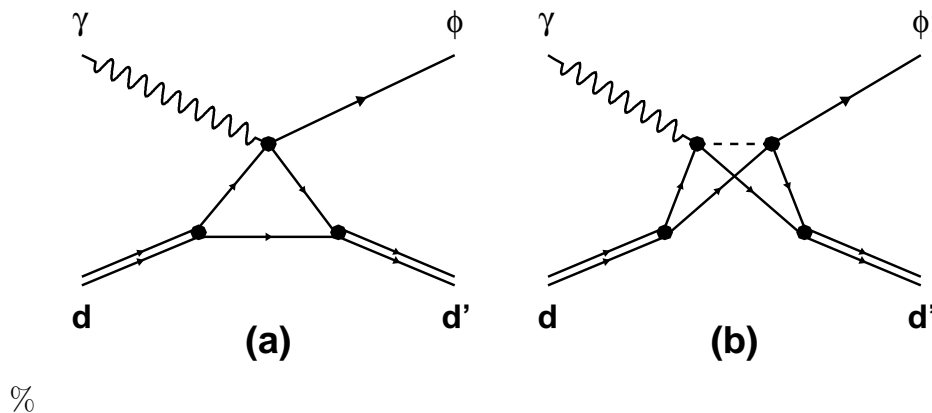
Figure 1.16:   Schematic diagrams for (a) single-scattering and (b) double-scattering processes.

be discussed due to the large systematic errors, the experimental data are obviously underestimated by the theoretical model.

Coherent photoproduction of vector mesons from nuclei has been described well by using the Glauber multiple-scattering theory [96]. In the case of a deuteron target, the coherent process consists of two sub-processes [Figs. 1.16(a) and (b)]: the one corresponds to the single-scattering process, which dominates at small $|t|$, whereas the other corresponds to the double-scattering process, which has a significant contribution at larger (intermediate) $|t|$ [97]. In ϕ-photoproduction at low energies with $E_\gamma < 3$ GeV and at forward production angles with $|t| \lesssim 0.4$ GeV^2, which is relevant for LEPS measurements, the single-scattering assumption is a good approximation. Titov et $al.$ [94] related the differential cross section for the coherent $\gamma d \to \phi d$ reaction $(d\sigma^{\gamma d}/dt)$ to that for ϕ-photoproduction from free nucleons via isoscalar t-channel exchange processes $(d\sigma^{\gamma N; T=0}/dt)$. as

$$\frac{d\sigma^{\gamma d}}{dt} \simeq 4Z(t)\frac{d\sigma^{\gamma N; T=0}}{dt}, \tag{1.36}$$

where a factor of 4 comes from the nuclear mass number $A = 2$, and $Z(t)$ is a structure factor, which is given by

$$Z(t) = F_{\mathcal{C}}^2(t) + 4F_{\mathcal{Q}}^2(t), \tag{1.37}$$

where $F_{\mathcal{C}}(t)$ and $F_{\mathcal{Q}}(t)$ are the charge and quadrupole form factors for deuterons, respectively. At small $|t|$ under consideration, the structure function $Z(t)$ is

also related to the well-known structure function $A(t)$ for elastic $ed \to ed$ scattering[15] as

$$A(t) \simeq Z(t)G_N^2(t), \tag{1.40}$$

where $G_N(t) = 1/(1 - t/0.71)^2$ is the dipole nucleon form factor.

Using Eq. (1.36), one can deduce the energy dependence of the $d\sigma^{\gamma N; T=0}/dt$ at zero degrees from the coherent $\gamma d \to \phi d$ data. Figure 1.17 shows the energy dependence of the deduced $d\sigma^{\gamma N; T=0}/dt$ at zero degrees, together with available forward cross section data for the $\gamma p \to \phi p$ reaction $(d\sigma^{\gamma p}/dt)$. A solid curve represents a theoretical calculation for the Pomeron and η exchanges, whereas a dashed curve represents a model calculation for the Pomeron, π and η exchanges [94]. Interestingly, the two highest data points for $d\sigma^{\gamma N; T=0}/dt$ exhibit a different energy dependence from that for $d\sigma^{\gamma p}/dt$; that is, a smooth rise with energy, which is compatible with the theoretical calculation. Due to the large systematic errors, any definitive conclusion cannot be drawn, but this may hint at the origin of the non-monotonic behavior.

Although the LEPS measurement on the coherent $\gamma d \to \phi d$ reaction successfully demonstrated the elimination of the π exchange, there still remain the following issues:

- The large systematic errors caused by the disentanglement of the coherent events make it difficult to precisely determine the energy dependence of the forward amplitude for any specific process.

---

[15]The cross section for the elastic $ed \to ed$ scattering can be written in terms of two structure functions $A(Q^2)$ and $B(Q^2)$ as a function of the virtual photon four-momentum (Q^2) (Rosenbluth separation);

$$\frac{d\sigma}{d\Omega} = \left(\frac{d\sigma}{d\Omega}\right)_{\text{Mott}} \left[A(Q^2) + B(Q^2)\tan^2\frac{\theta_e}{2}\right], \tag{1.38}$$

where $(d\sigma/d\Omega)_{\text{Mott}}$ is the Mott cross section and θ_e is the electron scattering angle. The structure functions $A(Q^2)$ and $B(Q^2)$ are related to the charge (G_C), quadrupole (G_Q) and magnetic (G_M) form factors:

$$A(Q^2) = G_C^2(Q^2) + \frac{8}{9}\eta^2 G_Q^2(Q^2) + \frac{2}{3}\eta G_M^2(Q^2),$$
$$B(Q^2) = \frac{4}{3}\eta(1+\eta)G_M^2(Q^2), \tag{1.39}$$

where $\eta = Q^2/(4m_d^2)$ and m_d is the deuteron mass. $G_C(Q^2)$, $G_Q(Q^2)$ and $G_M(Q^2)$ are normalized according to $G_C(0) = 1$, $G_Q(0) = Q_d$ and $G_M(0) = \mu_d m_d/m_N$, where Q_d and μ_d are the electric quadrupole moment and magnetic dipole moment of deuterons, respectively, and m_N is the nucleon mass.
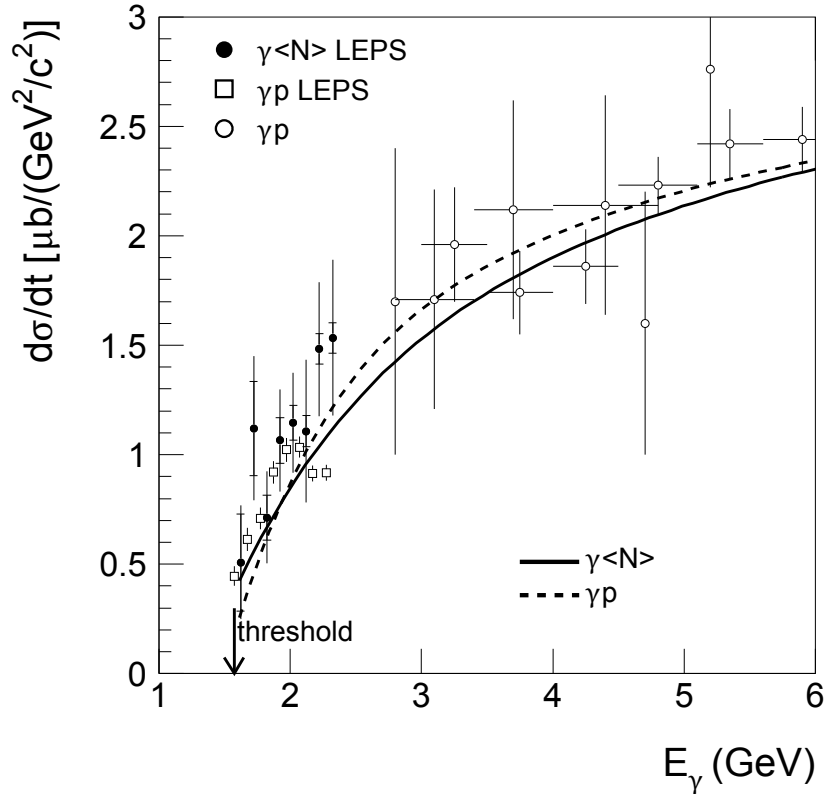
Figure 1.17:   Energy dependence of the differential cross section at zero degrees for the ϕ-photoproduction from free nucleons by isoscalar t-channel exchange processes $d\sigma^{\gamma N; T=0}/dt$ (Filled circles). Open squares and open circles show the LEPS data [85] and old experimental data, respectively, on the $\gamma p \to \phi p$ reaction ($d\sigma^{\gamma p}/dt$). Solid and dashed curves represent theoretical calculations for $d\sigma^{\gamma N; T=0}/dt$ and $d\sigma^{\gamma p}/dt$, respectively, with a Pomeron exchange model including the π and η exchanges [94]. Here, $d\sigma^{\gamma N; T=0}/dt$ has no contribution from the π-exchange. Note that the LEPS γp data are shifted by -50 MeV for clarity. The figure is taken from Ref. [95].

- There still exists a possibility of unnatural-parity exchange processes other than the π exchange, which could be background processes for investigating the Pomeron exchange and other gluonic interactions at low energies.

1.7 Aim of this study

The aim of this study is to investigate gluonic interactions at low energies. Since gluons are flavor-blind, the information on gluonic interactions obtained here would be universal and applicable to all hadronic processes: for example, the possible formation of a bound state of a charmonium [a meson made of a charm quark (c) and an anti-charm quark ($\bar{c}$)] with a nucleon or a nucleus has been discussed for many years on the basis of the static force mediated by gluons, known as the QCD van der Waals force[16] [98–101]. Recently, since the observation of new resonance states $P_c(4380)^+$ and $P_c(4450)^+$ with the minimum quark contents of $uudc\bar{c}$ was announced by the LHCb Collaboration [102], theoretical interest in such a bound state has been revived regarding the internal structures of these new states. There are intensive discussions on their internal structures, including non-resonant interpretations as well [see Ref. [103] for a recent review on the exotic hadronic states with hidden-charm ($c\bar{c}$) contents]. As these new states were observed in the $J/\Psi p$ channel, one naively expects them to be a bound state of a charmonium with a proton [104–108].

Furthermore, low-energy coherent ϕ-meson photoproduction off ^{4}He will offer a new insight on the Pomeron exchange. The Pomeron is a universal object appearing in all high-energy hadronic processes, especially in the diffractive regime (i.e., at very forward scattering angles). The concept of the Pomeron exchange successfully explains various phenomena inherent in high-energy hadron-hadron collisions. However, very little is known about its fundamental properties, and its derivation from QCD is yet to come. For example, we do not know exactly how the Pomeron couples to hadrons. The measurement of the decay angular distributions of photo-produced ϕ-mesons will answer this question (see Sect. 1.4).

The importance of this study is further emphasized by the recent observations of the non-monotonic behavior of the forward ($\theta = 0°$) cross sec-

---

[16]In atomic and molecular physics, the van der Waals force refers to a relatively weak electric force that binds neutral atoms or molecules together, which arises from instantaneous fluctuations of the internal charge of a neutral particle.

tion present in the $\gamma p \to \phi p$ reaction [85–88] (see also Sect. 1.6.1). Several theoretical models [38, 44, 84, 90–92, 109] have been proposed to explain the non-monotonic behavior, but all of them are not conclusive. This is mainly because all the models strongly depend on the near-threshold behavior of the Pomeron-exchange amplitude.

Coherent ϕ-meson photoproducion off deuteron was thought to be a simple and useful reaction for investigating the Pomeron and multi-gluon exchanges at low energies because of the absence of the isovector π exchange, which is a main background contribution for this purpose [93, 94]. In the previous LEPS measurement [95], however, the systematic errors coming from the disentanglement of the coherent production events were too large to discuss the energy dependence of the forward ($\theta = 0°$) cross section in detail. By contrast, in coherent ϕ-photoproduction off ^{4}He, one expects better separation of the coherent events than that with a deuteron target because of the large separation energy of ^{4}He nuclei ($\sim$ 28 MeV; cf. $\sim$ 2.2 MeV for deuteron; see Fig. 1.14). Therefore, one can investigate the Pomeron and multi-gluon exchanges at low energies with better accuracies.

We have measured the differential cross sections and decay angular distributions for coherent ϕ-meson photoproduction from ^{4}He at forward angles ($-t < 0.2$ GeV^2) in the energy range of $E_\gamma = 1.685$–2.385 GeV with linearly polarized photons at LEPS/SPring-8. In this thesis, we present the first-ever results on both the differential cross sections and decay angular distributions for this reaction.

This thesis is organized as follows. Section 2 describes the LEPS/SPring-8 facility and the experimental setup. Section 3 describes the reconstruction of the charged particles detected by a spectrometer, the determination of photon energy, the event selection and the analysis on the coherent-ϕ-production events. The results and discussions for the decay angular distributions and the differential cross sections are presented in Sect. 4, in which we first look at the decay angular distributions to verify the absence of unnatural-parity exchange processes in this reaction, and then discuss the results on the cross sections. This thesis ends with a conclusion in Sect. 5.

2 Experiment

The experiment was carried out at the LEPS/SPring-8 facility. It is a unique facility in the world, which can provide a high-intensity and highly linearly-polarized photon beam. Linearly-polarized photons are produced via backward Compton scattering between laser photons and the 8-GeV electrons circulating in the storage ring [110]. The maximal beam energy reaches 2.4 GeV or 2.9 GeV, depending on the wavelength of the laser used. The beam energy is sufficient to produce, especially, hadrons with a strange (or anti-strange) quark.

A spectrometer was used to detect the K^+K^- pairs from the $\phi \to K^+K^-$ decay and to analyze their momenta. The K^+K^- pairs were identified through the reconstructed mass and charge of charged particles detected by the LEPS spectrometer.

A series of experiments using a linearly polarized photon beam has been started since 2000. Based on Refs. [111–113], the details of the LEPS/SPring-8 facility and the LEPS spectrometer are described here.

2.1 SPring-8 facility

SPring-8 (Super-Photon ring-8 GeV) is a third-generation synchrotron-radiation (SR) facility, which has been completed in 1997. Third-generation facilities are optimized to achieve a high-brightness Synchrotron Orbital Radiation (SOR) light source [Vacuum UV (VUV) and soft X-ray source) by using insertion devices, mainly undulators. There are three third-generation SR facilities with the electron energy $E_e > 5$ GeV in the world; ESRF (Grenoble), APS (Argonne) and SPring-8 (Japan). Among them, SPring-8 is the largest facility, and provides the brightest light source.

The accelerator complex of SPring-8 consists of an injector Linear Accelerator (LINAC), a booster synchrotron, and a low-emittance and high-brightness storage ring. Figure 2.1 shows a schematic view of the accelerator complex of SPring-8. Electrons are generated at the electron gun, and accelerated up to an energy of 1 GeV in the injector LINAC with a length of 140 m. The 1-GeV electrons are transported to the booster synchrotron with a circumference of 396 m, and are accelerated up to 8 GeV. The 8-GeV electrons are injected from the synchrotron into the storage ring with a circumference of 1436 m, and are stored.

The 8-GeV electrons form a bunch and circulate in the storage ring with
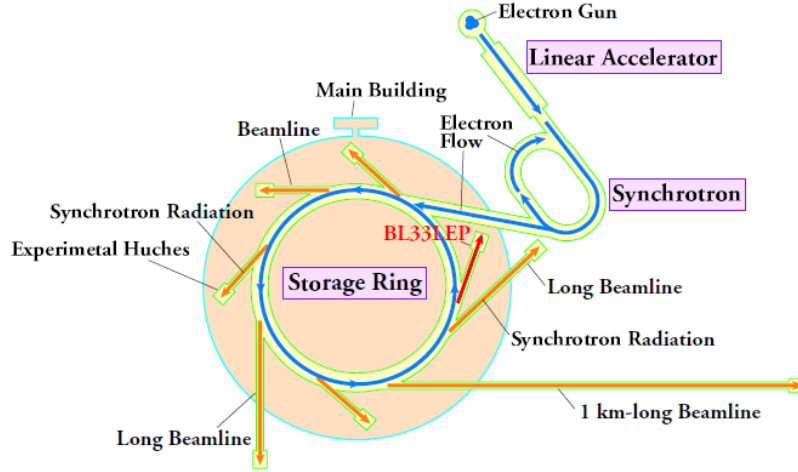
Figure 2.1:   Schematic view of the accelerator complex of SPring-8. The picture is taken from the SPring-8 web cite [114].

a frequency of 0.2088 MHz. The time interval of successive electron bunches is 1.966 nsec. In the storage ring, there are about 2440 electron bunches, which are filled with several filling patterns[17] [114]. The nominal current of the stored beam is 100 mA. The electron beam has a small emittance of 2.4 nm · rad with average beam widths of $\sigma_x = 75$ μm and $\sigma_y = 25$ μm in the horizontal and vertical directions, respectively.

The stored electron beam is used to generate synchrotron radiation photons at bending magnets, undulators and wigglers. The photons produced via synchrotron radiation are provided to various beamlines in the experimental hall. The photon beams with a high brightness and low emittance are commonly used for researches mainly on material and life science. There are 57 beamlines in SPring-8, and 56 of them are now under operation. One of these beamlines is used by our LEPS group, called BL33LEP. In the LEPS beamline, High-energy photon beam produced via backward Compton scattering are used for hadron physics, instead of radiation photons.

---

[17]The time interval between successive bunches is basically equal to 1.966 nsec, except that it corresponds to 23.6 nsec for A-mode (one of the bunch modes).

2.2 LEPS facility

At the Laser-Electron-Photon (LEPS) facility at SPring-8, a multi-GeV photon beam is produced via Backward Compton Scattering (BCS) between laser photons and the 8-GeV electrons circulating in the storage ring.

A schematic view of the LEPS beamline is shown in Fig. 2.2. The LEPS beamline consists of three parts; (a) a laser-electron collision part in the storage (SR) ring, (b) a laser hatch for laser injection, and (c) an experimental hatch, where the spectrometer is placed. A BCS process is illustrated in the same figure: laser photons, which are optimized in the laser hatch, are injected to the storage ring. As shown in Fig. 2.2, we have a 7.8 m long straight section between two bending magnets in the storage ring. In this straight section, the BCS process takes place when a laser photon collides with an 8-GeV electron. The photons produced via the BCS process are delivered to the experimental hatch, and irradiate an experimental target. The recoil electrons are detected and momentum-analyzed by a tagging system placed at the exit of the bending magnet to measure the photon energy.

In the next section, the BCS process and devices to produce linearly-polarized photons are described.

2.2.1 Backward Compton scattering

General properties of backward Compton scattering are summarized here. Kinematic variables of backward Compton scattering (BCS) process in the laboratory frame are defined as shown in Fig. 2.3: E_e (E'_e) is the energy of the incident (scattered) electron, k_1 is the energy of the laser photon, E_γ is the energy of the BCS (scattered) photon, $\theta_1 \simeq 180°$ is the relative angle between the directions of the incident electron and the laser photon, and θ_2 is the scattering angle of the BCS photon with respect to the direction of the incident electron. If $E_e \gg k_1$, a photon is scattered in an extremely-forward direction due to the Lorentz boost. In such case, the scattered (BCS) photon gains an enormous energy from the incident electron by the Fitzgerald-Lorentz effect in the recoil process. Then the energy of the BCS photon is given by

$$E_\gamma = k_1 \frac{1 - \beta \cos \theta_1}{1 - \beta \cos \theta_2 + \frac{k_1(1-\cos\theta)}{E_e}}, \tag{2.1}$$

where β is the velocity of the incident electron in unit of the speed of light c, and $\theta = \theta_2 - \theta_1$. Assuming that the incident electron is relativistic; i.e.,
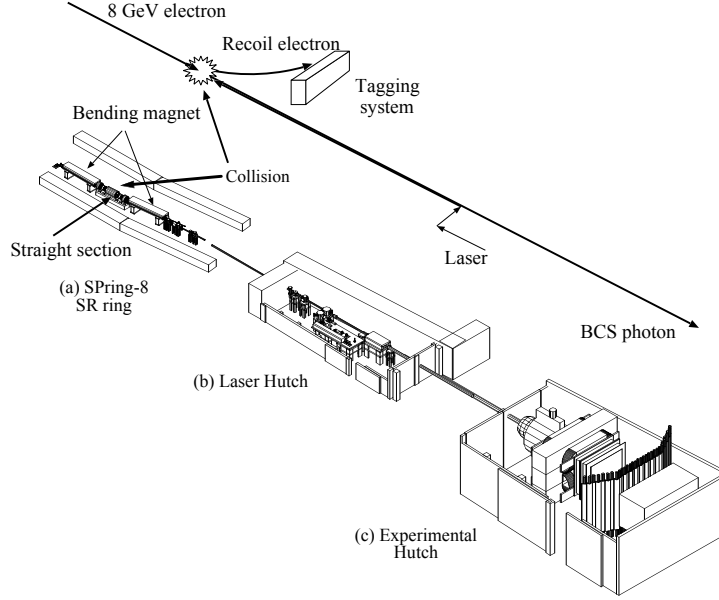
Figure 2.2:   Schematic view of the LEPS facility at SPring-8. The LEPS facility consists of three parts: (a) a laser-electron collision part in the storage ring (SR). (b) a laser hutch for laser injection. (c) an experimental hatch. The explanation of the collision between a 8-GeV electron and a laser photon in the backward Compton scattering is illustrated in this figure.

$\gamma = E_e/m_e \gg 1$, $\beta \simeq 1$, $\theta_1 \simeq 180°$ and $\theta_2 \ll 1$, Eq. (2.1) can be rewritten as

$$E_\gamma = \frac{4E_e^2 k_1}{m_e^2 + 4E_e k_1 + \theta_2^2 \gamma^2 m_e^2}, \tag{2.2}$$

where m_e is the electron mass (= 0.511 MeV) and $\gamma \sim 1.6 \times 10^4$ for 8-GeV electrons. The maximum energy of the BCS photon, i.e., the Compton edge, is obtained at $\theta_2 = 0°$:

$$E_\gamma^{\mathrm{max}} = \frac{4E_e^2 k_1}{m_e^2 + 4E_e k_1}. \tag{2.3}$$

The differential cross section of a BCS process as a function of the (BCS)
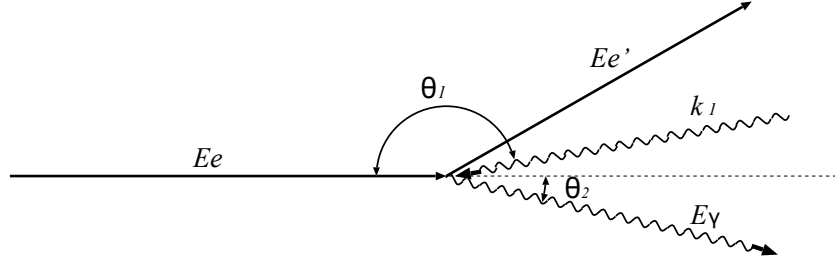
Figure 2.3: Kinematic variables of backward Compton scattering in the laboratory frame.

photon energy is given by [115]

$$
\begin{aligned}
\frac{d\sigma}{dE_\gamma} &= \frac{2\pi r_e^2 a}{E_\gamma^{\max}}(\chi + 1 + \cos^2 \alpha), \\
a &= \frac{m_e^2}{m_e^2 + 4E_e k_1}, \\
\chi &= \frac{\rho^2(1-a)^2}{1-\rho(1-a)}, \\
\cos \alpha &= \frac{1-\rho(1+a)}{1-\rho(1-a)}, \\
\rho &= \frac{E_\gamma}{E_\gamma^{\max}},
\end{aligned}
\tag{2.4}
$$

where $\gamma_e = 2.818$ fm is the classical electron radius. Figure 2.4 shows the differential cross section for the BCS process between the 8-GeV electrons and the laser photons with a wavelength of 355 nm as a function of the photon energy. A sub-GeV photon beam can be sufficiently obtained through the BCS process.

Linearly-polarized (circularly-polarized) BCS photons can be produced by using linearly-polarized (circularly-polarized) laser photons. Since the spin-flip amplitude is small in BCS process, the BCS photons retain most of the polarization of the incident laser photons. The degree of the BCS photon polarization is proportional to that of the laser photons (P_{laser}), and is given by

$$
P_\gamma = P_{\mathrm{laser}} \frac{(1 - \cos \alpha)^2}{2(\chi + 1 + \cos^2 \alpha)} \text{ for linear polarization,} \tag{2.5}
$$
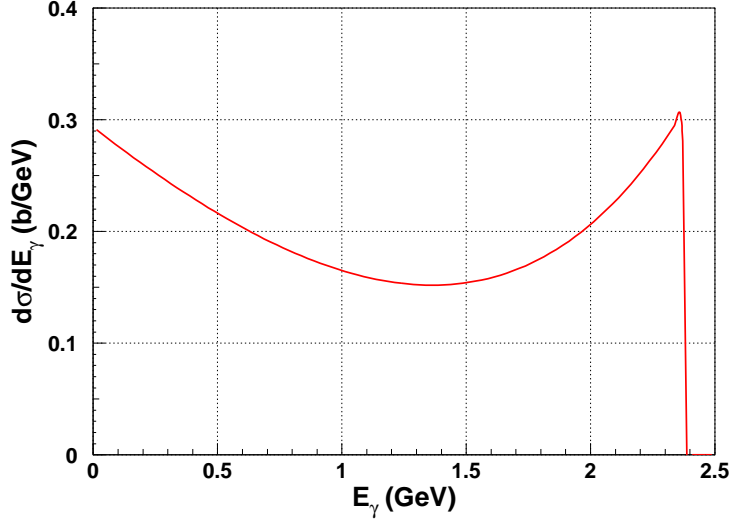
Figure 2.4: Differential cross section of the BCS process between the 8-GeV electrons and the laser photons with a wavelength of 355 nm as a function of photon energy.

and

$$P_\gamma = P_{\text{laser}} \left| \frac{(2 + \chi) \cos \alpha}{\chi + 1 + \cos^2 \alpha} \right| \text{ for circular polarization.} \qquad (2.6)$$

Figure 2.5 shows the degrees of linear and circular polarization for the photons produced via the BCS process between the 8-GeV electrons and the laser photons with a wavelength of 355 nm as a function of the photon energy, with the assumption of 100% laser polarization. The degree of polarization is maximum at the Compton edge, where the spin-flip amplitude for highly-relativistic electrons vanishes, and the scattered photons almost retain the initial laser polarization. In the case of linear polarization, the maximum polarization is obtained as $P_\gamma = P_{\text{laser}}[2a/(1 + a^2)]$ from Eq. (2.5). This gives about 94% of polarization at maximum with the 8-GeV electrons and the 351-nm laser photons with 100% polarization.

In the present experiment, a linearly-polarized photon beam was produced from the laser photons with a wavelength of 355 nm. The size of the BCS photon beam for $E_\gamma = 1.5$–2.4 GeV corresponds to $\sigma_x \sim 3.5$ mm and $\sigma_y \sim 2.0$ mm in the horizontal and vertical directions, respectively. Note
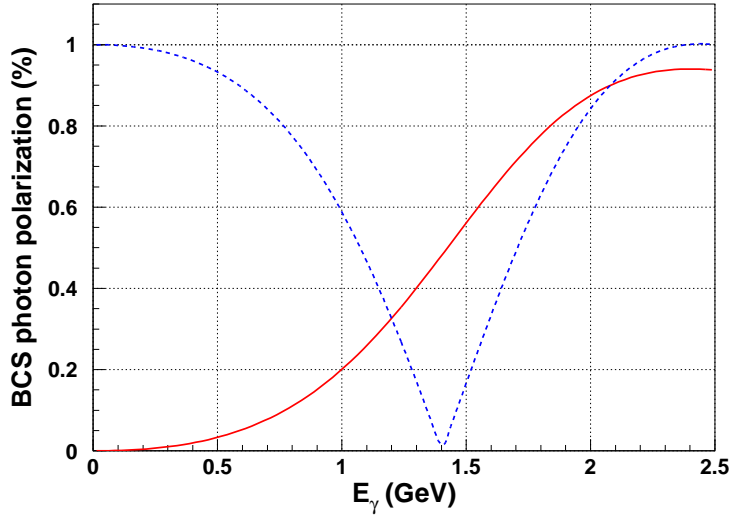
Figure 2.5:   Polarization of the photons produced via the BCS process between the 8-GeV electrons and the laser photons with a wavelength of 355 nm as a function of the photon energy, with the assumption of 100% laser polarization. A red solid curve represents linear polarization, whereas a blue dashed curve represents circular polarization.

that the difference between the sizes σ_x and σ_y is due to the emittance of the 8-GeV electron beam.

2.2.2   Laser operating system

Figure 2.6 shows a schematic drawing of the laser operating system. In order to achieve a intense LEP beam, the photons from two laser systems are injected simultaneously into the storage ring. Two solid -state lasers (Coherent Paladin) are used as a photon source. A typical power of the lasers is 8 W. The lasers oscillate with a single line mode with a wavelength of 355 nm. The corresponding maximal LEP beam energy is 2.385 GeV. The size of the laser beams is 1 mmϕ. The laser photons are vertically-polarized initially. The beam intensity was typically 1.0 Mcps in the present experiment.

The laser photon beams travel about 36 m before colliding with the circulating electrons. Beam expanders are used to tune the beam size at the collision point. The beam expanders enlarge and focus the laser beams with

1. Paladin laser   6. Prism
2. Beam expander   7. 2nd mirror
3. $\lambda/2$ wave length plate   8. 1st mirror
4. 4th mirror   9. Monitor
5. 3rd mirror
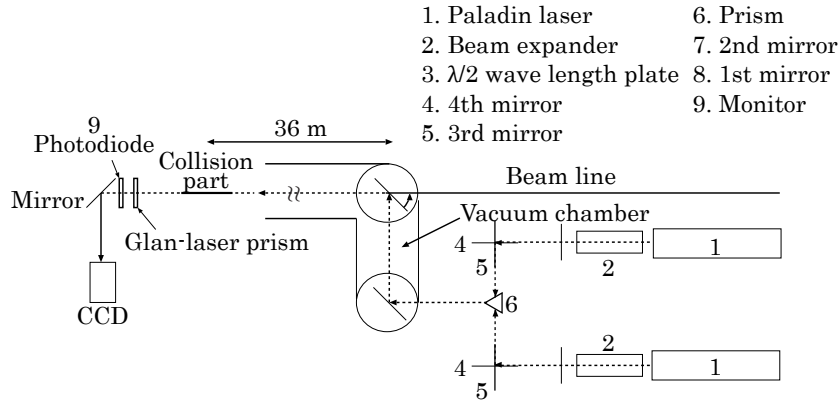
Figure 2.6:   Schematic drawing of the laser operating system.

a set of concave and convex lenses made of UV grade quartz. The magnification factor of the beam expander is 28, corresponding to 28 mm of the laser beam size just after the expander.

The polarization of the laser beams is controlled by $\lambda/2$ plates. Since the laser beams themselves are vertically-polarized, the optic axis of the $\lambda/2$ plates is set to 0 degrees to obtain vertically-polarized photons, whereas it is set to 45 degrees to obtain horizontally-polarized photons. The laser polarization was changed once a day during data-taking periods.

Four mirrors and one prism are used to guide the laser beams to the storage ring. The angles of the 3rd and 4th mirrors are controlled by pulse motors to tune the directions of the laser beams. The 3rd and 4th mirrors are made of quartz with a size of 80 mm$\phi \times 12$ mm in thickness. The two laser beams are reflected by the both sides of the prism, which is made of quartz (Fig. 2.7), and are guided to the 2nd mirror. The 1st and 2nd mirrors are placed inside a vacuum chamber. They are made of Si base with aluminum coating which have a good heat conductivity. The sizes of the 1st and 2nd mirrors are 100 mm$\phi \times 6$ mm in thickness and 100 mm$\phi \times 19$ mm in thickness, respectively. The 1st mirror is made thin and is cooled by water circulation because a LEP beam passes it.

The laser polarization is determined by measuring the polarization of the laser photons that do not interact with the circulating electrons using a Glan-laser prism as a polarimeter. The Glan-laser prism has a special axis such that only the photons with polarization parallel to it can pass through the prism. Therefore, with the rotation of the prism, the intensity of the laser
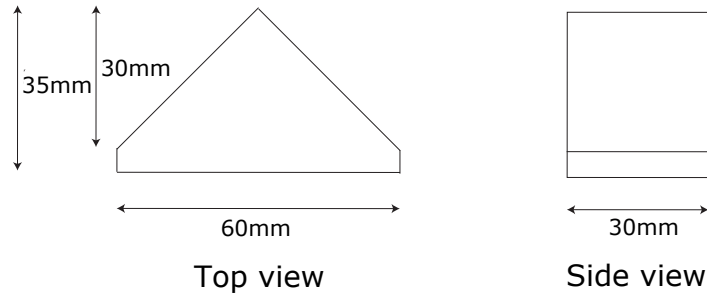
Figure 2.7:   Schematic view of the prism.
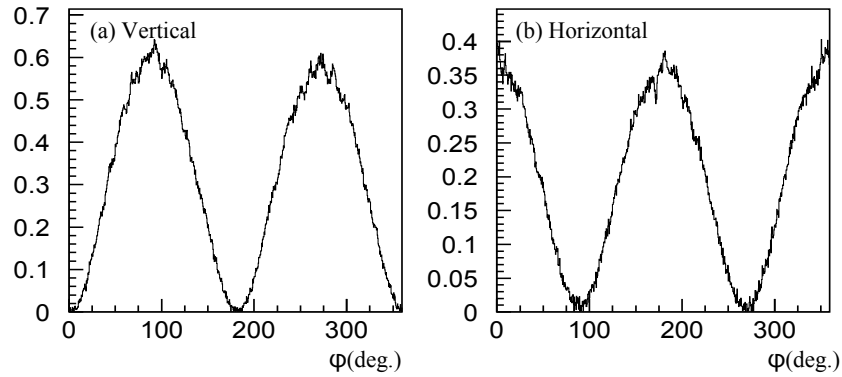
Figure 2.8:   Typical intensity distributions of the laser photons measured by the photo-diode as a function of the rotation angle (ϕ) of the prism (a) for vertical and (b) horizontal polarization.

photons that can pass through the prism would exhibit a oscillation pattern. The intensity distribution as a function of the rotation angle (ϕ) of the prism is measured by a photo-diode (HAMAMATSU S1406-05). Figures 2.8(a) and (b) show typical intensity distributions of the laser photons measured by the photo-diode as a function of the angle ϕ for vertical and horizontal polarization, respectively. By fitting these distributions with a function $\sin\phi$, the angle and degree of the laser polarization are determined. Note that the laser beams are optimized to maximize the polarization.
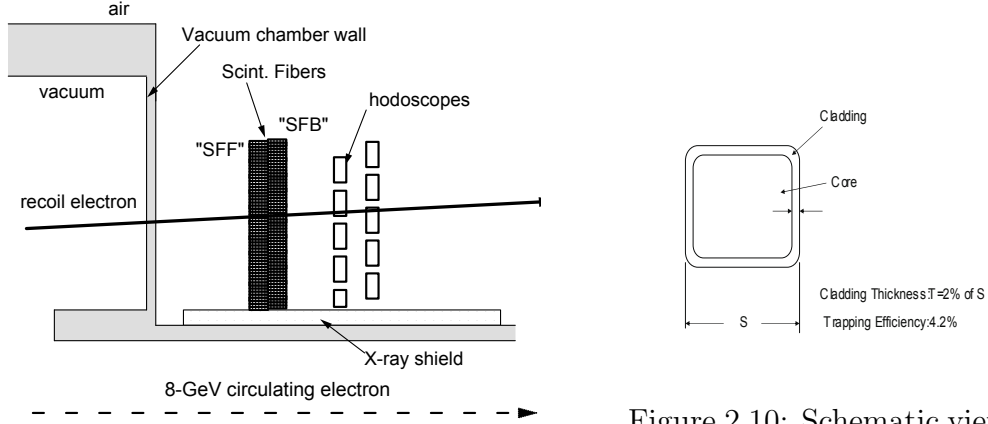
Figure 2.9: Schematic view of the tagging system

Figure 2.10: Schematic view of the fiber

2.2.3   Tagging system

The energy of the BCS photons, E_γ, is determined by measuring the energy of the recoil electrons, $E_{e'}$, as

$$E_\gamma = E_e - E_{e'}. \tag{2.7}$$

The energy of the electrons circulating in the storage ring, E_e, was calculated on the basis of the measured magnetic field distributions in the storage ring, and was determined to be 7.975 ± 0.003 GeV [116]. The recoil electron energy $E_{e'}$ is measured by a tagging system, which is located in the storage ring. Since the scattered electrons in the BCS process loose their energy, they are kicked rather strongly by the bending magnet at the end of the straight section (see Fig. 2.2), and deviate from a normal orbit in the storage ring. To detect such recoil electrons, the tagging system is placed just downstream of the bending magnet at the end of the straight section.

Figure 2.9 shows a schematic view of the tagging system. The tagging system is put outside a beam vacuum pipe for 8-GeV electrons. It covers an energy region of 4.0–6.6 GeV for the recoil electrons, corresponding to an energy region of 1.5–3.5 GeV for the BCS photons. The lower limit of the photon energy is determined by the acceptance of the tagging system, which is closest to a nominal orbit for the circulating electrons. The tagging system consists of scintillating fibers (TAG-SF) and plastic scintillator hodoscope (TAG-PL).

A hit position of electron tracks is measured by TAG-SF, which consists of two layers (TAG-SFF and TAG-SFB). Each fiber layer consists of 55 fiber bundles. Each fiber bundle is made of six fibers with a cross section of 1×1 mm^2 . Figure 2.10 shows a schematic view of the fiber. There exists a 4.2% inefficient region in one fiber. Two layers are arranged with an overlap of 0.5 mm to cover the inefficient region in one layer. The signals from the fiber bundles are read by the photomultiplier tubes (HAMAMATSU PMT R5900-00-M4, H6568-10).

Since the tagging system is placed near the vacuum pipe for the circulating electrons, it could be suffered from accidental backgrounds. To avoid them, a coincidence signal from TAG-SF and TAG-PL is required at the trigger stage (see Sect. 2.6 for the trigger circuit). TAG-PL consists of 2 layers of 5 plastic scintillation counters. The size of the plastic scintillator is 10.0 mm (hight) $\times$ 7.4 mm (width) $\times$ 5.5 mm (thickness). The width for the plastic scintillator closest to the circulating electrons is 5.5 mm. The plastic scintillators are arranged with an overlap of 2.7 mm. The signals from TAG-PL are read through the PMTs (HAMAMATSU H3164-10). The timing information of TAG-PL is used for solving a "2-ns ambiguity" of the RF signals for the time-of-flight measurement.

2.2.4   Beamline setup

The BCS photons travel from the collision point to the experimental hutch through the laser hutch. Figure 2.11 illustrates the setup of the LEPS beamline. There are several materials in the path of the BCS photon beam: the 1st mirror, aluminum windows of the beam pipes and a X-ray absorber. If the BCS photons hit the materials, some of them would convert into e^+e^- pairs. Table 2.1 summarizes the materials and their conversion rates to e^+e^- pairs. The 1st mirror is made of silicon with a thickness of 6 mm. Since the 1st mirror is tilted by 45 degrees to inject the laser photons to the storage ring, the effective thickness is $\sqrt{2} \times 6$ mm. Al plates with a thickness of 0.55 mm are used as a window of the beam pipes, i.e., the exit of the beam pipe from the SR ring and the enter and exit of the beam pipe that connect the laser and experimental hutches. In total, three aluminum plates are used in the beamline. A lead absorber with a thickness of 2.0 mm is placed downstream of the beam pipe connected to the SR ring to absorb X-rays. All the detectors of the spectrometer are protected from radiation damages by the absorber. Its thickness was determined to be 2.0 mm for radiation
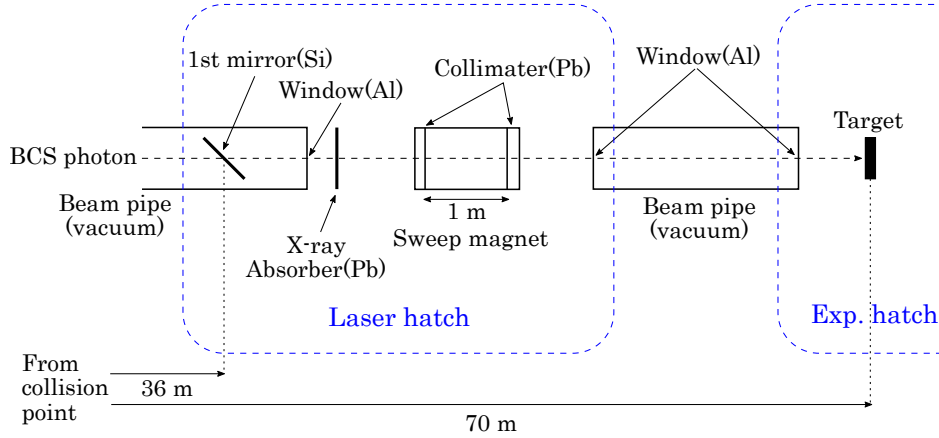
Figure 2.11:   Schematic view of the LEPS beamline setup.

safety and detector performance. The conversion rate of the BCS photons is 32.5% in total. The intensity of the BCS photons is reduced by 32.5% before arriving at a target in the experimental hutch. The transmission of the BCS photons from the collision point to the target was measured by the tagging counters and gamma counters. The BCS electrons with an energy of 6.7 GeV, corresponding to the photon energy of 1.3 GeV, hit the wall of the shield, and would cause electro-magnetic (EM) showers. The EM showers hitting the tagging counters are discarded in an offline analysis. The effective transmission including the EM shower effects was measured to be 53%.

The e^+e^- pairs produced in the materials must be removed before arriving at the target. To remove them, a sweep magnet is placed in the laser hutch. Figure 2.12 shows the structure of the sweep magnet. The size of an iron yoke is 176 mm (hight) $\times$ 560 mm (width) $\times$ 1000 mm (depth). Two permanent magnets are attached on the top and bottom of the iron yoke. The size of

Table 2.1: Materials inserted in the beamline.

	Material	Radiation length (mm)	Thickness (mm)	Conversion rate (%)
First mirror	Si	93.6	$6 \times \sqrt{2}$	6.77
Vacuum windows	Al	89.0	0.55×3	0.44×3
Absorber	Pb	5.6	2.0	24.25

Iron yoke

58 mm

35 mm

N

44 mm

Beam

Magnet

176 mm

31 mm

S

560 mm

Front view
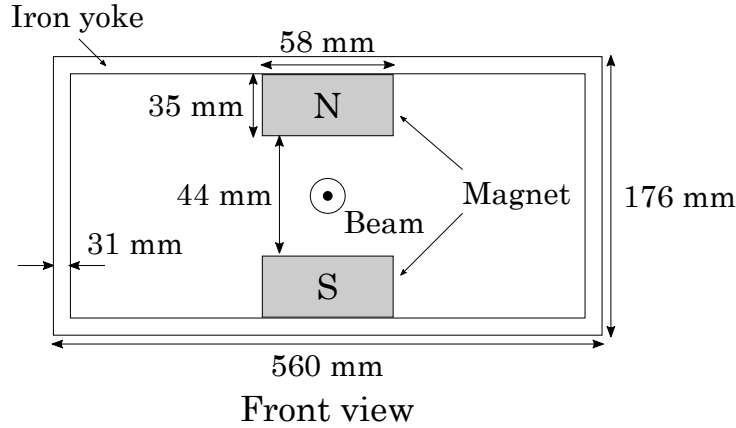
Figure 2.12: Structure of the sweep magnet.

each magnet is 35 mm (hight) × 58 mm (width) × 1000 mm (depth). The strength of the magnetic field is 0.6 T at the center. With the use of the sweep magnet, the e^+e^- pairs produced at the 1st mirror, the aluminum windows, the X-ray absorber and the residual gas in the beam pipe are swept out from the beamline. Lead collimators are placed upstream and downstream of the sweep magnet. The thickness of the upstream (downstream) collimator is 50 (150) mm. The upstream (downstream) collimator has a hole with a diameter of 20 (25) mm. The e^+e^- pairs with a momentum of < 2.1 GeV/c are blocked by the downstream collimator, whereas those with a momentum > 2.1 GeV/c could pass through the hole of the downstream collimator.

2.3 LEPS spectrometer

The LEPS spectrometer is located in the experimental hutch to detect the charged particles produced at the target and to analyze their momenta. Figure 2.13 shows an overview of the LEPS spectrometer. The incident photons come from the bottom-left side of this figure. The LEPS spectrometer consists of an upstream-veto counter (UPveto), trigger counters, a silica-aerogel Čelenkov counter (AC), a dipole magnet, four multi-wire drift chambers (DC0, DC1, DC2 and DC3) and a TOF wall. The charged particles produced upstream of the experimental hutch are vetoed by the upstream veto counter. The silica-aerogel Čerenkov counter is used to eliminate the e^+e^- background events at the trigger stage. The four multi-wire drift chambers, together with the dipole magnet, are used as a tracking device to measure
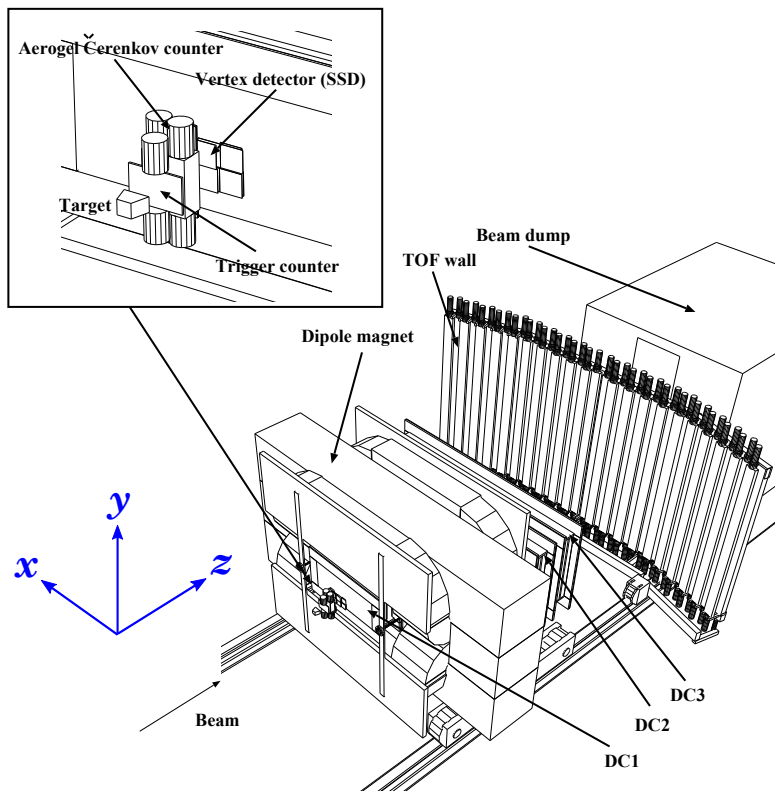
Figure 2.13:   Overview of the LEPS spectrometer. In the data-taking period of this work, a vertex detector (SSD) is replaced with a multi-wire drift chamber (DC0), and a target chamber and a trigger counter are replaced with different ones. See the text for details. Blue arrows indicate a definition of the coordinate system used in the present analysis (see Sect. 3.3 for details).

the momenta of charged particles. The time-of-flights of charged particles are measured by using the TOF wall. There exists a beam dump behind the LEPS spectrometer for a radiation shielding.

Besides the LEPS spectrometer, a solenoid magnetic spectrometer, which consists of a Time Projection Chamber (TPC), trigger counters and a solenoid magnet, is equipped surrounding a liquid helium-4 target to detect the charged particles emitted sideway. Therefore, the experimental setup for this experiment is different from standard LEPS experiments [111, 112], in which the solenoid spectrometer system is not equipped. Note that the hit information on the TPC and its trigger counters was not used in the present analysis.

2.3.1 Upstream-veto counter (UPveto)
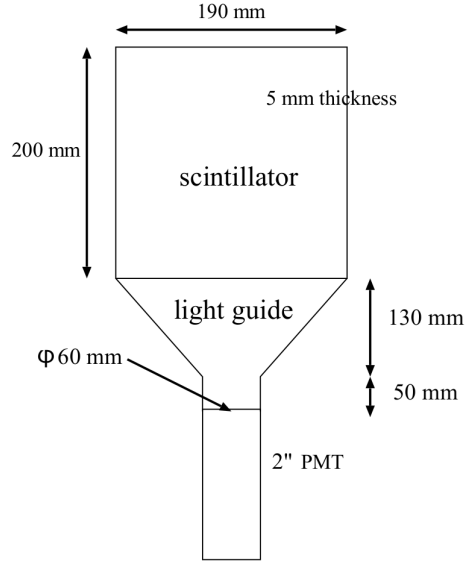
Figure 2.14: Schematic drawing of the upstream-veto counter.

Some of the BCS photons would convert to charged particles mostly by the e^+e^- pair production in air, the residual gas, or aluminum windows of the beam pipe. Such charged particles must be vetoed at the trigger stage to reduce the trigger rate.

An upstream-veto counter, which is located 4 m upstream of the target, is used to reject the events triggered by such charged particles at the trigger stage. Figure 2.14 shows a schematic drawing of the upstream-veto counter. It is made of a plastic scintillator (BC-408) with a size of 200 mm (hight) × 190 mm (width) × 5 mm (thickness). The plastic scintillator is viewed by a 2-inch fine-mesh PMT (HAMAMATSU H7195) through a light guide.

2.3.2 Liquid helium-4 target

A liquid helium-4 target was used in this work. The target system is combined with the solenoid magnetic spectrometer, which is described in detail later. Figures 2.15 and 2.16 show schematic drawings of the target system and the target cell, respectively. The target system has a long nose with a length of 700 mm. The target cell is attached to the distal end of

the nose. The target cell has a cylindrical shape, and is made of capton film. The size of the target cell is 40 mmϕ × 150 mm (length). The target cell is covered by a CFRP cap in order to sustain vacuum. The thickness of the CFRP cap is 1 mm. The nose of the target system is inserted into the inner bore of the TPC. The center of the target cell corresponds to 1710 mm upstream of the center of the dipole magnet.
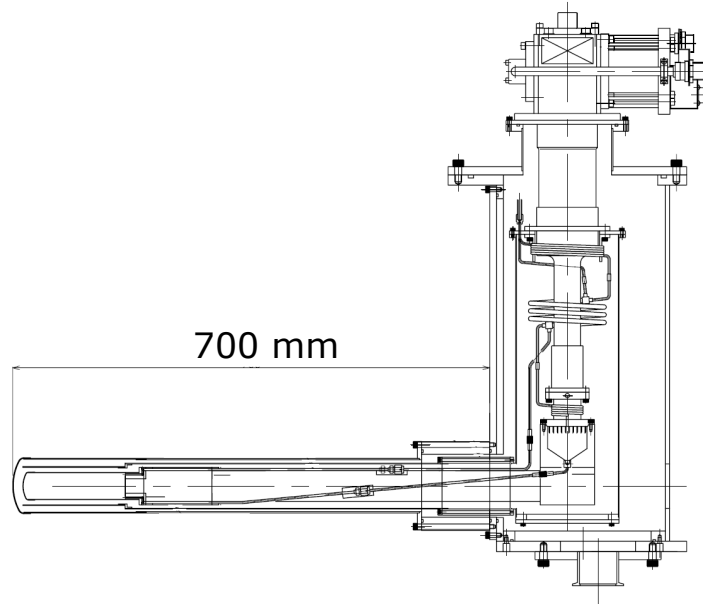
Figure 2.15:   Schematic drawing of the liquid helium-4 target system.
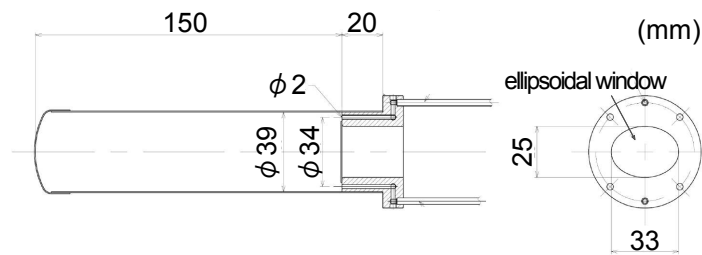
Figure 2.16:   Schematic drawing of the target cell.

2.3.2.1 Forward counter (FWD)

To identify the charged particles produced at the target and entering into the acceptance of the LEPS spectromter at the trigger stage, two plastic scintillation counters (forward counters, FWDs) are placed 995 mm downstream of the center of the target. Figure 2.17 shows a schematic drawing of the forward counters. Two plastic scintillators with a size of 340 mm (hight) × 780 mm (width) × 10 mm (thickness) are vertically arranged. Each plastic scintillator is viewed by two 2-inch fine-mesh PMTs (HAMAMATSU H6614) from the left and right sides through light guides. The FWD counters are used as a reference counter in time-of-flight measurements. Note that the time-of-flight of forward charged tracks can be also obtained in a different manner (see Sect. 3.4.2).
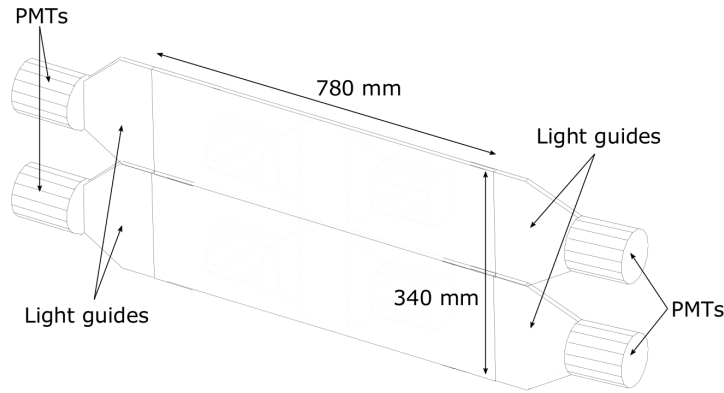
Figure 2.17: Schematic drawing of the forward counters.

2.3.3 Silica-aerogel Čerenkov counter (AC)

The main background in the present experiment is the e^+e^- pair production from the target and the FWD counters. Since the cross section of the e^+e^- pair production from liquid helium-4 or from plastic scintillator is two orders of magnitude larger than those for hadronic reactions, it have to be suppressed at the trigger stage to reduce the trigger rate.

A silica-aerogel Čerenkov counter (AC) is used to reject such e^+e^- events at the trigger stage. Figure 2.18(a) shows the relation between momentum and velocity β for e^+e^-, π and K particles. Since during passing through a material with a refractive index of n, a charged particle with a velocity of
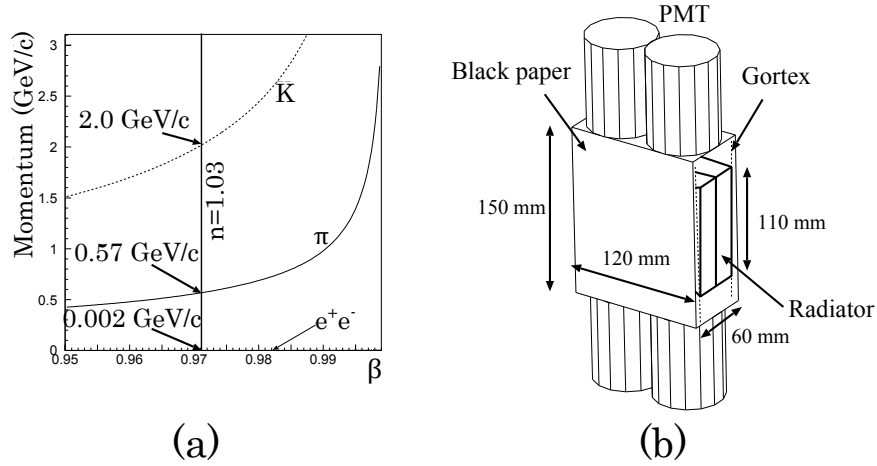
Figure 2.18:   (a) Relation between momentum and velocity β for e^+e^-, π and K particles. A vertical line corresponds to an index of $n = 1.03$. (b) Design of the silica-aerogel Čerenkov counter.

$\beta > 1/n$ emits Čerenkov lights, the refractive index of the radiator is set to be 1.03. It corresponds to the threshold momenta of 0.002 GeV/c, 0.57 GeV/c and 2.0 GeV/c for pions, kaons and protons, respectively. The signals from the AC counter are used as a veto signal in the trigger logic to reject the e^+e^- events.

Figure 2.18(b) shows the design of the AC counter. The body of the counter is made of black paper. The size of the counter box is 150 mm (hight)$\times$ 120 mm (width) $\times$ 60 mm (thickness). Two sheets of the silica-aerogel radiator are arranged in a column as shown in Fig. 2.18(b). The size of each radiator is 110 mm (hight)$\times$110 mm (width)$\times$25 mm (thickness). The radiators are viewed by four 2-inch fine-mesh PMTs (HAMAMATSU H6614-01), two of which are from the upper side and the others are from the bottom side. To collect Čerenkov lights efficiently, the inside of the counter box except for the photocathodes is covered with GORTEX sheets (white sheets) as a random reflector. The reflectivity of GORTEX sheets is about 95% [117]. The AC counter is placed just behind the FWD counters. Even such a configuration makes it possible to detect e^+e^- pairs efficiently because e^+e^- pairs are produced at the target with a small relative angle ($< 12°$). The efficiency for the e^+e^- detection is about 99.9%.

2.3.4 e^+e^- **Blocker**

The e^+e^- pairs produced in the target and FWD counters, which are initially emitted in a small relative angle, are spread out mostly in a horizontal direction due to the magnetic field of the dipole magnet. Some of electrons or positrons with a low energy would escape from the acceptance of the beam dump, which is located behind the LEPS spectrometer, and would hit directly a thin wall of the experimental hutch. This causes a problem on radiation safety.
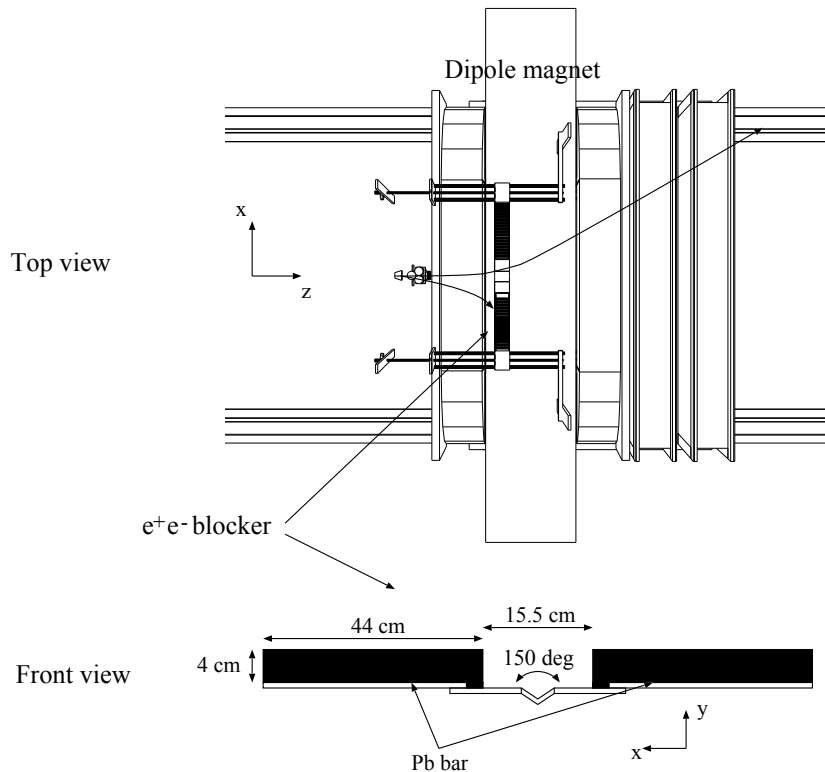
Figure 2.19:   Schematic view of the e^+e^- blocker.

A e^+e^- blocker is used in the dipole magnet to absorb such low-energy particles. Figure 2.19 shows a schematic view of the e^+e^- blocker. The e^+e^- blocker, made of two lead bars, is placed 20 cm downstream of the center of the dipole magnet and is allowed to move within ± 2 m in the beam direction. The y-position of the e^+e^- blocker is set to the beam hight. The size of each Pb bar is 4 cm (hight) $\times$ 44 cm (width) $\times$ 10 cm (thickness). The gap distance

between two Pb bars is 15.5 cm. e^+e^- pairs with momenta above 1 GeV/c can go through the gap. The gap distance can be adjusted by using small pieces of Pb blocks. Most of e^+e^- pairs are asymmetric in energy. In such case, one of a e^+e^- pair is blocked by the Pb bars, whereas the other escapes through the 15.5 cm gap and is stopped by the beam dump. The Pb bars are supported by two thin channels with a thickness of 0.2 cm. The thin channels are connected to each other at the center with a V-shaped thin bar (SUS) with a thickness of 0.5 cm. The V-shaped structure is open with an angle of 150° and has the depth of 15 cm to allow the photon beam to pass through (see Fig. 2.19).

2.3.5 Multi-wire drift chamber (DC)
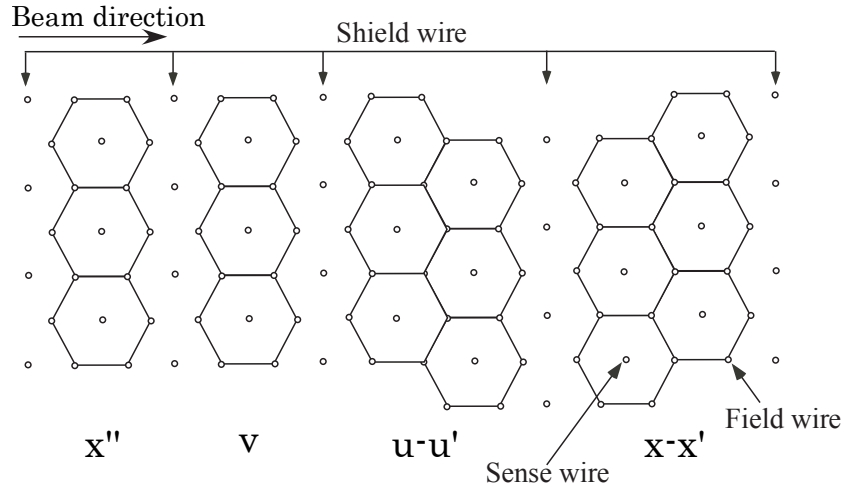
Figure 2.20: Configuration of the field, shield and sense wires for the multi-wire drift chambers.

Four multi-wire drift chambers (DC0, DC1, DC2 and DC3) are used as a tracking device for the charged particles entering the acceptance of the LEPS spectrometer. The design parameters for the multi-wire drift chambers are summarized in Table 2.2.

DC1 is placed at the entrance of the dipole magnet. The active area is 600×300 mm^2. Figure 2.20 shows the configuration of the field, shield and sense wires for DC1. DC1 has six planes (X1 X2 U1 U2 V X3). The X3 plane is added because charged particles begin to be spread out due to

Table 2.2: Design parameters for the multi-wire drift chambers. The orientation of wires is defined with respect to the horizontal axis. Each drift chamber is centered in the x-y plane. The position of $z = 0$ is defined as the center of the dipole magnet.

	Coordinate	Orientation	Number of sence wires	Wire spacing (mm)	Active area $x \times y$ (mm^2)	Position z (mm)
DC0	Y1–Y2	90°	48	14	600 mmϕ (hexagonal)	-832.0
	U1–U2	30°	48	14		
	V1–V2	150°	48	14		
DC1	X1–X2	0°	48	6	600 × 300	-466.0
	U1–U2	45°	48	6		
	V	135°	48	12		
	X3	0°	48	12		
DC2	X1–X2	0°	104	10	2000 × 800	860.5
	U1–U2	120°	78	10		
	V	60°	79	20		
DC3	X1–X2	0°	104	10	2000 × 800	1260.5
	U1–U2	120°	78	10		
	V	60°	79	20		

the magnetic field around DC1. The planes X1, X2, U1 and U2 have a 6-mm sense-wire spacing, whereas the X3 plane has a 12-mm one. The field wires are arranged in a hexagonal shape. There exist shield wires along the windows to shape the electric field. The wires of the U1 and U2 planes are tilted by 45° with respect to the horizontal axis. DC2 and DC3 are placed at the exit of the dipole magnet. They have an active area of 2000 × 800 mm^2 and consist of five planes (X1 X2 U1 U2 V). The designs of DC2 and DC3 are almost the same as that of DC1, except that DC1 and DC2 do not have the X3 plane. The planes X1, X2, U1 and U2 have a 10-mm sense-wire spacing, whereas the V plane has a 20-mm one. The wires of the UV planes are tilted by ±30° with respect to the vertical axis. DC0 is newly installed instead of a silicon vertex detector (SVTX) to reconstruct the reaction vertices of charged particles together with the other drift chambers. It is placed just behind the solenoid spectrometer (see Fig. 2.27). It has a hexagonal-shaped active area with a diameter of 600 mm, and consists of six wire planes (Y1 Y2 U1 U2 V1 V2) with a 14-mm spacing. Aluminized-mylar sheets with a thickness

of 12.5 μm are inserted between every two planes as a cathode plane. Each sense wire is spaced with an interval of 14 mm. The wires of the Y planes are parallel to the horizontal axis, whereas those of the U and V planes are tilted by $\pm 30°$ with respect to the vertical axis. The sense wires are made of gold-plated tungsten (Au-W) with a diameter of 25 μm for DC1 and 30 μm for DC0, DC2 and DC3, respectively. The field and shield wires are made of Au-BeCu with a diameter of 80 μm for DC0, and 100 μm for DC1, DC2 and DC3, respectively. The windows for all the DCs are made of mylar with a thickness of 125 μm. All the DCs are operated at a gas mixture of 70% argon and 30% isobutane. The efficiencies for the DCs are achieved to be more than 98%, and are typically 99%.

2.3.6 TOF wall
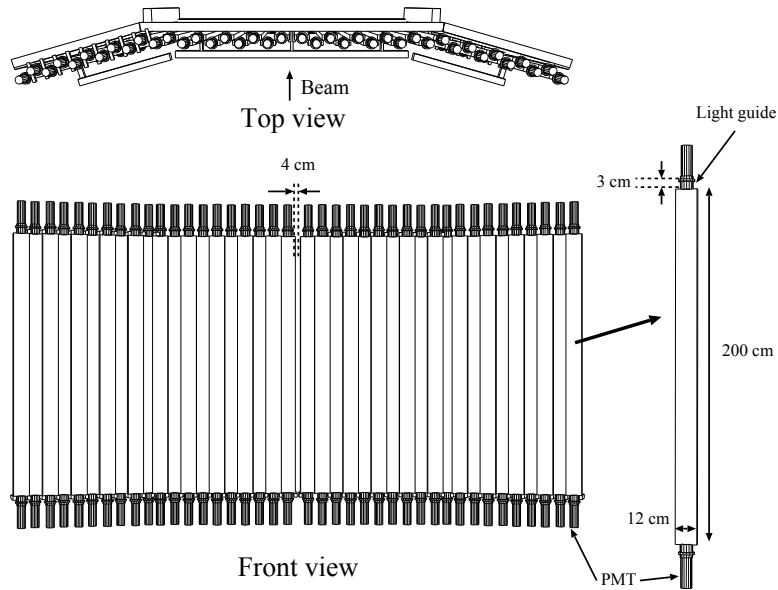
Figure 2.21: Schematic view of the TOF wall.

The time-of-flight of charged particles is measured by a TOF wall. The TOF wall is placed at the downstream end of the LEPS spectrometer. Figure 2.21 shows a schematic view of the TOF wall. The TOF wall consists of 40 plastic scintillator bars (BC-408) with a size of 200 cm (length) $\times$ 12 cm (width) $\times$ 4 cm (thickness). Each plastic scintillator bar is viewed by

two 2-inch PMTs (HAMAMATSU H7195) from the both sides through light
guides with a length of 3 cm, and is overlapped with the adjacent bars by 1
cm. Twenty sideway bars are aligned in the planes tilted by $\pm 15°$, as shown
in the upper half of Fig. 2.21. Ten of them are in the right side, while the
others in the left sides. There exists a 4-cm gap between the middle two
counters to allow a photon beam to pass through. The TOF wall is movable
on the rails between 1.5 and 4.5 m downstream of the center of the dipole
magnet. In the present experiment, the z-position of the TOF wall was set
to be 3151.5 mm downstream of the center of the dipole magnet.

2.3.7   Dipole magnet
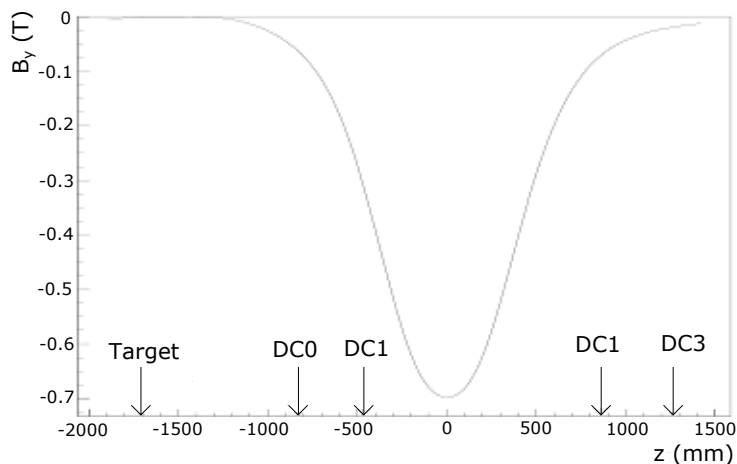
Figure 2.22: y-component of the magnetic field B_y for the dipole magnet
as a function of the z-position on the beam axis $(x, y = 0)$. Note that the
z-position $z = 0$ corresponds to the center of the dipole magnet (see Sect. 3.3
for details).

   A dipole magnet is used as a momentum-analyzer magnet to bent charged
particles, which is placed at the center of the LEPS spectrometer. It has an
aperture of 55 cm (hight) $\times$ 135 cm (width). The depth along the beam axis
is 60 cm. The current for the magnet was set to 800 A, providing a magnetic
field with a strength of 0.7 T at the center (designed value). Figure 2.22
shows the y-component of the magnetic field B_y for the dipole magnet as a
function of the z-position on the beam axis $(x, y = 0)$, which was calculated

by a TOSCA simulation program. The magnetic field map obtained by TOSCA was used in the track reconstruction. The simulation was tuned to reproduce the measured magnetic field with a hole probe. The differences between the calculated and measured values of the magnetic field are at most 0.001 T (0.5%).

2.4   Solenoid spectrometer

As already mentioned before, a solenoid spectrometer is equipped surrounding the target in addition to the LEPS spectrometer. Since the information on the TPC was not used in the present analysis, the solenoid spectrometer system is briefly described here. More details about the solenoid spectrometer system can be found in Ref. [113].

2.4.1   Solenoid magnet
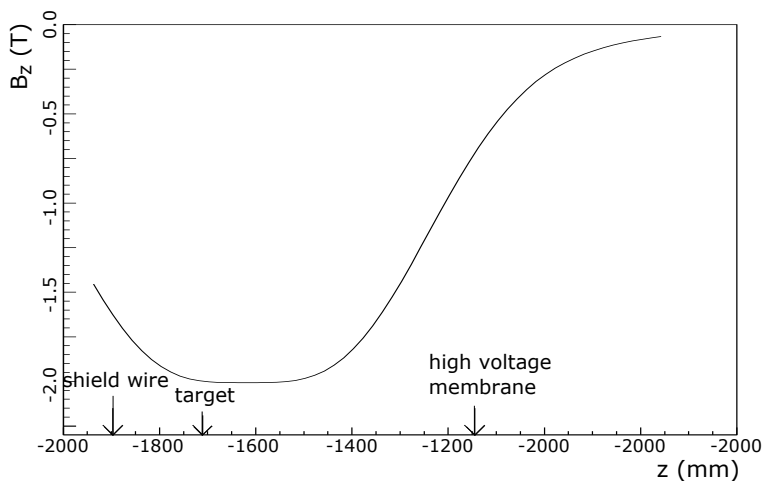
Figure 2.23: z-component of the magnetic field B_z for the solenoid magnet as a function of the z-position on the beam axis $(x, y = 0)$. The definition of the $x.y.z$-coordinates is common through this thesis. The high-voltage membrane corresponds to the downstream end of the TPC.

A superconducting solenoid magnet is used to analyze the momenta of the charged particles detected by the TPC. The solenoid magnet has an aperture of 300 mm in radius and a depth of 1000 mm. The center of the

magnet is placed at $z = -1617$ mm along the beam axis[18], surrounding
the target (the target center: $z = -1710$ mm). The designed value of the
field strength is 2 T at the center of the magnet. The magnetic field map
for the solenoid magnet was calculated by the TOSCA simulation program,
which is the same one as described in Sect. 2.3.7. The differences between
the calculated and measured values of the magnetic field are at most 0.01
T (4%)[19] Figure 2.23 shows the TOSCA result for the z-component of the
magnetic field as a function of the z-position on the beam axis $(x, y = 0)$.
Note that the magnetic field map used in the present analysis takes into
account the effects of the solenoid magnetic field.

2.4.2 Time Projection Chamber (TPC)
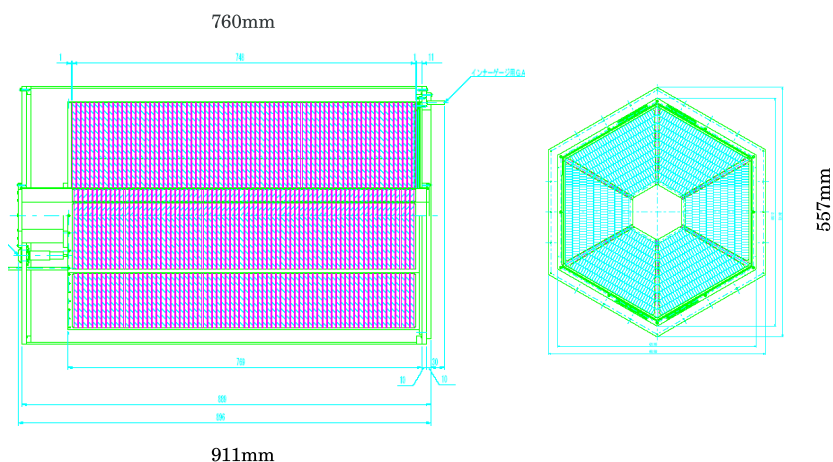
Figure 2.24:   Schematic drawing of the time projection chamber.

A time projection chamber (TPC) is used to detect charged particles
nearby the target. Figure 2.24 shows a schematic drawing of the TPC. The
TPC has a hexagonal-cylinder shape with a length of 910 mm and a circum-
radius of 280 mm. It also has a hexagonal bore with a circumradius of 60
mm to insert the liquid target system. The active volume of the TPC is

---

[18]$z = 0$ corresponds to the center of the dipole magnet.

[19]Such discrepancies happen around the overlapped region of the solenoid and dipole
magnetic fields at a large radial distance. Therefore, this does not affect the momentum
measurement of forward-going particles.

hexagonal-cylinder-shaped with a length of 760 mm and a arm length of 225 mm, and is filled with the P_{10} gas (Ar:CH$_4$ = 90%:10%). The azimuthal and polar angular coverages of the TPC are 2π and 0.35–2.25 rad, respectively. The signals from the TPC are read through 1,350 rectangular cathode pads. The spatial resolutions in the x-y plane and in the beam direction (z-axis) are typically 200–400 μm and 400–4000 μm, respectively, depending on the direction of charged particles.

2.4.3 Trigger counter for TPC

2.4.3.1 Inner counter (TPCInner)

Six plastic scintillation counters (inner counters, TPCInners), surrounding the liquid helium-4 target, are used to detect the charged particles entering the TPC acceptance nearby the target and to determine the start time of the TPC events. Figure 2.25 shows a schematic drawing of the inner plastic scintillator. The size of each plastic scintillator is 230 mm (length) × 542 mm (width) × 3 mm (thickness). Each plastic scintillator is bend by 30° at the length of 170 mm to detect the forward-going particles, and has a tapered shape to be combined with other inner counters in a hexagonal shape, as shown in Figs. 2.25 and 2.26. Each plastic scintillator is viewed by a fine-mesh PMT through a scintillation-fiber light guide.
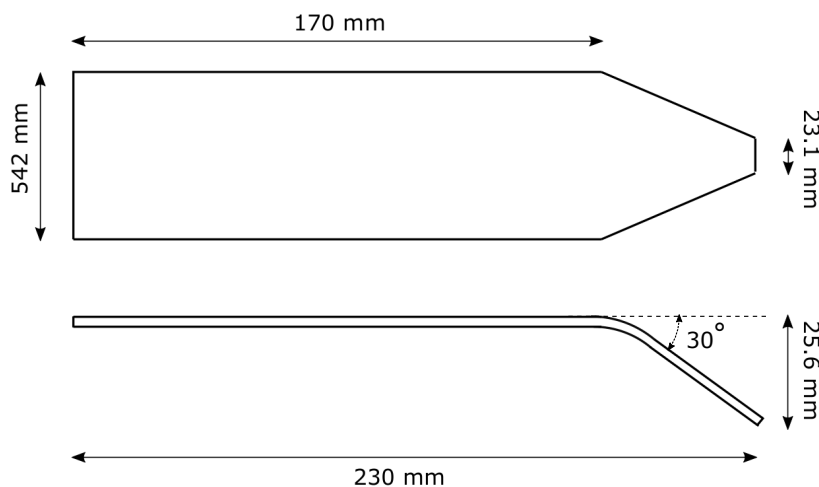
Figure 2.25: Schematic drawing of the inner plastic scintillator.

Figure 2.26:   Picture of the combined six inner plastic scintillators.

2.4.3.2   Outer counter (TPCOuter)

Twelve plastic scintillation counters (outer counters, TPCOuters), surrounding the TPC, are used to detect the charged particles from the target, together with the inner counters. The size of each plastic scintillator is 850 mm (length) × 145 mm (width) × 5 mm (thickness). Each plastic scintillator is viewed by two fine-mesh PMTs from the both sides through light guides. One rectangle side of the TPC hexagonal cylinder is covered by two outer counters.

An enlarged view around the target cell is illustrated in Fig. 2.27.
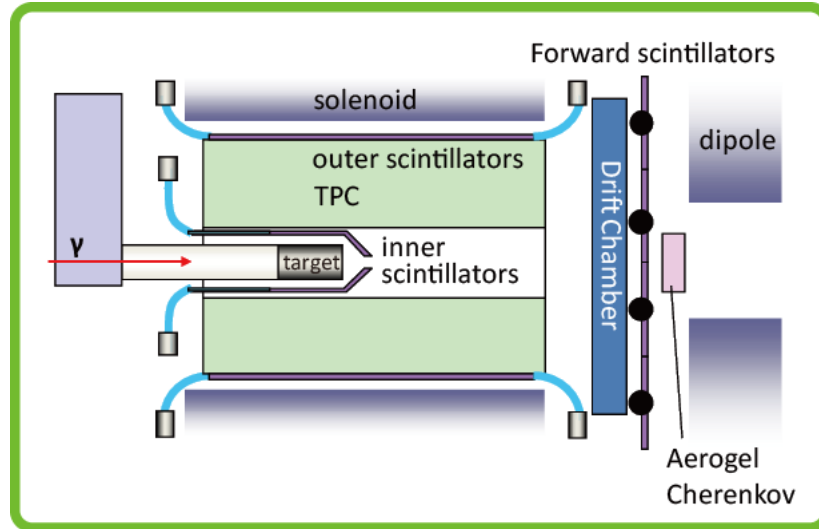
Figure 2.27: Enlarged view around the target cell.

2.5 RF signal

The electrons circulating in the 8-GeV storage ring lose their energies by emitting synchrotron radiation when they are deflected by the magnetic field. A 508 MHz radio frequency (RF) system is used to restore these energy losses. This frequency corresponds to the time interval of successive electron bunches, i.e., 1.966 nsec. In the LEPS experiment, the RF signals are used to determine the start time in time-of-flight measurements. Figure 2.28 shows the circuit diagram for the RF signals. The RF signals are pre-scaled by a factor of 1/87 by the prescaler modules (DIGITAL LABORATORY 17K32 508-MHz 30 bit). Two of the three output signals, one of which is delayed by 86 nsec , are read by the FASTBUS TDC 1877S module and are used for time-of-flight measurements. The other signal is sent to the prescaler with a factor of 1/28, and the three output signals, two of which are delayed by 1.8 μsec and 3.6 μsec, respectively, are read by the FASTBUS TDC 1877A module and are used to study an accidental-hit rate in the tagging system.

RF signal

Prescaler 1/87

86 nsec

Prescaler 1/28

1.8 μsec   3.6 μsec

TDC1875A   TDC1877S

Use as a Start timing
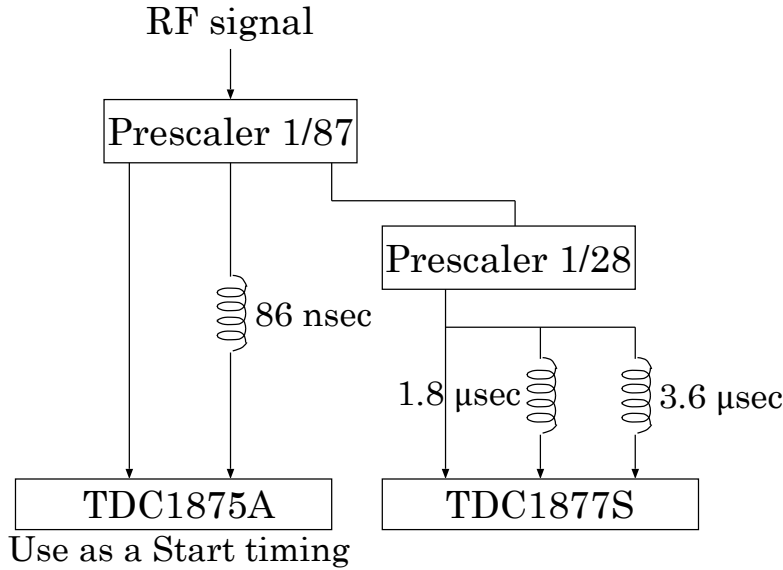
Figure 2.28:   Circuit diagram for the RF signals.

2.6   Electronics and circuit

Four types of readout modules are used to collect the ADC and TDC data from the detectors. The readout modules for each detector system are summarized in Table 2.3. LeCroy 4300B FERA (Fast Encoding & Read-out ADC) modules are used with a CAMAC system to read out the analog signals from the plastic scintillator hodoscopes of the tagging system, the upstream-veto counter, the FWD counters, the AC counter, the TPC inner and outer counters, and the TOF counters. FASTBUS 1877S TDC modules, which provide a timing resolution of 0.5 nsec/channel with a dynamic range of 1 μsec, are used with a FASTBUS system to read out the logic signals from the TAF-SFF and TAG-PL detectors, and the multi-wire drift chambers (DC0, DC1, DC2and DC3). LeCroy FASTBUS 1875A TDC modules, which provide a timing resolution of 0.25 nsec/channel with a dynamic range of 100 nsec, are used with a FASTBUS system to read out the logic signals from the TAG-PL counters, upstream-veto counters, the FWD counters, the AC counter, the TPC inner and outer counters, and the TOF counters.

Figure 2.29 shows the circuit diagrams for the tagging system, the upstream-veto counter, the FWD counters, the AC counter and the TOF counters. A trigger for the LEPS spectrometer system, which we call the "standard (STD)

60

Table 2.3: Readout modules (digitizers) for the detectors.

Detector	ADC	TDC	Abbrev. for trig.
TAG-PL	FERA	FASTBUS 1875A/1877S	TAG
TAG-SF	–	FASTBUS 1877S	TAG
UPveto	FERA	FASTBUS 1875A	UPveto
FWD	FERA	FASTBUS 1875A	FWD
AC	FERA	FASTBUS 1875A	AC
DCs	–	FASTBUS 1877S	–
TPCInner	FERA	FASTBUS 1875A	SECTOR
TPCOuter	FERA	FASTBUS 1875A	SECTOR
RF	–	FASTBUS 1875A/1877S	–

trigger", is made of trigger signals from each detector system (TAG, UPveto, FWD, AC and TOF).

TAG

To identify the recoil electrons from the BCS process at the trigger level, a coincidence signal between the TAG-SF and TAG-PL is used. For TAG-SF, at least one hit is required in either of the SFF or SFB.

UPveto

A logic signal from the upstream-veto counter is used to reject the events triggered by charged particles at the trigger stage.

FWD

To identify the production of forward-going charged particles, at least one hit is required in either of the two counters. A coincidence signal between the PMTs on the both sides of the counter is used.

AC

A logic signal from the AC counter is used to reject e^+e^- production events at the trigger stage.

TOF

At least one hit is required in the TOF counters at the trigger level. Two signals from the top and bottom PMTs of a TOF counter are sent to the mean timer module (CAMAC C561), and the output signal is

sent to the majority logic unit module (CAMAC 4532) to select the multiplicity of the TOF counters at the trigger level.

The STD trigger is a logical sum of two trigger signals, namely signals from the "hadron trigger" and the "e^+e^- trigger" as shown in Fig. 2.32:

$$
\begin{aligned}
\text{hadron trig.} &= \text{TAG} \otimes \overline{\text{UPveto}} \otimes \text{FWD} \otimes \overline{\text{AC}} \otimes \text{TOF}, \\
e^+e^- \text{ trig.} &= \text{TAG} \otimes \overline{\text{UPveto}} \otimes \text{FWD} \otimes \text{TOF},
\end{aligned}
\tag{2.8}
$$

where $\otimes$ represents a logical product. Since the trigger rate for the e^+e^- events is too high to be taken by the DAQ system, signals from the e^+e^- trigger are pre-scaled to be $\sim 20\%$ of the rate for the hadron trigger. To obtain the trigger timing definitively, a logical sum of the signals from the FWD counters and the hadron or e^+e^- trigger is taken at the final stage (see Fig. 2.32).

A trigger signal for the Solenoid spectrometer, which we call the "TPC trigger", is made of some combination of the logic signals from the TPC inner and outer counters ("Sector triggers"): A Sector trigger is a coincidence signal between one inner counter and one of the six corresponding outer counters, as shown in Figs. 2.30 and 2.31. Then we have six Sector triggers in total. The TPC trigger is a logical sum of six Sector triggers ("SectorOR trigger"):

$$
\text{SectorOR} = \text{Sector } 1 \oplus \text{Sector } 2 \oplus \text{Sector } 3 \oplus \text{Sector } 4 \oplus \text{Sector } 5 \oplus \text{Sector } 6,
\tag{2.9}
$$

where $\oplus$ represents a logical sum.

The data analyzed here was basically taken with the STD trigger. Therefore, when we consider the acceptance of a specific reaction, the hit information of the Solenoid spectrometer system can be completely ignored.
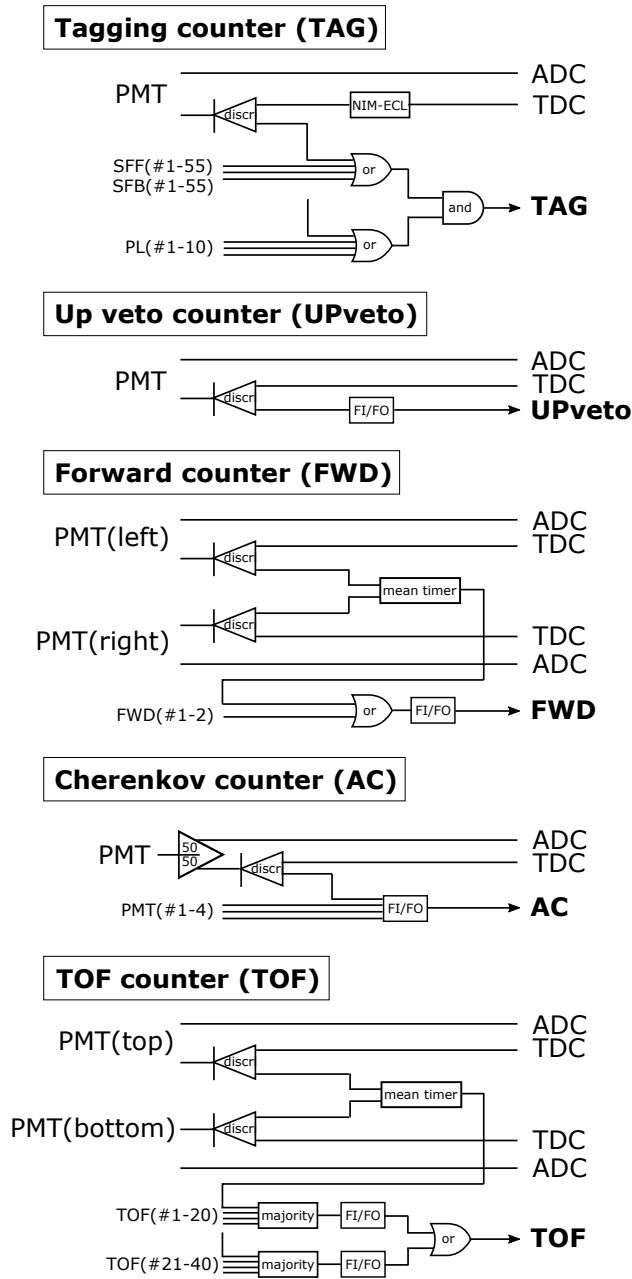
Figure 2.29:   Circuit diagrams for readouts and triggers.
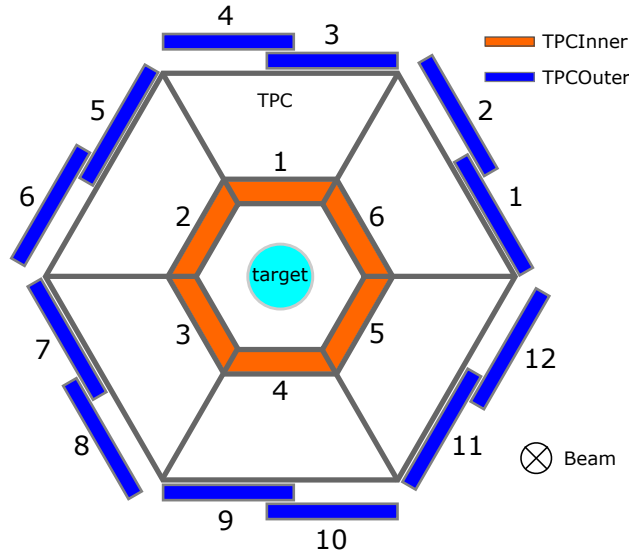
Figure 2.30:   Configuration of the inner (TPCInner) and outer counters (TP-COuter).
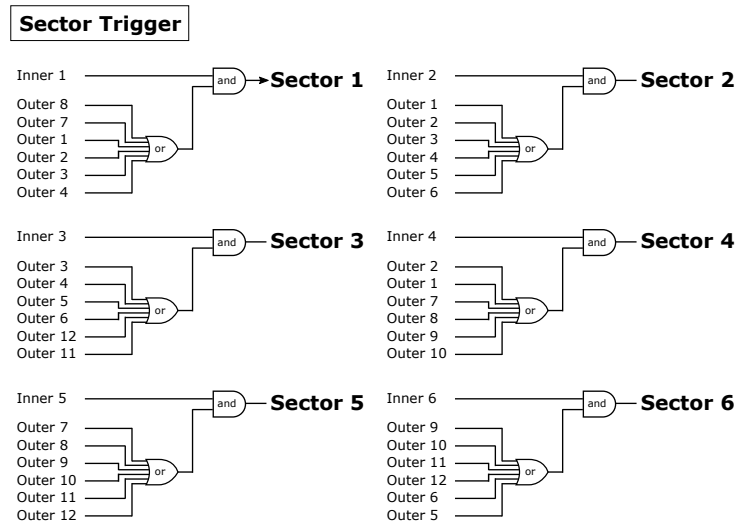
Figure 2.31:   Logic diagrams for the Sector triggers.
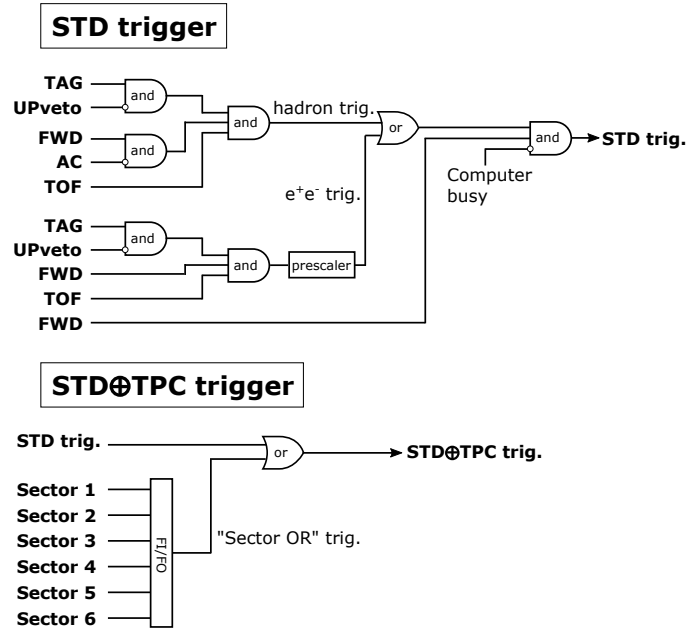
Figure 2.32:   Logic diagrams for the "STD" and "STD $\oplus$ TPC" triggers.

2.7   Data summary

The experiment had been carried out from 29th November in 2008 to 24th July in 2009. The data was taken with the liquid helium-4 (LHe) target, as well as with a liquid hydrogen (LH$_2$) target, which was used for data calibration and consistency check with previous LEPS measurements. The LHe data was taken with the STD trigger, whereas the LH$_2$ data was taken with the STD $\oplus$ TPC trigger. The total beam time for the LHe (LH$_2$) data was about 47 (39) days. At the end of each data-taking period, the empty (gas) target data was also taken, which was used for vertex studies (see Appendix G).

4.6×10^{12} (1.1×10^{12}) tagged photons irradiated the LHe (LH$_2$) target in total. Here, a beam transmission from the collision point to the target (52.6%) and a dead time correction for the tagging counters [112] (see also Appendix L) are taken into account in the total number of photons. The hit rate of the tagging counters was 1.0–2.0 MHz[20], and the trigger rate

---

[20]The hit rate of the tagging counters, which corresponds to the beam rate, depends

was 100–200 Hz through the data-taking periods. The beam polarization was changed once a half-day to balance the amount of the data with each polarization (horizontal and vertical). The ratio between the two data sets is Horizontal : Vertical = 1.00 : 0.98 (1.00 : 0.92) for the LHe (LH$_2$) data. The integrated luminosity is 0.679 (0.653) pb^{-1} for the LHe (LH$_2$) data.

During the data-taking periods, DC1 was broken twice, and DC0 and DC1 were moved to repair DC1. Thus, we have three data sets with different DC alignment parameters (, denoted in order as data-1, data-2 and data-3; see Appendix C for DC alignment). Note that the LHe data is a part of data-3.

---

on the condition of the laser optics as well as the filling pattern of the electron bunches. During data-taking, the positions and angles of the 3rd and 4th mirrors were tuned to keep the hit rate of the tagging counters constant (see Sect. 2.2.2 for the laser operating system).

3 Data analysis

3.1 Overview of data analysis

The present analysis aims to measure the differential cross sections and decay angular distributions [see Eqs. (1.27)–(1.31)] for coherent ϕ-meson photoproduction from ^{4}He. The production of ϕ-mesons was identified according to the invariant mass of the K^+K^- pairs [M(K^+K^-)] detected with the LEPS spectrometer:

$$\mathrm{M}(K^+K^-) = \sqrt{(p_{K^+} + p_{K^-})^2},\qquad(3.1)$$

where $p_{K^+} = (E_{K^+}, \boldsymbol{p_{K^+}})$ [$p_{K^-} = (E_{K^-}, \boldsymbol{p_{K^-}})$] is the four-momentum of a K^+ (K^-). The coherent-production events were disentangled from the incoherent ones on the basis of the missing mass for the ^{4}He(γ, K^+K^-)X reaction [MM(K^+K^-)]:

$$\mathrm{MM}(K^+K^-) = \sqrt{(E_\gamma + M_\alpha - E_{K^+} - E_{K^-})^2 - (\boldsymbol{p_\gamma} - \boldsymbol{p_{K^+}} - \boldsymbol{p_{K^-}})^2},\;\;(3.2)$$

where $p_\gamma = (E_\gamma, \boldsymbol{p_\gamma})$ is the four-momentum of a photon beam and M_α is the ^{4}He mass. Thus, in order to identify the coherent ϕ-production events, we need to measure the photon energy (E_γ) and the four-momenta of a K^+K^- pair (p_{K^+} and p_{K^-}).

In the present analysis, we finally obtain the differential cross sections as a function of the momentum transfer t [$= (p_\gamma - p_\phi)^2$, where p_ϕ is the four-momentum of a ϕ-meson] for several photon-energy bins:

$$\frac{d\sigma}{dt} = \frac{N_{\mathrm{coh}\text{-}\phi}/B_{\phi \to K^+K^-}/\varepsilon_{\mathrm{acc}}}{N_\gamma \cdot N_{\mathrm{targ}} \cdot \Delta t},\qquad(3.3)$$

where $N_{\mathrm{coh}\text{-}\phi}$ is the number of the coherent-ϕ-production events, $B_{\phi \to K^+K^-}$ is the branching ratio of the $\phi \to K^+K^-$ decay, $\varepsilon_{\mathrm{acc}}$ is the acceptance for K^+K^- pairs from the $\phi \to K^+K^-$ decay, N_γ is the number of photons arriving at the target, and Δt is the t-bin size. Since $\varepsilon_{\mathrm{acc}}$ is a function of two momentum vectors $\boldsymbol{p_{K^+}}$ and $\boldsymbol{p_{K^-}}$, we have to know a three-dimensional $\phi \to K^+K^-$ decay angular distribution as defined by Eq. (1.19) even when $d\sigma/dt$ is calculated. The details about the acceptance evaluation are described in Sect. 3.9.

The following sections describe a common analysis procedure to measure the differential cross sections and the decay angular distributions. Since the

absolute scale of the photon energy is determined using the $p(\gamma, K^+)\Lambda(1116)$ and $p(\gamma, \pi^+\pi^-)p$ reactions with the LH$_2$ data, we start with the four-momentum reconstruction of forward charged particles (Sect. 3.4). Then the absolute scale of the photon energy is determined (Sect. 3.5). After the determination of the absolute scale of the photon energy, we move onto the analysis of K^+K^- events with the LHe data. The selection criteria for K^+K^- events are described in Sect. 3.6. Once K^+K^- events are selected, the number of the coherent ϕ-production events can be evaluated from M(K^+K^-) and MM(K^+K^-) distributions (Sect. 3.7). As for the acceptance calculation, we use a GEANT3 [118]-based Monte Calro simulation code, which is introduced in the next section.

The detector calibration and the adjustment of DC alignment parameters are described in Appendices B and C.

3.2   GEANT3-based Monte Calro Simulation

A GEANT3 [118]-based Monte Calro (MC) simulation code was used to calculate the acceptance of the LEPS spectrometer and to check the performance of the spectrometer system. It simulates the generation of particles in a specific reaction and various processes during the passage of particles through materials such as decay in flight, energy loss and multiple scattering. The GEISHA package was used to simulate such processes. The photon energy resolution, the timing resolutions of the TOF counters and the spatial resolutions and detection efficiencies of the DCs were evaluated from the data (see Appendices D, B.1, B.2 and E, respectively), and were taken into account in MC simulation.

3.3   Definition of coordinate system

Before getting into the data analysis, we introduce a coordinate system used in this analysis (Fig. 3.1). The z-axis is defined as the direction of the beam axis, the y-axis is defined along the vertical direction, and the x-axis is defined as a vector product $\hat{y} \times \hat{z}$, where $\hat{y}$ and $\hat{z}$ are the unit vectors which determine the y and z-axes, respectively. The origin of the coordinate system is defined as the center of the dipole magnet. Note that this coordinate system is different from that used in the analysis on the decay angular distributions (see Sect. 1.4.4).
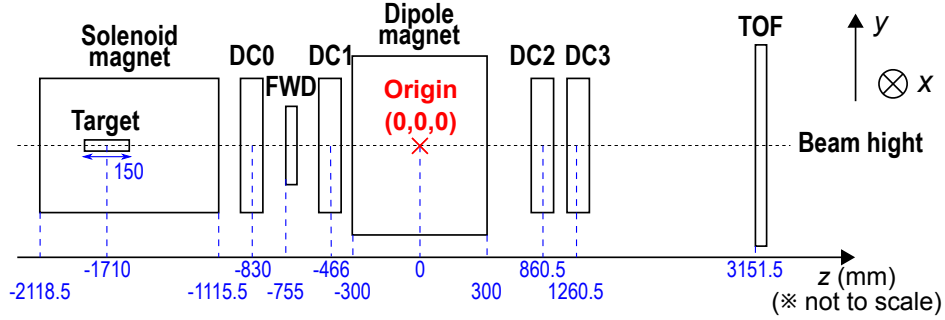
Figure 3.1: Definition of the coordinate system for the present analysis, together with the *z*-positions of each detector component.

3.4 Four-momentum reconstruction

The vertex point and 3-momentum of a charged particle were reconstructed from the hit information of the DCs, whereas its mass was reconstructed from the measured momentum and the time-of-flight between the vertex point and the TOF wall and was used for particle identification.

3.4.1 Momentum reconstruction

The momentum of a charged particle was reconstructed from the particle trajectory in the magnetic field. The trajectory of a charged particle was reconstructed from the hit information of DC0, DC1, DC2 and DC3.

The tracking procedure in an off-line analysis program [111] consists of the following steps:

Step-1: To collect nearby hits in each DC, and to form a cluster.

Step-2: To perform a straight-line fit to all combinations of clusters in DC0 and DC1 or in DC2 and DC3, and to select full-track candidates (i.e. combinations of upstream and downstream tracks).

Step-3: To perform a track fit with a Runge-Kutta method to each full-track candidate, and to determine its momentum.

In Step-1, a clustering is performed in each DC. Here, a "cluster" does not mean a combination of adjacent hits in the same plane, but a combination of hits in each plane of (X, U, V, Y) in the same DC. To form a cluster, at

69

least two different planes of (X, U, V, Y) are required to have a hit. At this stage, each DC is required to form at least one cluster, and if the number of cluster in a DC exceeds 100, such an event is skipped.

In Step-2, a straight-line fit is performed to all combinations of clusters in DC0 and DC1 or in DC2 and DC3 separately to search for upstream or downstream track candidates. Since the DCs only measure the drift distances, one cannot distinguish whether a particle has passed the left or right side of the wire (so-called "left-right ambiguity"). A left-right ambiguity is once solved by a straight-line fit in Step-2. However, for low-momentum particles, the left-right ambiguity cannot be correctly solved at this stage because a straight-line fit is not applicable for low-momentum particles due to the magnetic field. Therefore, the left-right ambiguity is solved again with a full-track fit in Step-3 so as to obtain a better fit χ^2 [112].

The best 30 combinations of clusters, given in terms of χ^2 in straight-line fits, are selected as an upstream/downstream track candidate. Among them, the combinations of upstream and downstream tracks which have passed the consistency checks between upstream and downstream tracks (i.e., the slopes of two tracks in the y-z plane, and the crossing point of two tracks in the x-z plane) are accepted as a full-track candidate, and proceed to Step-3.

The goodness of a full-track fit in Step-3 is judged in terms of the probability of χ^2, which is given by

$$Prob(\chi^2; ndf) = \int_{\chi^2}^{\infty} f(\chi'^2; ndf) d\chi'^2, \qquad (3.4)$$

where $f(\chi^2; ndf)$ is the standard χ^2 distribution with the number of degree of freedom ndf. If a track fit fails, the χ^2 probability yields a small value.

The momentum resolution of the LEPS spectrometer was estimated by MC simulations. Figure 3.2 shows the momentum resolution as a function of the kaon momentum. The momentum resolution for 1-GeV/c kaons is $\sim 0.9\%$ in $\delta p/p$, which is relevant for kaons from the ϕ-meson decay in the present experiment.

The validity of estimating the momentum resolution as well as the photon energy resolution was checked by comparing the missing mass resolutions for the the $p(\gamma, K^+)\Lambda(1116)$, $p(\gamma, K^+)\Sigma(1192)$, $p(\gamma, K^+)\Lambda(1520)$, $p(\gamma, \pi^+\pi^-)p$ and $p(\gamma, K^+K^-)p$ reactions with those obtained by MC simulations. The results are presented in Appendix F.
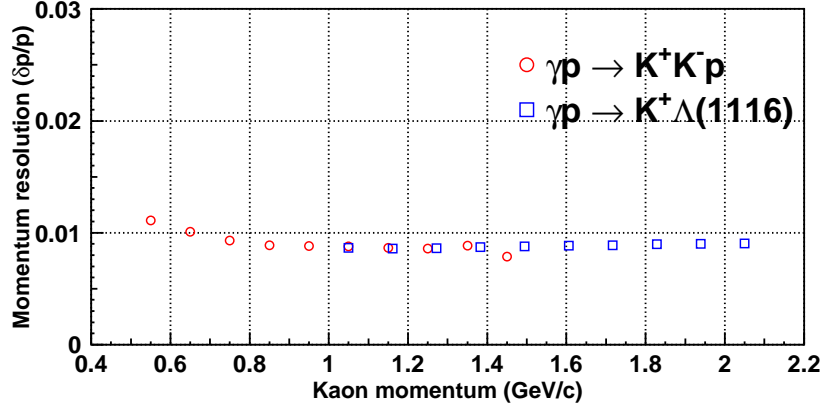
Figure 3.2:   Momentum resolution ($\delta p/p$) of the LEPS spectrometer as a function of the kaon momentum. Red circles represent those obtained from MC data on non-resonant K^+K^- production, whereas blue squares represent those obtained from MC data on the $\gamma p \to K^+\Lambda(1116)$ reaction.

3.4.2   Time-of-flight measurement

The time-of-flight of a charged particle (ΔT_{TOF}) is given by

$$\Delta T_{\mathrm{TOF}} = T_{\mathrm{stop}} - T_{\mathrm{start}}, \tag{3.5}$$

where T_{start} (T_{stop}) is the start (stop) time. T_{stop} was determined from the timing information of the TOF counters, whereas T_{start} was determined in two different ways: the one uses the timing information of the RF signals ($T_{\mathrm{start}}^{\mathrm{RF}}$), and the other uses the timing information of the FWD counters ($T_{\mathrm{start}}^{\mathrm{FWD}}$). The time-of-flight using the RF signal (the FWD counters) is denoted as $\Delta T_{\mathrm{TOF}}^{\mathrm{RF}} = T_{\mathrm{stop}} - T_{\mathrm{start}}^{\mathrm{RF}}$ ($\Delta T_{\mathrm{TOF}}^{\mathrm{FWD}} = T_{\mathrm{stop}} - T_{\mathrm{start}}^{\mathrm{FWD}}$). Since the RF signal has a good timing resolution of 12 ps, the timing resolution for $\Delta T_{\mathrm{TOF}}^{\mathrm{RF}}$ is much better than that for $\Delta T_{\mathrm{TOF}}^{\mathrm{FWD}}$. A typical timing resolution is 150 ps and 220 ps for $\Delta T_{\mathrm{TOF}}^{\mathrm{RF}}$ and $\Delta T_{\mathrm{TOF}}^{\mathrm{FWD}}$, respectively (see Appendix B.1).

Since the electrons circulating in the storage ring are bunched according to the RF signal, the collision time of a laser photon and an electron is synchronized with the RF signal. Therefore, one can know the arrival time of a BCS photon at the target from the timing information of the RF signal because the traveling time of BCS photons between the collision point and the target is constant. Figure 3.3 shows the TDC difference between the RF signal and the TAG-PL slat of the tagging counter that detects a BCS

electron. Here, to select a TAG-PL slat hit by a BCS electron correctly, the corresponding TAG-SF channel was required to have a hit. A clear time-structure corresponding to the electron bunches is seen with an interval of ~ 2 ns.
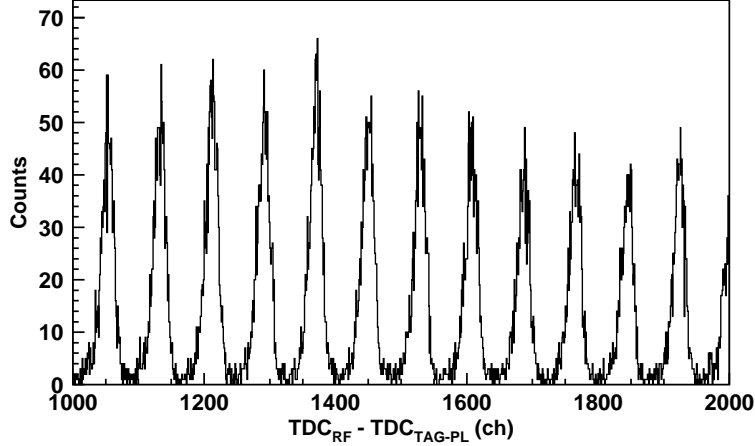
Figure 3.3: TDC difference between the RF signal and the TAG-PL slat corresponding to the BCS electrons. One TDC channel corresponds to 0.025 ns.

How to solve a "2-ns ambiguity"

To determine the start time ($T_{\text{start}}^{\text{RF}}$), one has to know which of the peaks in Fig. 3.3 corresponds to the collision time for a BCS process (a so-called "2-ns ambiguity"). Here, we explain how to solve the 2-ns ambiguity: let t_i be the i-th peak position, and find an integer n so that $(t_{n-1} + t_n)/2 \leq T_{\text{diff}} < (t_n + t_{n+1})/2$, where T_{diff} denotes the TDC difference between the RF signal and TAG-PL. This t_n corresponds to a time offset due to the 2-ns ambiguity. Therefore, the start time ($T_{\text{start}}^{\text{RF}}$) is obtained from the time offset t_n as

$$T_{\text{start}}^{\text{RF}} = (TDC_{\text{RF}} - t_n) \times 0.025 \ (\text{ns/ch}), \tag{3.6}$$

where TDC_{RF} is the TDC channel of the RF signal, and 0.025 ns/channel corresponds to the timing resolution of the TDC modules.

3.4.3   Mass reconstruction

The mass of a charged particle (m) was reconstructed by using the momentum ($p = |\boldsymbol{p}|$), the time-of-flight (ΔT_{TOF}) and the path length (L) as

$$
\begin{aligned}
m^2 &= E^2 - p^2 = p^2 \left(\frac{1}{\beta^2} - 1 \right), \\
\beta &= \frac{v}{c} = \frac{L}{\Delta T_{\mathrm{TOF}} \cdot c},
\end{aligned}
\tag{3.7}
$$

where c is the speed of light. We see from Eq. (3.7) that the resolution of the reconstructed mass depends on the resolutions in momentum and time-of-flight measurements. In the present analysis, a time-of-flight was obtained with two different methods ($\Delta T_{\mathrm{TOF}}^{\mathrm{RF}}$ and $\Delta T_{\mathrm{TOF}}^{\mathrm{FWD}}$; see Sect. 3.4.2). The former one provides a better mass resolution thanks to a better timing resolution of the start timing in time-of-flight measurements.

Figure 3.4 shows a distribution of the square of the reconstructed mass. Here, the mass was calculated by using $\Delta T_{\mathrm{TOF}}^{\mathrm{RF}}$. Clear peaks corresponding to pions, kaons, protons, deuterons and tritons/helium-3 are seen.
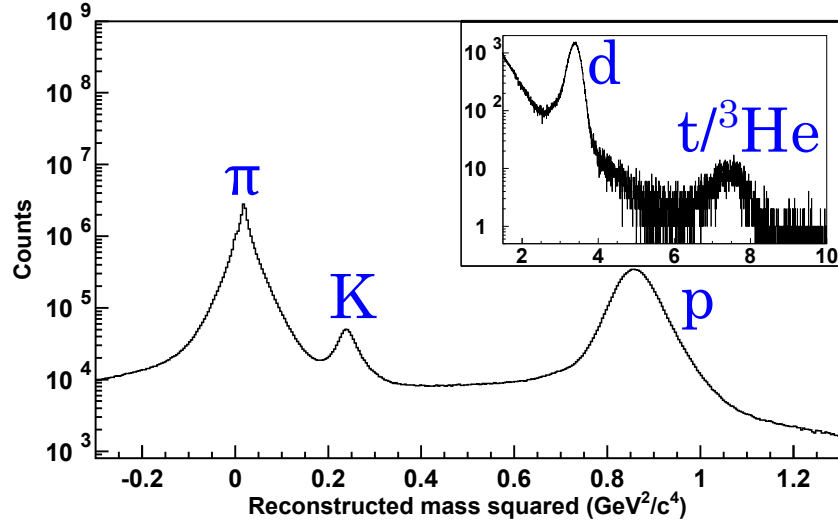
Figure 3.4:   Distribution of the square of the reconstructed mass. The mass was calculated by using $\Delta T_{\mathrm{TOF}}^{\mathrm{RF}}$. The inset shows the same distribution for a higher mass region.

3.4.4   Vertex reconstruction

The vertex point of a charged particle was reconstructed by tracing back the trajectory with a Runge-Kutta method. For the events in which one track was reconstructed, the closest point between the beam and the track was regarded as a vertex point. On the other hand, for the events in which two tracks were reconstructed, the closest point between the tracks was regarded as a vertex point.

We found that a reconstructed z-vertex position is shifted depending on the configuration of tracks due to an imperfect magnetic field map. To obtain a better z-vertex resolution, a reconstructed z-vertex position was corrected event by event according to the track configuration (see Appendix G for details). A z-vertex distribution with the empty-target data is well reproduced by MC simulation (see Fig. G.2).

Figure 3.5 shows distributions of the reconstructed z-vertex position for $\pi^+\pi^-$ tracks and that for a single π^+ track and a beam, respectively, after the correction. A clear peak for the CFRP cap of the target chamber is seen in the z-vertex distribution for $\pi^+\pi^-$ tracks, whereas it disappears in the z-vertex distribution for single π^+ tracks. This is because a beam direction cannot be measured and was assumed to be identical to the z-axis in the vertex reconstruction.
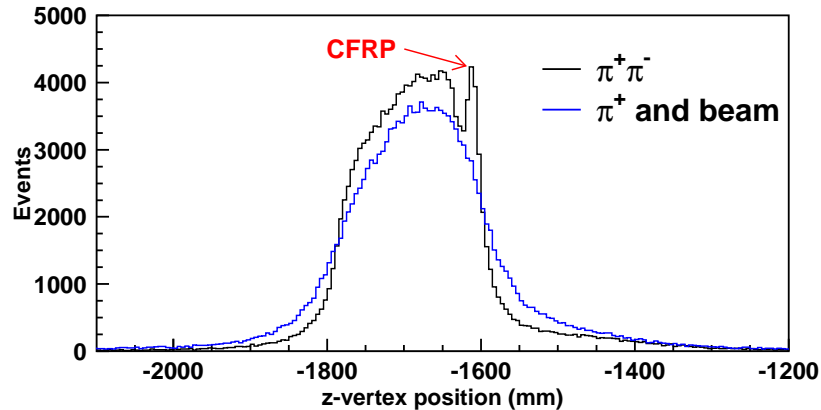
Figure 3.5:   Distributions of the reconstructed z-vertex position for $\pi^+\pi^-$ tracks (black) and for a single π^+ track and a beam (blue) with the LH$_2$ data. A peak around $z = -1600$ mm corresponds to the CFRP cap of the target chamber.

3.4.5   Energy loss correction

When a charged particle passes through materials, it looses the energy. Therefore, the momentum measured at the dipole magnet is different from that at the vertex point due to the energy loss. There are several materials between the target and the entrance of the dipole magnet: a CRFP cap of the target chamber, plastic scintillators, silica-aerogel of AC and a structure (a frame) of the TPC field cage made of aluminum or G10 (see Fig. 3.1). A energy loss correction was applied to each track after particle identification (see for kaon ID Sect. 3.6).

The energy loss per unit length, dE/dx in MeV/mm, for each material was evaluated by using a GEANT3 package [118], and was obtained as a function of particle velocity $\beta(= v/c)$. The energy loss of each track was corrected by tracing back the trajectory with a Runge-Kutta method from the entrance of the dipole magnet to the vertex point. Note that the velocity was calculated in each Runge-Kutta step and was used for calculating the energy loss in the next step.

3.5   Photon energy and Momentum scaling

The photon energy was determined event by event by measuring the hit-position of an electron track with TAG-SF. A photon energy function, i.e. a conversion function from a TAG-SF channel to photon energy, was obtained by using the $p(\gamma, K^+)\Lambda(1116)$ and $p(\gamma, \pi^+\pi^-)p$ reactions with the LH$_2$ data. Once the $K^+\Lambda(1116)$ final state is selected, the photon energy is calculated as[21]

$$E_\gamma^{\text{cal}} = \frac{M_{\Lambda(1116)}^2 - M_p^2 - M_K^2 + 2M_p E_{K^+}}{2(M_p - E_{K^+} + p_{K^+}^z)}, \tag{3.8}$$

where $p_{K^+}^z$ is the z-component of the K^+ momentum, E_{K^+} is the energy of K^+, and M_{K^+}, $M_{\Lambda(1116)}$ and M_p are the masses of K^+, $\Lambda(1116)$ and protons, respectively. On the other hand, if the $\pi^+\pi^- p$ final state is selected, then the photon energy is calculated as

$$E_\gamma^{\text{cal}} = \frac{2M_p E_{2\pi} - (E_{2\pi}^2 - \boldsymbol{p}_{2\pi}^2)}{2(M_p - E_{2\pi} + p_{2\pi}^z)}, \tag{3.9}$$

---

[21]A beam direction is assumed to be parallel to the z-axis.
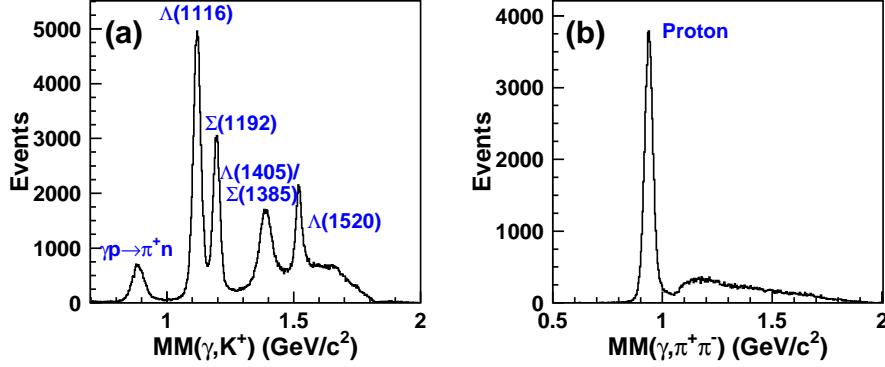
Figure 3.6:   Missing mass distributions for (a) the $p(\gamma, K^+)X$ and (b) $p(\gamma, \pi^+\pi^-)X$ reactions.

where $p_{2\pi}^z$ is the z-component of the momentum $(\boldsymbol{p}_{2\pi})$ of the $\pi^+\pi^-$ system. Thus, two photon energy functions were obtained separately with Eqs. (3.8) and (3.9), and were finally averaged.

Figures 3.6(a) and (b) show missing mass spectra for the $p(\gamma, K^+)X$ and $p(\gamma, \pi^+\pi^-)X$ reactions, respectively. Clear peaks for hyperon resonances and protons are seen in each spectrum.

Figures 3.7(a) and (b) show the E_γ^{cal} calculated by Eq. (3.8) $[p(\gamma, K^+)$ $\Lambda(1116)]$ as a function of the TAG-SFF and TAG-SFB channels, respectively. The photon energy functions for SFF and SFB were separately obtained by fitting these plots with a 3rd-polynomial function. Figures 3.8(a) and (b) show the same plots for the $p(\gamma, \pi^+\pi^-)p$ reaction.

In the actual analysis, the photon energy was determined as follows. When only one of the SFF and SFB layers had a hit, the photon energy was calculated by the photon energy function for the corresponding layer (SFF or SFB). On the other hand, when both layers had hits, two values of the photon energy calculated by the photon energy functions for each layer were averaged.

Since the determination of the photon energy function is strongly coupled to the momentum scale of the LEPS spectrometer in the above methods, a momentum scaling factor, which is introduced to tune the momentum scale of the spectrometer, was also determined at the same time. To obtain the photon energy functions and the momentum scaling factor correctly, the following procedure (1–3) was iterated:
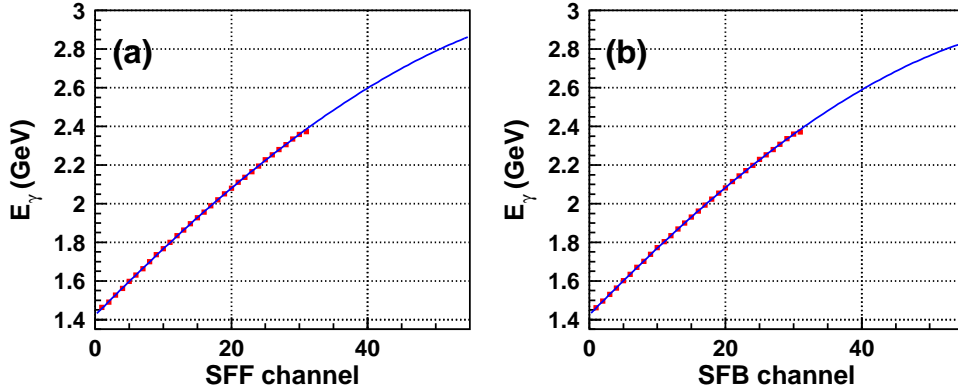
Figure 3.7: E_γ^{cal} calculated by Eq. (3.8) $[p(\gamma, K^+)\Lambda(1116)]$ as a function of (a) the TAG-SFF channel and (b) the TAG-SFB channel. Blue curves are the fits to the data with a 3rd polynomial function.
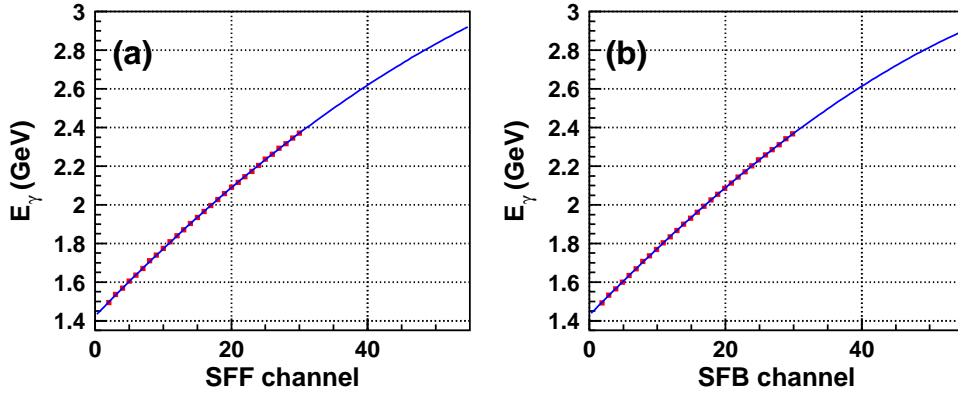
Figure 3.8: Same plots as Fig 3.7, but for the $p(\gamma, \pi^+\pi^-)p$ reaction.

1. The photon energy functions are determined with the above method.

2. The momentum scaling factor is roughly determined so that the positions of missing-mass peaks for the $p(\gamma, K^+K^-)p$, $p(\gamma, pK^-)K^+$ and $p(\gamma, \pi^+\pi^-)p$ reactions are consistent with the PDG values.

3. The positions of the Compton edges in photon energy spectra calculated by Eqs. (3.8) and (3.9) are checked, and the momentum scaling factor is adjusted if necessary.
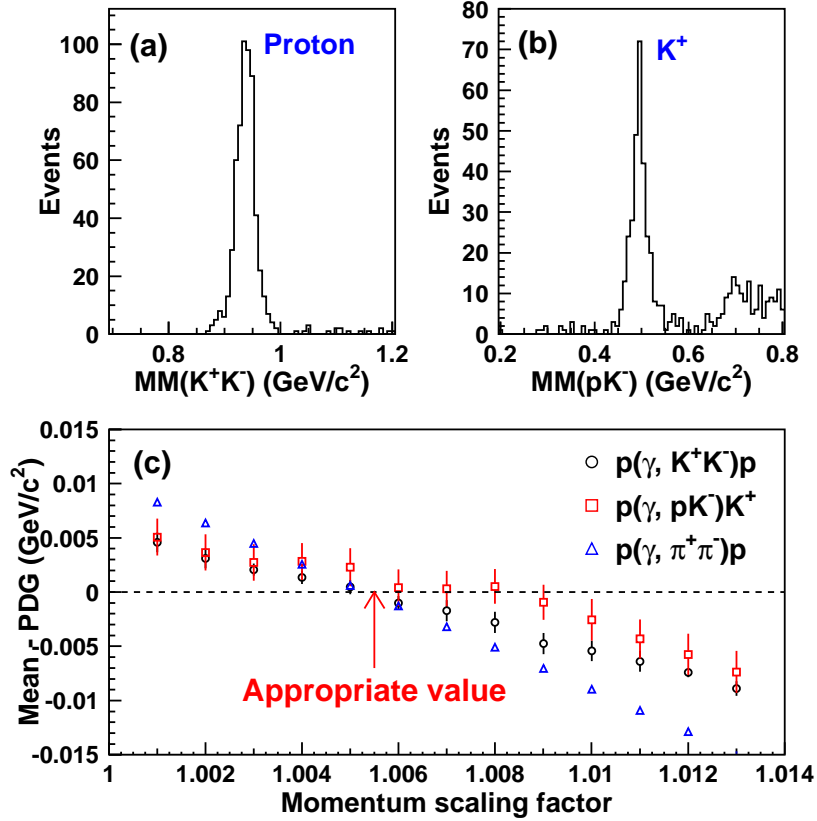
Figure 3.9:   (a) Missing mass spectra for the $p(\gamma, K^+K^-)X$ and (b) $p(\gamma, pK^+)X$ reactions.   (c) Positions of missing mass peaks for the $p(\gamma, \pi^+\pi^-)p$, $p(\gamma, K^+K^-)p$ and $p(\gamma, pK^-)K^+$ reactions as a function of the momentum scaling factor. The values on the vertical axis are those after subtracting the PDG values. A dashed horizontal line corresponds to the PDG values. An appropriate value of 1.0055 is obtained from this figure.

Figure 3.9(a) and (b) show missing mass spectra for the $p(\gamma, K^+K^-)X$ and (b) $p(\gamma, pK^+)X$ reactions. Clear peaks for protons and kaons are seen in each plot. Figure 3.9(c) shows the positions of missing mass peaks for the the $p(\gamma, \pi^+\pi^-)p$, $p(\gamma, K^+K^-)p$ and $p(\gamma, pK^-)K^+$ reactions as a function of the momentum scaling factor. From this figure, an appropriate value for the momentum scaling factor is 1.0055.

Figures 3.10(a) and (b) show distributions of the photon energy calculated by Eq. (3.8) $[p(\gamma, K^+)\Lambda(1116)]$ and Eq. (3.9) $[p(\gamma, \pi^+\pi^-)p]$, respectively. The Compton edge in Fig. 3.10(a) was fitted with an error function (i.e., Gaussian-convoluted step function). Since the spectrum in Fig. 3.10(b) rapidly rises toward the Compton edge, the edge was fitted with the following function:

$$
\begin{aligned}
h(x) &= A \int_{\infty}^{\infty} f(t) \cdot g(x - t)dt, \\
f(x) &= \begin{cases} Bx + 1 & (x < C) \\ 0 & (x \geq C), \end{cases} \\
g(x) &= \frac{1}{\sqrt{2\pi D^2}} \exp\left(-\frac{x^2}{2D^2}\right),
\end{aligned}
\tag{3.10}
$$

where A, B, C and D are free parameters. By fitting the spectra in Figs. 3.10(a) and (b), the positions of the Compton edges are obtained to be 2.3839 ± 0.0004 GeV and 2.3856 ± 0.0006 GeV, respectively, which are consistent with the expected value ($E_\gamma = 2.385$ GeV[22]).

Table 3.1 summarizes the momentum scaling factor for each data set. Note that since the momentum scaling factor includes the effects due to displacement of DCs, the scaling factor was determined for each data set (see Sect. 2.7 for the data summary).

Table 3.1: Summary of the momentum scaling factor for each data set.

Data set	Momentum scaling factor
data-1	1.0040
data-2	1.0045
data-3	1.0055

[22]It is assumed that the electron energy is $E_e = 7.975$ GeV, and the wavelength of laser photons is $\lambda_{\text{laser}} = 355$ nm.
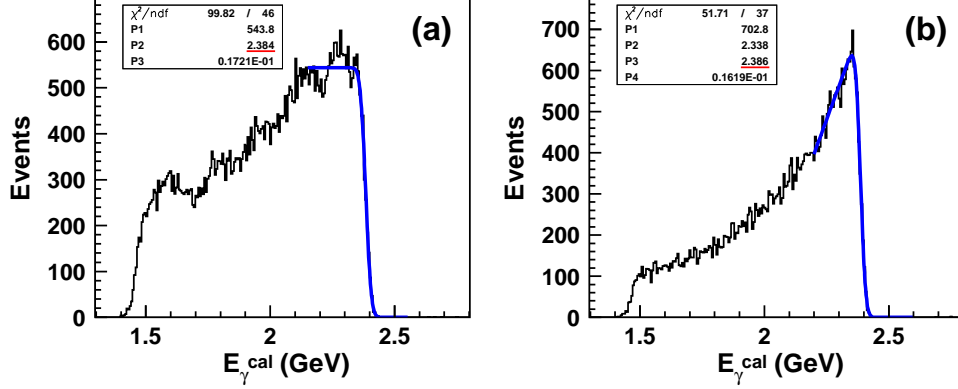
Figure 3.10:   Distributions of the photon energy calculated by (a) Eq. (3.8) $[p(\gamma, K^+)\Lambda(1116)]$ and (b) Eq. (3.9) $[p(\gamma, \pi^+\pi^-)p]$. From these plots, the positions of the Compton edges are obtained to be (a) 2.3839 ± 0.0004 GeV and (b) 2.3856 ± 0.0006 GeV, respectively.
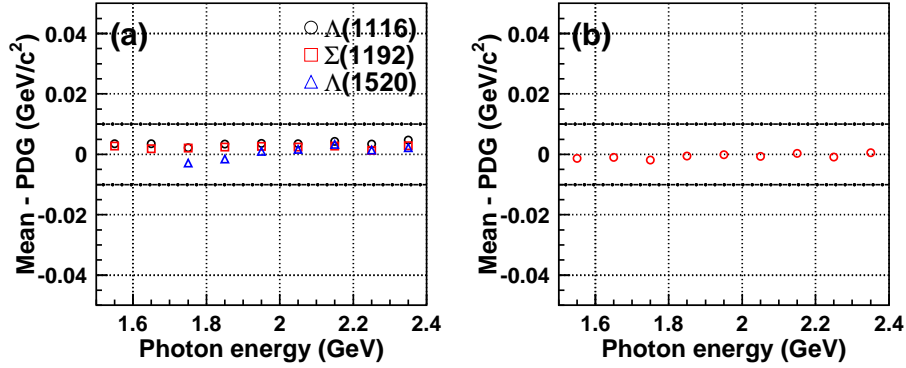
Figure 3.11:   (a) Peak positions of $\Lambda(1116)$, $\Sigma(1192)$ and $\Lambda(1520)$ in missing mass $p(\gamma, K^+)X$ spectra as a function of the photon energy. Black open circles, red open squares and blue open triangles represent the peak positions of $\Lambda(1116)$, $\Sigma(1192)$ and $\Lambda(1520)$, respectively. (b) Proton peak position in missing mass $p(\gamma, \pi^+\pi^-)X$ spectra as a function of the photon energy. For both plots, the values on the vertical axis are those after subtracting the PDG values. Dash-dotted horizontal lines correspond to a ± 1 MeV/c^2 deviation from the PDG values.

Finally, we checked the photon energy dependence of the peak positions of hyperon resonances in missing mass $p(\gamma, K^+)X$ spectra and that of protons in missing mass $p(\gamma, \pi^+\pi^-)X$ spectra [Figs. 3.11(a) and (b)]. The peak positions are consistent with the PDG values, and are independent of the photon energy.

3.6   Selection of K^+K^- event

Now we are ready for analyzing the LHe data. In this section, the criteria for selecting K^+K^- events are described. Table 3.2 summarizes the number of the survived events and the ratio of the survived events under selection cuts. The details are explained in the following paragraphs.

Table 3.2: Cut summary: the number of the survived events, and the ratio of the survived events. See the text for the details.

Cut	Number of events	Survived ratio	Comment
All	109,710,616	−	
Tagger	82,590,960	0.75	$fntag = 1$
$ntrk = 2$	1,516,435	0.018	# of tracks
PID (K^+K^-)	9,896	0.0065	4σ
TOF match	9,845	0.99	
χ^2 prob.	7,619	0.77	$prbchi2 > 0.02$
Decay-in-flight	7,619	1.00	$noutl < 7$
e^+e^- cut	7,362	0.97	e^+e^- veto
z-vertex	6,145	0.83	
MM(K^+K^-) cut	4,523	0.74	π rejection

Tagger cut

An electron track in the tagging system was identified by searching for hits in TAG-SF and the corresponding TAG-PL channel. Here, at least one hit was required in either of TAG-SFF or TAG-SFB. Since the tagging system is placed near the orbit of the circulating electrons, there would be multiple tracks in the tagging system. In such case, one cannot distinguish a true electron track from the others. Therefore, the number of electron tracks in the tagging system ($fntag$) was required to equal one ($fntag = 1$).

81

Kaon identification

Kaon tracks were identified according to the square of the reconstructed mass by the LEPS spectormeter [Eq (3.7)]. Figure 3.12 (a) shows a scatter plot for the momentum/charge versus the square of the reconstructed mass by using $\Delta T_{\text{TOF}}^{\text{RF}}$. Black curves correspond to the 4σ boundaries for the kaon identification, where σ is the momentum-dependent resolution of the reconstructed mass squared. The momentum-dependent mass resolution was evaluated from the data by fitting mass distributions in different momentum slices with a Gaussian function.

Since TAG-PLs, which are used for solving the 2-ns ambiguity, are placed near the electron orbit in the storage ring, they suffer from accidental hits by electrons. This would cause a failure in solving the 2-ns ambiguity. If one fails to solve the 2-ns ambiguity, it makes a locus in a scatter plot for the momentum versus the reconstructed mass squared, as can be seen in Fig. 3.12(a). To reduce the pion/proton contamination due to such events, two types of particle identification (PID) were combined: the one uses $\Delta T_{\text{TOF}}^{\text{RF}}$ (PID-RF), and the other uses $\Delta T_{\text{TOF}}^{\text{FWD}}$ (PID-FWD). Figure 3.12 (b) show a scatter plot for the momentum/charge versus the reconstructed mass squared after roughly selecting kaons with PID-FWD. You see that the contamination of low-momentum pions and protons are removed after the rough selection of kaons with PID-FWD.

Figures 3.13(a) and (b) show scatter plots for the momentum/charge versus the square of the reconstructed mass by using $\Delta T_{\text{TOF}}^{\text{FWD}}$ before and after PID-RF, respectively. Black curves show the boundaries for roughly selecting kaons with PID-FWD. The boundary for the low mass side was set to 4σ, whereas that for the high mass side was set to 5.5σ.

Even after applying PID-FWD, there still exists the contamination of high-momentum pions inside the PID boundaries [see Fig. 3.12(b)]. Figure 3.14 shows a missing mass distribution for the ${}^4\text{He}(\gamma, K^+K^-)X$ reaction after applying the PID cuts with PID-RF and PID-FWD. A peak around a mass of $3.5~\text{GeV}/c^2$ corresponds to the events in which pions are misidentified as a kaon. By requiring the missing mass of the ${}^4\text{He}(\gamma, K^+K^-)X$ reaction to be above $3.62~\text{GeV}/c^2$, such pion events can be reduced to a negligible level [a $\text{MM}(K^+K^-)$ cut].

If one fails to solve the 2-ns ambiguity, K^+K^- tracks are lost. The K^+K^- event loss in the kaon identification was estimated by using the $p(\gamma, p)\pi^0$ reaction, and was found to be 3% (see Appendix H).
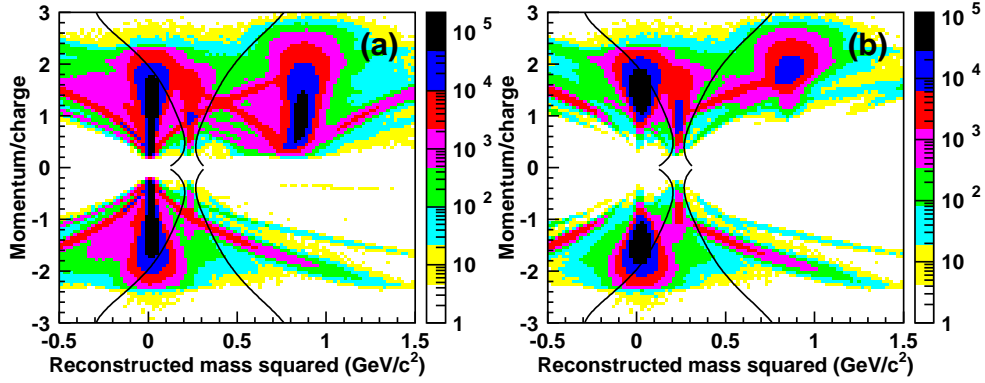
Figure 3.12:   Scatter plots for the momentum/charge versus the square of the reconstructed mass by using $\Delta T_{\mathrm{TOF}}^{\mathrm{RF}}$ (a) before and (b) after roughly selecting kaons with PID-FWD (see the text for the definition). Black curves show the boundaries for the kaon identification (4σ). Besides the pion, kaon and proton bands, there exist loci, which are due to a failure in solving the 2-ns ambiguity.
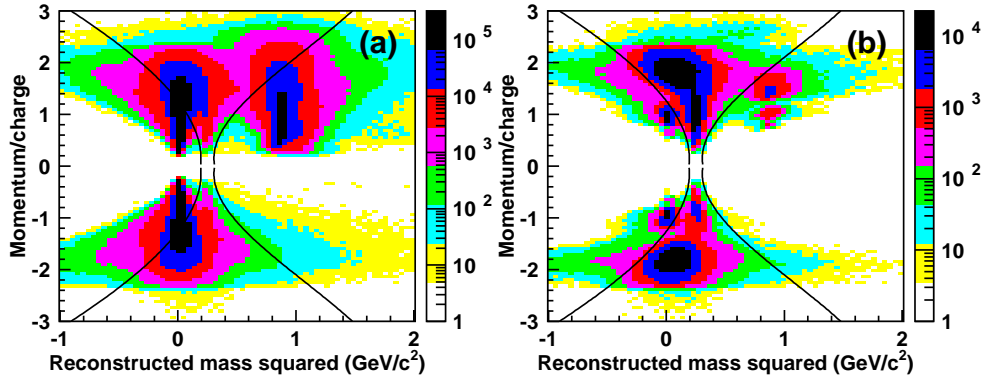
Figure 3.13:   Scatter plots for the momentum/charge versus the square of the reconstructed mass by using $\Delta T_{\mathrm{TOF}}^{\mathrm{FWD}}$ (a) before and (b) after the kaon identification with PID-RF. Black curves show the boundaries for roughly selecting kaons ($4\sigma/5.5\sigma$ for a lower/higher mass region).
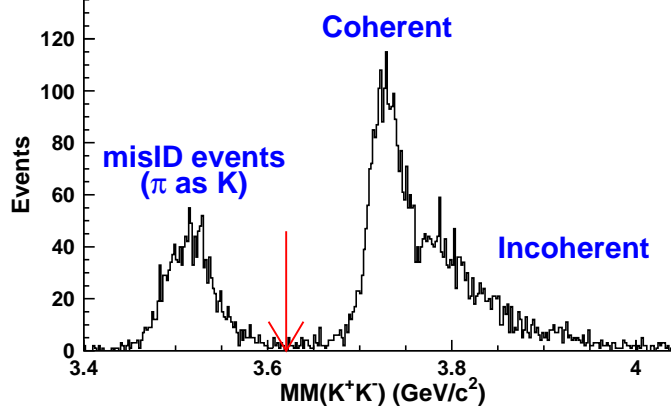
Figure 3.14:   Missing mass distribution for the ^{4}He$(\gamma, K^+K^-)X$ reaction after applying the PID cuts with PID-RF and PID-FWD. A red arrow represents the cut point for pion rejection.

Track quality cut

The quality of tracks was checked on the basis of the χ^2 probability in track fits and the consistency of the hit positions of tracks at the TOF wall.

The probability of χ^2 in a track fit is given by Eq. (3.4). A typical distribution of the χ^2 probabilities is shown in Fig. 3.15. A sharp peak around zero corresponds to the tracks for which the quality of the track fit is poor. Therefore, the χ^2 probability was required to be greater than 0.02 (*prbchi2* > 0.02).

In addition, we checked the consistencies between the hit position obtained from the TOF hit information and that predicted from a track. Figure 3.16(a) shows the difference between the TOF slat predicted from a track ($iTof_{\mathrm{trk}}$) and the fired TOF slat nearest to the predicted one ($iTof_{\mathrm{tof}}$). Figure 3.16(b) shows the difference between the y-position at TOF predicted from a track (y_{trk}) and that obtained from the TDC information of the TOF counter (y_{tof}). The difference of the TOF slat was required to be within 1 ($|iTof_{\mathrm{trk}} - iTof_{\mathrm{tof}}| \leq 1$), whereas the difference of the y-hit position was required to be within 80 mm ($|y_{\mathrm{trk}} - y_{\mathrm{tof}}| < 80$ mm).

84
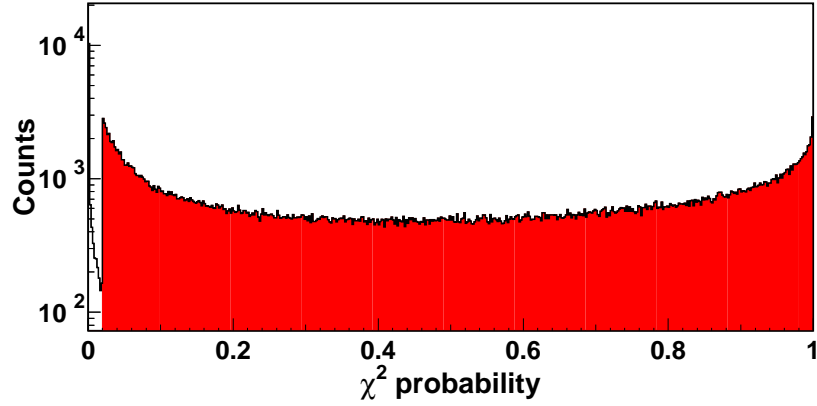
Figure 3.15:   A typical distribution of the χ^2 probabilities.   A red filled histogram represents the distribution for the tracks passing the χ^2 cut (*prbchi2* > 0.02). A sharp peak around zero corresponds to tracks with poor fit quality.
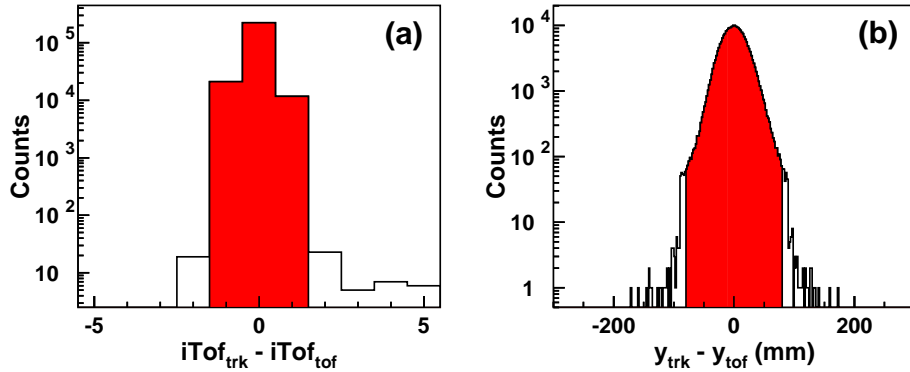
Figure 3.16:   (a) A typical distribution of the difference of the TOF slat ($iTof_{\mathrm{trk}} - iTof_{\mathrm{tof}}$). A red filled histogram shows the distribution for the tracks passing the $iTof$ cut ($|iTof_{\mathrm{trk}} - iTof_{\mathrm{tof}}| \leq 1$). (b) A typical distribution of the difference of the y-hit position ($y_{\mathrm{trk}} - y_{\mathrm{tof}}$). A red filled histogram shows the distribution for the tracks passing the y-TOF cut ($|y_{\mathrm{trk}} - y_{\mathrm{tof}}| < 80$ mm).

Decay-in-flight cut

Some of kaon tracks decay mainly into $\mu^+\nu_\mu$ ($\mu^-\bar\nu_\mu$) before arriving at the TOF wall with a life time of $c\tau = 3.711$ m. In such case, a muon track deviates from its parent trajectory. In the tracking procedure (see Sect. 3.4.1 for details), the hits largely deviating from the expected trajectory are regarded as an outlier hit, and are excluded in a track fit. Figure 3.17 shows a distribution of the number of outlier hits for kaon tracks in the $\gamma p \to \phi p$ reaction followed by the $\phi \to K^+K^-$ decay (MC data). The number of outlier hits decreases rapidly up to 6, and then rises up. This is due to the kaon tracks decaying in flight. Therefore, the number of outlier hits was required to be less than 7 (*noutl* < 7).
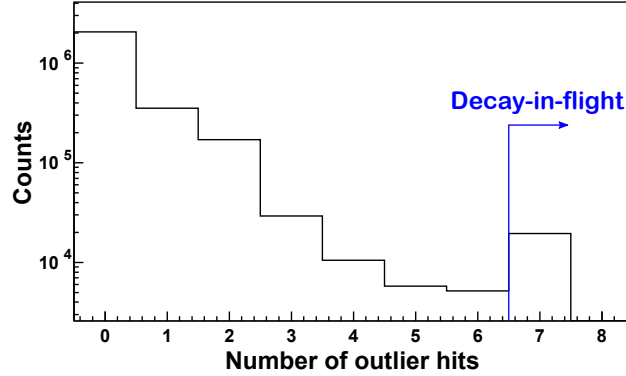
Figure 3.17: Number of outlier hits for kaon tracks in the $\gamma p \to \phi p$ reaction followed by the $\phi \to K^+K^-$ decay. The data was obtained by MC simulation.

e^+e^- cut

The e^+e^- blocker is placed inside the dipole magnet to block e^+e^- pairs. A cut on the y-coordinate of tracks at the e^+e^- blocker was used to reject the e^+e^- events in the off-line analysis. Figure 3.18 shows a typical distribution of the y-coordinate of tracks at the e^+e^- blocker. A dip around $y \sim 0$ corresponds to the e^+e^- blocker. Therefore, the y-coordinate at the e^+e^- blocker was required to be less than -35 mm or greater than 16 mm (*ybar* < -35 mm or *ybar* > 16 mm).
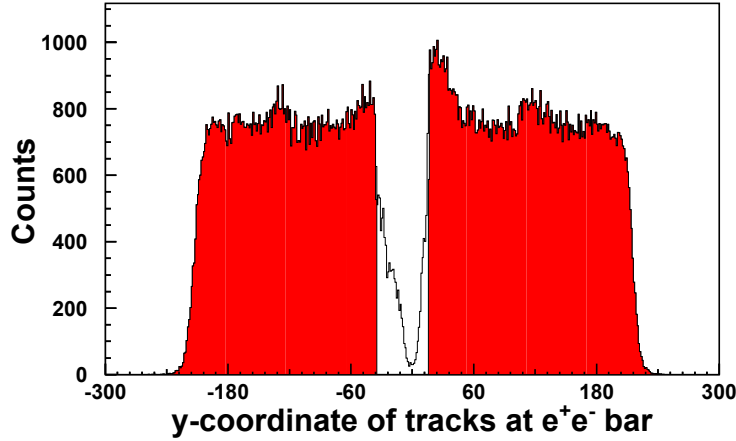
Figure 3.18:   A typical distribution of the y-coordinate of tracks at the e^+e^- blocker. A red filled histogram shows the distribution for the tracks passing the e^+e^- cut ($ybar < -35$ mm or $ybar > 16$ mm).

z-vertex cut

To select the K^+K^- pairs produced inside the target, a cut was imposed on the reconstructed z-vertex position of K^+K^- pairs. Figure 3.19(a) shows the z-vertex distribution of K^+K^- pairs with the LHe data. A shoulder-like structure around $z \sim -1600$ mm corresponds to the CFRP cap of the target chamber (see also Fig. 3.5). Cut points for this selection were set to $z = -1820$ mm and $z = -1620$ mm, respectively, as indicated by arrows in Fig. 3.19(a).

Under the z-vertex cut, the contamination of the K^+K^- events from the CFRP cap was estimated by fitting the z-vertex distribution with two MC-simulated distributions (templates): the one is a template for K^+K^- tracks from the CFRP cap, and the other is that for K^+K^- tracks from the target. Since the z-vertex resolution depends on the opening angle of a K^+K^- pair, the events from ϕ-production and those from non-resonant K^+K^- production were mixed in MC simulation according to the ratio determined from a $M(K^+K^-)$ distribution (e.g., see Fig. 3.20). The fit result is represented by colored histograms in Fig 3.19(a). The sum of the MC-simulated distributions (a blue histogram) well reproduces the z-vertex distribution with the LHe data. From the fit, the contamination of the K^+K^- events from the CFRP cap was evaluated to be 2.3%.
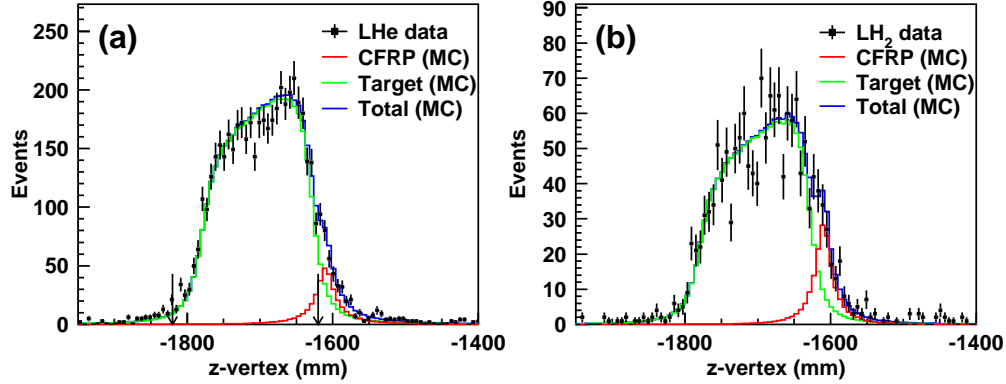
Figure 3.19: z-vertex distributions of K^+K^- pairs with (a) the LHe data and (b) the LH$_2$ data. Red and green histograms show MC-simulated z-vertex distributions of the K^+K^- pairs produced from the CFRP cap and the target, respectively, and blue histogram shows the sum of them (explained in the text in detail). Arrows represent cut points for the z-vertex cut.

To check the validity of the above evaluation, a template fit was also applied to the z-vertex distribution for the LH$_2$ data [Fig. 3.19(b)], and the number of the CFRP events divided by the number of photons was compared with that obtained with the LHe data. Here, the number of photons for each target data was corrected on the basis of the DAQ efficiency and the dead time of NIM modules. The number of the CFRP events per the number of photons obtained with the LH$_2$ data $[= (8.45 \pm 0.87) \times 10^{-11}]$ was found to be consistent with that with the LHe data $[= (8.01 \pm 0.68) \times 10^{-11}]$.

The systematic error on the event contamination from the CFRP cap was evaluated to be 0.2% by fixing the number of the CFRP events in the template fit to be the value determined from the LH$_2$ data.

3.7   Yield calculation for coherent ϕ-production

There are three steps in the yield calculation for the coherent ϕ-production events. First, the ϕ-meson yields including both the coherent and incoherent production events (N_ϕ) were evaluated from M(K^+K^-) spectra. Second, the ratios of the coherent production events to the total events (R_{coh}) were evaluated from MM(K^+K^-) spectra. Finally, the ϕ-meson yields for coherent production (N_{coh}) were calculated by multiplying the total ϕ yields N_ϕ and

the coherent ratios R_{coh} as

$$N_{\mathrm{coh}} = N_\phi \times R_{\mathrm{coh}}. \tag{3.11}$$

3.7.1 Total ϕ-meson yield

The ϕ-meson yields including both the coherent and incoherent production events, N_ϕ, were obtained by fitting $\mathrm{M}(K^+K^-)$ spectra with MC-simulated distributions (templates) for signal and background processes. Here, quasi-free $K^+\Lambda(1520)$ production followed by the $\Lambda(1520) \to K^-p$ decay was found to be negligible at small momentum transfers of our interest ($-t < 0.2$ GeV^2). Therefore, we considered non-resonant K^+K^- production as a background process. Here, "non-resonant" production means that particles are generated uniformly in the phase space. Realistic spectral shapes of $\mathrm{M}(K^+K^-)$ distributions for each process were reproduced by MC simulation. To model the kinematical distributions for ϕ-photoproduction in MC simulation, a phenomenological function was used in the event generator (see Sect 3.9 for details).

A template fit was performed by minimizing a negative log-likelihood with a Poisson distribution, which is defined by

$$
\begin{aligned}
L(\boldsymbol{\theta}) &= -\ln \mathcal{L}(\boldsymbol{\theta}) = -\ln \prod_{i=1}^{N} \mathcal{F}(X_i|\boldsymbol{\theta}), \\
\mathcal{F}(X_i|\boldsymbol{\theta}) &= f(X_i = x; \ \theta_1 c_1^{(i)} + \theta_2 c_2^{(i)} = \lambda) \\
&= \frac{e^{-\lambda}\lambda^x}{x!},
\end{aligned}
\tag{3.12}
$$

where $\boldsymbol{\theta} = \{\theta_1, \theta_2\}$ is a set of parameters representing a normalization factor for each MC template, X_i denotes the histogram contents of the i-th bin for the present data, $c_1^{(i)}$ and $c_2^{(j)}$ denote the histogram contents of the i-th bin for each MC template and N denotes the number of bins. Here, each MC template was normalized so that the total histogram contents were equal to 1. The value of each parameter θ_j is then exactly the same as the number of events for each process. A minimization was done by using a MINUIT package [119]. The error on each parameter was defined as the change of the parameter which makes a change of the log-likelihood [Eq. (3.12)] equal to 0.5.
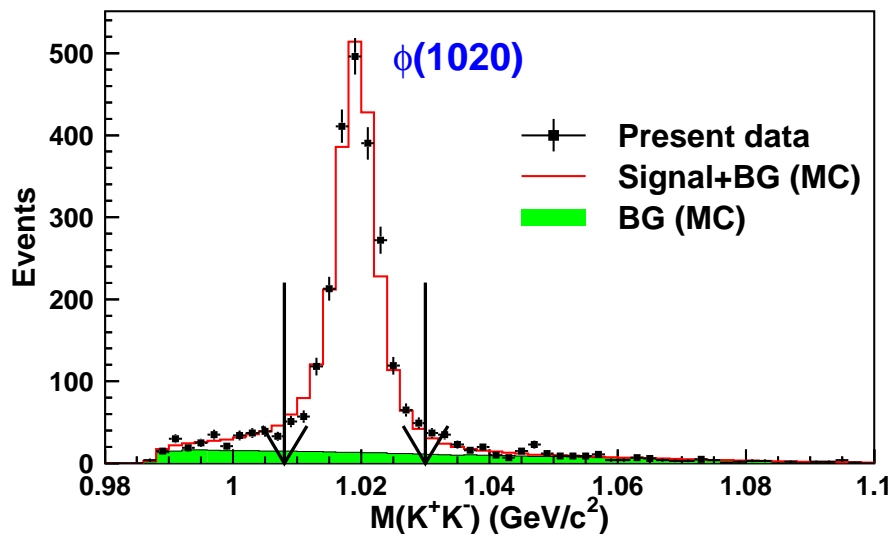
Figure 3.20:   M(K^+K^-) spectrum. A green filled histogram shows the MC-simulated background (BG). A red histogram shows the result for the template fit (Signal+BG). See the text for the MC templates. Arrows represent cut points for the disentanglement of the coherent production events (Sect. 3.7.2).

Figure 3.20 shows a typical M(K^+K^-) spectrum, together with the result for the template fit. A clear peak for ϕ-mesons is seen around M(K^+K^-) $\sim$ 1.02 GeV/c^2 on a small background contribution from the non-resonant K^+K^- production events. The sum of the signal and background templates well reproduces the spectrum.

It turned out that a template fit sometimes underestimates the data point on the top of a peak. This may result in incorrect evaluation of the ϕ-meson yields. To avoid this, the ϕ-meson yields were calculated according to the following equation:

$$N_\phi = \sum_{i=1}^{N} X_i \frac{\theta_1 c_1^{(i)}}{\theta_1 c_1^{(i)} + \theta_2 c_2^{(i)}}, \tag{3.13}$$

where θ_1 denotes the parameter for the signal ($\phi \to K^+K^-$) events.
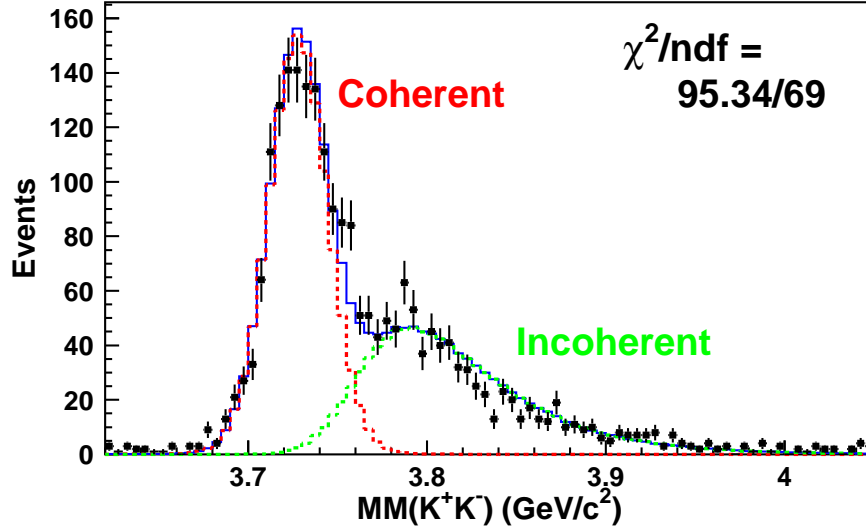
Figure 3.21:   MM(K^+K^-) spectrum after selecting the ϕ-meson production events. Red and green dashed histograms show the MC templates for the coherent and incoherent production events, respectively. A blue histogram shows the sum of the MC templates. The reduced χ^2 for this fit is shown on the right top corner.

3.7.2   Disentanglement of coherent production events

The coherent production events can be distinguished from the incoherent ones by looking at the missing mass MM(K^+K^-) (see Fig. 1.14 for the deuteron case). The ratios of the coherent ϕ-production events to the total-ϕ events, R_{coh}, were evaluated by fitting MM(K^+K^-) spectra with two MC-simulated spectra (templates) for the coherent and incoherent production events. The details of the MC simulation for the incoherent process are described in the next section (Sect. 3.8). To select the ϕ-production events, the invariant mass M(K^+K^-) was required to be within $1.008 <$ M(K^+K^-) $<$ 1.030 GeV/c^2, as indicated by arrows in Fig. 3.20. Figure 3.21 shows a typical MM(K^+K^-) spectrum after selecting the ϕ-meson production events, together with the result for the template fit. A clear peak for the coherent production events is seen around MM(K^+K^-) ≈ 3.73 GeV/c^2, corresponding to the mass of ^{4}He nuclei. The reduced χ^2 for this fit was found to be $95.34/69 = 1.34$. The missing mass spectrum is nicely reproduced by the

91
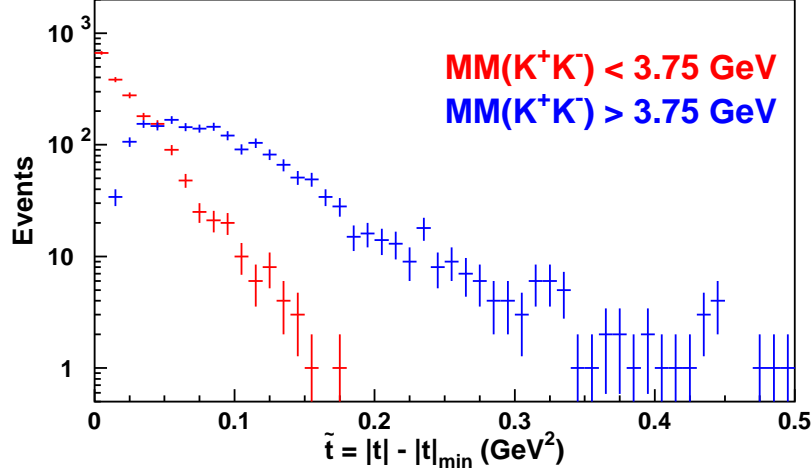
Figure 3.22:   The number of the ϕ-production events as a function of the momentum transfer $\tilde{t}$ ($= |t| - |t|_{\min}$).   Red points show the t-distribution with $\mathrm{MM}(K^+K^-) < 3.75$ GeV/c^2, whereas blue ones show that with $\mathrm{MM}(K^+K^-) > 3.75$ GeV/c^2.

MC-simulated spectra of the coherent and incoherent events.

   To check the validity of the above evaluation, t-distributions were examined for two event samples with different $\mathrm{MM}(K^+K^-)$ [i.e., $\mathrm{MM}(K^+K^-) <$ 3.75 GeV/c^2 and $\mathrm{MM}(K^+K^-) >$ 3.75 GeV/c^2].   Figure 3.22 shows the number of the ϕ-production events as a function of the momentum transfer $\tilde{t}$ ($\equiv |t| - |t|_{\min}$), where $|t|_{\min}$ is the minimum momentum transfer $|t|$ for a ^{4}He target.   Red points show the t-distribution with $\mathrm{MM}(K^+K^-) < 3.75$ GeV/c^2, whereas blue ones show that with $\mathrm{MM}(K^+K^-) > 3.75$ GeV/c^2.   The t-distribution with small $\mathrm{MM}(K^+K^-)$ is much steeper than that with large $\mathrm{MM}(K^+K^-)$.   This implies that the events with small $\mathrm{MM}(K^+K^-)$ come mostly from the coherent reaction because in the case of the coherent process, a quite strong t-dependence is expected due to the ^{4}He form factor [see for example Eq. (1.36)].

   With the above method, a value of R_{coh} could be affected by shapes of MC-simulated $\mathrm{MM}(K^+K^-)$ distributions for each process, and thus this could be a source of systematic errors.   In the analysis on the coherent $\gamma d \rightarrow \phi d$ reaction [95] (see also Sect. 1.6.2), the systematic errors caused by the disentanglement of the coherent events were estimated by studying
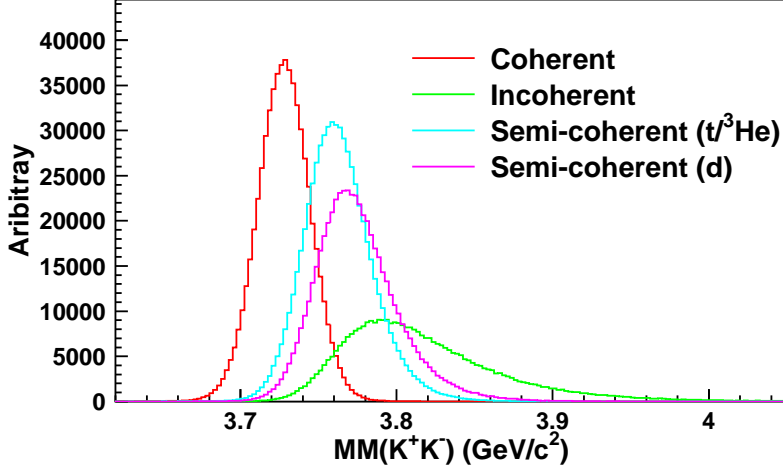
Figure 3.23:   MC-simulated MM(K^+K^-) spectra for the coherent (red), incoherent (green), semi-coherent $\gamma t/\gamma^3$He (cyan) and semi-coherent γd processes (pink).

two kinds of the off-shell correction for the incoherent process in MC simulation (see Sect. 3.8.1 for the off-shell correction). In the present analysis, such systematic errors were estimated by considering additional processes, in MM(K^+K^-) fits, such that

$$\gamma + \text{`}t\text{'} \to \phi + t,$$
$$\gamma + \text{`}^3\text{He'} \to \phi + {}^3\text{He}, \tag{3.14}$$

and

$$\gamma + \text{`}d\text{'} \to \phi + d, \tag{3.15}$$

where 't' ('d') represents the wave function of a triton (deuteron) cluster inside a ^{4}He nucleus[23]. In this thesis, these processes are called "semi-coherent" processes. Figure 3.23 shows MC-simulated MM(K^+K^-) spectra for the semi-coherent processes, together with those for the coherent and incoherent processes. The semi-coherent events are distributed between the coherent and incoherent ones. This is because the masses of deuteron, triton and ^{3}He lie between those of nucleon and ^{4}He. Thus, the systematic errors on R_{coh}

---

[23]These reactions mean that a photon interacts with a nuclear cluster inside a ^{4}He nucleus "coherently", and a ϕ-meson is produced.

93

due to event contamination other than the coherent ones can be estimated by taking into account the semi-coherent processes in $\mathrm{MM}(K^+K^-)$ fits. We found that there is not much change in fit χ^2 whichever of the semi-coherent processes [Eq. (3.14) or Eq. (3.15)] is used. Therefore, the semi-coherent process of Eq. (3.14) was used in the estimation of the systematic errors as an extreme case.

3.8 Monte Carlo simulation for non-coherent process

In the present analysis, it is essential to reproduce realistic shapes of $\mathrm{MM}(K^+K^-)$ distributions for "non-coherent" processes, i.e. the incoherent and semi-coherent processes. In this section, the details of the MC simulations for the incoherent and semi-coherent processes are described.

3.8.1 Incoherent process

The slope of $d\sigma/dt$ and the $\phi \to K^+K^-$ decay angular distributions for this process were taken into account in MC simulation. Since there is no available data on them, they were assumed to be the same as those for the $\gamma p \to \phi p$ reaction [85].
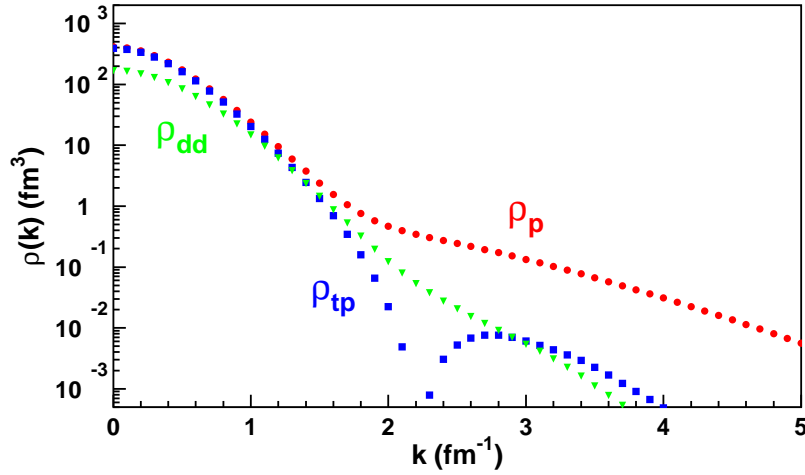
Figure 3.24: Momentum distributions of a proton (red circles), a triton (blue squares) and a deuteron (green triangles) inside a ^{4}He nucleus. These distributions were obtained by VMC calculations [120].

The Fermi momenta of nucleons inside a ^{4}He nucleus were simulated according to the numerical results of Variational Monte Carlo (VMC) calculations [120]. Figure 3.24 shows the momentum distribution of a proton inside a ^{4}He nucleus obtained by the VMC method, together with those for nuclear cluster states inside a nucleus. There are several efficient methods for solving the Schrödinger equations for four-nucleon bound states accurately (e.g.,the Faddeev-Yakubovsky method). The reliability of seven different many-body methods including the VMC method has been proven in a benchmark test of a four-nucleon bound state [121].

The treatment of the off-shell effects of nucleons inside a ^{4}He nucleus is essential because it could affect the shapes of MM(K^+K^-) distributions. In the analysis on the coherent $\gamma d \rightarrow \phi d$ reaction [95], two schemes for the off-shell correction were examined:

"Full off-shell correction"

In the initial state, the spectator nucleon is assumed to be on-shell, whereas the target nucleon is assumed to be off-shell to the full scale; namely, the energy of the target nucleon in the laboratory frame is given by

$$E_{\text{targ}} = M_d - \sqrt{M_N^2 + \boldsymbol{p}_{\text{spec}}^2},$$

where M_d and M_N are the masses of a deuteron and a nucleon, respectively, and $\boldsymbol{p}_{\text{spec}}$ denotes the three-momentum of the spectator nucleon. In the final state, both nucleons are assumed to be on-shell.

"Random off-shell correction"

In the initial state, both the target and spectator nucleons are assumed to be off-shell, and the degree of "off-shellness" is randomly determined event by event; namely, the energy of the target nucleon is given by

$$E_{\text{targ}} = x \left(\sqrt{M_N^2 + \boldsymbol{p}_{\text{spec}}^2} \right) + (1 - x) \left(M_d - \sqrt{M_N^2 + \boldsymbol{p}_{\text{spec}}^2} \right),$$

where x represents the degree of off-shellness, ranging between 0 and 1. In the final state, both nucleons are assumed to be on-shell.

In the present analysis, the full off-shell correction was adopted because in the random off-shell correction the energy conservation law is obviously violated. Note that the residue nucleons were assumed to form a nucleus in both the initial and final states for simplicity.
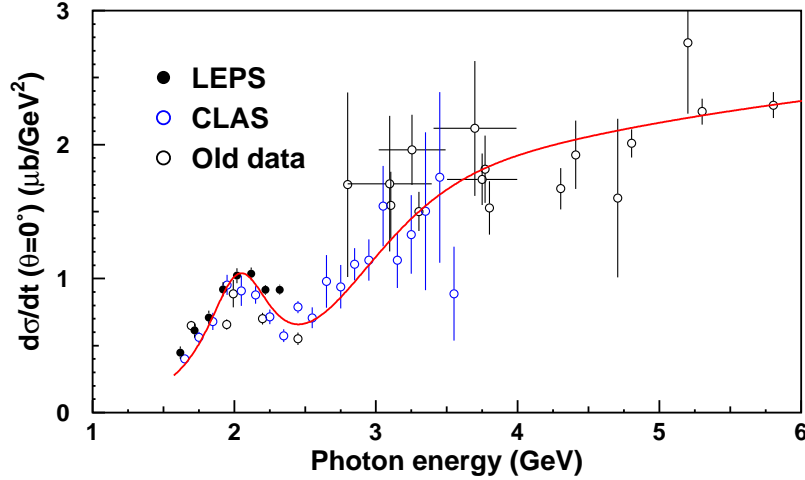
Figure 3.25:   Weight function (a red curve) as a function of the photon energy, together with experimental data on the energy dependence of the forward cross section ($\theta = 0°$) for the $\gamma p \to \phi p$ reaction. Black filled, blue open and black open circles show the LEPS data [85], the CLAS data [87] and old data [64, 81, 122–125], respectively.

Since the energy region of the present measurement is near the production threshold for the $\gamma N \to \phi N$ reaction, the cross section for ϕ-production would drastically change even at a specific photon energy, depending on the Fermi motion of the target nucleons. Here, we introduce an effective photon energy as defined by

$$E_\gamma^{\text{eff}} = \frac{s - M_N^2}{2M_N}, \tag{3.16}$$

where $\sqrt{s}$ represents the center-of-mass energy of a photon and an off-shell target nucleon. Thus, the incoherent events were weighted according to the effective photon energy E_γ^{eff}. A weight function was determined from available experimental data on the energy dependence of the forward cross section ($\theta = 0°$) for the $\gamma p \to \phi p$ reaction by assuming isospin symmetry[24] in ϕ-photoproduction from free nucleons. Figure 3.25 shows the weight function as a function of the photon energy, together with available experimental data on the forward cross section for the $\gamma p \to \phi p$ reaction. Since there exists a

---

[24]Here, isospin symmetry means that the cross sections for the $\gamma p \to \phi p$ and $\gamma n \to \phi n$ reactions are the same.

96

non-monotonic structure around $E_\gamma \sim 2$ GeV, the weight function was made so as to reproduce the non-monotonic structure, as depicted by a red curve.

3.8.2 Semi-coherent process

Since there is no available data on the slope of $d\sigma/dt$ and the decay angular distributions for the coherent $\gamma t / \gamma^3$He reaction, they were determined as follows: (i) The slope of $d\sigma/dt$ was simply determined from the charge r.m.s radii for triton and ^{3}He ($r_t = 1.86$ fm and $r_{^3\text{He}} = 1.96$ fm [126]) by assuming a Gauss-type form factor. (ii) The decay angular distributions were determined from the measured ones with the assumption of the semi-coherent process. Note that the extracted SDMEs were found to be very similar to those for the $\gamma p \to \phi p$ reaction [85].

The fermi momenta of nuclear clusters inside a helium-4 nucleus were simulated according to the numerical results of VMC calculations [120], as shown in Fig 3.24. Here, the momentum distribution for ^{3}He clusters was assumed to be the same as that for triton clusters. The off-shell effects were corrected by the full off-shell correction.

The semi-coherent events were also weighted according to the effective photon energy E_γ^{eff} [Eq. (3.16)]. Since there is no available data on the coherent $\gamma t / \gamma^3$He reaction, a weight function was made from the forward cross
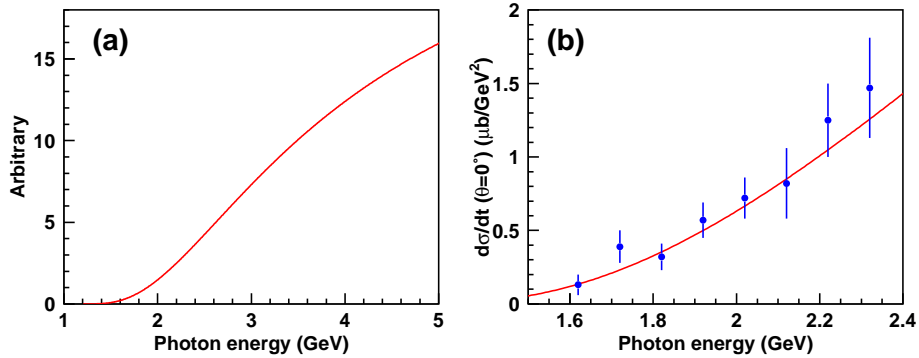
Figure 3.26:   (a) Weight function for the semi-coherent γt reaction as a function of the photon energy. (b) Energy dependence of the forward cross section ($\theta = 0°$) for the coherent γd reaction with a simple calculation in comparison with available experimental data [95]. See the text for the calculation.

section for the elementary process and the form factor, as with a deuteron target [see Eq. (1.36)]. Here, the Pomeron exchange was considered as the reaction mechanism for the elementary process, and the form factor was assumed to be a Gauss-type one. Figure 3.26(a) shows the weight function for the semi-coherent γt reaction as a function of the photon energy. To check the validity of the simple assumption, the same calculation was made for the coherent γd reaction, and was compared with available experimental data [95], as shown in Fig. 3.26(b). The experimental data are well reproduced by the simple calculation.

3.9 Acceptance evaluation

The acceptance was evaluated by MC simulation. Here, the acceptance includes the geometrical acceptance of the LEPS spectrometer, the detector efficiencies, the tracking efficiency and the efficiencies for all the selection cuts described in Sect. 3.6. Since there is a difference in the geometrical acceptance of the LEPS spectrometer between horizontal and vertical polarization data, MC data for each polarization were separately generated, and were mixed according to the ratio determined from the number of photons for each polarization (see Sect. 2.7). The same analysis criteria and selection cuts as those for the data analysis were applied to MC data. The acceptance is given by the number of accepted events divided by the number of generated events in MC simulation.

In the event generator, coherent ϕ-photoproduction off ^{4}He was simulated as follows. First, a ϕ-meson was generated according to the following phenomenological function:

$$\frac{d\sigma}{d\tilde{t}} = \sigma_0(E_\gamma)\exp(-b\tilde{t}), \tag{3.17}$$

where $\sigma_0(E_\gamma)$ is the differential cross section $d\sigma/d\tilde{t}$ at $\tilde{t} = 0$ ($t = -|t|_{\min}$), which is a function of the photon energy E_γ, and b is a slope of $d\sigma/d\tilde{t}$. Next, the ϕ-meson decayed into a K^+ and a K^- according to the three-dimensional decay angular distribution $W(\cos\Theta, \Phi, \Psi)$ [Eq. (1.19)] in the GJ frame.

Since all the input parameters for the event generator [i.e. $\sigma_0(E_\gamma)$, b and the SDMEs] are unknown and to be measured, they must be determined iteratively by changing their values so that MC data reproduces both the measured t-distribution and decay angular distributions.

For $\sigma_0(E_\gamma)$, it was simply assumed, as a starting point, that $\sigma_0(E_\gamma)$ follows the energy dependence determined from that for the elementary process and the form factor (see Sect. 4.2.6), as with a deuteron target [see Eq. (1.36)]. Here, the form factor was assumed to be a Gauss-type one with a r.m.s. radius of 1.68 fm, i.e. the charge r.m.s. radius of ^{4}He nuclei [127]. We found that such a simple assumption can explain the measured $\sigma_0(E_\gamma)$ (see Sect. 4.2.6).

The slope b was initially set to 26 GeV^{-2}, which was estimated from the charge r.m.s radius of ^{4}He nuclei. After three iterations, the slope parameter obtained from acceptance-corrected t-distributions became stable, which means that no further iteration was needed.

The SDMEs were initially set by assuming helicity-conserving and pure natural-parity exchange processes; namely

$$\rho_{00}^0 = \text{Re}\rho_{10}^0 = \text{Re}\rho_{1-1}^0 = \rho_{11}^1 = \rho_{00}^1 = \text{Re}\rho_{10}^1 = \text{Im}\rho_{10}^2 = 0,$$
$$\rho_{1-1}^1 = -\text{Im}\rho_{1-1}^2 = 0.5.$$

After one iteration, the extracted SDMEs became stable, and no further iteration was needed. Note that the effect of the slope b on the SDMEs was found to be negligibly small [i.e., a variation of the slope b just affects the overall normalizations of the decay angular distributions of Eqs. (1.27)–(1.31).].

To check the validity of evaluating the geometrical acceptance of the spectrometer including the detector efficiencies, as well as that of the normalization of the photon flux for the cross section measurement (Sect. 4.2), we compared the differential cross sections for the $\gamma p \to K^+\Lambda(1116)$, $\gamma p \to K^+\Sigma(1192)$, $\gamma p \to \pi^0 p$ and $\gamma p \to \phi p$ reactions obtained with the LH$_2$ data with the previous LEPS measurements [85, 128, 129]. These results are presented in Appendix I.

4 Results and Discussion

4.1 $\phi \to K^+K^-$ decay angular distribution for $\gamma^4\text{He} \to \phi^4\text{He}$ reaction

First, we verify the absence of unnatural-parity exchange processes in the $\gamma^4\text{He} \to \phi^4\text{He}$ reaction by looking at the $\phi \to K^+K^-$ decay angular distributions. The decay angular distributions measured here are given by

$$W(\cos\Theta) = \frac{3}{2}\left[\frac{1}{2}(1 - \rho_{00}^0)\sin^2\Theta + \rho_{00}^0\cos^2\Theta\right], \tag{4.1}$$

$$W(\Phi) = \frac{1}{2\pi}(1 - 2\text{Re}\rho_{1-1}^0\cos 2\Phi), \tag{4.2}$$

$$W(\Phi - \Psi) = \frac{1}{2\pi}\left[1 + 2P_\gamma\bar{\rho}_{1-1}^1\cos 2(\Phi - \Psi)\right], \tag{4.3}$$

$$W(\Phi + \Psi) = \frac{1}{2\pi}\left[1 + 2P_\gamma\Delta_{1-1}\cos 2(\Phi + \Psi)\right], \tag{4.4}$$

$$W(\Psi) = 1 - P_\gamma(2\rho_{11}^1 + \rho_{00}^1)\cos 2\Psi, \tag{4.5}$$

where Θ and Φ denote the polar and azimuthal angles, respectively, of a K^+ in the GJ frame, and Ψ denotes the azimuthal angle of the photon polarization vector with respect to the production plane. ρ_{00}^0, $\text{Re}\rho_{1-1}^0$, $\bar{\rho}_{1-1}^1$, Δ_{1-1} and $2\rho_{11}^1 + \rho_{00}^1$ are the SDMEs to be extracted. These distributions were measured at forward angles, i.e., $0 < |t| - |t|_{\min} < 0.2$ GeV^2. The incident photon energy was divided into two regions (E$_l$: $1.985 < E_\gamma < 2.185$ GeV, E$_h$: $2.185 < E_\gamma < 2.385$ GeV), where sufficient statistics were obtained. Each angle [$\cos\Theta \in [0, 1]$, $\Phi, \Phi - \Psi, \Phi + \Psi, \Psi \in [0, 2\pi]$] was divided into 10 bins with an equal width (a-1, a-2, $\cdots$, a-10). In order to get better statistics and to identify the coherent production events more clearly, the horizontal and vertical polarization data were merged.

4.1.1 Number of coherent-ϕ-production events as a function of $\cos\Theta$, Φ, $\Phi - \Psi$, $\Phi + \Psi$ and Ψ

The number of the coherent-ϕ-production events for each angular and energy bin was evaluated in the same method as described in Sect. 3.7. For the disentanglement of the coherent production events, the property of symmetries in each distribution was taken into account; namely, the events in the i-th and j-th ($j = 11 - i$) angular bins were merged for $W(\cos\Theta)$, whereas

the events in the i-th and j-th $(j = i + 5)$ angular bins were merged for other distributions.

The total ϕ-meson yields were obtained by fitting the $\mathrm{M}(K^+K^-)$ spectra with the MC templates for the $\phi \to K^+K^-$ and background events, as shown in Fig. 4.1. Figure 4.2 shows the total ϕ-meson yields as a function of the angles $\cos\Theta$, Φ, $\Phi - \Psi$, $\Phi + \Psi$ and Ψ for each energy region.

The ratios of the coherent production events (R_{coh}) were evaluated by fitting the $\mathrm{MM}(K^+K^-)$ spectra with the MC templates for the coherent and incoherent events, as shown in Fig. 4.3. Figure 4.4 shows the ratios R_{coh} as a function of the angles $\cos\Theta$, Φ, $\Phi - \Psi$, $\Phi + \Psi$ and Ψ for each energy region.

The yields for the coherent ϕ production events were calculated using Eq. (3.11). Figure 4.5 shows the yields for the coherent ϕ production events as a function of the angles $\cos\Theta$, Φ, $\Phi - \Psi$, $\Phi + \Psi$ and Ψ for each energy region. The estimation of the systematic errors due to the contamination of the events other than the coherent ones is described in Appendix K.

4.1.2 Acceptance as a function of $\cos\Theta$, Φ, $\Phi - \Psi$, $\Phi + \Psi$ and Ψ

The acceptance was evaluated by MC simulation, as described in Sect. 3.9. Figure 4.6 shows the acceptance as a function of the angles $\cos\Theta$, Φ, $\Phi - \Psi$, $\Phi + \Psi$ and Ψ for each energy region.
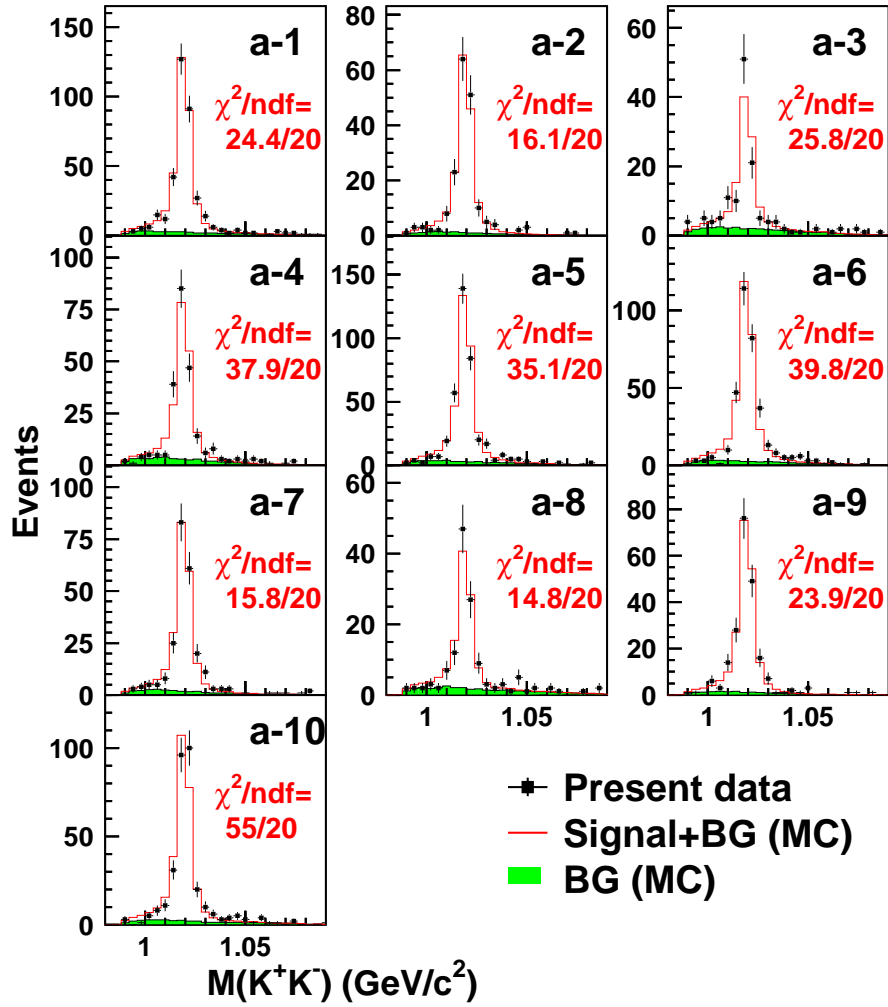
Figure 4.1: M(K^+K^-) spectra for the angle $\Phi - \Psi$ in the E_h region. Red histograms show the results for the template fits. Green filled areas show the MC-simulated distributions for the background events.
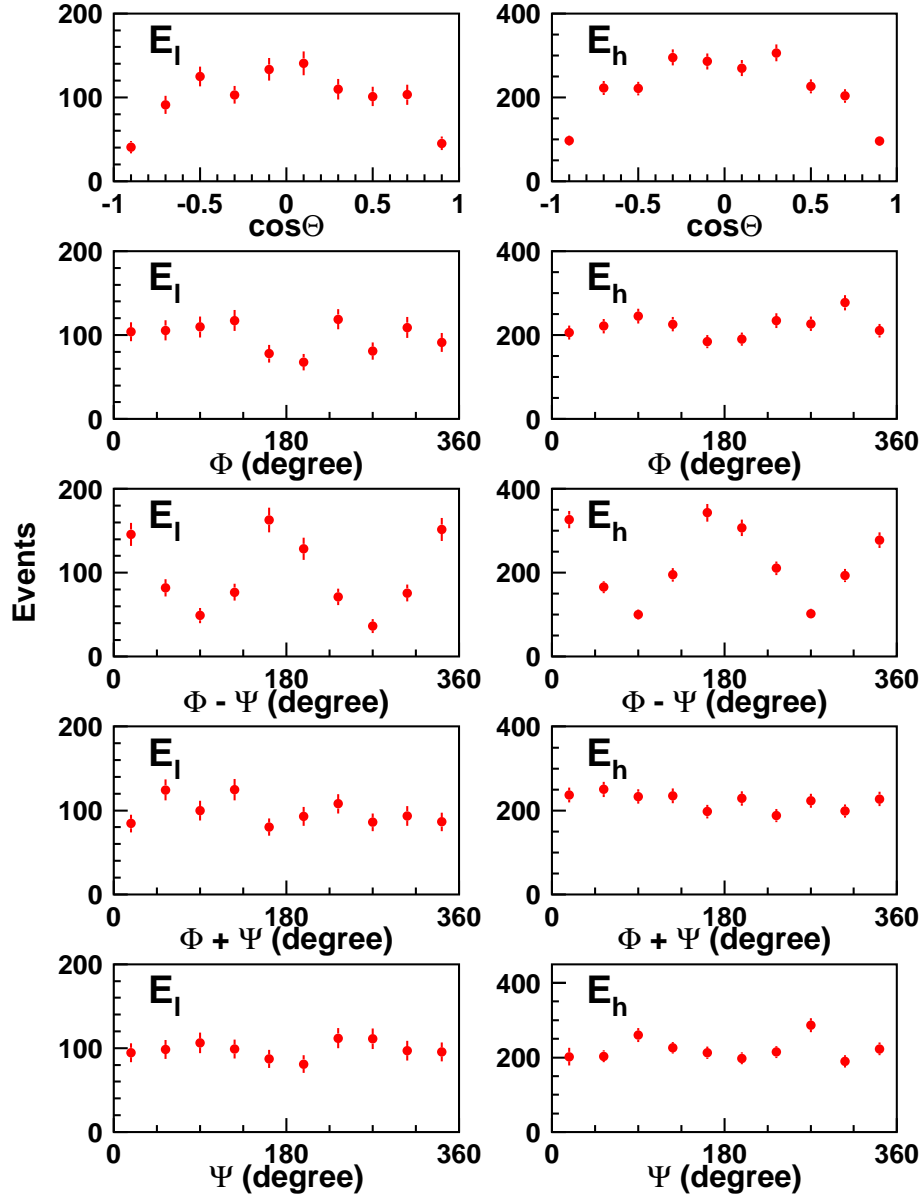
Figure 4.2: Total ϕ-meson yields as a function of the angles; $\cos\Theta$, Φ, $\Phi - \Psi$, $\Phi + \Psi$ and Ψ for the E_l (left figures) and E_h (right figures) regions.
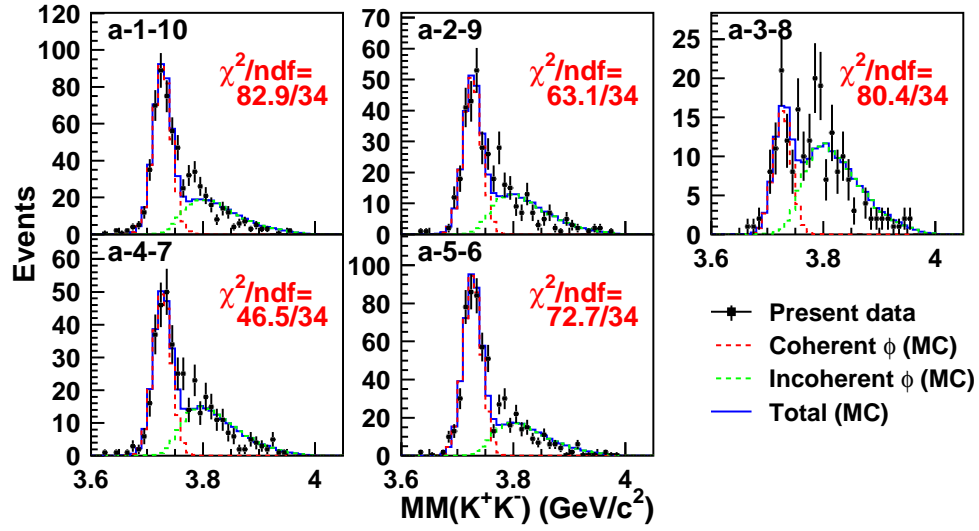
Figure 4.3: MM(K^+K^-) spectra for the angle $\Phi - \Psi$ in the E_h region. Blue histograms show the results for the template fits. Red and green dashed histograms show the MC templates for the coherent and incoherent production events, respectively.
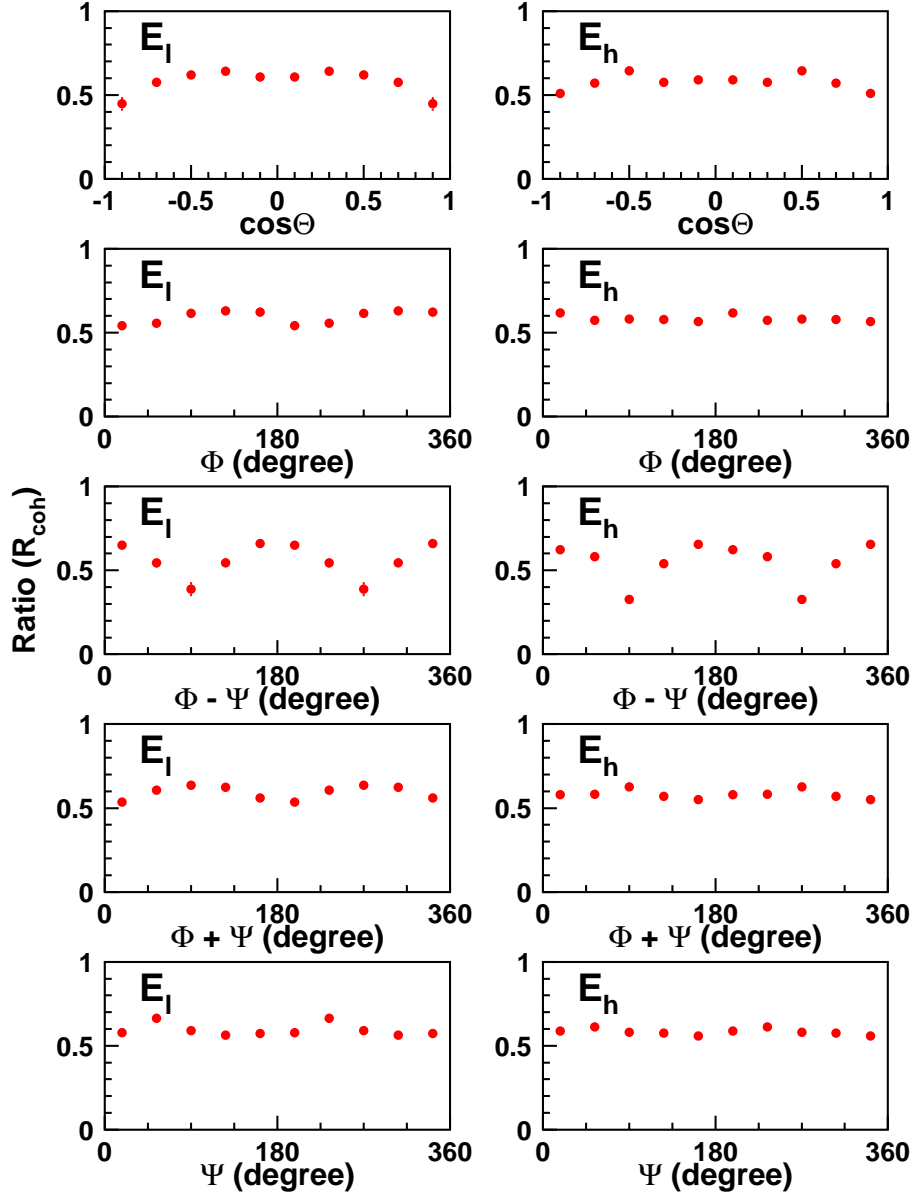
Figure 4.4:   Ratios of the coherent events (R_{coh}) as a function of the angles; $\cos\Theta$, Φ, $\Phi - \Psi$, $\Phi + \Psi$ and Ψ for the E_l (left figures) and E_h (right figures) regions.
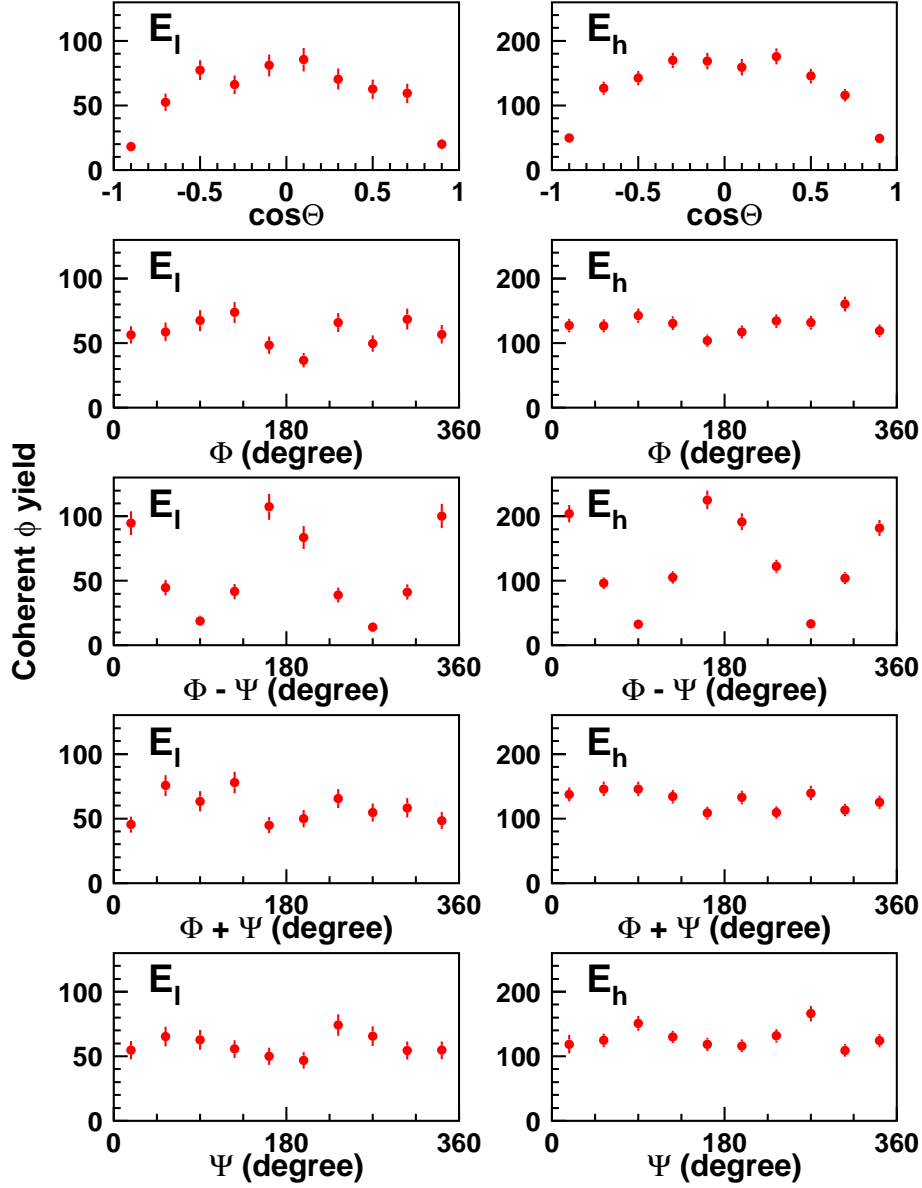
Figure 4.5:   Yields for the coherent ϕ production events as a function of the angles; $\cos\Theta$, Φ, $\Phi - \Psi$, $\Phi + \Psi$ and Ψ for the E_l (left figures) and E_h (right figures) regions.
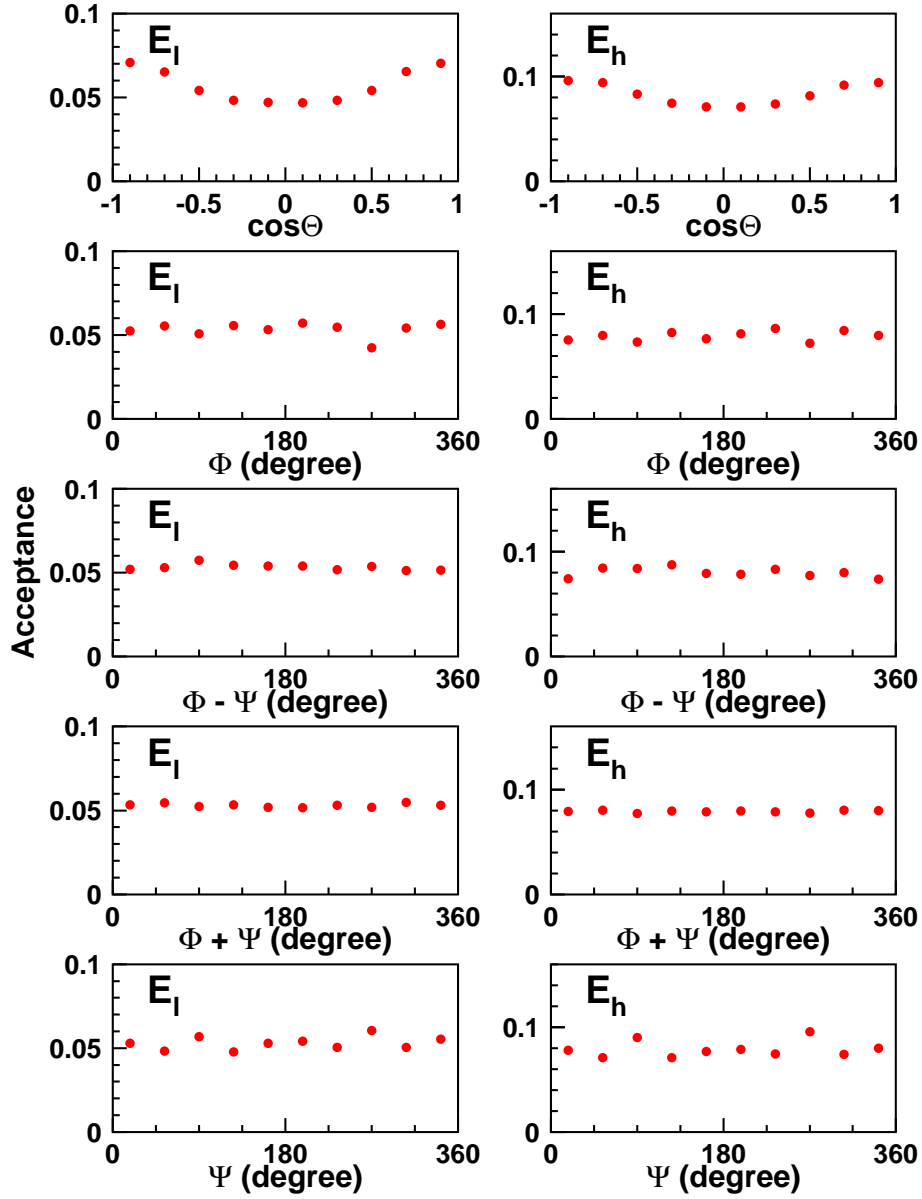
Figure 4.6: Acceptance as a function of the angles; $\cos\Theta$, Φ, $\Phi - \Psi$, $\Phi + \Psi$ and Ψ for the E_l (left figures) and E_h (right figures) regions.

4.1.3 Spin density matrix elements (SDMEs)

To extract the SDMEs (ρ_{00}^0, $\mathrm{Re}\rho_{1-1}^0$, $\bar{\rho}_{1-1}^1$, Δ_{1-1} and $2\rho_{11}^1 + \rho_{00}^1$), the acceptance-corrected distributions were fitted by Eqs. (4.1)–(4.5). Here, in the fitting procedure, the SDMEs and the overall normalizations of Eqs. (4.1)–(4.5) were treated as free parameters. Since the degree of BCS photon polarization P_γ is a function of the photon energy, i.e., not a constant value (see Fig. 2.5), it was evaluated for each energy region: $P_\gamma = 0.8847$ and 0.9158 for the E_l and E_h regions, respectively[25]. The details are described in Appendix J.

Figure 4.7 shows the acceptance-corrected distributions $W(\cos \Theta)$, $W(\Phi)$, $W(\Phi - \Psi)$, $W(\Phi + \Psi)$ and $W(\Psi)$ for each photon energy region. Here, the data are normalized so that

$$
\int_{-1}^{1} W(\cos \Theta) d(\cos \Theta) = 1,
$$
$$
\int_{0}^{2\pi} W(x) dx = 1 \ (x = \Phi, \Phi - \Psi, \Phi + \Psi, \Psi). \tag{4.6}
$$

As shown in Fig. 4.7, a quite large oscillation is seen in $W(\Phi - \Psi)$, and therefore a finite bin size could affect the extracted values of the SDMEs. To avoid such a finite-bin-size effect, a fit chi-square, χ^2, was newly defined as

$$
\chi^2(\tilde{\rho}, \alpha) = \sum_{i=1}^{N} \frac{\left(\hat{O}_i - \alpha \hat{E}_i\right)^2}{\sigma_i^2},
$$
$$
\hat{E}_i = \frac{1}{\Delta x} \int_{\bar{x}_i - \frac{1}{2}\Delta x}^{\bar{x}_i + \frac{1}{2}\Delta x} W(x) dx \ (x = \cos \Theta, \Phi, \Phi - \Psi, \Phi + \Psi, \Psi), \tag{4.7}
$$

where $\tilde{\rho}$ is a SDME to be determined, N is the number of data points (bins), $\hat{O}_i$ is the number of counts in the i-th bin, α denotes an overall normalization factor being a free parameter, σ_i is the statistical error in the i-th bin, Δx is the bin size, and $\bar{x}_i$ is the mean value of the i-th bin.

The fit results are depicted as blue curves in Fig. 4.7. The numerical results are summarized in Tables 4.1 and 4.2 for the E_l and E_h regions, respectively. On the basis of the reduced chi-squares χ^2/ndf, the quality of the fits is reasonably good for all the distributions.

---

[25]Errors in the laser polarization measurement are taken into account as a systematic error (see Sect. 4.1.4).

The SDMEs obtained in this measurement are summarized in Table 4.3. Systematic errors on the extracted SDMEs are discussed in the next section.

Table 4.1: Summary of the fit results and the extracted SDMEs for the E_l region.

Angle	SDME	χ^2	ndf	χ^2/ndf
$\cos\Theta$	-0.015 ± 0.016	4.68	8	0.59
Φ	0.116 ± 0.030	11.36	8	1.42
$\Phi - \Psi$	0.454 ± 0.024	5.78	8	0.72
$\Phi + \Psi$	-0.111 ± 0.033	11.69	8	1.46
Ψ	0.132 ± 0.066	9.52	8	1.19

Table 4.2: Summary of the fit results and the extracted SDMEs for the E_h region.

Angle	SDME	χ^2	ndf	χ^2/ndf
$\cos\Theta$	0.016 ± 0.012	3.54	8	0.44
Φ	0.054 ± 0.020	11.38	8	1.42
$\Phi - \Psi$	0.436 ± 0.014	8.90	8	1.11
$\Phi + \Psi$	-0.034 ± 0.017	17.86	8	2.23
Ψ	0.074 ± 0.041	4.91	8	0.61

Table 4.3: Summary of the extracted SDMEs for the E_l and E_h regions. The first and second uncertainties represent the statistical and systematic ones, respectively.

SDME	E_l	E_h
ρ^0_{00}	$-0.015 \pm 0.016^{+0.000}_{-0.002}$	$0.015 \pm 0.012^{+0.002}_{-0.000}$
$\mathrm{Re}\rho^0_{1-1}$	$0.116 \pm 0.030^{+0.000}_{-0.006}$	$0.054 \pm 0.020^{+0.000}_{-0.004}$
$\bar{\rho}^1_{1-1}$	$0.454 \pm 0.024^{+0.014}_{-0.000}$	$0.436 \pm 0.014^{+0.004}_{-0.000}$
Δ_{1-1}	$-0.111 \pm 0.033^{+0.006}_{-0.000}$	$-0.034 \pm 0.017^{+0.009}_{-0.000}$
$2\rho^1_{11} + \rho^1_{00}$	$0.132 \pm 0.066^{+0.000}_{-0.033}$	$0.074 \pm 0.041^{+0.011}_{-0.000}$

Figure 4.7: Decay angular distributions $W(\cos\Theta)$, $W(\Phi)$, $W(\Phi-\Psi)$, $W(\Phi+\Psi)$ and $W(\Psi)$ for the E_l (left figures) and E_h (right figures) regions. Blue curves are the fits to the data points with Eqs. (4.1)–(4.5).

4.1.4 Systematic errors on SDMEs

Systematic errors on the SDMEs are as follows:

- The systematic errors due to the event contamination other than the coherent ones were estimated by considering the semi-coherent process in the template fits on the MM(K^+K^-) spectra. These results are presented in Appendix K.

- The systematic error in the degree of BCS photon polarization. This is caused by systematic errors in the laser polarization measurements. It was estimated to be 0.1% and 0.08% for the horizontal and vertical polarizations, respectively (see Appendix J for details).

The systematic errors due to the event contamination other than the coherent ones were found to be smaller than the statistical errors (see Table 4.3). The systematic error caused by the laser polarization measurements was found to be negligibly small.

4.1.5 Discussion on the extracted SDMEs

The matrix elements ρ^0_{00}, which reflect the probability of single helicity-flip transitions ($\lambda_\gamma = \pm 1 \to \lambda_\phi = 0$), were found to be consistent with zero and to exhibit no energy dependence. This indicates the dominance of helicity-conserving processes in t-channel. The obtained matrix elements ρ^0_{00} were compared with those obtained in the $\gamma p \to \phi p$ and $\gamma d \to \phi d$ reactions, as shown in Fig. 4.8. The matrix elements ρ^0_{00} obtained here are in good agreement with those for the γp and γd reactions. The smallness of ρ^0_{00} at small $|t|$ is compatible with a conventional Pomeron exchange model [47]. In contrast to the LEPS measurements at small $|t|$, a non-zero value of ρ^0_{00} was observed in the $\gamma p \to \phi p$ reaction at large momentum transfers ($-t > 2.5$ GeV^2) by CLAS [130]. This suggests that the u-channel contribution to ϕ-photoproduction would begin to dominate at large $|t|$ [131].

The decay asymmetry $\overline{\rho}^1_{1-1}$ determines the relative contribution of natural and unnatural-parity exchange processes in t-channel, and gives $+0.5$ (-0.5) for pure natural-parity (unnatural-parity) exchange processes when helicity-conservation holds. $\overline{\rho}^1_{1-1}$ was found to be very close to $+0.5$ for both the E$_l$ and E$_h$ regions. This indicates the strong dominance ($> 94\%$) of natural-parity exchange processes. Figure 4.9 shows the comparison of $\overline{\rho}^1_{1-1}$ between those obtained in the $\gamma p \to \phi p$, $\gamma d \to \phi d$ and γ^4He $\to \phi^4$He reactions. For
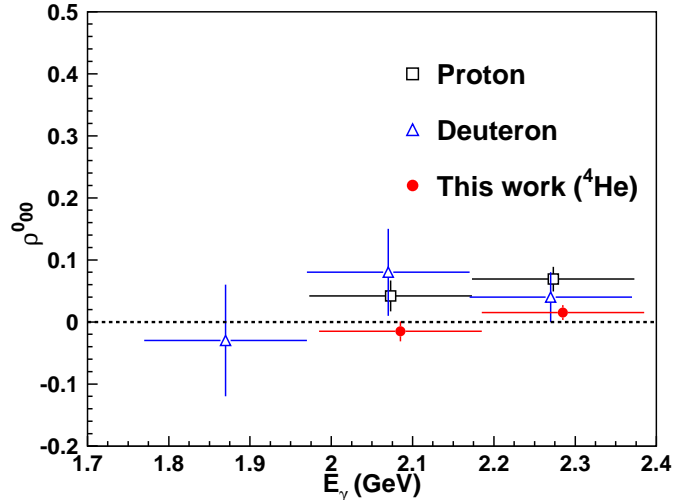
Figure 4.8: Comparison of ρ_{00}^0 between the γp (black open squares) [85], γd (blue open triangles) [89] and $\gamma^4\mathrm{He}$ data (red filled circles). Here, the momentum transfer t is selected as $|t| - |t|_{\min} < 0.2$ GeV^2 for the γp and $\gamma^4\mathrm{He}$ data, and $|t| - |t|_{\min} < 0.05$ GeV^2 for the γd data. The error bars represent the sum of the statistical and systematic errors in quadrature.
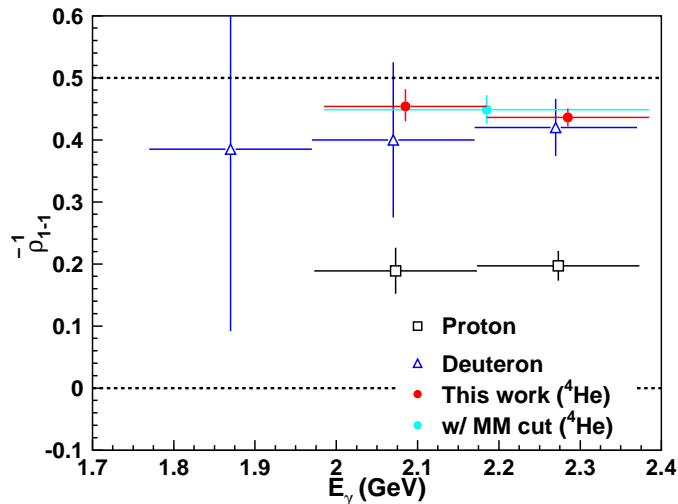
Figure 4.9: Same as Fig. 4.8, but for $\bar{\rho}_{1-1}^1$. A cyan filled circle shows the result with a tight missing mass cut (see the text for details).

the γd and $\gamma^4\text{He}$ reactions, $\overline{\rho}^1_{1-1}$ is very close to $+0.5$, whereas, for the γp reaction, it is positive but largely deviates from $+0.5$. This can be understood by the unnatural-parity π exchange. In the former cases, the isovector π exchange is forbidden, whereas it is allowed in the latter case. Further, for the $\gamma^4\text{He}$ reaction, $\overline{\rho}^1_{1-1}$ sizably deviates from $+0.5$ (, corresponding to a 4.6σ deviation for the E_h region). In this case, unnatural-parity exchange processes are forbidden.

As pointed out by Titov *et al.*, the existence of helicity-flip processes modifies Eq. (1.32) into [47]:

$$\overline{\rho}^1_{1-1} = \frac{1}{2} \frac{\sigma^N - \sigma^U + |T_1^{1-1}|^2}{\sigma^N + \sigma^U + |T^{10}|^2 + |T_2^{1-1}|^2}, \tag{4.8}$$

where $|T^{10}|^2 = \text{Tr}[T_{\alpha;10}T^\dagger_{\alpha;10}]$ represents the contribution from single helicity-flip transitions ($\lambda_\gamma = \pm 1 \to \lambda_\phi = 0$), whereas $|T_1^{1-1}|^2 = \text{Tr}[T_{\alpha;1-1}T^\dagger_{\alpha;-11}]$ and $|T_2^{1-1}|^2 = \text{Tr}[T_{\alpha;1-1}T^\dagger_{\alpha;1-1}]$ represent the contribution from double helicity-flip transitions ($\lambda_\gamma = \pm 1 \to \lambda_\phi = -\lambda_\gamma$). Therefore, the observed deviation of $\overline{\rho}^1_{1-1}$ from $+0.5$, along with the smallness of ρ^0_{00}, strongly indicates the existence of double helicity-flip transitions. In fact, a rather large oscillation was observed in $W(\Phi)$ for the E_l region (see Fig. 4.7), giving $\text{Re}\rho^0_{1-1}$ of ~ 0.11. This means that the interference between helicity-nonflip and double helicity-flip amplitudes has a non-zero value. A non-zero value of $\text{Re}\rho^0_{1-1}$ was also observed in the γp [85, 88] and γd reactions [89]. In order to make sure that the observed deviation of $\overline{\rho}^1_{1-1}$ is not due to the contamination from the incoherent events with $\overline{\rho}^1_{1-1} \approx 0.25$ [132], the decay asymmetry with a tight mass cut, $\text{MM}(K^+K^-) < 3.72 \text{ GeV}/c^2$, was examined. In this case, the event contamination other than the coherent ones was evaluated to be 0.6%. The result is indicated by a cyan filled circle in Fig. 4.9. $\overline{\rho}^1_{1-1}$ was found to be 0.44 ± 0.02, and still deviates from $+0.5$. Therefore, the observed deviation is not due to the contamination from the incoherent events.

The presence of double-helicity flip transitions indicates that the helicity of the particle exchanged in t-channel is ± 2 [see Eq. (1.35)]. A model that treats the Pomeron exchange as an effective tensor exchange [133, 134] successfully describes the experimental data on the helicity structure of elastic pp scattering at $\sqrt{s} = 200$ GeV and small $|t|$ from the STAR experiment [135] as well.

In the modified DL Pomeron model [47], motivated by the analogy between the Pomeron and two-gluon exchanges, the term responsible for dou-
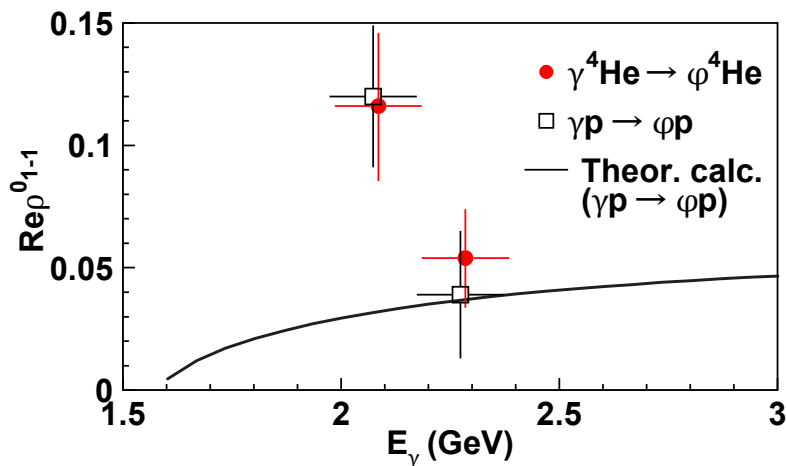
Figure 4.10:   Comparison of $\mathrm{Re}\rho^0_{1-1}$ between the γp (black open squares) [85] and γ^4He data (red filled circles). The both data are for a t-range of $0 < |t| - |t|_{\min} < 0.2$ GeV^2, where $|t|_{\min}$ represents the minimum $|t|$ for each reaction. The error bars represent the sum of the statistical and systematic errors in quadrature. A solid curve represents a theoretical calculation for the Pomeron, π and η exchanges in the $\gamma p \rightarrow \phi p$ reaction [47, 94]. Here, the calculation is averaged over the t region ($0 < |t| - |t|_{\min} < 0.2$ GeV^2) for comparison.

ble helicity-flip transitions [last term in Eq. (1.16)] naturally arises to restore the guage invariance. In the original DL Pomeron model, on the other hand, the Pomeron exchange does not contribute to helicity-flip amplitudes [see Eq. (3.1) of Ref [45] for an explicit form of the Pomeron amplitude]. Therefore, the non-zero value of $\mathrm{Re}\rho^0_{1-1}$ obtained here supports the modified DL model, i.e., the Pomeron-two-gluon analogy. However, there is one problem: Figure 4.10 shows the energy dependence of $\mathrm{Re}\rho^0_{1-1}$ for the γp and γ^4He reactions, in comparison with a theoretical calculation for the Pomeron, π and η exchanges in the γp reaction [47, 94]. The experimental data for both reactions are in good agreement, whereas they are in contradiction with the model calculation. As pointed out by Titov *et al.* [94], a double helicity-flip transition comes from the spin-orbital interaction generated by the two-gluon exchange [see Eq. (1.17)], and its contribution should monotonically increase with energy. This contradiction may be accounted for by the appearance of additional natural-parity exchange processes beyond the Pomeron exchange

such as the tensor $f_2'(1525)$ exchange[26].

---

[26]It is followed from Eq. (1.35) that besides the Pomeron exchange, the tensor f_2' exchange can also contribute to double helicity-flip transitions.

4.2   Differential cross section for γ^4He $\to \phi^4$He reaction

In the previous sections, we have demonstrated the strong dominance ($>$ 94%) of natural-parity exchange processes in the γ^4He $\to \phi^4$He reaction. In this section, the differential cross sections for the γ^4He $\to \phi^4$He reaction are presented as a function of the momentum transfer $\tilde{t}$ ($= |t| - |t|_{\min}$) for various photon energy bins. The momentum transfer $\tilde{t}$ from 0 to 0.16 GeV^2 was binned with an equal width of 0.02 GeV^2 (t-1, t-2, ..., etc.). The photon energy was divided into six bins as defined in Table 4.4.

Table 4.4: Definition of the photon energy bins.

Photon energy bin	E_γ range (GeV)
e-1	1.685–1.885
e-2	1.885–1.985
e-3	1.985–2.085
e-4	2.085–2.185
e-5	2.185–2.285
e-6	2.285–2.385

The differential cross section as a function of the momentum transfer $\tilde{t}$ is given by

$$\frac{d\sigma}{d\tilde{t}} = \frac{Y_{\mathrm{coh}\,\phi}}{N_\gamma \cdot N_{\mathrm{targ}} \cdot \varepsilon_{\mathrm{acc}} \cdot B_{\phi \to K^+ K^-} \cdot \Delta t}, \tag{4.9}$$

where $Y_{\mathrm{coh}\,\phi}$ is the number of the coherent ϕ production events in each $\tilde{t}$ and E_γ bin, N_γ is the number of photons in each E_γ bin, N_{targ} is the number of target nuclei (^{4}He), $\varepsilon_{\mathrm{acc}}$ is the acceptance for each $\tilde{t}$ and E_γ bin, $B_{\phi \to K^+ K^-}$ is the branching ratio of the $\phi \to K^+ K^-$ decay ($= 0.489$), and Δt is the width of t bins ($= 0.02$ GeV^2).

The number of target nuclei N_{targ} was calculated as follows:

$$N_{\mathrm{targ}} = \rho \cdot \frac{N_A}{A_r} \cdot L_{\mathrm{eff}}, \tag{4.10}$$

where ρ is the density of liquid ^{4}He ($= 0.1249$ g/cm^3), N_A is the Avogadro constant ($= 6.0221 \times 10^{23}$ mole^{-1}), A_r is the standard atomic weight for ^{4}He atoms ($= 4.0026$ g/mole), and L_{eff} is an effective target length, which is given as

$$L_{\mathrm{eff}} = 15 \text{ cm} \times (1 - R_{\mathrm{CFRP}}). \tag{4.11}$$

116

Here, $R_{\mathrm{CFRP}} = 0.023$ represents the contamination of the K^+K^- events from the CFRP cap of the target chamber (see Sect. 3.6).

The number of photons N_γ in each E_γ bin was calculated in an ordinary way. The details are described in Appendix L.

4.2.1 Number of coherent ϕ production events as a function of $\tilde{t}$ and E_γ

The number of the coherent-ϕ-production events for each t and E_γ bin was evaluated as described in Sect. 3.7. The total ϕ-meson yields were obtained by fitting the $\mathrm{M}(K^+K^-)$ spectra with the MC templates for the $\phi \to K^+K^-$ and background events. Figure 4.11 shows the $\mathrm{M}(K^+K^-)$ spectra for various $\tilde{t}$ bins in the e-6 bin, together with the fit results. The contribution from non-resonant K^+K^- production becomes larger as $\tilde{t}$ increases. This is because the production of K^+K^- pairs with large $\mathrm{M}(K^+K^-)$, which come from non-resonant K^+K^- production, involves a large momentum transfer. Figure 4.12 shows the total ϕ-meson yields as a function of $\tilde{t}$ for various E_γ bins.

The ratios of the coherent production events R_{coh} were obtained by fitting the $\mathrm{MM}(K^+K^-)$ spectra with the MC templates for the coherent and incoherent events. Figure 4.13 shows the $\mathrm{MM}(K^+K^-)$ spectra for various $\tilde{t}$ bins in the e-6 bin, together with the fit results. While the events in large-$\tilde{t}$ bins are spread over a wide mass region, those in small-$\tilde{t}$ bins are concentrated in a low-mass region. This means that the coherent production events are concentrated in a small $\tilde{t}$ region, whereas the incoherent ones are distributed in a large $\tilde{t}$ region (see Fig. 3.22). Figure 4.14 shows the ratios R_{coh} as a function of $\tilde{t}$ for various E_γ bins.

The yields for the coherent ϕ production events were calculated by Eq. (3.11). Figure 4.5 shows the yields for the coherent ϕ production events as a function of $\tilde{t}$ for various E_γ bins. The estimation of the systematic errors due to the contamination of the events other than the coherent ones is described in Appendix M.
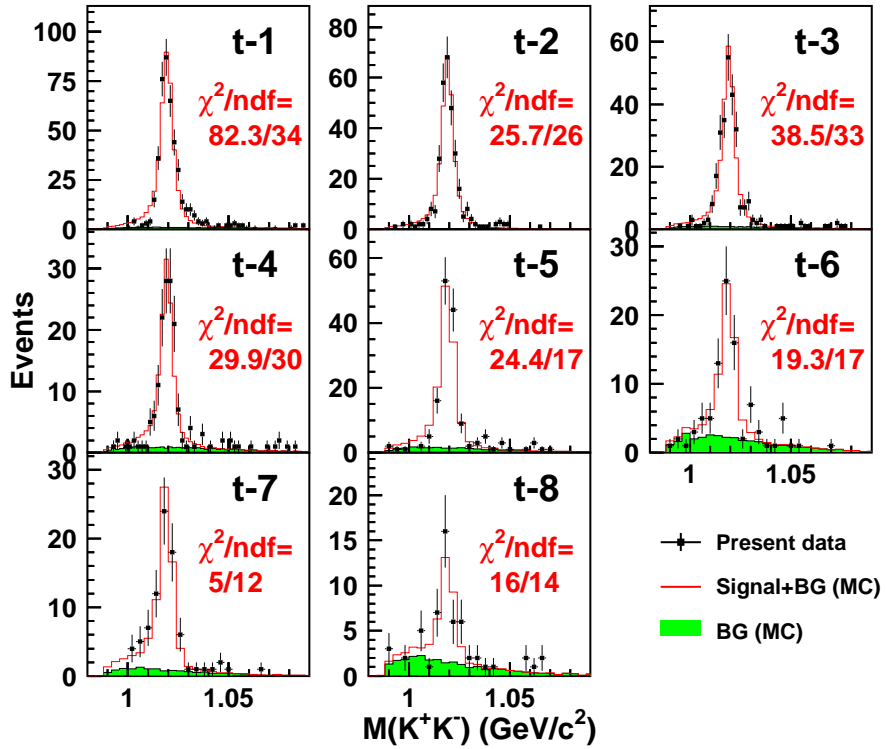
Figure 4.11:   M(K^+K^-) spectra for various $\tilde{t}$ bins in the e-6 bin. Red histograms show the results for the template fits. Green filled areas show the MC-simulated distributions for the background events.
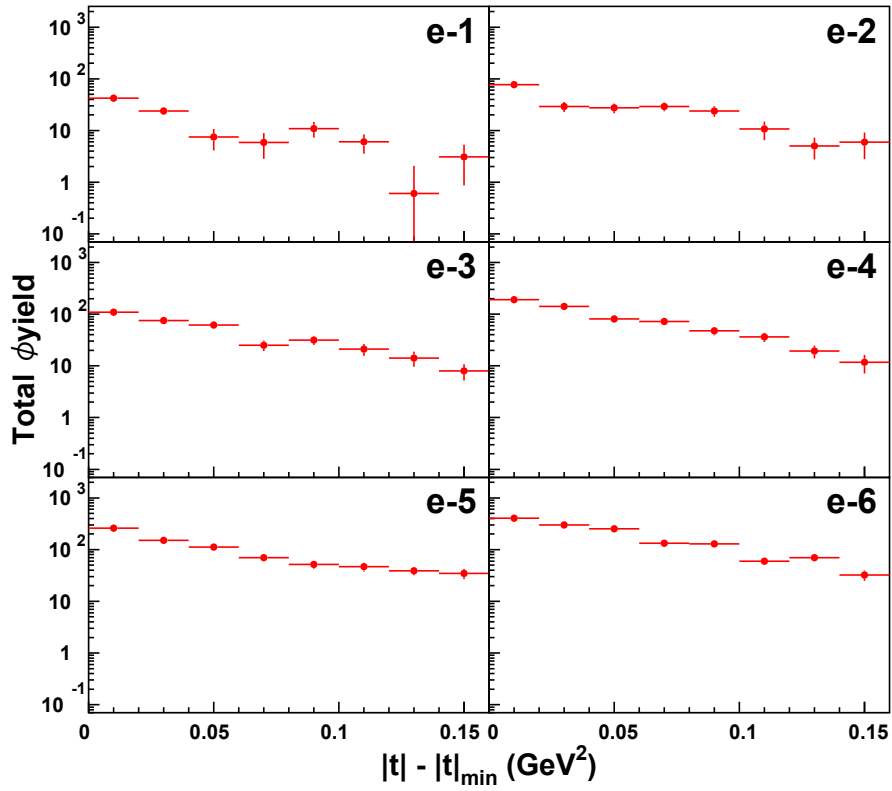
Figure 4.12:   Total ϕ-meson yields as a function of $\tilde{t}$ for various E_γ bins.
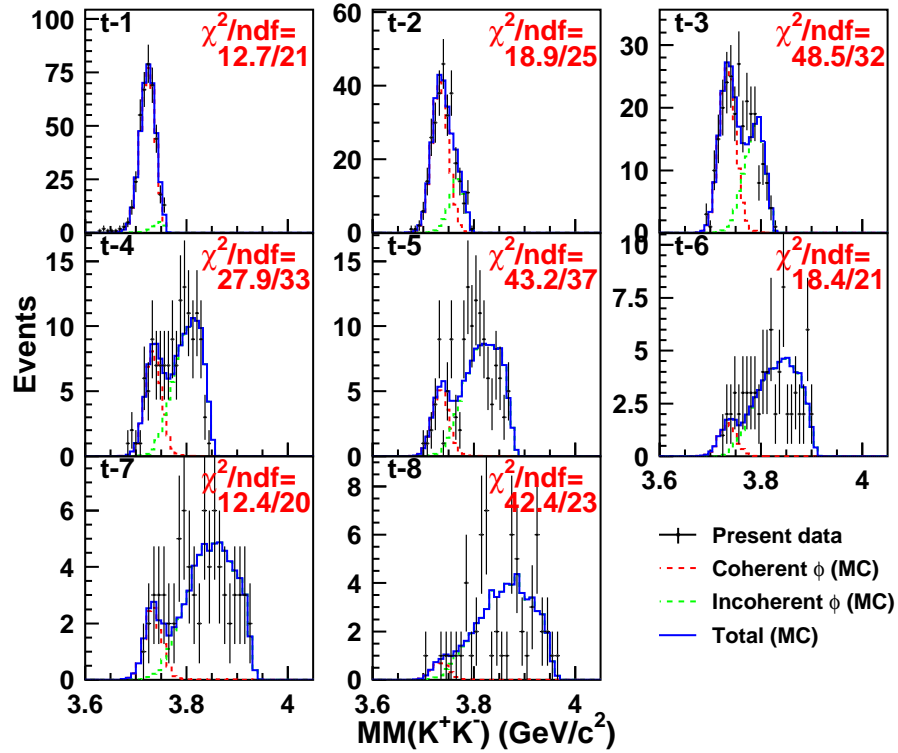
Figure 4.13: MM(K^+K^-) spectra for various $\tilde{t}$ bins in the e-6 bin. Blue histograms show the results for the template fits. Red and green dashed histograms show the MC templates for the coherent and incoherent production events, respectively.
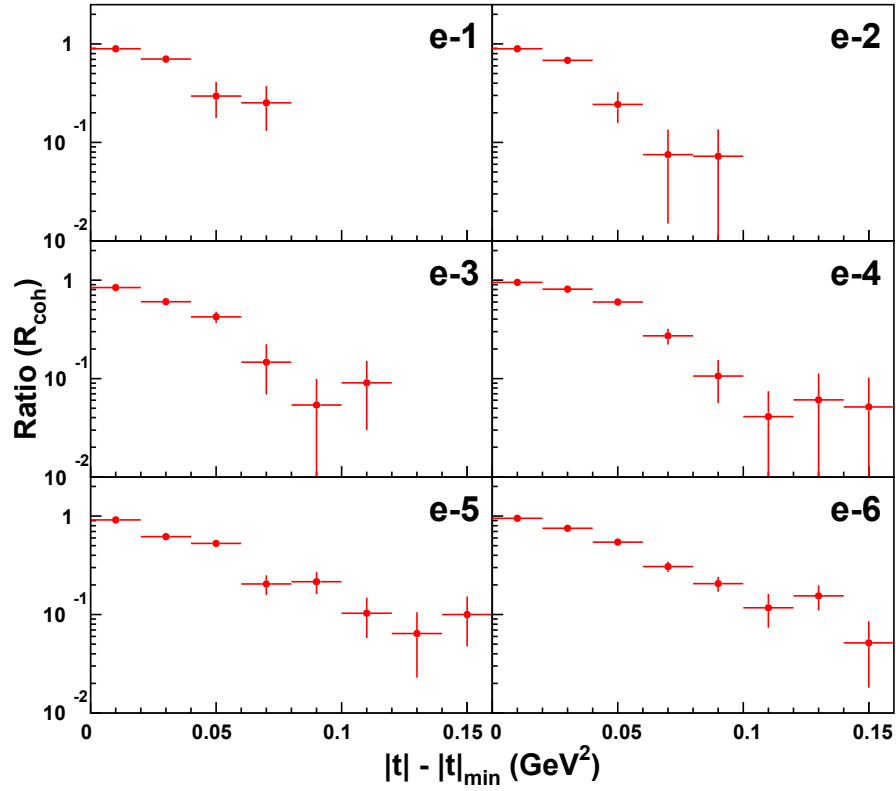
Figure 4.14: Ratios of the coherent events (R_{coh}) as a function of $\tilde{t}$ for various E_γ bins.
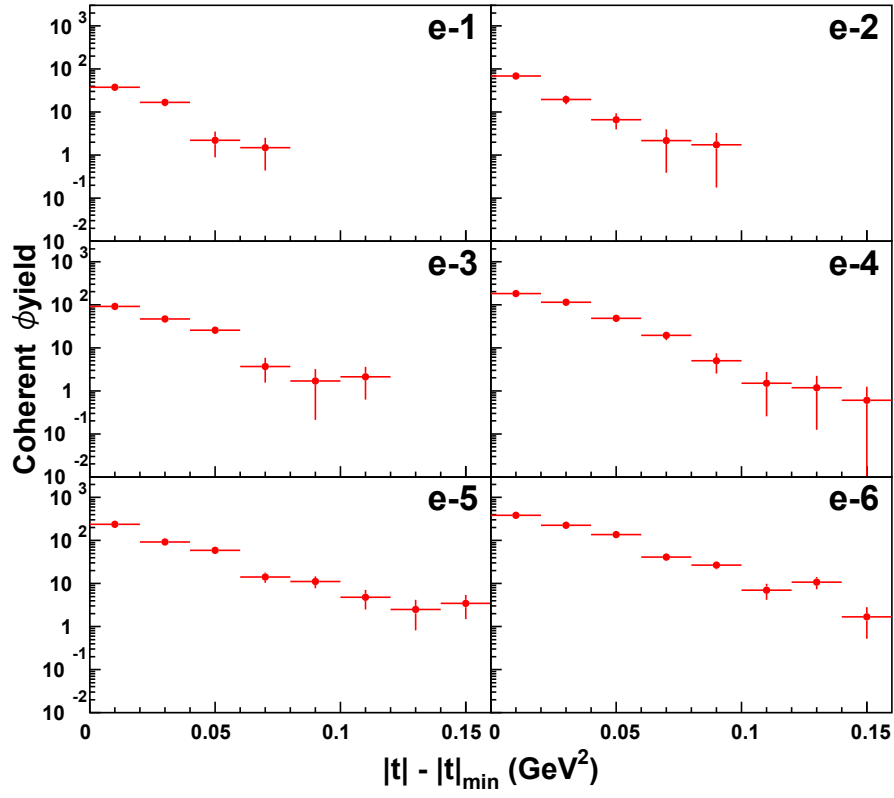
Figure 4.15: Yields for the coherent ϕ production events as a function of $\tilde{t}$ for various E_γ bins.

4.2.2   Acceptance as a function of $\tilde{t}$ and E_γ

The acceptance for each t and E_γ bin was calculated by MC simulation, as described in Sect. 3.9. Figure 4.16 shows the acceptances as a function of $\tilde{t}$ for various E_γ bins with a slope parameter of $b = 24$ GeV^{-2}. The validity of the acceptance calculation was checked with the LH$_2$ data (see Appendix I).
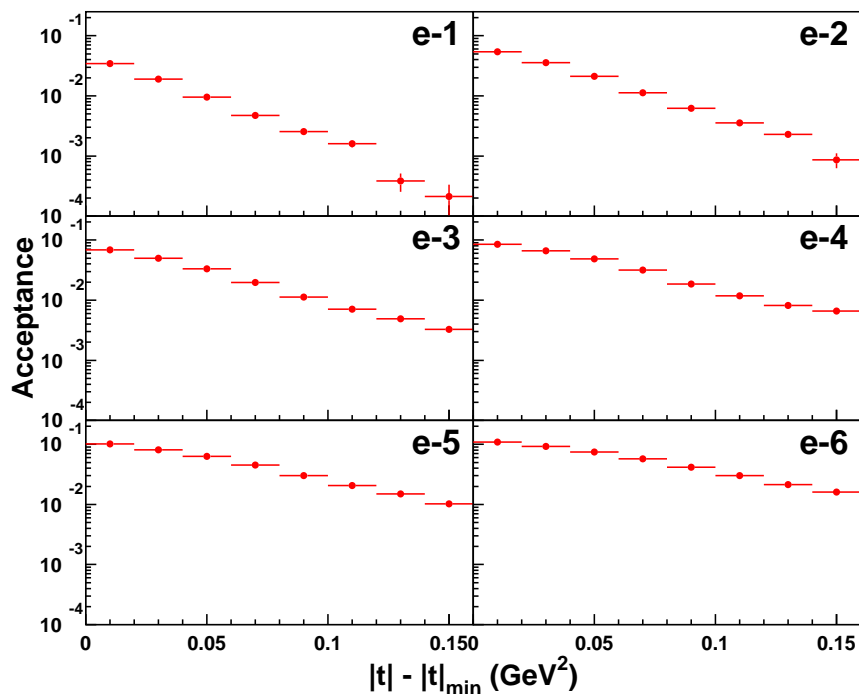
Figure 4.16:   Acceptance as a function of $\tilde{t}$ for various E_γ bins. These plots were obtained with a slope parameter of $b = 24$ GeV^{-2}.

4.2.3   Systematic errors on $d\sigma/d\tilde{t}$

Systematic errors in the cross section measurement are as follows:

- The systematic errors due to the event contamination other than the coherent ones were estimated by considering the semi-coherent process in the fits on the missing mass MM(K^+K^-) spectra. These results are presented in Appendix M.

- The systematic error on the normalization of the photon flux was estimated to be 3%.

- The systematic error on the K^+K^- event loss in the kaon identification was estimated to be 1% (see Appendix H).

- The systematic error on the contamination of the K^+K^- events from the CFRP cap of the target chamber was estimated to be 0.2% (see Sect. 3.6).

4.2.4 $d\sigma/d\tilde{t}$ for various E_γ

The differential cross sections $d\sigma/d\tilde{t}$ for various E_γ bins were calculated by using Eq. (4.9). Figure 4.17 shows $d\sigma/d\tilde{t}$ for various E_γ bins. A strong forward-peaking behavior of $d\sigma/\tilde{t}$ predominantly comes from the helium-4 form factor. To extract a slope parameter (b) and the $d\sigma/d\tilde{t}$ at $\tilde{t} = 0$ ($t = -|t|_{\min}$) $[(d\sigma/dt)_0]$, each spectrum was fitted with an exponential function, namely

$$\frac{d\sigma}{d\tilde{t}} = \left(\frac{d\sigma}{dt}\right)_0 \exp(-b\tilde{t}). \tag{4.12}$$

The fit results are summarized in Table 4.5. Judging from the reduced chi-squares χ^2/ndf, the quality of the fits is reasonably good.

Figure 4.18 shows the energy dependence of the extracted slopes b. There is no strong energy dependence beyond the statistical errors, and the common slope was determined to be $23.81 \pm 0.95(\text{stat})^{+5.16}_{-0.00}(\text{sys})$ GeV^{-2}. Here, the systematic error comes solely from the assumption of the semi-coherent process in the MM(K^+K^-) fits (see Appendix M). The common slope b is consistent with a simple estimate from a single-scattering assumption (see Sect. 1.6.2), in which the slope b is approximately expressed as $b \approx b_0 + b_F$, where b_0 is the slope for the elementary $\gamma p \to \phi p$ reaction (3.38 ± 0.23 GeV^{-2} [85]) and b_F is the slope of the squared charge form factor of ^{4}He nuclei (≈ 22 GeV^{-2} [136]; see also Fig. 4.19). This indicates that the contribution from the double-scattering process is negligible. The common slope b is also quite reasonable in comparison with that for other elastic scattering of a hadron off ^{4}He in the diffractive regime [137, 138][27]. This suggests that the VMD framework works well in this energy region.

---

[27]In Ref. [137], the measurement of the absolute differential cross sections for the elastic αp scattering at small $|t|$ is reported with an α-beam momentum of 17.9 GeV/c. The slope was obtained to be $b = 33.2 \pm 0.6$ GeV^{-2}, which is consistent with a diffraction
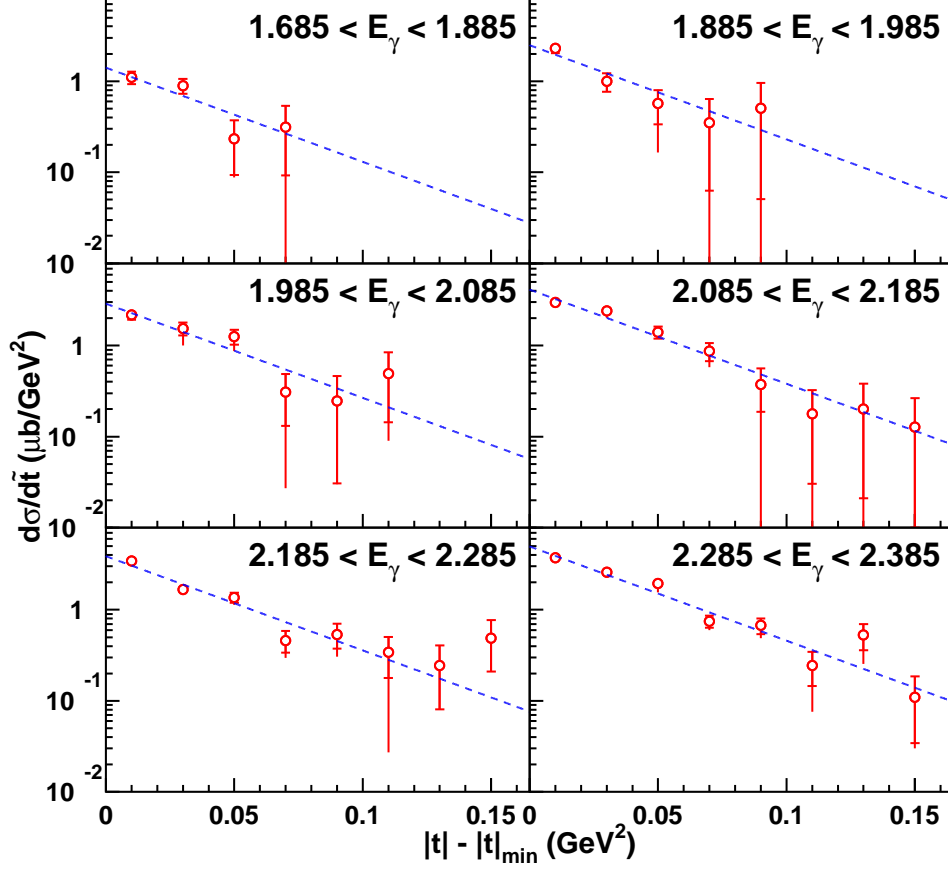
Figure 4.17: Differential cross section $d\sigma/d\tilde{t}$ for various E_γ bins. The smaller error bars represent the statistical error, whereas the larger ones represent the sum of the statistical and systematic errors in quadrature. Blue dashed curves show the fit results by an exponential function [Eq. (4.12)] with the common slope $b = 23.81$ GeV^{-2}.

multiple-scattering model (Glauber-Sitenko). In Ref. [138], the measurement of the absolute differential cross sections for the elastic $\pi\alpha$ scattering at small $|t|$ is reported with a π-beam momentum of 40.4 GeV/c. The slope was obtained to be $b = 29.3 \pm 1.1$ GeV^{-2}, which is in good agreement with a Glauber calculation.

125

Table 4.5: Summary of the fit results on $d\sigma/d\tilde{t}$ with a variable slope.

E_γ	N_0 (μb/GeV^2)	b (GeV)	χ^2	ndf	χ^2/ndf
e-1	1.704 ± 0.277	27.18 ± 7.42	3.35	2	1.67
e-2	3.293 ± 0.543	35.55 ± 8.40	1.03	3	0.34
e-3	3.415 ± 0.352	23.39 ± 3.78	5.66	4	1.41
e-4	4.088 ± 0.309	22.60 ± 2.07	5.32	6	0.89
e-5	4.331 ± 0.339	26.93 ± 2.52	11.14	6	1.86
e-6	4.902 ± 0.248	23.15 ± 1.27	15.94	6	2.82
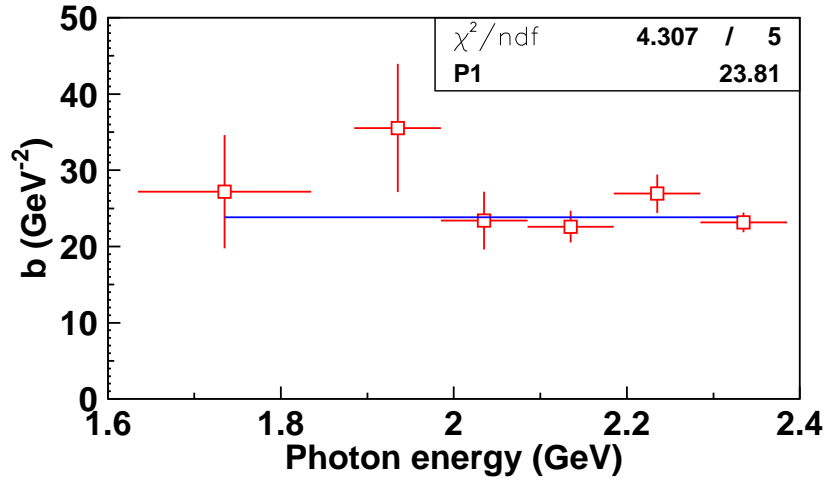
Figure 4.18:   Energy dependence of the slope b. A blue line represents an average value of $b = 23.81 \pm 0.95$ GeV^{-2}.
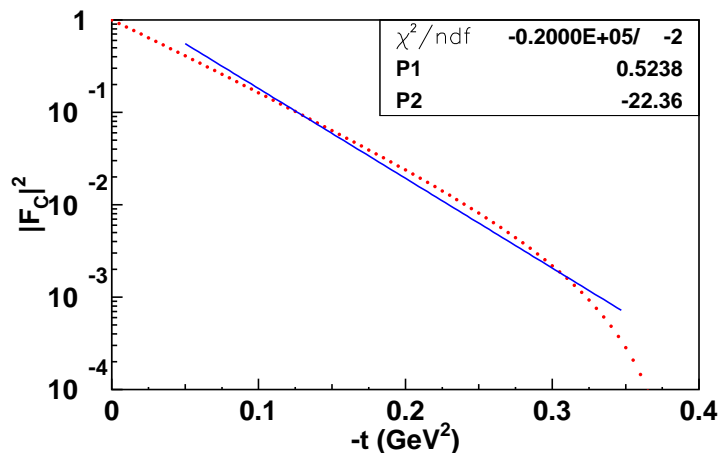
Figure 4.19:   Charge form factor $|F_C|^2$ as a function of the momentum transfer $-t$. The data were obtained from the numerical results of a VMC calculation [136] unfolded with a dipole nucleon form factor $G_d(q^2) = 1/(1 + q^2/0.71 \text{ GeV}^2)^2$. A blue curve represents the fit result by an exponential function for the relevant t region. A slope of $b \approx 22 \text{ GeV}^{-2}$ is obtained.

The differential cross sections $d\sigma/d\tilde{t}$ were also fitted by fixing a slope parameter to be the common one ($= 23.81 \text{ GeV}^{-2}$). The fit results are depicted as blue dashed curves in Fig. 4.17. The numerical results are summarized in Table 4.6. We found that it does not make any significant difference in fit quality whether a variable slope or a fixed one is used.

Table 4.6: Summary of the fit results on $d\sigma/d\tilde{t}$ with a fixed slope of $b = 23.8 \text{ GeV}^{-2}$.

E_γ	N_0 (μb/GeV^2)	χ^2	ndf	χ^2/ndf
e-1	1.604 ± 0.226	3.56	3	1.19
e-2	2.628 ± 0.229	3.49	4	0.87
e-3	3.443 ± 0.227	5.67	5	1.13
e-4	4.212 ± 0.265	5.64	7	0.81
e-5	3.985 ± 0.236	12.79	7	1.83
e-6	4.996 ± 0.231	17.20	7	2.45

4.2.5   Energy dependence of $d\sigma/d\tilde{t}$ at $\tilde{t} = 0$

Figure 4.20 shows the comparison of the intercepts $(d\sigma/dt)_0$ (i.e., $d\sigma/d\tilde{t}$ at $\tilde{t} = 0$) between those obtained with fixed and variable slopes. No difference was found in the intercepts $(d\sigma/dt)_0$ beyond the statistical errors. Therefore, the common slope $b = 23.81$ GeV^{-2} was used to evaluate the intercepts $(d\sigma/dt)_0$.

Figure 4.21 shows the energy dependence of $d\sigma/d\tilde{t}$ at $\tilde{t} = 0$ $[(d\sigma/dt)_0]$. The numerical results are summarized in Table 4.7. The present data exhibit a different energy dependence compared to that for the $\gamma p \to \phi p$ reaction (see Fig. 1.12). This is due to the ^{4}He form factor (, explained in the next section). The systematic errors due to the event contamination other than the coherent ones were found to be less than the statistical errors (see Appendix M).
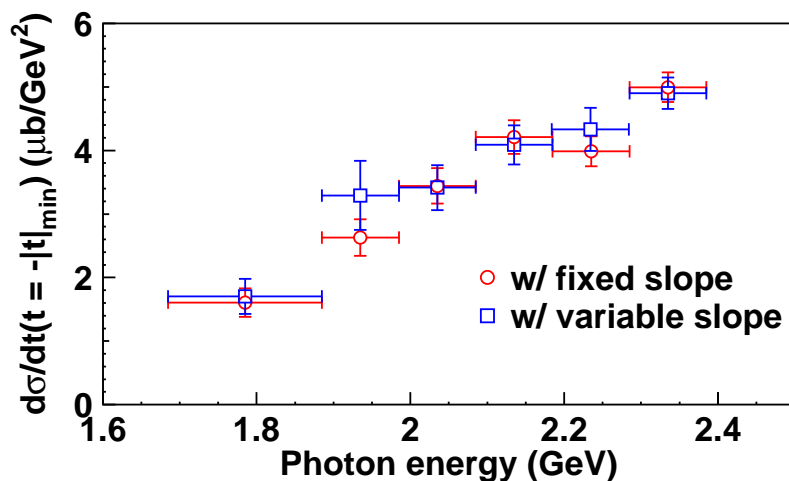
Figure 4.20: Comparison of the intercepts $(d\sigma/dt)_0$ between those obtained with fixed (red open circles) and variable slopes (blue open squares) as a function of the photon energy.
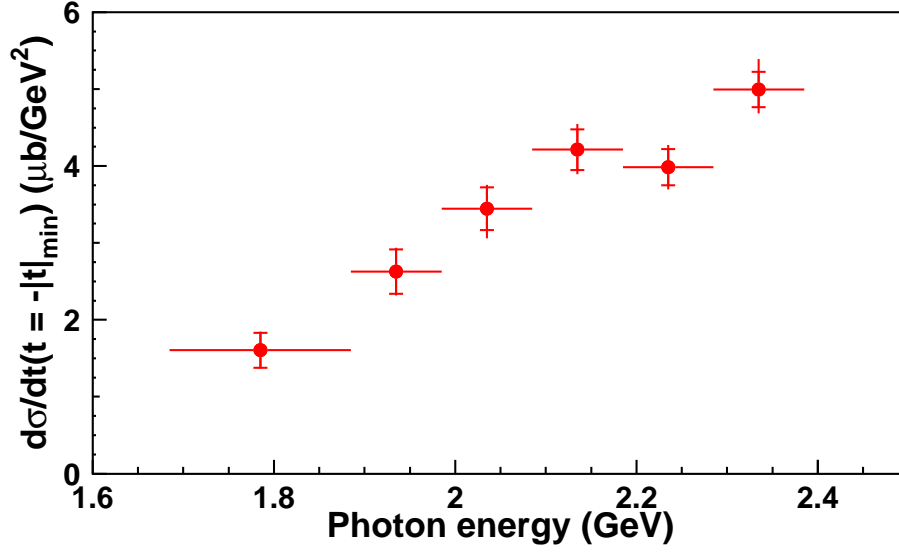
Figure 4.21:   Energy dependence of the $d\sigma/d\tilde{t}$ extrapolated to $\tilde{t} = 0$ with the common slope $b = 23.81$ GeV^{-2}. The meanings of the error bars are the same as in Fig. 4.17.

Table 4.7: Summary of $d\sigma/d\tilde{t}$ at $\tilde{t} = 0$ for various E_γ bins. The first and second uncertainties represent the statistical and systematic ones, respectively.

E_γ range (GeV)	$(d\sigma/dt)_0$ ($\mu b/$GeV^2)
1.685–1.885	$1.604 \pm 0.226^{+0.095}_{-0.068}$
1.885–1.985	$2.629 \pm 0.229^{+0.112}_{-0.119}$
1.985–2.085	$3.443 \pm 0.277^{+0.146}_{-0.268}$
2.085–2.185	$4.212 \pm 0.265^{+0.201}_{-0.179}$
2.185–2.285	$3.985 \pm 0.236^{+0.170}_{-0.169}$
2.285–2.385	$4.996 \pm 0.231^{+0.371}_{-0.212}$

4.2.6   Discussion on the energy dependence of $d\sigma/d\tilde{t}$ at $\tilde{t} = 0$

In this section, we first compare the present results with scaled $\gamma p \to \phi p$ data. We then discuss the Pomeron contribution to the forward cross section ($\theta = 0°$) for the elementary γp reaction as well as other possible natural-parity contribution, using the present data.

As already discussed in Sect. 1.6.2, a theoretical calculation for the coherent $\gamma d \to \phi d$ reaction was done by Titov *et al.* [93, 94], in which they describe the forward cross section ($\theta = 0°$) by using the amplitudes for the elementary $\gamma p \to \phi p$ reaction and the deuteron form factor [see Eq. (1.36)]. Similarly, the forward cross section ($\theta = 0°$) for the coherent $\gamma^4\mathrm{He} \to \phi^4\mathrm{He}$ reaction $[(d\sigma/dt)_0^{\gamma^4\mathrm{He}}]$ is described by using the ^{4}He charge form factor ($|F_C|^2$) as

$$\left(\frac{d\sigma}{dt}\right)_0^{\gamma^4\mathrm{He}} = 16|F_C|^2 \left(\frac{d\sigma}{dt}\right)_0^{\gamma p;\mathrm{NP}}, \tag{4.13}$$

where $(d\sigma/dt)_0^{\gamma p;\mathrm{NP}}$ denotes the forward cross section ($\theta = 0°$) for the γp reaction arising from natural-parity exchanges, a factor of 16 represents the square of the number of nucleons in a ^{4}He nucleus, and $|F_C|^2$ is evaluated at $t = -|t|_{\mathrm{min}}$.

By using Eq. (4.13), γp data can be scaled to that of the $\gamma^4\mathrm{He} \to \phi^4\mathrm{He}$ reaction if one neglects the π and η exchanges and other possible unnatural-parity exchanges in the γp reaction. Figure 4.22 shows the energy dependence of $(d\sigma/dt)_0^{\gamma^4\mathrm{He}}$ in comparison with scaled γp data. Here, the original γp data were taken from Refs. [85, 87], and the form factor $|F_C|^2$ was taken from the numerical results of a VMC calculation [136]. Even though the unnatural-parity π and η exchanges are absent in the $\gamma^4\mathrm{He}$ reaction, the present data $[(d\sigma/dt)_0^{\gamma^4\mathrm{He}}]$ are in excellent agreement with the scaled γp data. In particular, both the data exhibit a similar structure around $E_\gamma \sim 2.2$ GeV. Here, the structure present in the scaled γp data stems from the non-monotonic structure around $E_\gamma \sim 2$ GeV in the original data (see Fig. 1.12), but looks milder than the original one. This is due to the form factor $|F_C|^2$; that is, as shown in Fig. 4.23, $|t|_{\mathrm{min}}$ decreases largely with increasing energy for $1.5 < E_\gamma < 2.4$ GeV, and thus $|F_C|^2$ at $t = -|t|_{\mathrm{min}}$ rapidly increases with energy (see Fig. 4.19), thereby dominating over the energy dependence of the elementary cross section. Consequently, it is difficult to discuss any "structure" or the energy dependence of the Pomeron amplitude in detail, directly from the $\gamma^4\mathrm{He}$ data.
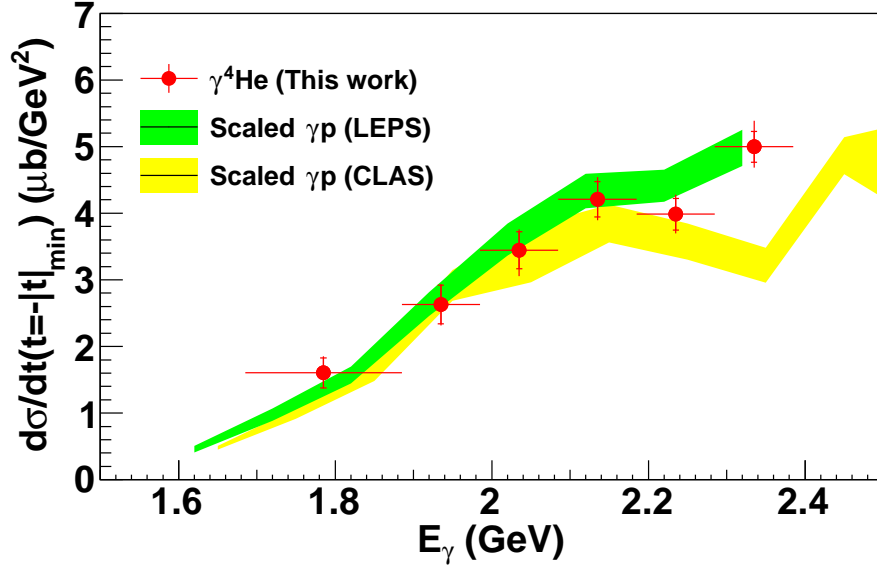
Figure 4.22: Energy dependence of $(d\sigma/dt)_0^{\gamma^4\mathrm{He}}$ in comparison with scaled γp data (see the text for scaled data). The meanings of the error bars are the same as in Fig. 4.17. The original γp data were taken from Refs. [85] (a green-filled band) and [87] (a yellow-filled band), respectively. The width of each band in the vertical direction represents experimental uncertainties.
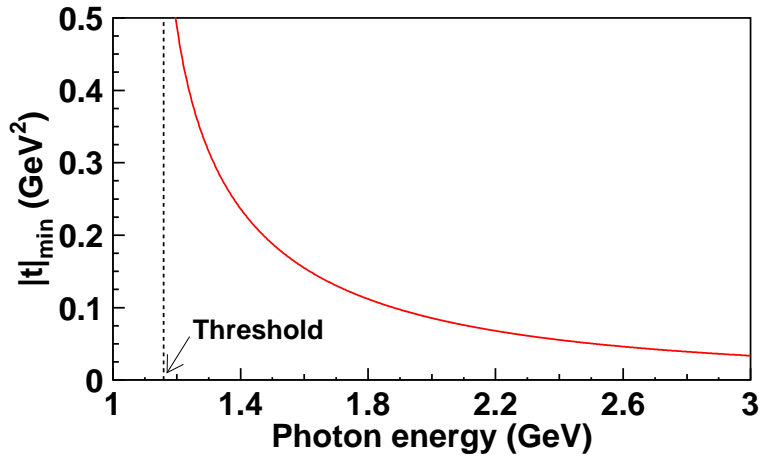
Figure 4.23: Minimum momentum transfer $|t|_{\min}$ as a function of the photon energy. A vertical dashed line represents the production threshold for the $\gamma^4\mathrm{He} \to \phi^4\mathrm{He}$ reaction.

131

In order to evaluate the Pomeron contribution to the forward cross section ($\theta = 0°$) for the elementary γp reaction as well as other possible natural-parity contribution, we constructed three models for describing the energy dependence of $(d\sigma/dt)_0^{\gamma p;\mathrm{NP}}$, where their overall strengths are unknown and to be determined:

Model-1

In this model, the amplitude is assumed to be independent of the energy s, and therefore the energy dependence of $(d\sigma/dt)_0^{\gamma p;\mathrm{NP}}$ is determined just kinematically [139]; namely

$$\left(\frac{d\sigma}{dt}\right)_0^{\gamma p;\mathrm{NP}} \propto \left(\frac{k_\phi}{k_\gamma}\right)^2, \tag{4.14}$$

where k_ϕ (k_γ) is the 3-momentum of ϕ-mesons (photons) in the center-of-mass frame. This model corresponds to a simple description of the Pomeron contribution[28].

Model-2

This model is a conventional Pomeron exchange model as described in Ref. [47] (see also Sect. 1.4.2). This model corresponds to just an extrapolation of the Pomeron exchange model established at high energies. The difference between models 1 and 2 is that model-1 yields exactly zero of the $(d\sigma/dt)_0^{\gamma p;\mathrm{NP}}$ at the threshold, whereas model-2 yields a finite value at the threshold.

Model-3

This model describes a threshold enhancement in the energy dependence of $(d\sigma/dt)_0^{\gamma p;\mathrm{NP}}$. This could be realized by modifying a conventional Pomeron exchange model and/or a manifestation of additional natural-parity exchanges near the threshold. For this model, we used the Pomeron and daughter Pomeron exchange model in Refs. [38, 47]. The relative strength of the daughter Pomeron contribution was adjusted so as to fit available γp data [64, 81, 85, 87, 122–125]. More details about this model are described in Appendix N.

To fix the overall strengths for the above models, we used the relation of Eq. (4.13) in the fits to the γ^4He data with the overall strengths being

---

[28]The forward Pomeron amplitude is approximately expressed as $T(s, t = 0) \sim s^{0.08}$, so it is almost independent of energy.

free parameters. Figure 4.24(a) shows the energy dependence of $(d\sigma/dt)_0^{\gamma^4\mathrm{He}}$, together with the best fits for models 1, 2 and 3. The reduced chi-squares, χ^2/ndf, are 48.5/5, 39.8/5 and 10.2/5 for models 1, 2 and 3, respectively. First of all, although model-3 is preferable on the basis of χ^2/ndf, all the models describe the measured energy dependence of $(d\sigma/dt)_0^{\gamma^4\mathrm{He}}$ fairly well. Therefore, all the models are treated "equally" hereafter. It is also worth noting that the Pomeron strength factor $C_\mathbb{P}$ [see Eq. (1.13)] determined here is in good agreement with the original one in Ref. [47] [= $(0.95 \pm 0.01)C_\mathbb{P}$], where the strength factor $C_\mathbb{P}$ was determined from a global fit to high-energy data for ρ, ω and ϕ-photoproduction off protons. This means that the present data are consistent with not only high-energy ϕ-photoproduction data but also other light vector meson photoproduction data at high energies [58–82].

Figure 4.24(b) shows the contribution from natural-parity exchanges to the forward cross section ($\theta = 0°$) for the γp reaction with each model, in comparison with the experimental data from LEPS [85, 88].

Models 1 and 2 give similar results, and we see that the both curves are slightly above the data points for $E_\gamma > 2.4$ GeV. On the other hand, the experimental data on the decay asymmetry $\bar{\rho}^1_{1-1}$ [88] show a sizable contribution of 20–30% from unnatural-parity exchanges to the γp reaction for $1.8 < E_\gamma < 2.9$ GeV (see Fig. 1.13). If the unnatural-parity contribution is simply added to the natural-parity one (i.e., the interference term is ignored), then models 1 and 2 obviously overestimate the data points. Therefore, to explain the experimental data, destructive interference between natural-parity and unnatural-parity exchanges is needed. This is in contradiction with a conventional model for ϕ-photoproduction off protons, in which interference effects between the natural-parity Pomeron exchange and the unnatural-parity π and η exchanges are small (see Sect. 1.4.2).

By contrast, model-3 gives a different result. We see that the curve is below the data points for $E_\gamma > 1.9$ GeV by $\sim 20\%$, except for a few data points. If the unnatural-parity contribution ($\sim 30\%$) is considered, model-3 can describe the experimental data fairly well. In this case, large interference effects are not needed, which is compatible with a conventional Pomeron, π, η exchange model. Note that destructive interference is also needed for $E_\gamma < 1.9$ GeV because simply adding the natural-parity contribution overestimates the experimental data.

From the above discussion, it turns out that enhancement of the forward cross section arising from natural-parity exchanges and/or destructive inter-

ference between natural-parity and unnatural-parity exchanges are needed in the $\gamma p \to \phi p$ reaction near the threshold. This suggests the presence of additional natural-parity exchange processes beyond the Pomeron exchange such as the daughter Pomeron exchange and/or the need to modify a conventional Pomeron exchange model, specifically the phase term of the Pomeron amplitude in a conventional model. In particular, the necessity of modifying the phase term of the Pomeron amplitude implies that Regge theory is inapplicable to the low-energy regime because the phase of the Pomeron amplitude is definitively determined by Regge theory.

The information on the phase of the Pomeron amplitude is important not only for modeling the Pomeron exchange at low energies but also for ϕ-photoproduction experiments concerning the strange degree of freedom in a nucleon [140] or light vector meson (ρ, ω and ϕ) photoproduction experiments searching for so-called missing resonances [141]: in such experiments, a "signal", whose contribution is in general small compared to the major contribution of the Pomeron exchange and thus is undetectable in cross sections, can be seen in polarization observables that are generated by interference terms of the contributing amplitudes.
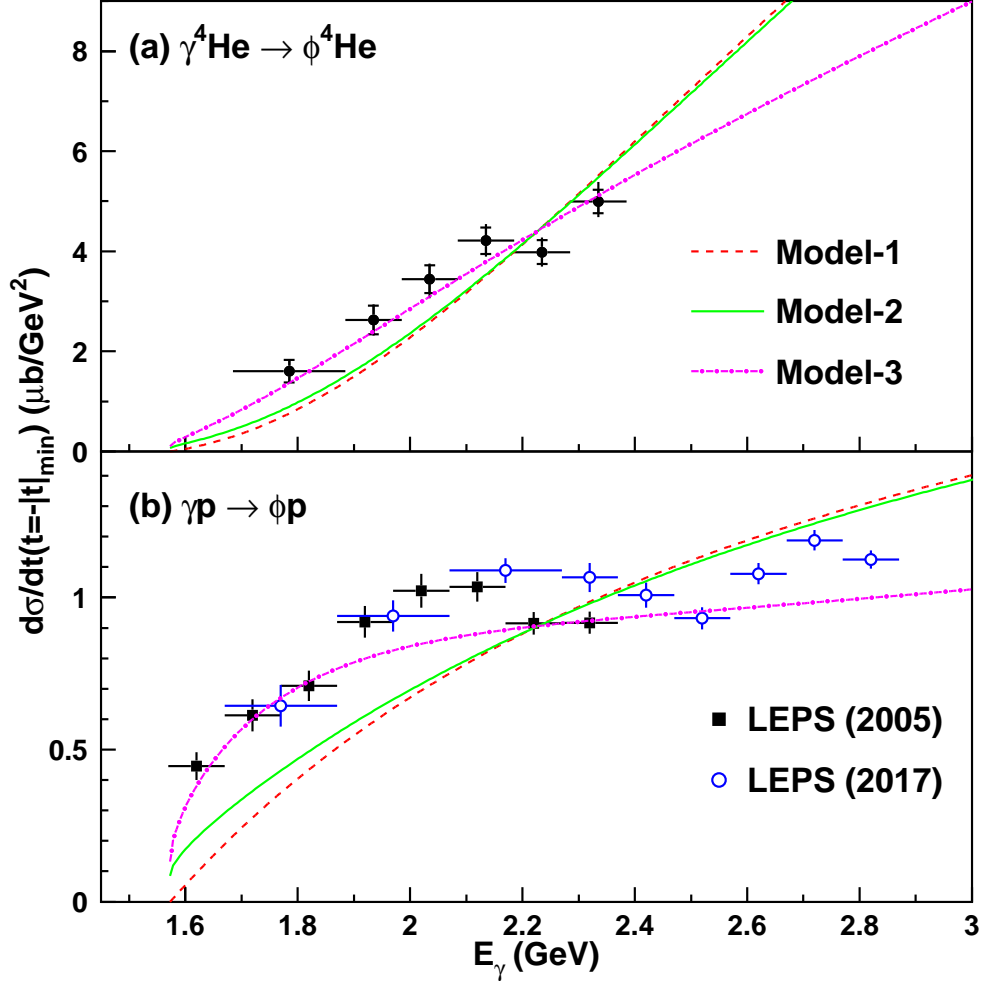
Figure 4.24:   (a) Energy dependence of $(d\sigma/dt)_0^{\gamma^{4}\mathrm{He}}$. The meanings of the error bars are the same as in Fig. 4.17. Red dashed, green solid and pink dash-dotted curves are the best fits for models 1, 2 and 3 (explained in the text), respectively. (b) Contribution from natural-parity exchanges to the forward cross section ($\theta = 0°$) for the γp reaction with models 1 (red dashed), 2 (green solid) and 3 (pink dash-dotted), in comparison with available experimental data. The experimental data are represented by black filled squares [85] and blue open circles [88].

5 Conclusion

In this thesis, we have presented the differential cross sections and decay angular distributions for coherent ϕ-meson photoproduction from helium-4 at forward angles with linearly polarized photons in the energy range of $E_\gamma = 1.685$–2.385 GeV. This measurement provides the first-ever data for this reaction. The production of ϕ-mesons was identified in the invariant mass spectra of K^+K^- pairs from the $\phi \to K^+K^-$ decay, whereas the coherent production events were separated from the incoherent ones by looking at the missing mass distributions for the ${}^4\mathrm{He}(\gamma, K^+K^-)X$ reaction. Thanks to the target with spin-parity $J^P = 0^+$, this reaction completely eliminates the contribution from unnatural-parity exchanges. As a result, this reaction provides a unique and clean way of investigating the Pomeron and multi-gluon exchanges at low energies.

The five one-dimensional $\phi \to K^+K^-$ decay angular distributions were measured in the Gottifried-Jackson frame, and the corresponding spin density matrix elements were extracted. The spin density matrix element ρ^0_{00}, which measures the probability of single helicity-flip transitions ($\lambda_\gamma = \pm 1 \to \lambda_\phi = 0$), was found to be consistent with zero. This indicates the dominance of helicity-conserving processes in t-channel. The decay asymmetry $\bar{\rho}^1_{1-1}$, which determines the relative contribution of natural-parity and unnatural-parity exchanges, was shown to be very close to the maximal value. This ensures the strong dominance ($> 94\%$) of natural-parity exchanges in this reaction. Further, we found that the decay asymmetry $\bar{\rho}^1_{1-1}$ sizably deviates from the maximal value. This, in conjunction with the observed non-zero value of $\mathrm{Re}\rho^0_{1-1}$, strongly indicates the existence of double helicity-flip transitions ($\lambda_\gamma = \pm 1 \to \lambda_\phi = -\lambda_\gamma$). Our observation supports the modified Donnachie-Landshoff Pomeron model based on the Pomeron-two-gluon analogy.

The differential cross section was measured as a function of the momentum transfer, and the slope parameter b and the intercept $(d\sigma/dt)_0$ were extracted. No strong energy dependence of the slope b was found, and the common slope b was determined to be $23.81 \pm 0.95(\mathrm{stat})^{+5.16}_{-0.00}(\mathrm{sys})$ GeV^{-2}. The common slope b is consistent with a simple estimate from a single-scattering assumption, i.e., the sum of the slope for the elementary reaction and that of the form factor. This indicates that the contribution from the double-scattering processes is negligibly small. Further, the common slope is reasonably compared to the slope for other elastic scattering of a hadron

off helium-4 in the diffractive regime, showing that the VMD picuture is still valid in this energy regime.

Based on the SDMEs ρ_{00}^0, $\mathrm{Re}\rho_{1-1}^0$ and $\bar{\rho}_{1-1}^1$ and the common slope b, we confirmed that the coherent production events are successfully separated from the incoherent ones, and thus the unnatural-parity contribution is absent (i.e., the natural-parity Pomeron exchange is dominant).

To evaluate the Pomeron contribution to the forward cross section ($\theta = 0°$) for the elementary $\gamma p \to \phi p$ reaction as well as other possible natural-parity contribution, three models were constructed for describing the energy dependence of the forward cross section ($\theta = 0°$) arising from natural-parity exchanges for the elementary process, and their overall strengths were determined from the present data. The comparison of them to available γp data revealed that threshold-enhancement of the forward cross section arising from natural-parity exchanges and/or destructive interference between natural-parity and unnatural-parity exchanges are needed in the $\gamma p \to \phi p$ reaction near the threshold. This suggests the presence of additional natural-parity exchange processes beyond the Pomeron exchange such as the daughter Pomeron exchange and/or the need to modify the phase term of the Pomeron exchange amplitude.

We have obtained the valuable information on the Pomeron exchange, i.e., the helicity structure of the Pomeron-quark couplings and the phase of the Pomeron amplitude. These information will be important constraints on modeling the Pomeron exchange especially at low energies. Further theoretical and experimental efforts are of great help for understanding the detailed mechanism of the Pomeron exchange.

References

[1] E. D. Bloom *et al.*, Phys. Rev. Lett. **23**, 930 (1969).

[2] Henry W. Kendall, Rev. Mod. Phys. **63**, 597 (1991).

[3] Y. Nambu, Phys. Rev. **106**, 1366 (1957).

[4] W. R. Frazer and J. R. Fulco, Phys. Rev. Lett. **2**, 365 (1959).

[5] T. H. Bauer, R. D. Spital, D. R. Yennie, and F. M. Pipkin, Rev. Mod. Phys. **50**, 261 (1978).

[6] Y. Nambu and J. J. Sakurai, Phys. Rev. Lett. **8**, 191 (1962).

[7] N. Cartiglia, 1997, hep-ph/9703245.

[8] A. Donnachie and P. V. Landshoff, Phys. Lett. B **437**, 408 (1998).

[9] P. D. B. Collins, *An Introduction to Regge Theory and High-Energy Physics* (Cambridge University Press, 1977).

[10] G. Chew and S. C. Frautschi, Phys. Rev. Lett. **7**, 394 (1961).

[11] G. Chew and S. C. Frautschi, Phys. Rev. Lett. **8**, 44 (1962).

[12] P. Goddard, J. Goldstone, C. Rebbi, and C. B. Thorn, Nucl. Phys. B **56**, 109 (1973).

[13] G. S. Bali, Phys. Rep. **343**, 1 (2001).

[14] V. N. Gribov, J. Exp. Theor. Phys. Lett. **41**, 667 (1961).

[15] L. B. Okun and I. Y. Pomeranchuck, Sov. Phys. **3**, 306 (1956).

[16] L. F. Foldy and R. F. Peierls, Phys. Rev. **130**, 1585 (1963).

[17] A. Donnachie and P. V. Landshoff, Phys. Lett. B **296**, 227 (1992).

[18] A. Donnachie and P. V. Landshoff, Nucl. Phys. B **231**, 189 (1984).

[19] P. V. Landshoff, 1994, hep-ph/9410250.

[20] L. S. Kisslinger and W.-H. Ma, Phys. Lett. B **485**, 367 (2000).

[21] F. J. Llanes-Estrada, S. R. Cotanch, P. J. de A. Bicudo, J. E. F. T. Ribeiro, and A. Szczepaniak, Nucl. Phys. A **710**, 45 (2002).

[22] M. Derrick *et al.*, Phys. Lett. B **356**, 129 (1995).

[23] F. Abe *et al.*, Phys. Rev. Lett. **78**, 2698 (1997).

[24] F. Abe *et al.*, Phys. Rev. Lett. **79**, 2636 (1997).

[25] F. Abe *et al.*, Phys. Rev. Lett. **74**, 855 (1995).

[26] T. Affolder *et al.*, Phys. Rev. Lett. **87**, 141802 (2001).

[27] A. Donnachie and P. V. Landshoff, Nucl. Phys. B **244**, 322 (1984).

[28] E. Gotsman, E. M. Levin, and U. Maor, Phys. Rev. D **49**, R4321(R) (1984).

[29] K. Goulianos, Phys. Lett. B **358**, 379 (1995).

[30] S. Erhan and P. E. Schlein, Phys. Lett. B **427**, 389 (1998).

[31] K. Goulianos and J. Montanha, Phys. Rev. D **59**, 114017 (1999).

[32] R. Fiore, A. Flachi, L. L. Jenkovszky, F. Paccanoni, and A. Papa, Phys. Rev. D **61**, 034004 (1999).

[33] A. D. Martin, J. Phys.: Conf. Ser. **607**, 012002 (2015).

[34] F. E. Low, Phys. Rev. D **12**, 163 (1975).

[35] S. Nussinov, Phys. Rev. lett. **34**, 1286 (1975).

[36] S. Nussinov, Phys. Rev. D **14**, 246 (1976).

[37] P. V. Landshoff and O. Nachtmann, Z. Phys. C **35**, 405 (1987).

[38] A. I. Titov, T.-S. H. Lee, H. Toki, and O. Streltsova, Phys. Rev. C **60**, 035205 (1999).

[39] R. A. Williams, Phys. Rev. C **57**, 223 (1998).

[40] S. Okubo, Phys. Lett. **5**, 1975 (1963).

[41] G. Zweig, CERN report TH-412, (1964), (unpublished).

[42] J. Iizuka, Prog. Theor. Phys. Suppl. **37**, 38 (1966).

[43] V. Barger and D. Cline, Phys. Rev. Lett. **24**, 1313 (1970).

[44] T. Nakano and H. Toki, in *Proceedings of the International Workshop on Exciting Physics with New Accelerator Facilities, SPring-8, Hyogo, 1997*, p. 48, World Scientific, Singapore, 1998.

[45] A. Donnachie and P. V. Landshoff, Nucl. Phys. B **311**, 509 (1988/89).

[46] J. R. Cudell, A. Donnachie, and P. V. Landshoff, Nucl. Phys. B **322**, 55 (1989).

[47] A. I. Titov and T.-S. H. Lee, Phys. Rev. C **67**, 065205 (2003).

[48] P. V. Landshoff and P. J. Polkinghorne, Nucl. Phys. B **32**, 541 (1971).

[49] A. I. Titov, Y. Oh, S. N. Yang, and T. Morii, Phys. Rev. C **58**, 2429 (1998).

[50] G. S. Bali *et al.*, Phys. Lett. B **309**, 378 (1993).

[51] C. J. Morningstar and M. Peardon, Phys. Rev. D **56**, 4043 (1997).

[52] C. J. Morningstar and M. Peardon, Phys. Rev. D **60**, 034509 (1999).

[53] A. Vaccarino and D. Weingarten, Phys. Rev. D **60**, 114501 (1999).

[54] H. B. Meyer and M. J. Teper, Phys. Lett. B **605**, 344 (2005).

[55] Y. Chen *et al.*, Phys. Rev. D **73**, 014516 (2006).

[56] E. Gregory *et al.*, J. High Energy Phys. **10**, 170 (2012).

[57] The Aachen-Berlin-Bonn-Hamburg-Heidelberg-München Collaboration, Phys. Rev. **175**, 1669 (1968).

[58] H.-J. Behrend *et al.*, Nucl. Phys. B **144**, 22 (1978).

[59] J. Ballam *et al.*, Phys. Lett. B **30**, 421 (1969).

[60] R. Anderson *et al.*, Phys. Rev. D **1**, 27 (1970).

[61] J. Ballam *et al.*, Phys. Rev. D **5**, 545 (1972).

[62] W. Struczinski *et al.*, Nucl. Phys. B **47**, 436 (1972).

[63] C. Berger *et al.*, Phys. Lett. B **39**, 659 (1972).

[64] J. Ballam *et al.*, Phys. Rev. D **7**, 3150 (1973).

[65] G. Alexander *et al.*, Nucl. Phys. B **69**, 445 (1974).

[66] W. Struczinski *et al.*, Nucl. Phys. B **108**, 45 (1976).

[67] R. M. Egloff *et al.*, Phys. Rev. Lett. **43**, 657 (1979).

[68] D. Aston *et al.*, Nucl. Phys. B **209**, 56 (1982).

[69] M. Derrick *et al.*, Z. Phys. C **69**, 39 (1995).

[70] S. Aid *et al.*, Nucl. Phys. B **463**, 3 (1996).

[71] M. Derrick *et al.*, Z. Phys. C **73**, 253 (1997).

[72] R. M. Egloff *et al.*, Phys. Rev. Lett. **43**, 1545 (1979).

[73] M. Atkinson *et al.*, Nucl. Phys. B **231**, 15 (1984).

[74] D. P. Barber *et al.*, Z. Phys. C **26**, 343 (1984).

[75] J. Busenitz *et al.*, Phys. Rev. D **40**, 1 (1989).

[76] M. Derrick *et al.*, Z. Phys. C **73**, 73 (1996).

[77] G. McClellan *et al.*, Phys. Rev. Lett. **26**, 1593 (1971).

[78] H. Alvensleben *et al.*, Phys. Rev. Lett. **28**, 66 (1972).

[79] R. L. Anderson *et al.*, Phys. Rev. Lett. **30**, 149 (1973).

[80] D. P. Barber *et al.*, Phys. Lett. B **79**, 150 (1978).

[81] D. P. Barber *et al.*, Z. Phys. C **12**, 1 (1982).

[82] M. Derrick *et al.*, Phys. Lett. B **377**, 259 (1996).

[83] K. Schilling, P. Seyboth, and G. Wolf, Nucl. Phys. B **15**, 397 (1970).

[84] H.-Y. Ryu, A. I. Titov, A. Hosaka, and H.-C. Kim, Prog. Theor. Exp. Phys. 2014 , 023D03 (2014).

[85] T. Mibe *et al.*, Phys. Rev. Lett. **95**, 182001 (2005).

[86] B. Dey *et al.*, Phys. Rev. C **89**, 055208 (2014).

[87] H. Seraydaryan *et al.*, Phys. Rev. C **89**, 055206 (2014).

[88] K. Mizutani *et al.*, Phys. Rev. C **96**, 062201(R) (2017).

[89] W. C. Chang *et al.*, Phys. Rev. C **82**, 015205 (2010).

[90] S. Ozaki, A. Hosaka, H. Nagahiro, and O. Scholten, Phys. Rev. C **80**, 035201 (2009).

[91] A. Kiswandhi, J. J. Xie, and S. N. Yang, Phys. Lett. B **691**, 214 (2010).

[92] A. Kiswandhi and S. N. Yang, Phys. Rev. C **86**, 015203 (2012).

[93] A. I. Titov, M. Fujiwara, and T. S.-H. Lee, Phys. Rev. C **66**, 022202(R) (2002).

[94] A. I. Titov and B. Kämpfer, Phys. Rev. C **76**, 035202 (2007).

[95] W. C. Chang *et al.*, Phys. Lett. B **658**, 209 (2008).

[96] K. S. Kölbig and B. Margolis, Nucl. Phys. B **6**, 85 (1968).

[97] L. Frankfurt *et al.*, Nucl. Phys. A **622**, 511 (1997).

[98] S. J. Brodsky, I. Schmidt, and G. F. de Téramond, Phys. Rev. Lett. **64**, 1011 (1990).

[99] D. A. Wasson, Phys. Rev. Lett. **67**, 2237 (1991).

[100] A. B. Kaidalov and P. E. Volkovitsky, Phys. Rev. Lett. **69**, 3155 (1992).

[101] M. Luke, A. V. Manohar, and M. J. Savage, Phys. Lett. B **288**, 355 (1992).

[102] R. Aaij *et al.*, Phys. Rev. Lett. **115**, 072001 (2015).

[103] H.-X. Chen, W. Chen, X. Liu, and S.-L. Zhu, Phys. Rep. **639**, 1 (2016).

[104] U. G. Meißner and J. A. Oller, Phys. Lett. B **751**, 59 (2015).

[105] M. I. Eides, V. Y. Petrov, and M. V. Polyakov, Phys. Rev. D **93**, 054039 (2016).

[106] I. A. Perevalova, M. V. Polyakov, and P. Schweitzer, Phys. Rev. D **94**, 054024 (2016).

[107] M. Alberti *et al.*, Phys. Rev. D **95**, 074501 (2017).

[108] M. I. Eides, V. Y. Petrov, and M. V. Polyakov, Eur. Phys. J. C **78**, 36 (2018).

[109] B.-G. Yu, H. Kim, and K.-J. Kong, Phys. Rev. D **95**, 014020 (2017).

[110] N. Muramatsu *et al.*, Nucl. Instr. Meth. A **737**, 184 (2014).

[111] M. Sumihama, *Photon beam asymmetries for the $p(\gamma, K^+)\Lambda$ and $p(\gamma, K^+)\Sigma^0$ reactions at SPring-8/LEPS*, PhD thesis, Osaka University, 2003.

[112] Y. Kato, *Study of the Θ^+ via $\gamma d \to K^+ K^-$ reaction with high statistics data at SPring-8/LEPS*, PhD thesis, Osaka University, 2012.

[113] Y. Nakatsugawa, *Measurement of $\Lambda(1405)$ and $\Sigma^0(1385)$ photoproduction on the proton at $E_\gamma = 1.5-3.0$ GeV*, PhD thesis, Osaka University, 2013.

[114] Spring-8 home page, <http://www.spring8.or.jp>.

[115] A. Dángelo *et al.*, Nucl. Instr. and Meth. A **455**, 1 (2000).

[116] SPring-8 annual report No.132, 1998, (unpublished).

[117] R. Suda *et al.*, Nucl. Instr. and Meth. A **406**, 213 (1998).

[118] R. Brun and F. Carminati, CERN Program Library Long Writeup Report W5013, 1993, (unpublished).

[119] F. James, *Function Minimization and Error Analysis*, CERN-D506, 1994, (unpublished).

[120] R. B. Wiringa, R. Schiavilla, S. C. Pieper, and J. Carlson, Phys. Rev. C **89**, 024305 (2014).

[121] H. Kamada *et al.*, Phys. Rev. C **64**, 044001 (2001).

[122] H. J. Besch *et al.*, Nucl. Phys. B **70**, 257 (1974).

[123] H. J. Behrend *et al.*, Nucl. Phys. B **144**, 22 (1978).

[124] E. Anciant *et al.*, Phys. Rev. Lett. **85**, 4682 (2000).

[125] J. Barth *et al.*, Eur. Phys. J. A **17**, 269 (2003).

[126] A. Amroun *et al.*, Nucl. Phys. A **579**, 596 (1994).

[127] I. Sick, Phys. Lett. B **116**, 212 (1982).

[128] M. Sumihama *et al.*, Phys. Rev. C **73**, 035214 (2006).

[129] M. Sumihama *et al.*, Phys. Lett. B **657**, 32 (2007).

[130] K. McCormick *et al.*, Phys. Rev. C **69**, 032203(R) (2004).

[131] J.-M. Laget, Phys. Lett. B **489**, 313 (2000).

[132] W. C. Chang *et al.*, Phys. Lett. B **684**, 6 (2010).

[133] C. Ewerz, M. Maniatis, and O. Nachtmann, Ann. Phys. **342**, 31 (2014).

[134] C. Ewerz, P. Lebiedowicz, O. Nachtmann, and A. Szczurek, Phys. Lett. B **763**, 382 (2016).

[135] L. Adamczyk *et al.*, Phys. Lett. B **719**, 62 (2013).

[136] R. B. Wiringa, Phys. Rev. C **43**, 1585 (1991).

[137] Ableev V. G. *et al.*, Yad. Fiz. **36**, 1434 (1982), [Sov. J. Nucl. Phys. 36, 834 (1982)].

[138] Ableev V. G. *et al.*, Yad. Fiz. **34**, 769 (1981), [Sov. J. Nucl. Phys. 34, 428 (1981)].

[139] A. Sibirtsev and H.-W. Hammer, Eur. Phys. J. A **29**, 209 (2006).

[140] A. I. Titov, Y. Oh, and S. N. Yang, Phys. Rev. Lett. **79**, 1634 (1997).

[141] V. Crede and W. Roberts, Rep. Prog. Phys. **76**, 076301 (2013).

[142] T. Regge, Nuovo Cimento **14**, 951 (1959).

[143] S. Mandelstam, Phys. Rev. **112**, 1344 (1958).

[144] S. Donnachie, G. Dosch, P. Landshoff, and O. Nachtmann, *Pomeron Physics and QCD* (Cambridge University Press, 2002).

[145] I. Y. Pomeranchuck, Soviet Physics: J. Exp. Theor. Phys. **7**, 499 (1958).

[146] M. Froissart, Phys. Rev. **123**, 1053 (1961).

[147] A. Martin, Phys. Rev. **129**, 1432 (1963).

[148] A. Donnachie and P. V. Landshoff, Nucl. Phys. B **267**, 690 (1986).

[149] A. Donnachie and P. V. Landshoff, Phys. Lett. B **123**, 345 (1983).

[150] A. Donnachie and P. V. Landshoff, Nucl. Phys. B **244**, 322 (1984).

[151] L. Adamczyk *et al.*, Phys. Lett. B **719**, 62 (2013).

[152] A. Donnachie and P. V. Landshoff, Phys. Lett. B **478**, 146 (2000).

[153] Particle Data Group, C. Patrignani *et al.*, Chin. Phys. C **40**, 100001 (2016).

[154] D. Robson, Nucl. Phys. B **130**, 328 (1977).

[155] J. Z. Bai *et al.*, Phys. Rev. Lett. **76**, 3502 (1996).

[156] J. Z. Bai *et al.*, Phys. Rev. Lett. **81**, 1179 (1998).

[157] K. Benslama *et al.*, Phys. Rev. D **66**, 077101 (2002).

[158] R. M. Baltrusaitis *et al.*, Phys. Rev. Lett. **56**, 107 (1986).

[159] V. Crude and C. A. Meyer, Prog. Part. Nucl. Phys. **63**, 74 (2009).

Appendix A   Soft pomeron

In this Appendix, a soft pomeron and related topics are reviewed.

A.1   Regge theory and Pomeron trajectory

In the 1960s, before the arrival of QCD, Regge theory [9] was developed by the successive work of T. Regge, S. Mandelstam, M. Froissart, G. Chew and S. C. Frautschi, and served as an effective tool for describing high-energy scattering processes between strongly-interacting particles, i.e. hadrons. Regge theory, as its name suggests, originates from the work of Tullio Regge [142]: he studied the analytic properties of the non-relativistic scattering equation for a spherically-symmetric potential with the introduction of complex angular momenta, in which angular momenta are not restricted to a non-negative integer, but can take any complex value. His original idea was for the non-relativistic case, but was soon taken over for application to relativistic scattering of hadrons.

It is commonly known that the scattering amplitude $\mathcal{A}(E, \theta)$ for two-particle collision, which is characterized by the total energy E and the scattering angle θ for one of the scattered particles, can be decomposed into a set of partial wave amplitudes $\mathcal{A}_l(E)$ with a fixed angular momentum $l = 0, 1, 2, \ldots$, etc. If the two particles are able to bind together to form a bound state or a resonance with a given angular momentum $l = L$, then the partial wave amplitude $\mathcal{A}_L(E)$ has a pole in the complex E plane. In the case of a stable bound state with a negative energy of E_B (< 0), for example, the pole locates at the negative real value $E = E_B$ in the complex E plane. Thus, the continuation of the energy E from real positive physical values to complex and negative values allows us to deal with scattering processes and the existence of bound states or resonances in a unified way.

In Regge theory, it has been proven that as $\mathcal{A}_L(E)$ has a pole at the energy E for which a bound state with the angular momentum $l = L$ exists, so the amplitude $\mathcal{A}(l, E)$, which is an analytic function of the partial wave amplitudes $\mathcal{A}_l(E)$ with the continuation of angular momenta to complex values, has a pole, i.e. a "Regge pole", in the complex angular momentum plane. The position of Regge poles can be written as a function of the energy E. By introducing the the Mandelstam variables (s, t, u) [143] and using the

146

properties of "crossing symmetry", it becomes

$$l = \alpha(t). \tag{A.1}$$

This is a so-called Regge trajectory. A Regge trajectory is associated with a family of the particles with the same quantum numbers except for spin: When a value of $\alpha(t)$ happens to be a non-negative integer, the Regge pole corresponds to a physical bound state or resonance with the mass of $M = \sqrt{t}$. A Regge trajectory $\alpha(t)$ can be approximated by a linear function of momentum transfer t

$$\alpha(t) \approx \alpha(0) + \alpha' t, \tag{A.2}$$

where $\alpha(0)$ is the Regge intercept and α' is the slope. Chew and Frautschi verified this linear relation by plotting the spins of hadrons versus their squared masses $t = M^2$ [10, 11]. Figure A.1 shows a typical Chew-Frautschi plot for mesonic Regge trajectories; ρ, ω, f_2 and a_2 trajectories. These leading meson trajectories are degenerate, and give almost the same intercepts of $\alpha(0) \approx 0.5$. Note that the experimentally observed mesons and baryons appear to lie on nearly linear and parallel Regge trajectories with $\alpha' \approx 0.9$ GeV^{-2} and $\alpha(0) \lesssim 0.5$.

Suppose that the amplitude $\mathcal{A}(l, t)$ has simple Regge poles at $l = \alpha(t)$, then the amplitude $\mathcal{A}(s, t)$, as a function of s and t, has an asymptotic form ($s \gg |t|$, $s \to \infty$):

$$\mathcal{A}(s \to \infty, t) \sim \frac{\beta(t)}{\Gamma(\alpha(t))} \frac{\left(1 + \eta e^{-i\pi\alpha(t)}\right)}{2 \sin \pi\alpha(t)} s^{\alpha(t)} \tag{A.3}$$

where $\beta(t)$ is the residue of Regge poles, $\Gamma(x)$ is the gamma function, and η is a signature that takes ± 1. The signature η is introduced when partial wave amplitudes $\mathcal{A}_l(E)$ are analytically continued to the complex angular momentum plane. This is because partial wave amplitudes $\mathcal{A}_l(E)$ cannot be represented by values of a single analytic function $\mathcal{A}(l, E)$ with the required properties for all integer l, and the partial wave amplitudes with even and odd spin l have to be treated separately. The signature is closely related to the crossing properties of scattering amplitudes under the interchange of s and u. Under the interchange $s \leftrightarrow u$, the amplitudes with $\eta = +1$ are symmetric (even), while those with $\eta = -1$ are antisymmetric (odd). For example, meson trajectories with even-spin (angular momentum) particles correspond to even signature $\eta = +1$, whereas those with odd-spin particles correspond to odd signature $\eta = -1$.
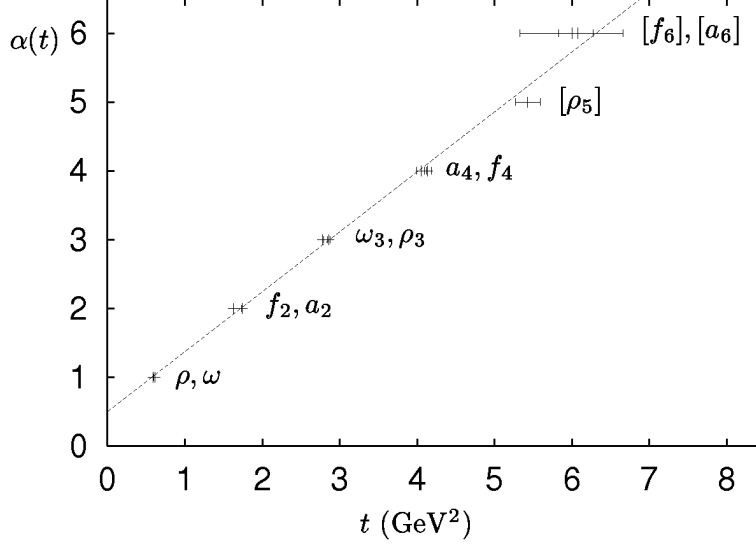
Figure A.1:   Relationship between squared mass and spin for various mesons (A Chew-Frautschi plot). ρ, ω, f_2 and a_2 trajectories are degenerate. The figure is taken from Ref. [144].

The term $s^{\alpha(t)}$ in Eq. (A.3) can be physically interpreted as the t-channel exchange of an object with its angular momentum equal to $\alpha(t)$. This, of course, not a physical particle since the angular momentum is not an integer (or half-integer) and is a continuous function of t. In the Regge picture, whatever is exchanged is called a "Reggeon". The t-channel exchange of a Reggeon corresponds to the superposition of amplitudes for the exchange of all possible particles in t-channel. On the other hand, $\beta(t)$ contains all the information on the coupling of a Reggeon to interacting particles. This coupling depends only on t, and thus it leads to the "factorization" property.

If the scattering process under consideration is elastic, the asymptotic behavior of the total cross section can be deduced from Eq. (A.3) by using the optical theorem, so that

$$\sigma^{\text{tot}} \sim \frac{1}{s}\text{Im}\mathcal{A}(s, t = 0) \sim s^{\alpha(0)-1}. \tag{A.4}$$

Since all the known Regge trajectories have an intercept of $\alpha(0) \lesssim 0.5$, one expects that the total cross section would fall down as a power of energy

148

$s^{-0.5}$. In fact, at $\sqrt{s} < 10$ GeV, the observed total cross sections for proton-proton and proton-antiproton scattering decrease as the energy $\sqrt{s}$ increases. However, above the energy of $\sqrt{s} \sim 10$ GeV, the total cross sections for both pp and $p\bar{p}$ collisions rise with increasing energy, which cannot be accounted for by the exchange of any known Regge trajectories (see Fig. A.2).

As Regge theory was developing, Pomeranchuk proved a theorem, i.e. the so-called Pomeranchuk theorem [145], which states that total cross sections for collisions of a particle and the corresponding antiparticle on the same target become asymptotically equal at high energies under the assumptions that the cross sections are asymptotically constant and that the ratio of real to imaginary parts of the forward scattering amplitude does not increase more rapidly than $\ln s$. Gribov introduced a new Regge trajectory which assures these assumptions [14]. This new Regge trajectory, which we call "Pomeron trajectory", named after Pomeranchuk, has an intercept greater than but nearly equal to unity, and carries the quantum numbers of the vacuum[29]. The exchange of Pomeron trajectory accounts for slowly-rising total hadron-hadron cross sections, as well as total photon-hadron cross sections.

A.2   Donnachie-Landshoff Pomeron model

Donachie and Landshoff analyzed high-energy hadron-hadron and photon-hadron scattering data. They fitted various types of hadronic total cross section data [17] by using the following formula:

$$\sigma^{ab}_{\text{tot}}(s) = X^{ab} s^{\epsilon} + Y^{ab} s^{\eta}, \tag{A.5}$$

where the first term represents the contribution from Pomeron trajectory, and the second one the contribution from mesonic Regge trajectories such as ρ, ω, f_2 and a_2 trajectories. $\epsilon = \alpha_{\mathbb{P}}(0) - 1$ refers to the Pomeron intercept and is positive, whereas $\eta = \alpha_{\mathbb{R}}(0) - 1$ refers to the intercept of the degenerate ρ, ω, f_2 and a_2 trajectories and is negative. The intercepts ϵ, η are the universal ones, while the coefficients X^{ab}, Y^{ab} depend on the reaction types $ab \to X(anything)$. Since a Pomeron carries the vacuum quantum number, its couplings to a particle a and its antiparticle $\bar{a}$ are the same, so that the coefficients X^{ab} and $X^{\bar{a}b}$ should be equal. A simultaneous fit to pp and $\bar{p}p$

---

[29]It has been proven that for a particular scattering process, if the total cross section does not fall down as $\sqrt{s}$ increases, then the process must be dominated by the exchange of vacuum quantum numbers [15, 16]

data for $\sqrt{s} > 10$ GeV [Fig. A.2(a)], by requiring the same values of X, ϵ and η, gives

$$\epsilon = 0.0808 \Rightarrow \alpha_{\mathbb{P}}(0) = 1.08 \tag{A.6}$$

and

$$\eta = -0.4525 \Rightarrow \alpha_{\mathbb{R}}(0) = 0.55. \tag{A.7}$$

Fits to the other data by using the same values of ϵ and η and also requiring that $X^{ab} = X^{\bar{a}b}$ are also shown in Figs. A.2(b)–(e). It is remarkable that a simple parametrization given by Eq. (A.5) well describes total cross section data for any reactions. Note that the obtained value of ϵ does not correspond to a simple, single Pomeron pole, but is an effective power, incorporating the effects of multiple Pomeron exchanges. It should be also noted here that the single Pomeron exchange is obviously in conflict with the Froissart-Martin bound[30] [146, 147]. It is, however, believed that multiple Pomeron exchanges could reduce the power ϵ effectively so as to meet the Froissart bound, although it has not been proven yet from QCD.

The fits to the total cross section data reveal the following features of the Pomeron exchange:

- Since a Pomeron carries the vacuum quantum numbers, the coefficients X^{ab} and $X^{\bar{a}b}$ should be equal. This could be extended to the cases for pp and pn data, namely $X^{pp} = X^{pn}$ (flavor-blind). A fit to pn data without this constraint gives $X^{pn} = 22.15$, which is almost equal to X^{pp}.

- The ratio of the coefficients X for πp and pp scattering is equal to 0.63, which is very close to the value $2/3$ of the "addictive quark rule". This means that a Pomeron couples to single quarks inside a hadron separately, and that the total cross sections is, to a good approximation, given by the sum of the quark-quark cross sections for each valence quark of two colliding hadrons.

- The magnitude of the Pomeron contribution to Kp scattering is a little less than that to πp scattering; namely, the coupling of a Pomeron to a strange quark is about 70% of that to a light (u, d) quark.

---

[30]It has been proven individually by Froissart [146] and Martin [147] that the total cross section for hadron-hadron collision can never grow with energy faster than $\ln^2 s$.
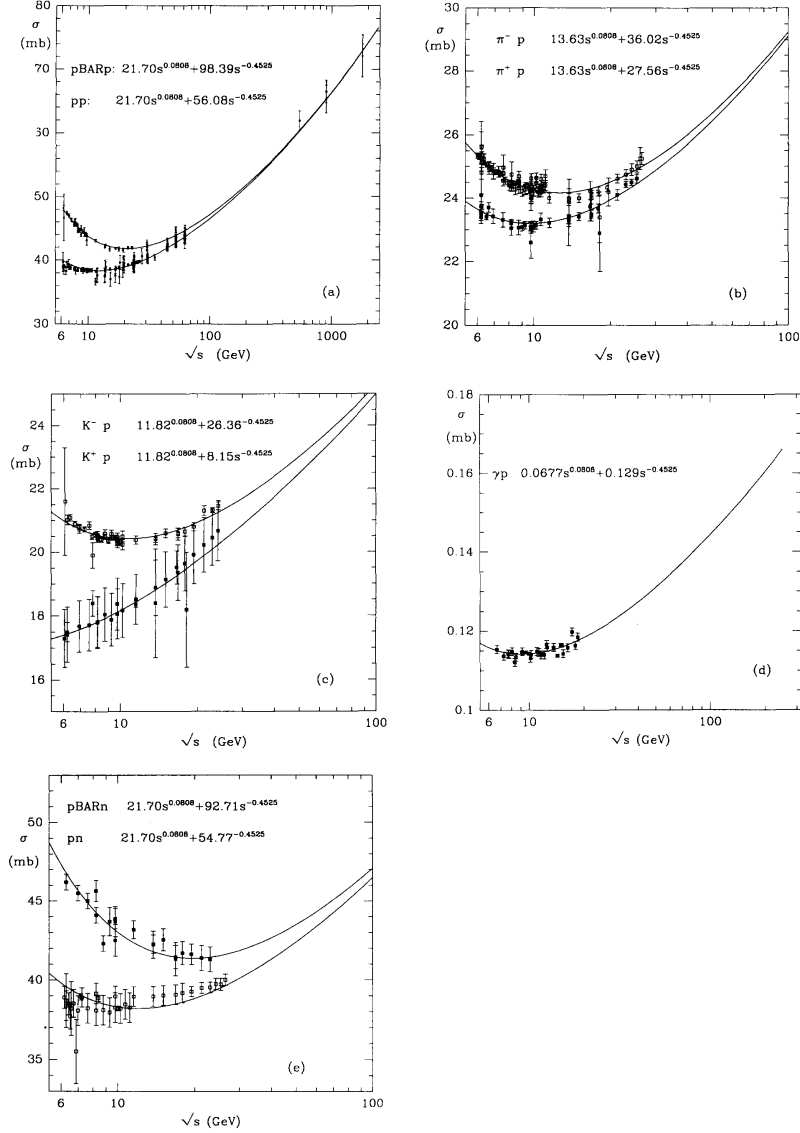
Figure A.2:   Total cross sections as a function of the total energy $\sqrt{s}$ for (a) $\bar{p}p$ and pp scattering, (b) $\pi^- p$ and $\pi^+ p$ scattering, (c) $K^- p$ and $K^+ p$ scattering, (d) γp scattering, and (e) $\bar{p}n$ and pn scattering. Solid curves are the fits to the data by Eq. (A.5). The figures are taken from Ref. [17].
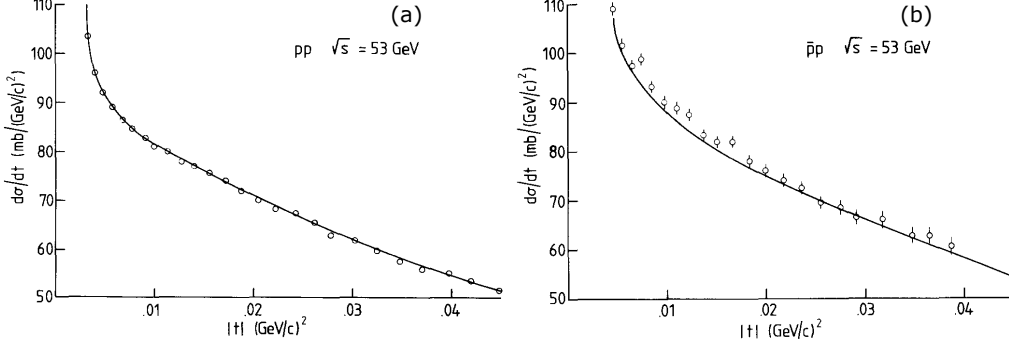
Figure A.3: Differential cross sections for elastic (a) pp and (b) $\bar{p}p$ scatterings as a function of the momentum transfer $|t|$ at small $|t|$ for $\sqrt{s} = 53$ GeV. Solid curves represent a Pomeron exchange model including the Coulomb (photon) exchange, which is responsible for a rise at very small $|t|$. The figures are taken from Ref. [148].

To determine the Pomeron slope $\alpha'_{\mathbb{P}}$, elastic pp and $\bar{p}p$ scattering data were also analyzed [18,148–150]. Since the Pomeron intercept $\alpha_{\mathbb{P}}(0)$ is nearly equal to 1, the coupling of a Pomeron to a quark would be vector-like at small $|t|$, so that the amplitude for quark-quark scattering can be written as

$$\mathcal{A}_{\mathbb{P}}^{qq}(s,t) \sim C_{\mathbb{P}}(\bar{u}_3\gamma^\mu u_1)(\bar{u}_4\gamma_\mu u_2) \left(\frac{s}{s_0}\right)^{\alpha_{\mathbb{P}}(t)} \exp\left(-\frac{i}{2}\pi\alpha_{\mathbb{P}}(t)\right), \qquad (\text{A.8})$$

where $C_{\mathbb{P}} = s_0\beta_{\mathbb{P}}^2$ is a constant, which determines the strength of the Pomeron-quark coupling, u_i ($\bar{u}_i$) denotes the Dirac spinors, γ^μ denotes the Dirac gamma matrices, and s_0 is an energy scale for long-distance strong interactions, which is set to $s_0 = 1/\alpha'_{\mathbb{P}}$[31]. For pp and $\bar{p}p$ scattering, one needs to consider the wave function of the valence quarks inside a nucleon, leading to some form factor as a consequence of elastic scattering processes. The analogy of the Pomeron-quark coupling with the photon-quark coupling, i.e. a γ^μ coupling, leads to the conjecture that this form factor would be the elastic Dirac form factor $F_1(t)$ for proton[32], so that the differential cross sections for

---

[31]The energy scale s_0 was originally taken to be the nucleon mass, but it was found that this choice, i.e. $s_0 = (\alpha'_{\mathbb{P}})^{-1}$, gives a better description of $\bar{p}p$ scattering [148].

[32]There exist two kinds of form factor; the Dirac form factor $F_1(t)$ and the Pauli form factor $F_2(t)$. These form factors have been measured in ep scattering, and the former is

elastic pp and $\bar{p}p$ scattering at small $|t|$ are given by

$$\frac{d\sigma}{dt} = \frac{[3\beta_{\mathbb{P}}F_1(t)]^4}{4\pi}(\alpha'_{\mathbb{P}}s)^{2(\epsilon_{\mathbb{P}}+\alpha'_{\mathbb{P}}t)}, \tag{A.9}$$

where a factor of 3 in the numerator arises from the addictive quark rule, and $\epsilon_{\mathbb{P}} = \alpha_{\mathbb{P}}(0) - 1$. The values of $\beta_{\mathbb{P}}$ and $\epsilon_{\mathbb{P}}$ are known from total cross section data, so the only free parameter is $\alpha'_{\mathbb{P}}$. The value of $\alpha'_{\mathbb{P}}$ was determined by fitting small-$|t|$ elastic pp and $\bar{p}p$ scattering data with Eq. (A.9) to be

$$\alpha'_{\mathbb{P}} = 0.25 \text{ GeV}^{-2}, \tag{A.10}$$

as shown in Fig. A.3. Donnachie and Landshoff extended the formula of Eq. (A.9) to larger $|t|$ data, and found that the formula also works well [148]. Further, it was found that formulae such as Eq. (A.9) (i.e. a Pomeron couples to a quark through a γ^μ coupling with a strength proportional to isoscalar elastic form factors.), together with the parameters of Pomeron trajectory, are also applicable to other high-energy reactions involving the Pomeron exchange [150, 152].

At small $|t|$, the differential cross sections for elastic pp and $\bar{p}p$ scattering are often parametrized by an exponential form, namely $(d\sigma/dt)_0 e^{-b|t|}$, where $(d\sigma/dt)_0$ is the differential cross section at $t = 0$ and b is a slope parameter. By comparing Eq. (A.9) with an exponential form, taking the natural logarithm of them, and solving it with respect to b, then one obtains

$$b = 2b_0 + 2\alpha'_{\mathbb{P}} \ln(\alpha'_{\mathbb{P}}s), \tag{A.11}$$

where b_0 is the slope for the Dirac form factor $|F_1(t)|^2$ at small $|t|$. Eq. (A.11) says that the slope b becomes larger as the energy s grows: this is just the "shrinkage" mechanism of the forward peak, as mentioned in Sect. 1.2.

---

responsible for helicity-nonflip processes and the latter for helicity-flip processes. In ep scattering, the exchanged particle is a photon, which has $C = -1$, not $C = +1$ for a Pomeron. To overcome this, it is simply assumed that the $C = +1$ and $C = -1$ form factors are the same. Further, it is assumed that the Pomeron exchange does not flip the nucleon helicity because the isoscalar part of $F_2(t)$ (the sum of $F_2(t)$ for proton and neutron), which is at $t = 0$ the sum of the anomalous magnetic moments of proton and neutron, is small. In fact, the smallness of $F_2(t)$ for the Pomeron exchange was turned out to be true [151]. For neutron, F_1 is, by definition, 0 at $t = 0$, and remains small away from $t = 0$. Accordingly, the form factor for the Pomeron-nucleon vertex is the $F_1(t)$ for proton.

A.3   Pomeron and glueball trajectories

According to Regge theory, Regge trajectories describing scattering processes should be also connected to physical hadron states. In fact, as you can see from Fig. A.1, all the experimentally observed hadronic resonances (both mesons and baryons) belong to Regge trajectories with an universal slope of $\alpha' \approx 0.9$ GeV^2 but a different intercept of $\alpha(0) \lesssim 0.5$. Therefore, one question naturally arises: *what are the physical particles lying on Pomeron trajectory?*

Since the Pomeron slope ($\alpha'_{\mathbb{P}} = 0.25$ GeV^{-2}) is quite different from the universal ones for meson trajectories, the physical particles on Pomeron trajectory cannot be associated with the usual flavor-singlet mesons. This leads to one conjuncture that the physical particles on Pomeron trajectory would be gluonic objects. The signature of Pomeron trajectory must be even because the signature term in Eq. (A.3), which determines the phase of the amplitude, with odd signature $\eta = -1$ has zero imaginary part at $t = 0$. This can be verified by rewriting the signature term as

$$\frac{\left(1 + \eta e^{-i\pi\alpha(t)}\right)}{2\sin\pi\alpha(t)} = \begin{cases} \frac{\cos\frac{\pi\alpha(t)}{2} - i\sin\frac{\pi\alpha(t)}{2}}{2\sin\frac{\pi\alpha(t)}{2}} & (\eta = +1) \\ \frac{\sin\frac{\pi\alpha(t)}{2} + i\cos\frac{\pi\alpha(t)}{2}}{2\cos\frac{\pi\alpha(t)}{2}} & (\eta = -1), \end{cases} \tag{A.12}$$

and substituting $\alpha_{\mathbb{P}}(t) = 1$ ($t \to 0$). Thus, the lowest physical state would be a tensor ($J^{PC} = 2^{++}$) glueball[33] with a mass of $M \sim 2$ GeV.

Interestingly, there are some experimentally observed tensor ($J^{PC} = 2^{++}$) states around a mass of 2 GeV: e.g., $f_2(1950)$ and $f_J(2220)$. While $f_2(1950)$ is a well-established state [153] and is located very close to Pomeron trajectory in the M^2–J plane (a Chew-Frautschi plot), $f_J(2220)$, alternatively known as $\xi(2230)$, is of particular interest for some reasons: (i) Its mass is well consistent with lattice QCD calculations for the tensor glueball [50–56]. (ii) A narrow decay width of ~ 23 MeV cannot be explained by $q\bar{q}$ mesons, multiquark states and $q\bar{q}g$ hybrids, and is consistent with a naive estimate of the width for a tensor glueball (~ 20 MeV) [154]. (iii) The decays of $f_J(2220)$ to K^+K^-, $\pi^+\pi^-$ and $\pi^0\pi^0$ are flavor-symmetric [155, 156]. (iv) The coupling of $f_J(2220)$ to a photon is very small[34] [157]. These experimental facts naturally

---

[33]A state with $J = 0$ is not a physical particle and would belong to its daughter trajectories because $M^2 = -\alpha_{\mathbb{P}}(0)/\alpha'_{\mathbb{P}} < 0$ for $J = \alpha_{\mathbb{P}}(t = M^2) = 0$

[34]Since gluons have no intrinsic charge, their coupling to a photon should be small.

lead to the expectation that $f_J(2220)$ may be the lightest tensor glueball, although positive results were obtained solely from the radiative decays of J/ψ [155,156,158] but none from $p\bar{p}$ annihilation (see Ref. [159] and therein).

Appendix B   Detector calibration

Physical quantities such as the time-of-flight and momentum of forward-going charged particles were obtained from raw data through an off-line analysis program with appropriate input parameters. In this appendix, the calibration for each detector system (the tagging counters, the TOF counters and the DCs) is described.

B.1   TOF calibration

A time-of-flight (ΔT_{TOF}) is given by the time difference between start time (T_{start}) and stop time (T_{stop}) as

$$\Delta T_{\mathrm{TOF}} = T_{\mathrm{stop}} - T_{\mathrm{start}}. \tag{B.1}$$

In the LEPS experiment, T_{stop} is obtained from the timing information of the TOF counters, whereas T_{start} is obtained in two different ways: the one uses the timing information of the RF signals ($T_{\mathrm{start}}^{\mathrm{RF}}$, and $\Delta T_{\mathrm{TOF}}^{\mathrm{RF}} \equiv T_{\mathrm{stop}}^{\mathrm{RF}} - T_{\mathrm{stop}}$), and the other uses the timing information of the FWD counters ($T_{\mathrm{start}}^{\mathrm{FWD}}$, and $\Delta T_{\mathrm{stop}}^{\mathrm{FWD}} \equiv T_{\mathrm{stop}}^{\mathrm{FWD}} - T_{\mathrm{start}}$). The former one provides a better timing resolution due to a good timing resolution of the RF signals (12 ps).

Since the circulating electrons are bunched according to the RF signal, the collision time of a laser photon and an electron, i.e., the arrival time of a BCS photon at the target[35], is synchronized with the RF signal. Therefore, one can use the timing information of the RF signal as start timing. Figure B.1(a) shows a scatter plot for the ADC channel of TAG-PL versus the difference between the TDC channels of the RF signal and TAG-PL. There exist loci with an interval of $\sim$ 40 channels, corresponding to the time interval of successive electron bunches ($\sim$ 2 ns). You also see a correlation between the ADC and TDC channels. To obtain a better separation between two adjacent loci, a time-walk correction was applied to the TDCs of each TAG-PL counter as follows:

$$T_{\mathrm{TAG\text{-}PL}} = \left(TDC_{\mathrm{TAG\text{-}PL}} - \frac{P1}{\sqrt{ADC_{\mathrm{TAG\text{-}PL}}}} - \frac{P2}{ADC_{\mathrm{TAG\text{-}PL}}} - P3 \right)$$
$$\times\, 0.025, \tag{B.2}$$

---

[35]The speed of light c is constant. Therefore, the collision time and the arrival time are equivalent.

where $TDC_{\text{TAG-PL}}$ and $ADC_{\text{TAG-PL}}$ represent the TDC and ADC channels of a TAG-PL counter, respectively, *P1* and *P2* are free parameters, and *P3* is an offset to compensate for differences in TDC channel between every counters, being also a free parameter. A factor of 0.025 represents the timing resolution of TDC modules (0.025 ns/ch). Figure B.1(b) shows a scatter plot for the ADC channel of TAG-PL versus the TDC difference between the RF signal and TAG-PL after the correction. The correlation between the ADC and TDC channels disappears. The timing resolution of TAG-PL was evaluated by projecting the two-dimensional plot [Fig. B.1(b)] onto the x-axis and fitting a peak with a Gaussian function. Figure B.2 shows the timing resolution of TAG-PL. A timing resolution of < 300 ps was achieved for all slats, and is good enough for distinguishing an individual electron bunch ($\lesssim 400$ ps).
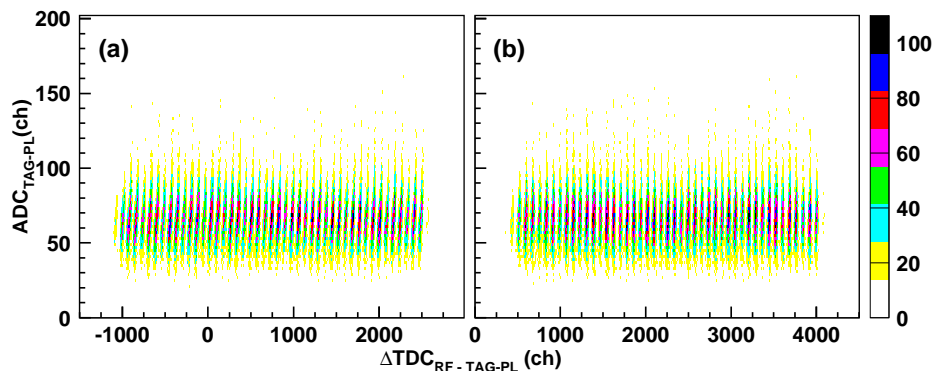
Figure B.1:   Scatter plots for the ADC channel of TAG-PL ($ADC_{\text{TAG-PL}}$) versus the TDC difference between the RF signal and TAG-PL ($\Delta TDC_{\text{RF}-\text{TAG-PL}} = TDC_{\text{RF}} - TDC_{\text{TAG-PL}}$) (a) before and (b) after a time-walk correction. One channel of the TDC channels corresponds to 0.025 ns.

To obtain a good resolution in time-of-flight measurements, a time-walk correction was also applied to the TOF counters. For this correction, charged-pion tracks were selected as $|pm2| < 0.15$ GeV^2, where *pm2* represents the square of the reconstructed mass by the LEPS spectrometer. Once a pion track is selected, the time-of-flight between the reaction vertex point and the TOF wall can be calculated from the track information (the momentum and
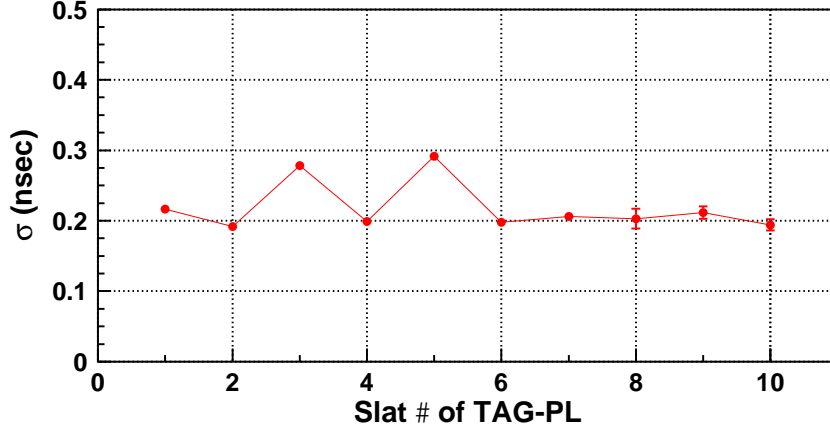
Figure B.2:   Timing resolution σ (nsec) of TAG-PL.

path length of a track) as

$$\Delta T_{\mathrm{TOF}}^{\mathrm{trk}} = L \times \frac{\sqrt{\boldsymbol{p}^2 + m_\pi^2}}{|\boldsymbol{p}|}, \tag{B.3}$$

where L is the flight length between the reaction vertex and the TOF wall, $\boldsymbol{p}$ is the 3-momentum of a pion track and m_π is the pion mass. Since the timing resolution of $\Delta T_{\mathrm{TOF}}^{\mathrm{trk}}$ is much better than that of $\Delta T_{\mathrm{TOF}}^{\mathrm{RF}}$ [36], $\Delta T_{\mathrm{TOF}}^{\mathrm{trk}}$ can be used as a timing reference. A correction function for the TOF counters is given by

$$\begin{aligned}\Delta T_{\mathrm{TOF}}^{\mathrm{RF;\ cor.}} =& \Delta T_{\mathrm{TOF}}^{\mathrm{RF}} \\ &- \left(P1 + \frac{P2}{\sqrt{ADC_{\mathrm{TOF}}^{\mathrm{top}}}} + \frac{P3}{\sqrt{ADC_{\mathrm{TOF}}^{\mathrm{bot.}}}} \right) \times 0.025, \end{aligned} \tag{B.4}$$

where $ADC_{\mathrm{TOF}}^{\mathrm{top}}$ and $ADC_{\mathrm{TOF}}^{\mathrm{bot.}}$ represent the ADC channels of the top and bottom PMTs, respectively, $P1$, $P2$ and $P3$ are free parameters, and a factor of 0.025 represents the timing resolution of TDC modules. Figures B.3(a) and (b) show correlation plots between the time difference $(= \Delta T_{\mathrm{TOF}}^{\mathrm{RF}} - \Delta T_{\mathrm{TOF}}^{\mathrm{trk}})$

---

[36]For typical 1 GeV/c pions, the momentum resolution of the LEPS spectrometer is $\delta p/p \sim 0.9\%$. Therefore, the timing resolution of $\Delta T_{\mathrm{TOF}}^{\mathrm{trk}}$ is estimated from Eq. (B.3) to be ~ 3 psec for 1 GeV/c pions.

and the ADC channel of the top/bottom PMT before and after the correction, respectively. You see no correlation between the ADC channel and the time difference after the correction. Figure B.4 shows the timing resolution of the TOF counters, which was evaluated from one-dimensional distributions of the time difference. A typical timing resolution of the TOF counters was estimated to be ~ 150 ps.
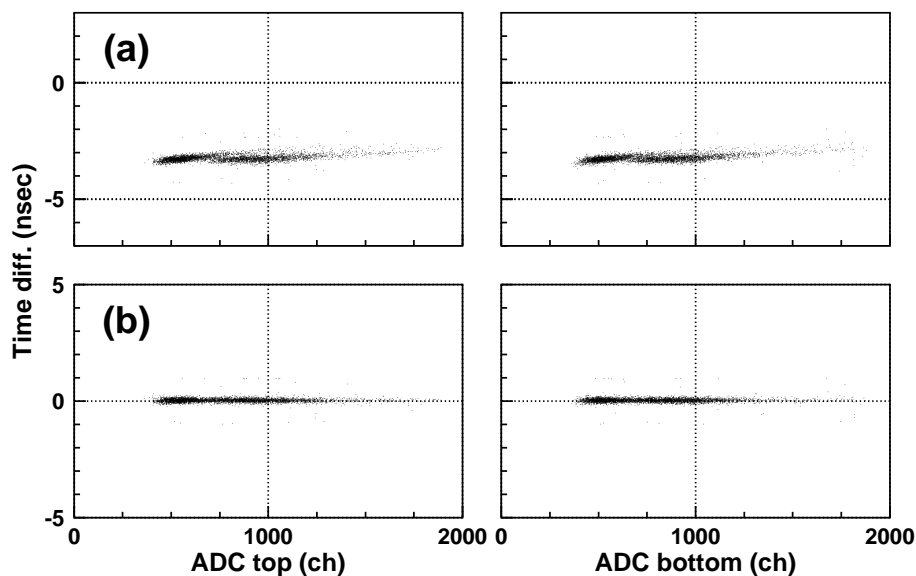
Figure B.3: Correlation between the time difference and the ADC channel of the top/bottom PMT (left/right figures) for the TOF counter (a) before and (b) after a time-walk correction.

A time offset for time-of-flight $(\Delta T_{\mathrm{TOF}}^{\mathrm{RF}})$ measurements, a so-called $t0$ parameter, was determined so that the square of the reconstructed mass for pion tracks peaked at the nominal value independently of the momentum. Figure B.5(a) and (b) show the run dependence of the peak position of the reconstructed mass squared for pion and proton tracks, respectively. For all the runs, the peak positions for pion and proton tracks are close to the nominal values (0.02 and 0.88 for pions and protons, respectively).

The timing information of the FWD counters were also used as start timing in time-of-flight measurements instead of that of the RF signals. Therefore, a time-walk correction, as well as the adjustment of $t0$ parameters, was made in the same manner as those for the TOF counters. Figures B.6(a) and

159
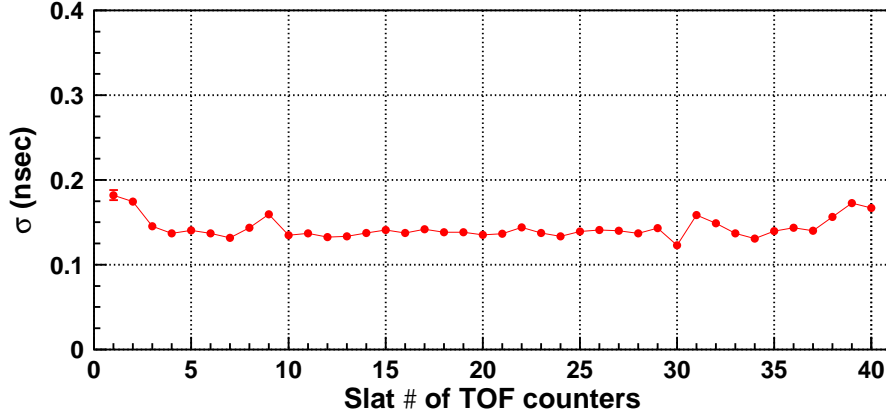
Figure B.4:   Timing resolution of the TOF counters.

(b) show correlation plots between the time difference ($= \Delta T_{\text{TOF}}^{\text{FWD}} - \Delta T_{\text{TOF}}^{\text{trk}}$) and the ADC channel of the left/right PMT before and after the correction, respectively. Obviously, a correlation disappears after the correction. The timing resolution of $\Delta T_{\text{TOF}}^{\text{FWD}}$ was evaluated by fitting a one-dimensional distribution of the time difference with a Gaussian function. Table B.1 summarizes the timing resolution of $\Delta T_{\text{TOF}}^{\text{FWD}}$, together with the intrinsic resolution of the FWD counters. The FWD counters have a good timing resolution (~ 150 ps) as a trigger counter. The $t0$ parameters for the FWD counters were determined so that a distribution of the time difference between $\Delta T_{\text{TOF}}^{\text{FWD}}$ and $\Delta T_{\text{TOF}}^{\text{trk}}$ peaked at zero after the time-walk correction. Figure B.7(a) and (b) show the run dependence of the mean value of the time difference ($= \Delta T_{\text{TOF}}^{\text{FWD}} - \Delta T_{\text{TOF}}^{\text{trk}}$) for the FWD counters #1 and #2, respectively.

Table B.1: Timing resolution of $\Delta T_{\text{TOF}}^{\text{FWD}}$ ($\sigma_{\text{TOF}}^{\text{FWD}}$) and the intrinsic timing resolution of the FWD counters ($\sigma_{\text{intr}}^{\text{FWD}}$). The intrinsic resolution is estimated by assuming the intrinsic resolution of the TOF counters to be 150 ps.

FWD ID	$\sigma_{\text{TOF}}^{\text{FWD}}$ (ps)	$\sigma_{\text{intr}}^{\text{FWD}}$ (ps)
#1	225 ± 3	167
#2	211 ± 3	148

160
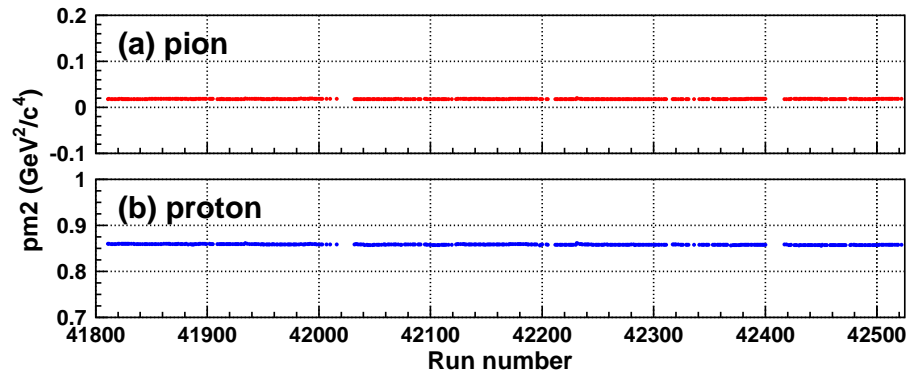
Figure B.5:   Run dependence of the peak position of the reconstructed mass squared (a) for pion and (b) proton tracks.
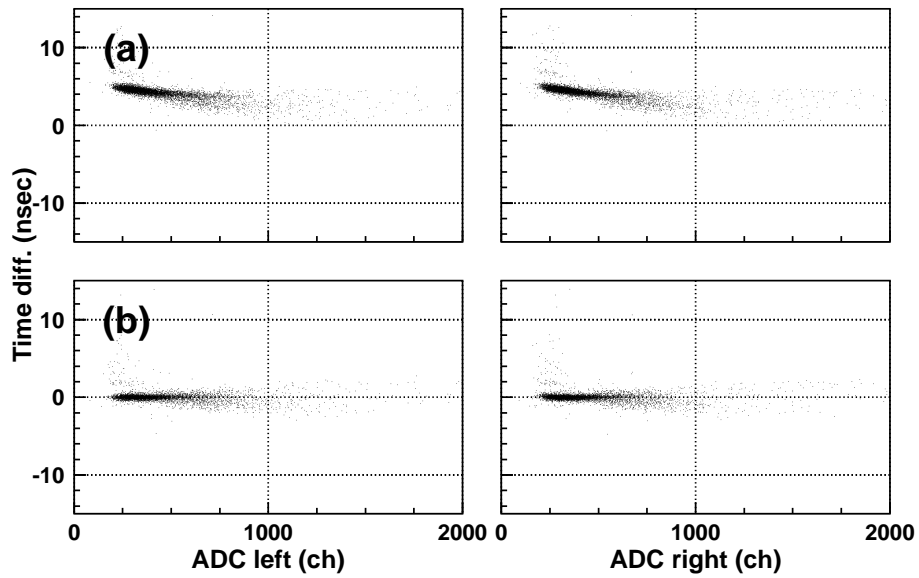
Figure B.6:   Correlation between the time difference and the ADC channel of the left/right PMT (left/right figures) for the FWD counter (a) before and (b) after a time-walk correction.
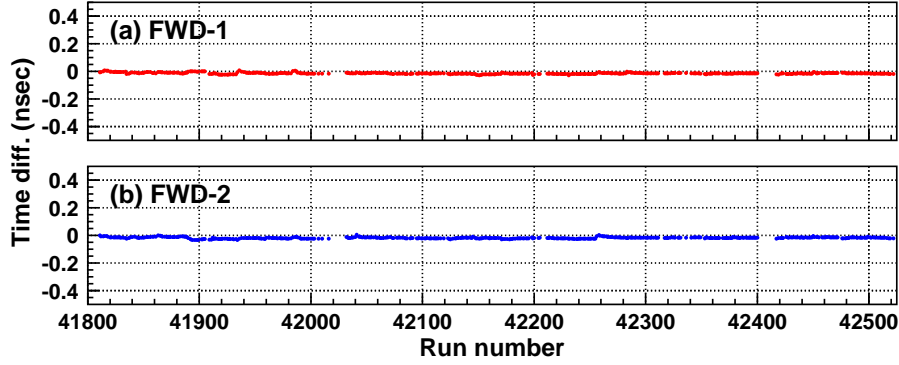
Figure B.7:   Run dependence of the mean value of the time difference ($=$ $\Delta T_{\mathrm{TOF}}^{\mathrm{FWD}} - \Delta T_{\mathrm{TOF}}^{\mathrm{trk}}$) for the FWD counters (a) #1 and (b) #2.

B.2 DC calibration

The trajectories of forward-going charged particles were reconstructed from the hit information of the multi-wire drift chambers (DC0, DC1, DC2 and DC3). To obtain hit-positions, the leading edge timing of the signals from fired wires was collected. A drift time t_{drift} was determined from the time difference between a timing offset T_0 and leading edge timing T, which is given by

$$t_{\mathrm{drift}} = -(T - T_0) \times 0.5 \text{ ns/ch.} \tag{B.5}$$

A drift length was calculated from the drift time t_{drift} through a x-t function (curve), which is given by

$$x_{\mathrm{drift}} = c_1 t_{\mathrm{drift}} + c_2 t_{\mathrm{drift}}^2 + c_3 t_{\mathrm{drift}}^3, \tag{B.6}$$

where c_1, c_2 and c_3 are the parameters for a x-t curve to be determined. The timing offsets T_0 were determined channel by channel (wire by wire), whereas the x-t curves (c_1, c_2 and c_3) were determined plane by plane.

Figure B.8 shows a typical TDC distribution of the DCs. The edge of the distribution corresponds to the timing offset T_0. The offsets T_0 for each wire were determined by fitting the TDC distributions with an error function (a Gaussian-convoluted step function), as indicated by a blue curve in the figure.

The x-t curves for each plane were determined from a relation between the drift time calculated by Eq. (B.5) and the drift length obtained from tracks. Here, a track fit was performed without the corresponding plane. According

162

to Ref. [112], the x-t curves were made for six incident angles of tracks, θ_{trk}, to obtain a better spatial resolution: $0 \leq \theta_{\text{trk}} < 5°$, $5 \leq \theta_{\text{trk}} < 10°$, $10 \leq \theta_{\text{trk}} < 15°$, $15 \leq \theta_{\text{trk}} < 20°$, $20 \leq \theta_{\text{trk}} < 25°$ and $\theta_{\text{trk}} \geq 25°$. Figure B.9 shows a typical correlation plot between the drift length and the drift time. The parameters c_1, c_2 and c_3 were determined by fitting such correlation plots with Eq. (B.6), as indicated by a blue curve in the figure.

The spacial resolution of the DCs was estimated plane by plane with the same method as described in Ref. [112]: let us consider, as an example, the intrinsic resolution for the DC1X1 plane (σ_{X1}). The width of the residual (σ_{res}) between the drift length determined from the TDC information and that from a track[37] is given by

$$\sigma_{\text{res}} = \sqrt{\sigma_{\text{X1}}^2 + \sigma_{\text{trk}}^2}, \tag{B.7}$$

where σ_{trk} represents a width due to track fits. Since σ_{trk} is common to the paired X1 and X2 planes (see Fig. 3.9 in Ref. [112]), its contribution could be canceled out by calculating the difference between the residuals for the X1 and X2 planes event by event. Consequently, the width of such a distribution (σ_{diff}) is given by

$$\sigma_{\text{diff}} = \sqrt{\sigma_{\text{X1}}^2 + \sigma_{\text{X2}}^2}, \tag{B.8}$$

where σ_{X2} is the intrinsic resolution for the X2 plane. By assuming that $\sigma_{\text{X1}} = \sigma_{\text{X2}}$, Eq. (B.8) can be rewritten as

$$\sigma_{\text{X1}} = \frac{1}{\sqrt{2}}\sigma_{\text{diff}}. \tag{B.9}$$

Thus, an approximate value of σ_{X1} can be obtained from the data. On the other hand, σ_{trk} can be evaluated by MC simulation with the approximate value of σ_{X1} as an input. As a result, σ_{X1} can be calculated by Eq. (B.7). Note that the resolutions for the planes which have no paired plane (i.e. DC1X3 and the V-planes) were evaluated in a different way[38] after the evaluations for the X- and U-planes. Figure B.10 shows the intrinsic resolution for each plane for two different periods (2008B and 2009A cycles). A spacial resolution of

---

[37]Of course, a track fit is performed without the corresponding plane (i.e., DC1X1)

[38]The widths σ_{trk} for DC1X3 and all the V-planes were evaluated simultaneously by MC simulation, in which the corresponding planes are not used in track fits. The intrinsic resolutions for each plane can be then calculated by Eq. (B.7)

$\lesssim 250\ \mu$m was achieved for all the planes, which is consistent with the LEPS 2006/2007 data [112].

The run dependence of the width (σ) of the residual distributions for various DC planes is shown in Fig. B.11. Note that the corresponding plane was included in the track fits for this evaluation. Figure B.12 shows the run dependence of the mean value of a χ^2 probability distribution in track fits. A mean value of $\gtrsim 0.5$ is achieved for all runs.
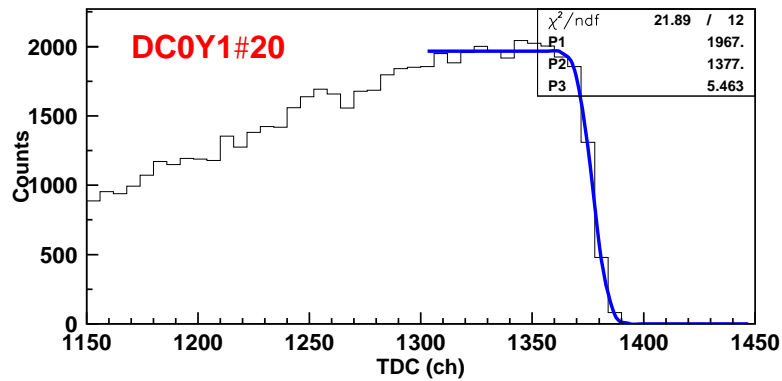
Figure B.8:   TDC distribution for the DC0Y1-#20 wire. A blue curve represents the fit to the data by an error function.
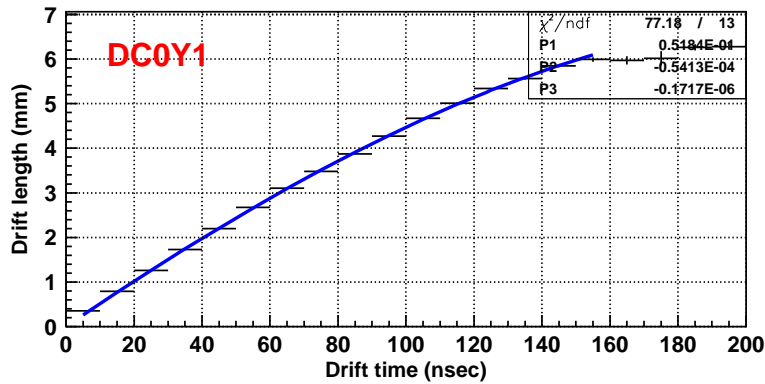
Figure B.9:   Relation between the drift length obtained from tracks and the drift time calculated by Eq. (B.5) for the DC0Y1 plane. A blue curve represents the fit to the data by Eq. (B.6).
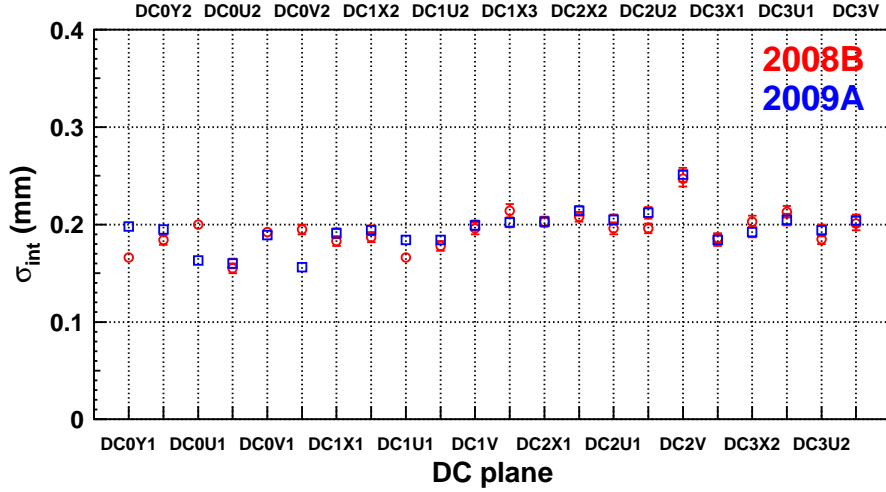
Figure B.10:   Intrinsic spatial resolution for the DC planes. Red open circles show the 2008B data, whereas blue open squares show the 2009B data.
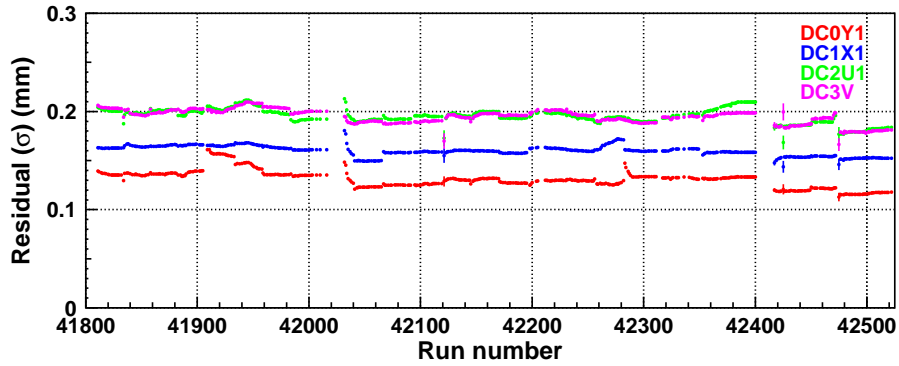
Figure B.11:   Run dependence of the width (σ) of the residual distributions for DC0Y1 (red), DC1X1 (blue), DC2U1 (green) and DC3V (pink). Here, the corresponding plane is included in track fits.

165
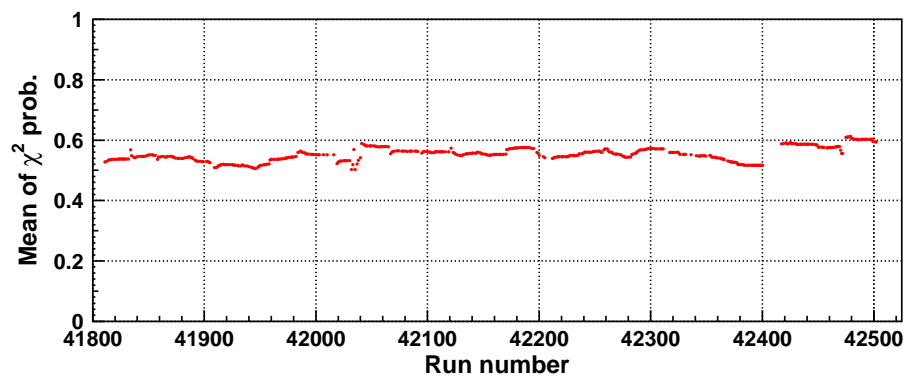
Figure B.12:   Run dependence of the mean value of a χ^2 probability distribution in track fits.

Appendix C   DC alignment

The alignment parameters for the DCs were basically determined from e^+e^- data without the magnetic field, which were taken before and after the experiment. During the experiment, however, DC0 and DC1 were moved twice to repair DC1. Therefore, the alignment parameters for DC0 and DC1 were tuned using the LH$_2$ data with the magnetic field.

The relative shifts and rotations for each wire plane were tuned by requiring the mean values of the residual distributions for each wire plane to be close to zero, whereas the global positions and rotations for each drift chamber (DC0 and DC1) were tuned by looking at the missing-mass peaks for the $p(\gamma, K^+)\Lambda(1116)$, $p(\gamma, K^+)\Sigma(1192)$, $p(\gamma, K^+)\Lambda(1520)$ and $p(\gamma, \pi^+\pi^-)p$ reactions. Figures C.1(a) and (b) show two-dimensional plots for the reconstructed mass squared versus the momentum, together with the boundaries for the kaon and pion identifications, respectively. In the kaon/pion identification, the square of the reconstructed mass was required to be within the $\pm 3\sigma$ regions, where σ is the momentum-dependent resolution of the reconstructed mass squared. For the kaon identification, besides the momentum-dependent boundaries, a boundary between pions and kaons was set at $0.16 \text{ GeV}^2/c^4$ as a straight line in order to reduce the pion contamination in a high-momentum region. Figures C.2(a) and (b) show missing mass distributions for the $p(\gamma, K^+)X$ and $p(\gamma, \pi^+\pi^-)X$ reactions, respectively. Clear peaks for Λ/Σ resonances and protons are seen.

Figures C.3(a) and (b) show the peak positions of the $\Lambda(1116)$, $\Sigma(1192)$ and $\Lambda(1520)$ hyperons as a function of the x and y-positions at DC1, respectively. Here, the peak positions for $\Lambda(1116)$ and $\Sigma(1192)$ were obtained simultaneously by fitting the spectra with two Gaussians plus a linear function, whereas the peak position for $\Lambda(1520)$ was obtained together with that for $\Lambda(1405)/\Sigma(1385)$ by the fits with two Gaussians plus a linear function. Figures C.4(a) and (b) show the peak position of protons as a function of the x and y-positions at DC1, respectively. The proton peak position was obtained by fitting the spectra with a Gaussian plus a linear function. To check the effects on positive-charged and negative-charged particles separately, it was required that $|\boldsymbol{p}_+| > 2|\boldsymbol{p}_-|$ ($|\boldsymbol{p}_-| > 2|\boldsymbol{p}_+|$) for the position dependence of π^+ (π^-), where $\boldsymbol{p}_+$ ($\boldsymbol{p}_-$) represents the 3-momentum of π^+ (π^-). There is no position dependence, and the peak positions for the hyperon resonances and protons are consistent with the PDG values.

Figure C.5(a) shows the peak positions of $\Lambda(1116)$, $\Sigma(1192)$ and $\Lambda(1520)$

167

as a function of the K^+ momentum, whereas Fig. C.5(b) shows the peak position of protons as a function of the π^+/π^- momentum. No momentum dependence is found, and all the peak positions are almost consistent with the PDG values within ± 1 MeV/c^2.
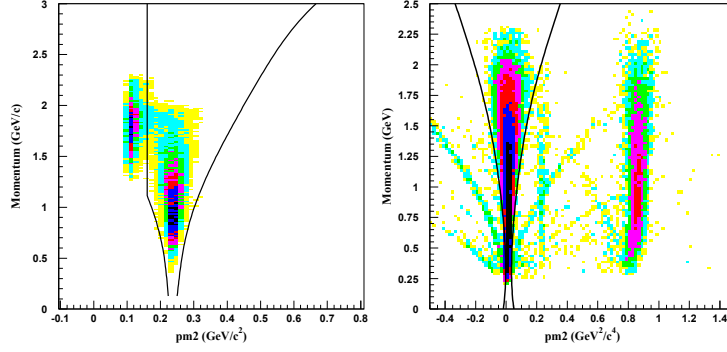
Figure C.1:   PID boundaries for (a) kaons and (b) pions in scatter plots for the momentum versus the reconstructed mass squared (*pm2*). A PID cut for kaons with this boundaries is applied after roughly selecting kaons by PID-FWD.
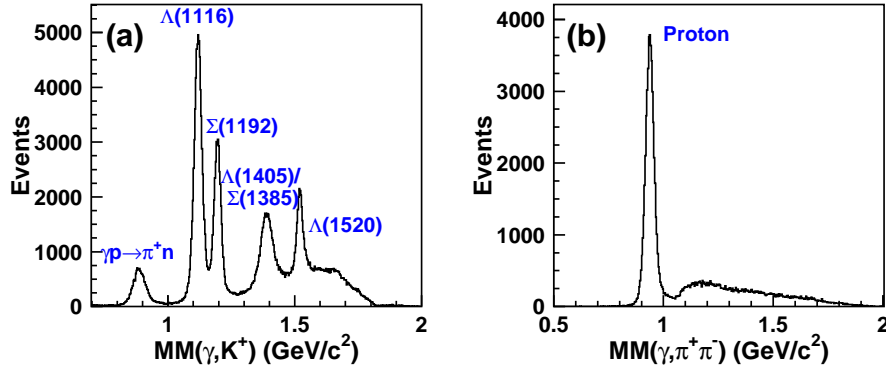
Figure C.2:   Missing mass distributions for the (a) $p(\gamma, K^+)X$ and (b) $p(\gamma, \pi^+\pi^-)X$ reactions.
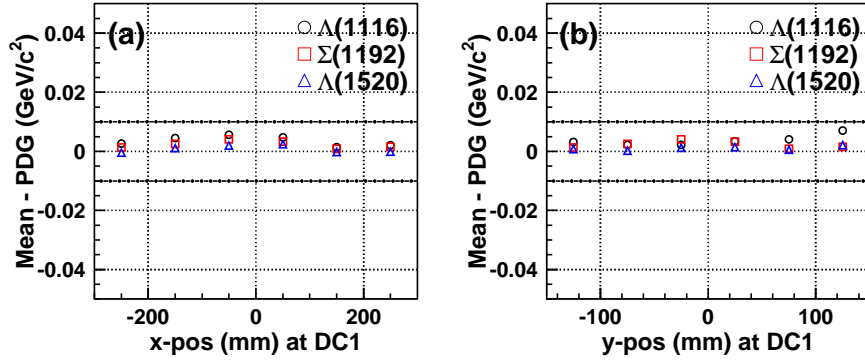
Figure C.3: Peak positions of $\Lambda(1116)$, $\Sigma(1192)$ and $\Lambda(1520)$ as a function of (a) the x-position and (b) the y-position at DC1. The values on the vertical axis are those after subtracting the PDG values. Horizontal dash-dotted lines correspond to a ± 1 MeV/c^2 deviation from the PDG value.
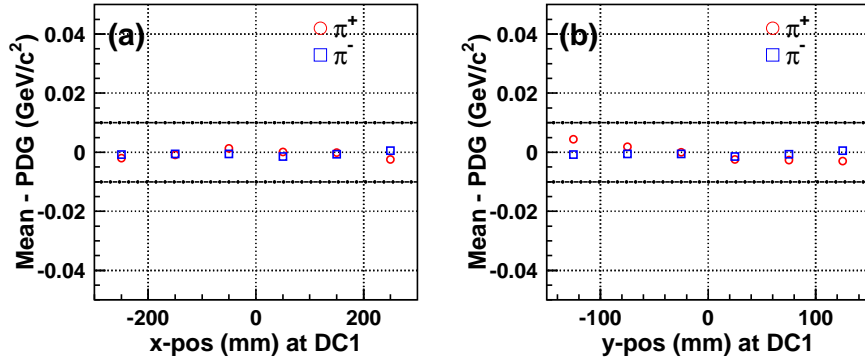
Figure C.4: Peak positions of protons as a function of (a) the x-position and (b) the y-position at DC1 for π^+ and π^- tracks. The values on the vertical axis are those after subtracting the PDG values. Horizontal dash-dotted lines correspond to a ± 1 MeV/c^2 deviation from the PDG value.
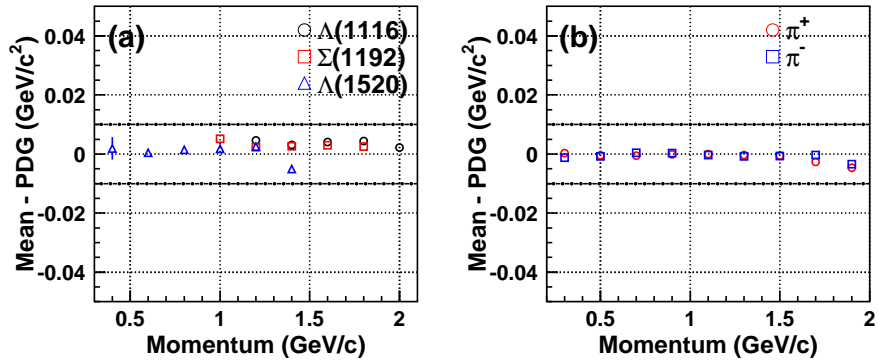
Figure C.5: (a) Peak positions of $\Lambda(1116)$, $\Sigma(1192)$ and $\Lambda(1520)$ as a function of the K^+ momentum. (b) Peak position of protons as a function of the π^+/π^- momentum. The values on the vertical axis are those after subtracting the PDG values. Horizontal dash-dotted lines correspond to a ± 1 MeV/c^2 deviation from the PDG value.

Appendix D   Photon energy resolution

The photon energy resolution was estimated as follows: let us consider the difference between the photon energy determined by the tagging system (E_γ) and that calculated by Eq. (3.8) or (3.9) (E_γ^{cal}):

$$\Delta E_\gamma = E_\gamma - E_\gamma^{\text{cal}}. \tag{D.1}$$

Here, the difference is calculated event by event. Then the width of the distribution of Eq. (D.1) is given by

$$\sigma_{\Delta E_\gamma} = \sqrt{\sigma_{E_\gamma}^2 + \sigma_{E_\gamma^{\text{cal}}}^2}, \tag{D.2}$$

where σ_{E_γ} is the photon energy resolution, and $\sigma_{E_\gamma^{\text{cal}}}$ is the resolution for the photon energy obtained from the $p(\gamma, K^+)\Lambda(1116)$ or $p(\gamma, \pi^+\pi^-)p$ reaction, which can be estimated by MC simulation. Here, $\sigma_{\Delta E_\gamma}$ can be evaluated from the LH$_2$ data, so the photon energy resolution σ_{E_γ} can be obtained from Eq. (D.2). In principle, σ_{E_γ} is determined by the size (width) of scintillation fibers, and should be independent of the photon energy. On the other hand, $\sigma_{E_\gamma^{\text{cal}}}$ depends on the momentum of K^+ or the $\pi^+\pi^-$ system, in other words, the photon energy [see Eqs. (3.8) and (3.9)]. Therefore, the intrinsic resolutions of the DCs (Appendix B.2) were worsened so that the photon energy dependence of σ_{E_γ} became flat.

Figure D.1(a) shows the $\sigma_{\Delta E_\gamma}$ obtained from the $p(\gamma, K^+)\Lambda(1116)$ reaction and the $\sigma_{E_\gamma^{\text{cal}}}$ estimated by MC simulation as a function of the photon energy. Figure D.1(b) shows the photon energy resolution calculated by Eq. (D.2) as a function of the photon energy. A flat dependence was obtained by worsening the intrinsic resolutions of the DCs by 30%. By averaging the obtained resolutions over the photon energy, the photon energy resolution was estimated to be 13.54 ± 0.05 MeV. Figures D.2(a) and (b) show the same plots for the $p(\gamma, \pi^+\pi^-)p$ reaction. In this case, a flat dependence was also obtained by worsening the intrinsic resolutions of the DCs by 30%. The average photon energy resolution was calculated to be 13.35 ± 0.06 MeV, which is consistent with that obtained from the $p(\gamma, K^+)\Lambda(1116)$ reaction.

In MC simulation, the photon energy resolution was set to $\sigma_{E_\gamma} = 13.5$ MeV.
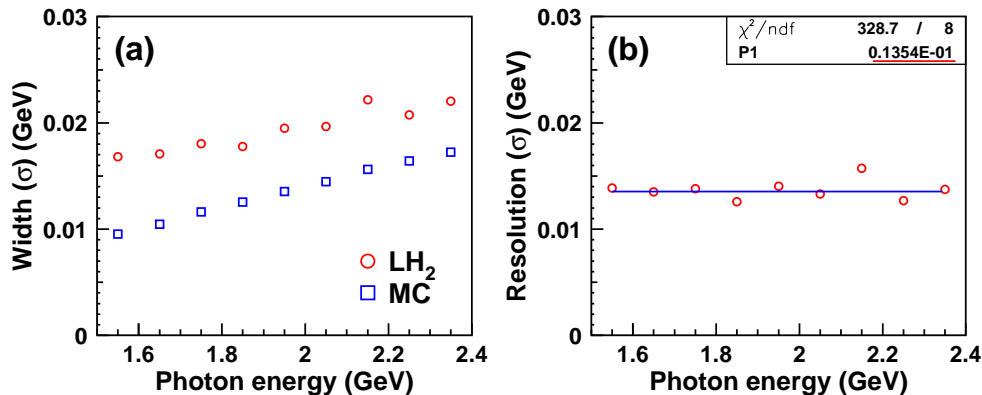
Figure D.1:   (a) The $\sigma_{\Delta E_\gamma}$ obtained from the $p(\gamma, K^+)\Lambda(1116)$ reaction (red open circles) and the $\sigma_{E_\gamma^{\mathrm{cal}}}$ estimated by MC simulation (blue open squares) as a function of the photon energy. (b) Photon energy resolution as a function of the photon energy. A blue line corresponds to the average value (13.54 ± 0.05 MeV).
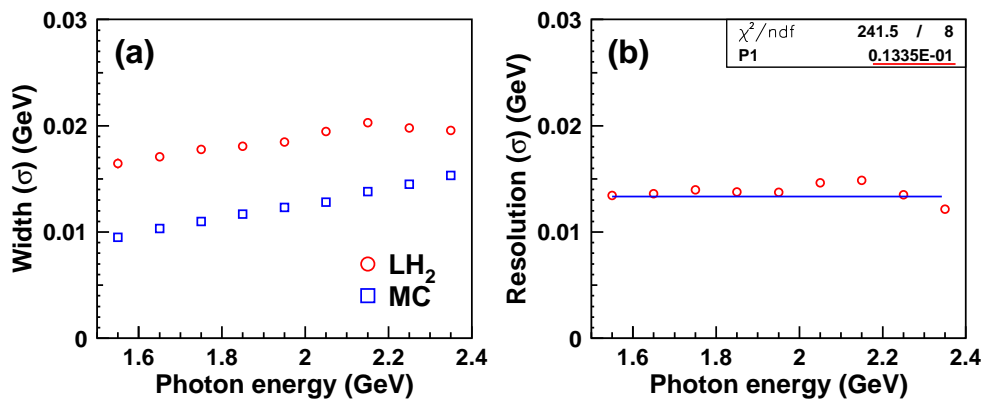
Figure D.2:   The $\sigma_{\Delta E_\gamma}$ obtained from the $p(\gamma, \pi^+\pi^-)p$ reaction (red open circles) and the $\sigma_{E_\gamma^{\mathrm{cal}}}$ estimated by MC simulation (blue open squares) as a function of the photon energy. (b) Photon energy resolution as a function of the photon energy. A blue line corresponds to the average value (13.35 ± 0.06 MeV).

Appendix E   DC efficiency

The efficiencies of the multi-wire drift chambers were evaluated channel by channel (wire by wire) from the data, and were taken into account in MC simulation.

The efficiency for the i-th wire of the a-plane is defined as

$$\text{Efficiency} = \frac{(\text{Number of hits in the } i\text{-th wire, judged from TDC info.})}{(\text{Number of hits in the } i\text{-th wire, predicted from tracks})}. \quad \text{(E.1)}$$

To select "good" events, it was required that $ntrk = 1$, $noutl = 0$, $prbchi2 > 0.02$ and $|ybar| > 30$ mm.

Figure E.1 shows the efficiencies of the wires in each DC planes for different data-taking periods (2008B and 2009A cycles). There is no significant difference between the data for two data-taking periods. Note that for the wires outside the spectrometer acceptance or those near the edge of the acceptance, the averaged value of the efficiencies for the corresponding plane was taken as an efficiency in MC simulation.

173
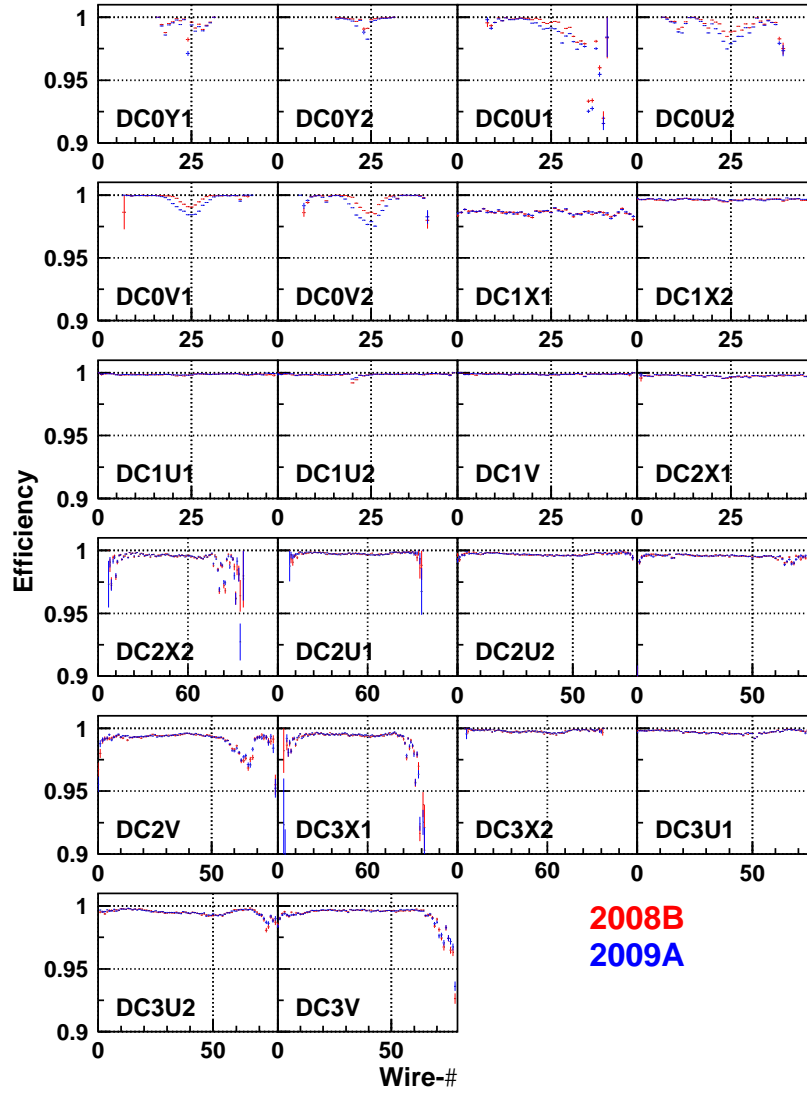
Figure E.1:   Efficiencies of the wires for each DC plane. Red and blue points show the data for the 2008B and 2009A cycles, respectively.

Appendix F   Missing mass resolution

The missing mass resolutions for the $p(\gamma, K^+)\Lambda(1116)$, $p(\gamma, K^+)\Sigma(1192)$, $p(\gamma, K^+)\Lambda(1520)$, $p(\gamma, \pi^+\pi^-)p$ and $p(\gamma, K^+K^-)p$ reactions were evaluated with the LH_2 data, and were compared with those obtained by MC simulations. Here, the photon energy resolution was set to 13.5 MeV in MC simulations (see Appendix D). As for the DC spatial resolutions, 30%-worsened values of the intrinsic resolutions were taken (see Appendices B.2 and D).

Figures F.1(a), (b), (c), (d) and (e) show the missing mass resolutions for the $p(\gamma, K^+)\Lambda(1116)$, $p(\gamma, K^+)\Sigma(1192)$, $p(\gamma, K^+)\Lambda(1520)$, $p(\gamma, \pi^+\pi^-)p$ and $p(\gamma, K^+K^-)p$ reactions, respectively, as a function of the photon energy. The MC data well reproduce the missing mass resolutions for all reactions. This validates the estimation of the photon energy resolution as well as the intrinsic spacial resolutions of the DCs (Appendices B.2 and D). In particular, the missing mass resolution for the $p(\gamma, K^+K^-)p$ reaction was found to be 12–14 MeV/c^2, which is important for reproducing missing mass distributions for the $^4\text{He}(\gamma, K^+K^-)X$ reaction.

By extending these MC studies to the case of a ^{4}He target, the missing mass resolution for the $^4\text{He}(\gamma, K^+K^-)^4\text{He}$ reaction was estimated. Figure F.2 shows the missing mass resolution for the $^4\text{He}(\gamma, K^+K^-)^4\text{He}$ reaction as a function of the photon energy. The missing mass resolution was found to be 14–17 MeV/c^2 in this case. The difference of the missing-mass resolutions between the γp and γ^4He reactions reflects the difference of the kinematics between the two reactions[39].

---

[39]In the $\gamma^4\text{He} \to K^+K^{-4}\text{He}$ reaction, the recoil momenta of ^{4}He nuclei are smaller due to the heavier target mass, compared to those in the $\gamma p \to K^+K^- p$ reaction. This results in larger momenta of K^+K^- pairs.
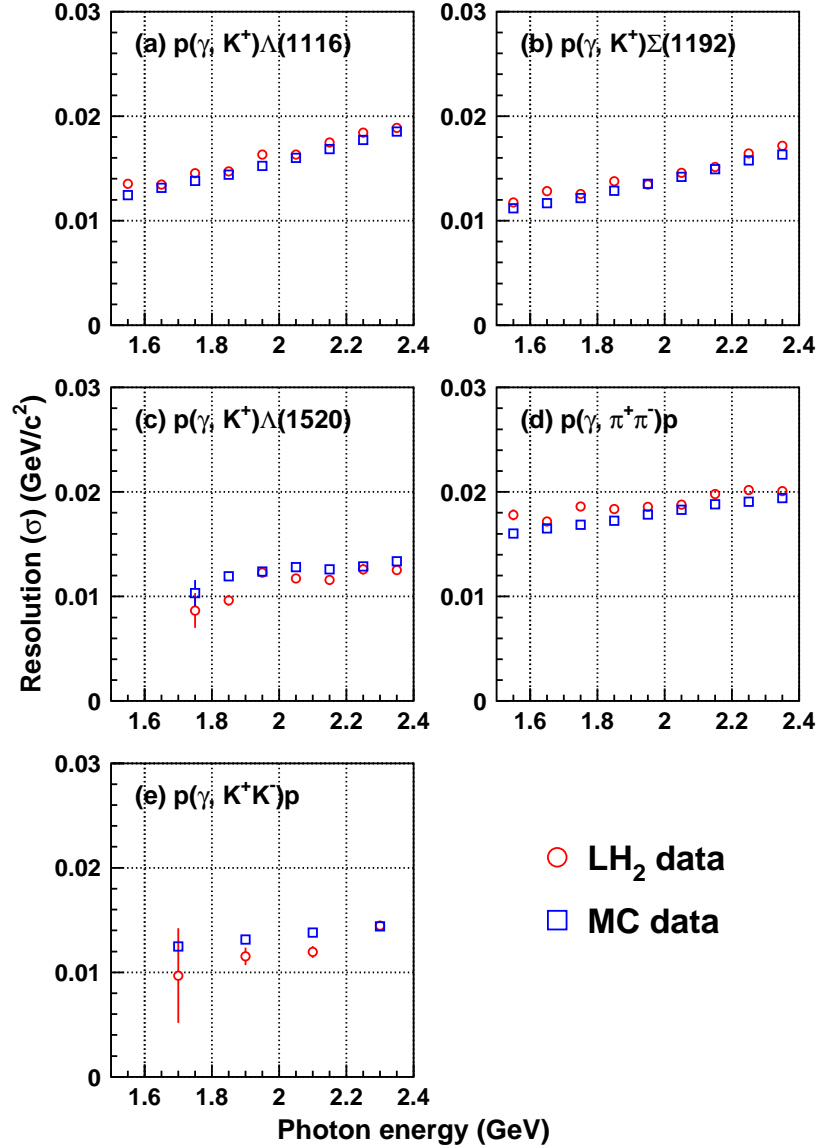
Figure F.1:   Missing mass resolution for the (a) $p(\gamma, K^+)\Lambda(1116)$, (b) $p(\gamma, K^+)\Sigma(1192)$, (c) $p(\gamma, K^+)\Lambda(1520)$, (d) $p(\gamma, \pi^+\pi^-)p$ and (d) $p(\gamma, K^+K^-)p$ reactions as a function of the photon energy. Red open circles show the results for the LH$_2$ data, whereas blue open squares show the results for MC simulations.
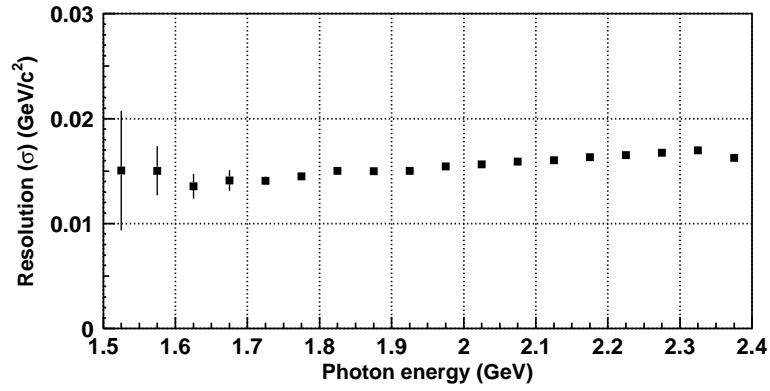
Figure F.2:   Missing mass resolution for the ^{4}He$(\gamma, K^+ K^-)^4$He reaction as a function of the photon energy. The data were obtained by MC simulation.

Appendix G Correction for reconstructed z-vertex position

In this appendix, a correction for the reconstructed z-vertex position is described.

Figure G.1(b) shows distributions of the reconstructed z-vertex position of two opposite-charged particles with the empty-target data. Each colored histogram corresponds to two different types of the track configurations (cases-1 and 2), respectively, as shown in Fig. G.1(a). Peaks around $z = -1600$ mm correspond to the CFRP cap just downstream of the target cell. A clear shift can be seen between the CFRP peaks for cases-1and 2. This is due to an imperfect magnetic field map. In fact, a shift becomes lager when a constructive interference region of the solenoid and dipole magnetic fields ($ydc0 < 0$, where $ydc0$ represents the y-coordinate of a track at DC0) is selected. To obtain a better z-vertex resolution, a reconstructed z-vertex position was corrected event by event according to the track configuration. The corrections for the reconstructed z-vertex position for several track configurations are summarized in Table G.1.
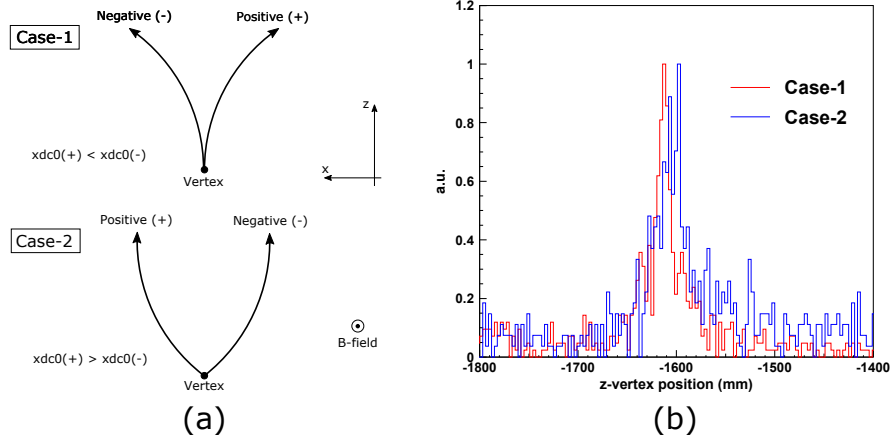
Figure G.1: (a) Configurations for two tracks with opposite charges (cases 1and 2). (b) Reconstructed z-vertex position of two opposite-charged particles for case-1 (red) and case-2 (blue) with the empty-target data. Peaks around $z = -1600$ mm correspond to the CFRP cap just downstream of the target cell.

Table G.1: Corrections for the reconstructed z-vertex positions. The first four rows represent those for one-track events, and the others for two-track events. $xdc0(+/-)$ $[ydc0(+/-)]$ represents the x (y) position of a positive/negative-charged track at DC0.

Configuration	Selection	z-correction (mm)
Conf#1 (1trk)	$xdc0(+) > 0,\ ydc0(+) > 0$	0
Conf#2 (1trk)	$xdc0(+) \leqq 0,\ ydc0(+) > 0$	26.7
Conf#3 (1trk)	$xdc0(+) \leqq 0,\ ydc0(+) \leqq 0$	3.6
Conf#4 (1trk)	$xdc0(+) > 0,\ ydc0(+) \leqq 0$	-14.7
Conf#1 (2trk)	$ydc0(+) > 0,\ ydc0(-) > 0$ $xdc0(+) > xdc0(-)$	0
Conf#2 (2trk)	$ydc0(+) > 0,\ ydc0(-) > 0$ $xdc0(+) \leqq xdc0(-)$	7.1
Conf#3 (2trk)	$ydc0(+) \leqq 0,\ ydc0(-) \leqq 0$ $xdc0(+) > xdc0(-)$	-4.8
Conf#4 (2trk)	$ydc0(+) \leqq 0,\ ydc0(-) \leqq 0$ $xdc0(+) \leqq xdc0(-)$	3.5
Conf#5 (2trk)	$ydc0(+) > 0,\ ydc0(-) \leqq 0$ $xdc0(+) > xdc0(-)$	-3.9
Conf#6 (2trk)	$ydc0(+) > 0,\ ydc0(-) \leqq 0$ $xdc0(+) \leqq xdc0(-)$	4.2
Conf#7 (2trk)	$ydc0(+) \leqq 0,\ ydc0(-) > 0$ $xdc0(+) > xdc0(-)$	-2.3
Conf#8 (2trk)	$ydc0(+) \leqq 0,\ ydc0(-) > 0$ $xdc0(+) \leqq xdc0(-)$	0.8
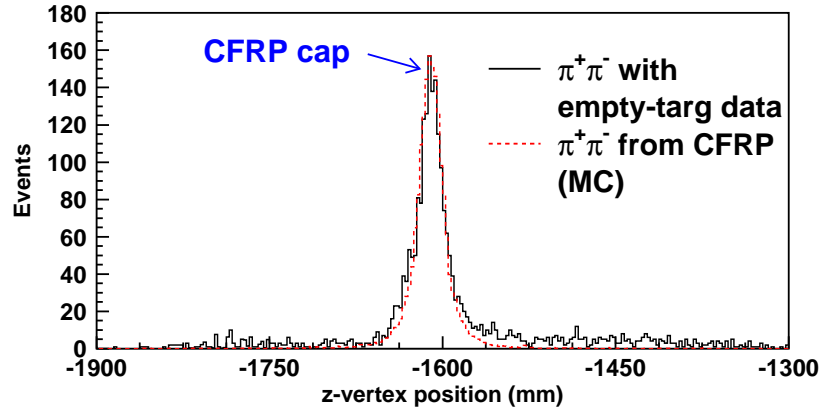
Figure G.2:   Reconstructed *z*-vertex position for $\pi^+\pi^-$ tracks with the empty-target-data after the correction (a black solid-line histogram). A red dashed-line histogram represents a MC-simulated *z*-vertex distribution for $\pi^+\pi^-$ tracks from the CFRP cap. Note that in MC simulation, $\pi^+\pi^-$ were generated by assuming the non-resonant $\pi + \pi^-$ production on free protons.

Figure G.2 shows a distribution of the reconstructed *z*-vertex position for $\pi^+\pi^-$ tracks with the empty-target data after the correction. For comparison, a MC-simulated *z*-vertex distribution for $\pi^+\pi^-$ tracks is overlaid in the same figure. The CFRP peak in the empty-target data is well reproduced by the MC-simulated distribution, and thus the *z*-vertex resolution is understood well.

Appendix H K^+K^- event loss

We estimated the K^+K^- event loss in the kaon identification due to the failure in solving the 2-ns ambiguity. The result is presented here.

As described in Sect. 3.6, while the contamination of pions and protons can be removed by the PID cuts and the $\mathrm{MM}(K^+K^-)$ cut, some of the K^+K^- events are lost if one fails to solve the 2-ns ambiguity. The rate of such events was estimated by comparing the π^0 yields in the $p(\gamma, p)\pi^0$ reaction obtained with two PID methods; namely, the proton identification was made individually by PID-RF and PID-FWD, the π^0 yields with each PID method were obtained as a function of the proton momentum, and were compared with each other[40]. Here, a π^0 loss rate (R_{loss}) is defined as

$$R_{\mathrm{loss}} = \frac{N_{\mathrm{FWD}} - N_{\mathrm{RF}}}{N_{\mathrm{FWD}}}, \tag{H.1}$$

where N_{RF} (N_{FWD}) is the π^0 yield obtained with PID-RF (PID-FWD). Note that R_{loss} is equivalent to the loss of proton events in the proton identification due to the failure in solving the 2-ns ambiguity.

Figures H.1(a1) and (a2) show the boundaries for the proton identification with PID-RF and PID-FWD, respectively. The boundaries for both the PID cuts were set to 4σ, where σ is the momentum-dependent mass resolution. Figure H.1 (b) shows squared missing mass spectra for the $p(\gamma, p)X$ reaction with PID-RF and PID-FWD, respectively. A clear peak for the π^0 production is seen around a squared mass of 0.02 GeV^2/c^4. The π^0 yields were obtained by fitting the squared missing mass spectra with two MC templates; the one for the π^0 production and the other for the non-resonant $\pi^+\pi^-$ production.

Figure H.1(c) shows the π^0 loss rate (R_{loss}) as a function of the proton momentum. The π^0 loss rate increases slightly with the proton momentum but is less than 5%. By extrapolating it to a relevant momentum region (~ 1 GeV/c), the rate of the K^+K^- event loss was estimated to be 3%. Since the event loss rate depends on the filling patterns of the electron bunches, the differences in R_{loss} between the filling patterns were assigned to the systematic error (1%).

---

[40]The proton identification with PID-FWD is an easy task because a proton band is well separated from pion and kaon bands in a scatter plot of momentum versus squared mass. Therefore, the proton sample obtained with PID-FWD can be used for estimating the event loss in PID-RF due to the failure in solving the 2-ns ambiguity.
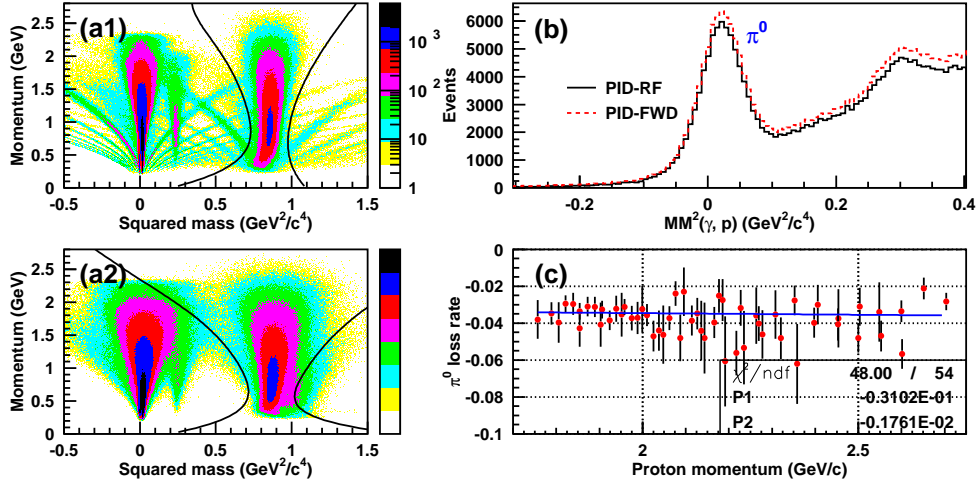
Figure H.1:   (a1) Scatter plots (momentum vs mass squared) for the proton identification with PID-RF and (a2) PID-FWD. Black curves correspond to boundaries for a 4σ cut. (b) Distributions of the square of the missing mass for the $p(\gamma, p)X$ reaction with the LH$_2$ data. Black solid and red dashed histograms represent the missing mass squared with PID-RF and PID-FWD, respectively. (c) π^0 loss rate (R_{loss}) as a function of the proton momentum. A blue line represents the fit to the data with a linear function. As a result, the π^0 loss rate was obtained as a function of the proton momentum: $R_{\mathrm{loss}} = -0.0310 - 0.0018 \cdot p$, where p is the proton momentum in unit of GeV/c.

Appendix I Consistency check with previous LEPS measurements

To check the validity of the acceptance calculation as well as the normalization of the photon flux, the differential cross sections for the $\gamma p \to K^+\Lambda(1116)$, $\gamma p \to K^+\Sigma(1192)$, $\gamma p \to \pi^0 p$ and $\gamma p \to \phi p$ reactions were calculated with the LH$_2$ data, and were compared with the the results obtained in the previous LEPS measurements [85, 128, 129].

Differential cross section for $\gamma p \to K^+\Lambda(1116)/\Sigma(1192)$ reaction

The differential cross sections for the $\gamma p \to K^+\Lambda(1116)/K^+\Sigma(1192)$ reactions were calculated at three production angles; $0.85 < \Theta^{\mathrm{CM}}_{K^+} < 0.90$, $0.90 < \Theta^{\mathrm{CM}}_{K^+} < 0.95$ and $0.95 < \Theta^{\mathrm{CM}}_{K^+} < 1.00$, where $\Theta^{\mathrm{CM}}_{K^+}$ denotes the K^+ production angle in the center-of-mass frame. The yields for $\Lambda(1116)$ and $\Sigma(1192)$ were simultaneously obtained by fitting the missing mass spectra for the $p(\gamma, K^+)X$ reaction with two signal templates and one background template. Here, the source of background events was found to be the $\gamma p \to \pi^+\pi^- p$ reaction with the π^+ detection as a K^+. The signal templates were obtained by MC simulations, whereas the background template was obtained from the missing mass spectra for the $p(\gamma., \pi^+)X$ reaction in real data. The contamination of the events from the CFRP cap of the target chamber was estimated with the empty-target data. The acceptance was calculated by MC simulations, in which a K^+ was assumed to be produced isotropically in the center-of-mass frame. Figures I.1(a), (b) and (c) show the differential cross sections $d\sigma/d(\cos\Theta)$ for the $\gamma p \to K^+\Lambda(1116)$ reaction as a function of the photon energy at each production angle, together with the LEPS 2006 results [128]. Figures I.2(a), (b) and (c) show the differential cross sections $d\sigma/d(\cos\Theta)$ for the $\gamma p \to K^+\Sigma(1192)$ reaction as a function of the photon energy at each production angle, in comparison with the LEPS 2006 results [128]. The present results for both reactions are in good agreement with the previous LEPS results.

183

Differential cross section for $\gamma p \to \pi^0 p$ reaction

The differential cross sections for the $\gamma p \to \pi^0 p$ reaction were calculated at four production angles; $-0.85 < \Theta^{\mathrm{CM}}_{\pi^0} < -0.80$, $-0.90 < \Theta^{\mathrm{CM}}_{\pi^0} < -0.85$, $-0.95 < \Theta^{\mathrm{CM}}_{\pi^0} < -0.90$ and $-1.00 < \Theta^{\mathrm{CM}}_{\pi^0} < -0.95$, where $\Theta^{\mathrm{CM}}_{\pi^0}$ denotes the π^0 production angle in the center-of-mass frame. The π^0 yields were obtained by fitting the missing mass spectra for the $p(\gamma, p)X$ reaction with two MC templates: the one for the π^0 production and the other for the non-resonant $\pi^+\pi^-$ production. The event contamination from the CFRP cap of the target chamber was estimated with the empty-target data. The acceptance was calculated by MC simulation, in which a π^0 was assumed to be produced isotropically in the center-of-mass frame. Figures I.3(a), (b), (c) and (d) show the differential cross sections $d\sigma/d(\cos\Theta)$ for the $\gamma p \to \pi^0 p$ reaction as a function of the photon energy at each production angle, together with the LEPS 2007 results [128]. The present results are in good agreement with the previous LEPS results.

Differential cross section for $\gamma p \to \phi p$ reaction

The differential cross sections $d\sigma/dt$ for the $\gamma p \to \phi p$ reaction were calculated at $0.0 < |t| - |t|_{\min} < 0.1$ GeV^2 as a function of photon energy. Here, $|t|_{\min}$ is the minimum momentum transfer $|t|$ for protons. The ϕ-meson yields were obtained by fitting the invariant mass spectra of K^+K^- pairs with two MC templates: the one for the ϕ-meson events and the other for the non-resonant K^+K^- production. The event contamination from the CFRP cap of the target chamber was estimated in the same manner as described in Sect. 3.6. The acceptance was calculated by MC simulation, in which the slope of $d\sigma/dt$ and the spin density matrix elements were set to the values obtained in the previous LEPS measurement [85]. Figure I.4 shows the comparison of $d\sigma/dt$ at $0.0 < |t| - |t|_{\min} < 0.1$ GeV^2 between the present results and the LEPS 2005 ones [85]. The present results are consistent with the previous LEPS results.
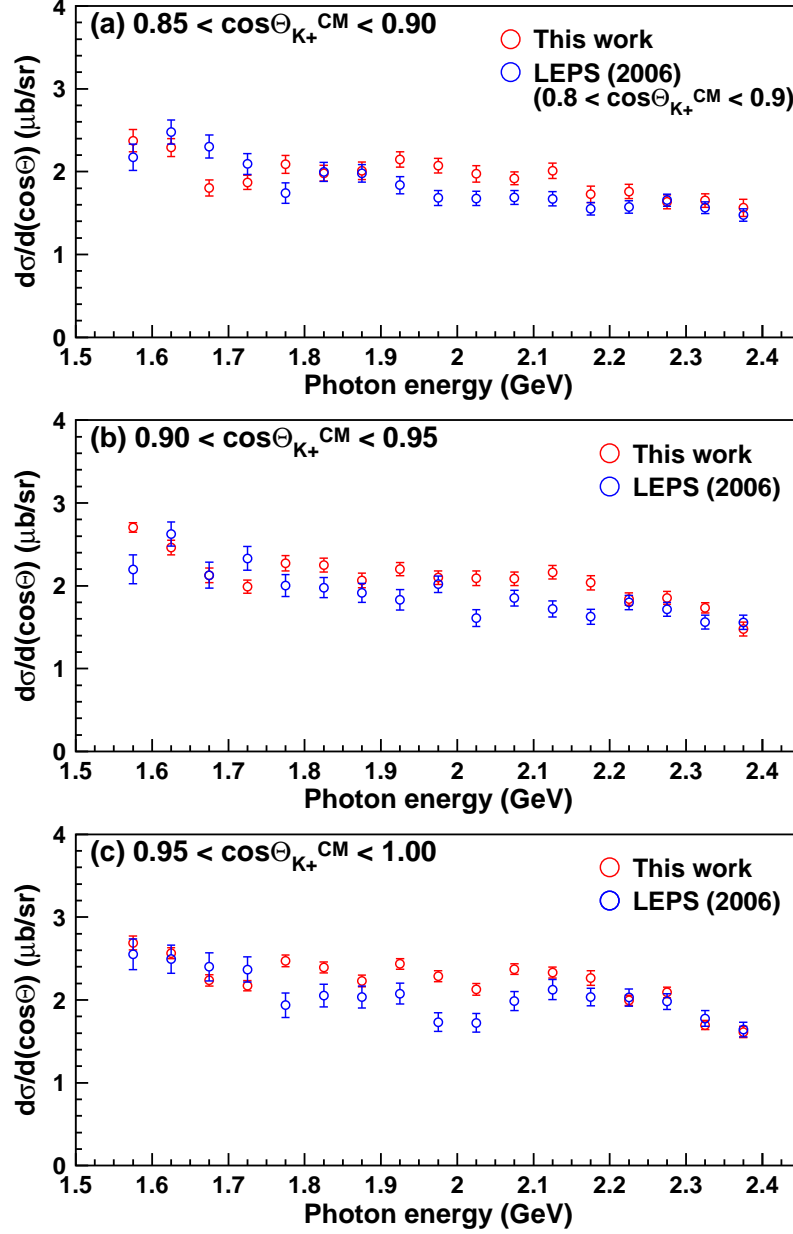
Figure I.1:   Differential cross sections $d\sigma/d(\cos\Theta)$ for the $\gamma p \to K^+\Lambda(1116)$ reaction as a function of the photon energy at (a) $0.85 < \Theta^{CM}_{K^+} < 0.90$, (b) $0.90 < \Theta^{CM}_{K^+} < 0.95$ and (c) $0.95 < \Theta^{CM}_{K^+} < 1.00$. Red circles shows the results for the present analysis, and blue ones show the results for the LEPS 2006 data [128].
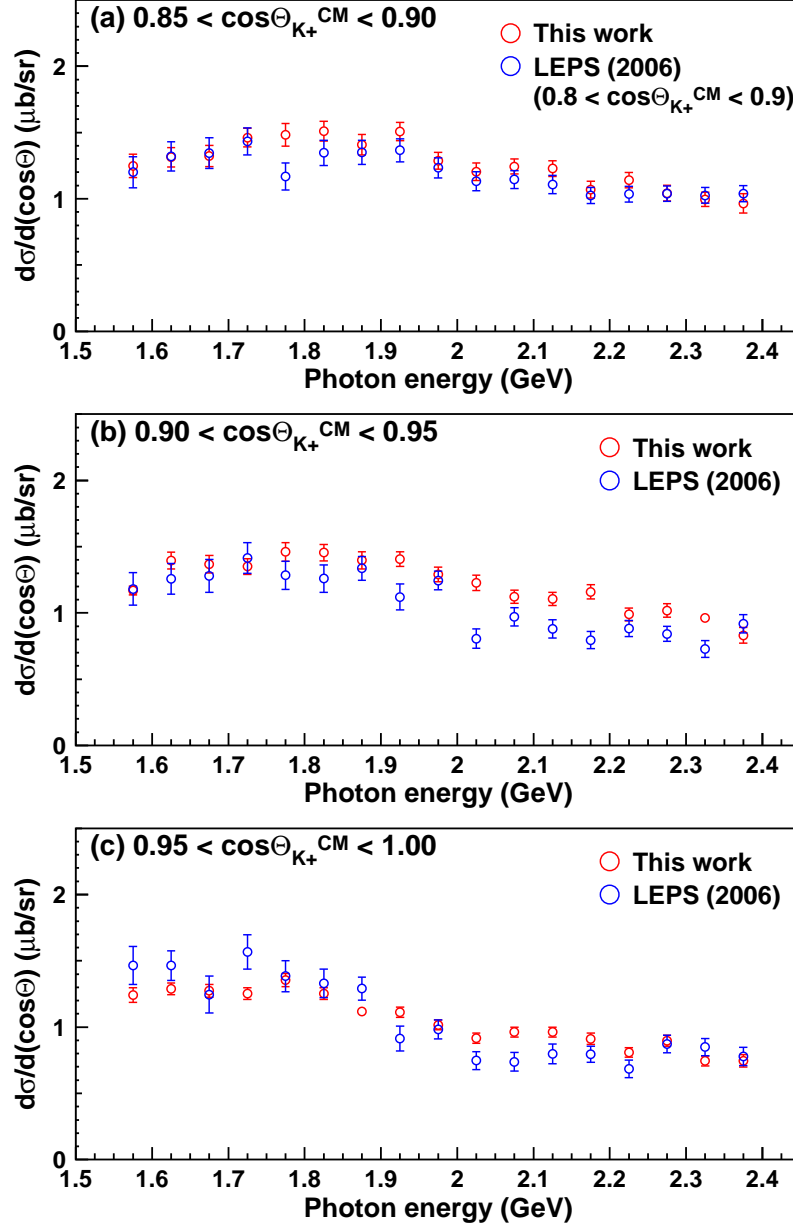
Figure I.2: Differential cross sections $d\sigma/d(\cos\Theta)$ for the $\gamma p \to K^+\Sigma(1192)$ reaction as a function of the photon energy at (a) $0.85 < \Theta^{\mathrm{CM}}_{K^+} < 0.90$, (b) $0.90 < \Theta^{\mathrm{CM}}_{K^+} < 0.95$ and (c) $0.95 < \Theta^{\mathrm{CM}}_{K^+} < 1.00$. Red circles shows the results for the present analysis, and blue ones show the results for the LEPS 2006 data [128].
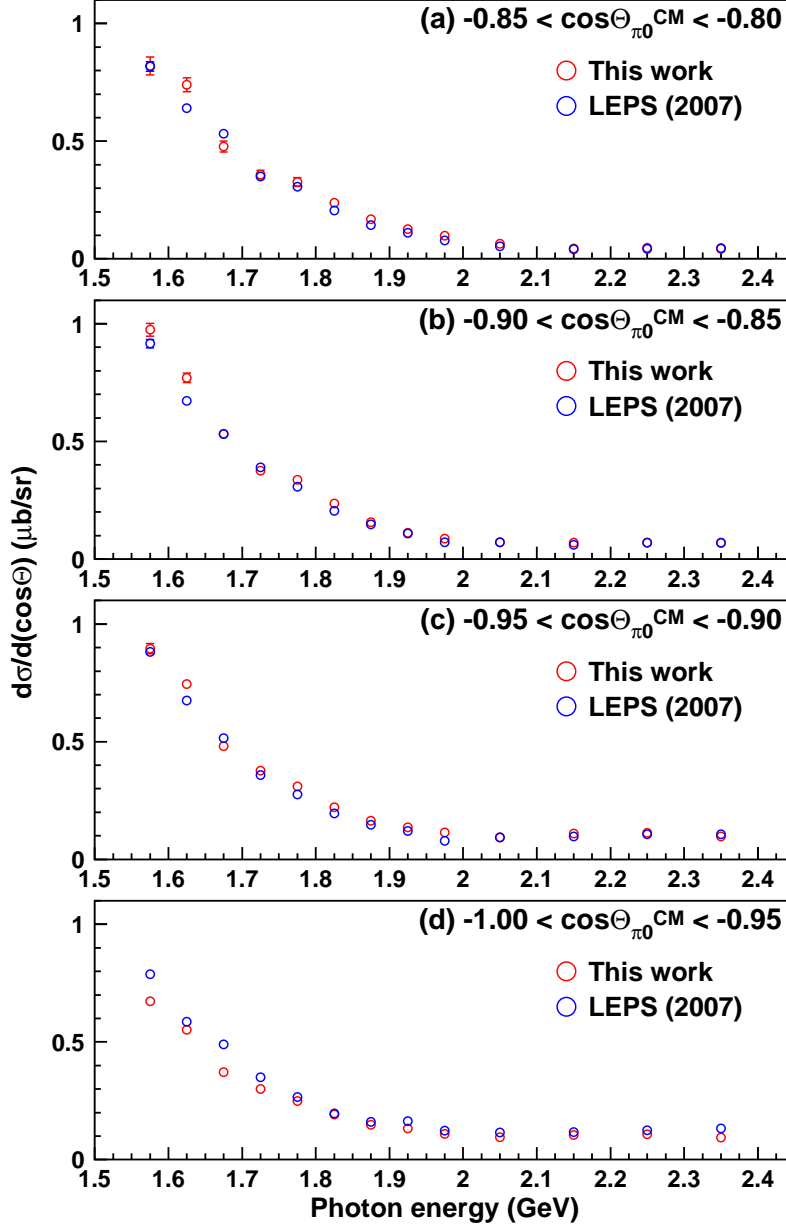
Figure I.3:   Differential cross sections $d\sigma/d(\cos\Theta)$ for the $\gamma p \to \pi^0 p$ reaction as a function of the photon energy at (a) $-0.85 < \Theta^{\mathrm{CM}}_{\pi^0} < -0.80$, (b) $-0.90 < \Theta^{\mathrm{CM}}_{\pi^0} < -0.85$, (c) $-0.95 < \Theta^{\mathrm{CM}}_{\pi^0} < -0.90$ and (d) $-1.00 < \Theta^{\mathrm{CM}}_{\pi^0} < -0.95$. Red circles shows the results for the present analysis, and blue ones show the results for the LEPS 2007 data [129].
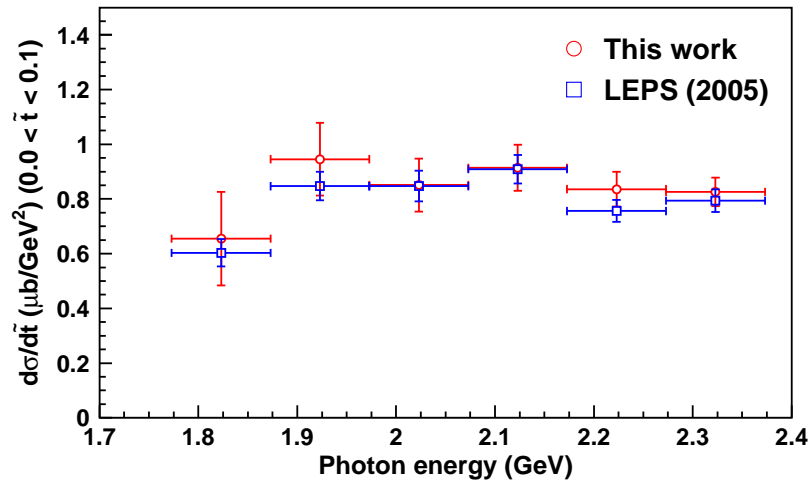
Figure I.4: Differential cross section $d\sigma/d\tilde{t}$ for the $\gamma p \to \phi p$ reaction as a function of the photon energy at $0.0 < \tilde{t} < 0.1$ GeV^2. Here, $\tilde{t} \equiv |t| - |t|_{\min}$. Red circles show the present result, whereas blue squares show the LEPS 2005 results [85].

Appendix J   Polarization degree of BCS photons

The degree of BCS photon polarization (P_γ) was calculated by the following equation:

$$P_\gamma = P_{\text{laser}} \times \mathcal{F}_{\text{conv}}(E_\gamma), \tag{J.1}$$

where P_{laser} is the laser polarization, and $\mathcal{F}_{\text{conv}}$ is a conversion function of polarization from laser photons to BCS photons, as shown in Fig. 2.5.

The laser polarization P_{laser} was measured run by run. Figure J.1 shows the run dependence of the laser polarization. Since the laser polarization does not change in principle, the measured ones were averaged over all the runs. Here, the data during r42065–42400 and the data with $P_{\text{laser}} > 100\%$ were excluded in the average because their measurements seem to have failed. The laser polarization was evaluated to be 0.9772 and 0.9818 for the horizontal and vertical polarizations, respectively.
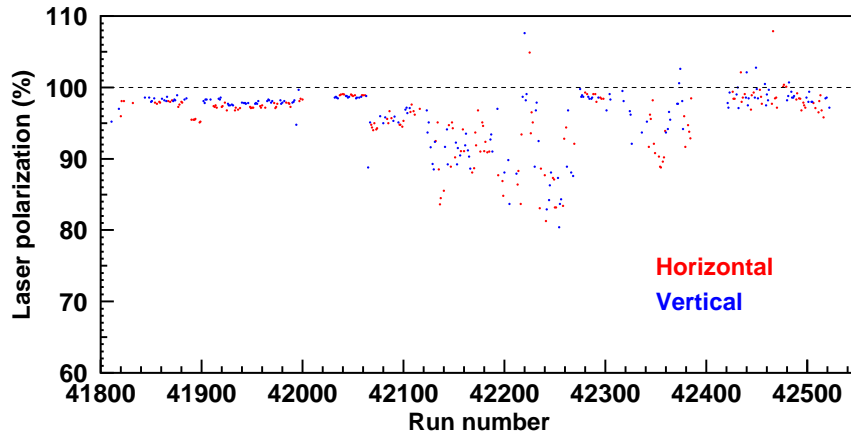
Figure J.1:   Run dependence of the laser polarization. Red and blue points represent the horizontal and vertical polarization, respectively.

Next, the BCS photon polarization was calculated event by event by Eq. (J.1) with the above values of P_{laser}. Here, the coherent ϕ production events were selected by the K^+K^- invariant mass and the missing mass for the ${}^4\text{He}(\gamma, K^+K^-)X$ reaction as $1.008 < \text{M}(K^+K^-) < 1.030$ GeV/c^2 and $\text{MM}(K^+K^-) < 3.72$ GeV/c^2, respectively. Figures J.2(a) and (b) show the distributions of the BCS photon polarization for the E1 and E2 regions,

respectively, after selecting the coherent ϕ production events. Thus, the averaged BCS photon polarization was determined to be 0.9929 (horizontal), 0.8878 (vertical) and 0.8847 (total) for the E1 region, and 0.9140 (horizontal), 0.9185 (vertical) and 0.9158 (total) for the E2 region.

The systematic error on the BCS photon polarization was estimated to be 0.1% and 0.08% for the horizontal and vertical polarizations, respectively, from the r.m.s. of the laser polarization measurements.
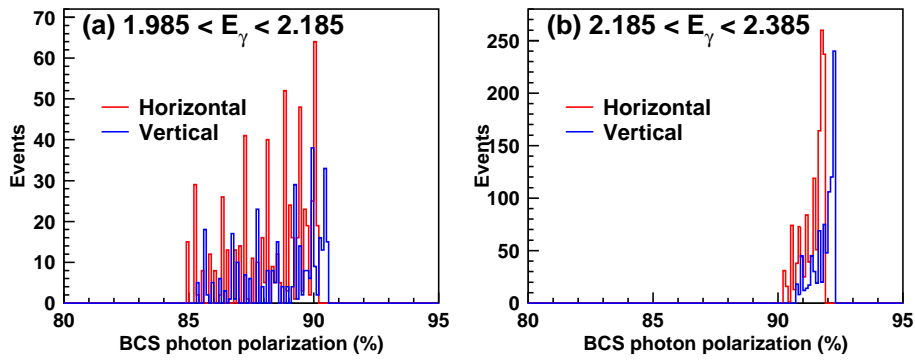
Figure J.2: Distributions of the BCS photon polarization for (a) E1: $1.985 < E_\gamma < 2.185$ GeV and (b) E2: $2.185 < E_\gamma < 2.385$ GeV after selecting the coherent ϕ production events. Red and blue histograms represent the horizontal and vertical polarization data, respectively.

Appendix K   Decay angular distribution with semi-coherent process

The systematic errors on the SDMEs due to the event contamination other than the coherent ones were estimated by considering the semi-coherent process in $MM(K^+K^-)$ fits. These results are presented here.

Figure K.1 shows the $MM(K^+K^-)$ spectra together with the fit results for the angle $\Phi - \Psi$ and the E_h region (see also Fig. 4.1 for comparison). The inclusion of the semi-coherent process improves the fit χ^2. Figure K.2 shows the ratios of the coherent production events (R_{coh}) as a function of the angles $\cos \Theta$, Φ, $\Phi - \Psi$, $\Phi + \Psi$ and Ψ for each energy region. For comparison, those obtained without the semi-coherent process are overlaid in the same figures. We found that the inclusion of the semi-coherent process slightly reduces the coherent production yields, but does not affect the shapes of the distributions so much.

Figure K.3 shows the acceptance-corrected distributions $W(\cos \Theta)$, $W(\Phi)$, $W(\Phi - \Psi)$, $W(\Phi + \Psi)$ and $W(\Psi)$ for each energy region, together with the fit results. The fit results and the extracted spin density matrix elements are summarized in Tables K.1 and K.2 for the E_l and E_h regions, respectively. The quality of the fits is reasonably good for all the distributions.

Figure K.4 shows the comparison of the extracted SDMEs between those obtained with and without the semi-coherent process. The systematic errors on the SDMEs due to the event contamination other than the coherent ones were found to be smaller than the statistical errors.

Table K.1: Summary of the fit results and the extracted SDMEs for the E_l region.

Angle	SDME	χ^2	ndf	χ^2/ndf
$\cos \Theta$	-0.017 ± 0.016	5.28	8	0.65
Φ	0.110 ± 0.031	13.01	8	1.63
$\Phi - \Psi$	0.468 ± 0.024	6.52	8	0.81
$\Phi + \Psi$	-0.105 ± 0.034	12.91	8	1.61
Ψ	0.099 ± 0.067	9.93	8	1.13

Table K.2: Summary of the fit results and the extracted SDMEs for the E_h region.

Angle	SDME	χ^2	ndf	χ^2/ndf
$\cos\Theta$	0.017 ± 0.013	2.89	8	0.36
Φ	0.051 ± 0.020	10.36	8	1.29
$\Phi - \Psi$	0.441 ± 0.014	9.06	8	1.13
$\Phi + \Psi$	-0.025 ± 0.008	19.20	8	2.40
Ψ	0.084 ± 0.043	5.34	8	0.67
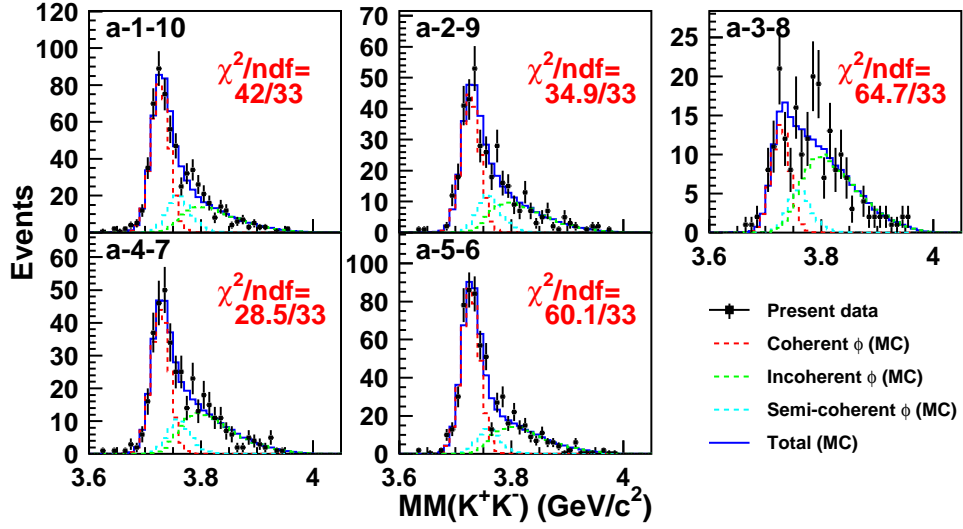
Figure K.1:   Results for the template fits on the $MM(K^+K^-)$ spectra for the angle $\Phi - \Psi$ and the E_h region. Blue histograms show the results for the template fits. Red, green cyan dashed histograms show the MC templates for the coherent, incoherent and semi-coherent production events, respectively.
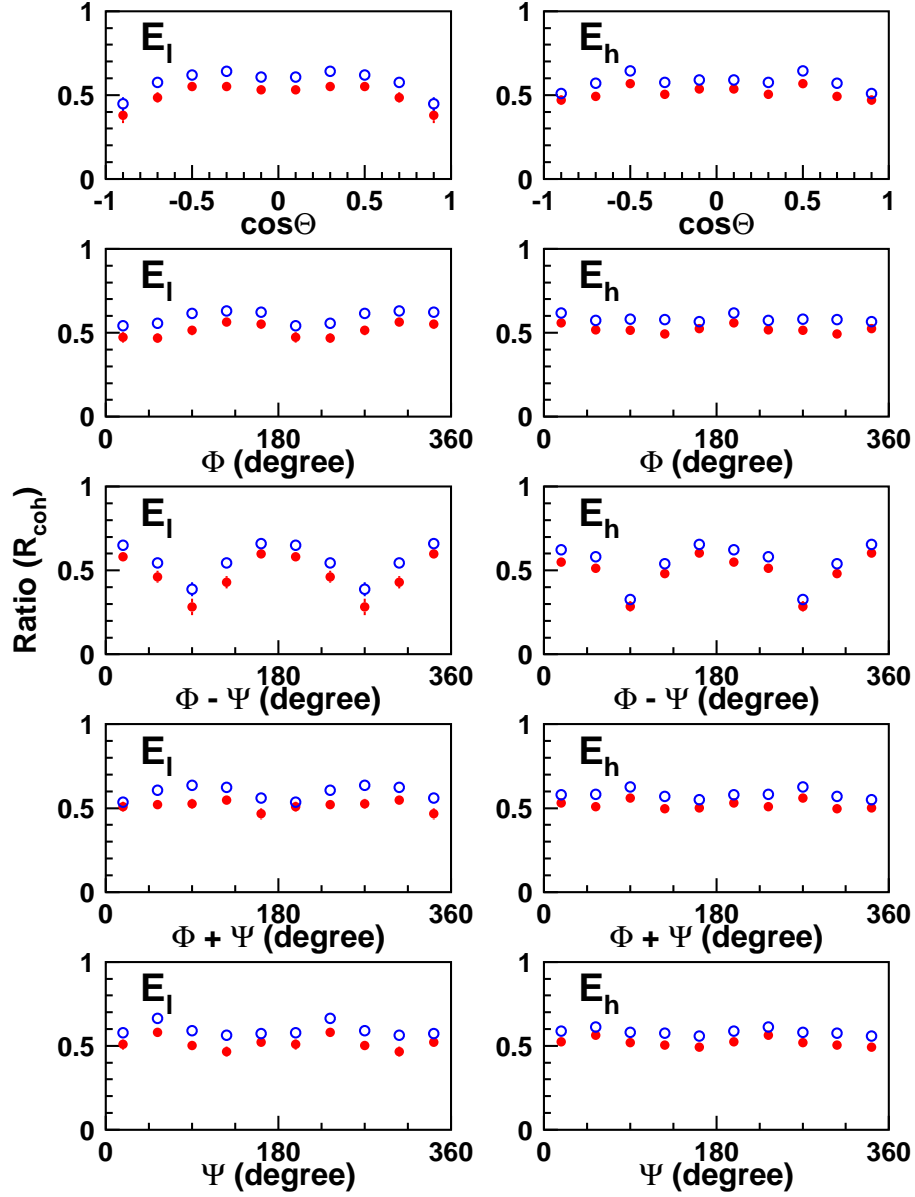
Figure K.2:   Ratios of the coherent events (R_{coh}) as a function of the angles $\cos\Theta$, Φ, $\Phi - \Psi$, $\Phi + \Psi$ and Ψ for the E_l (left figures) and E_h (right figures) regions. Red filled circles show the results with the semi-coherent process, whereas blue open circles show the results without the semi-coherent process.
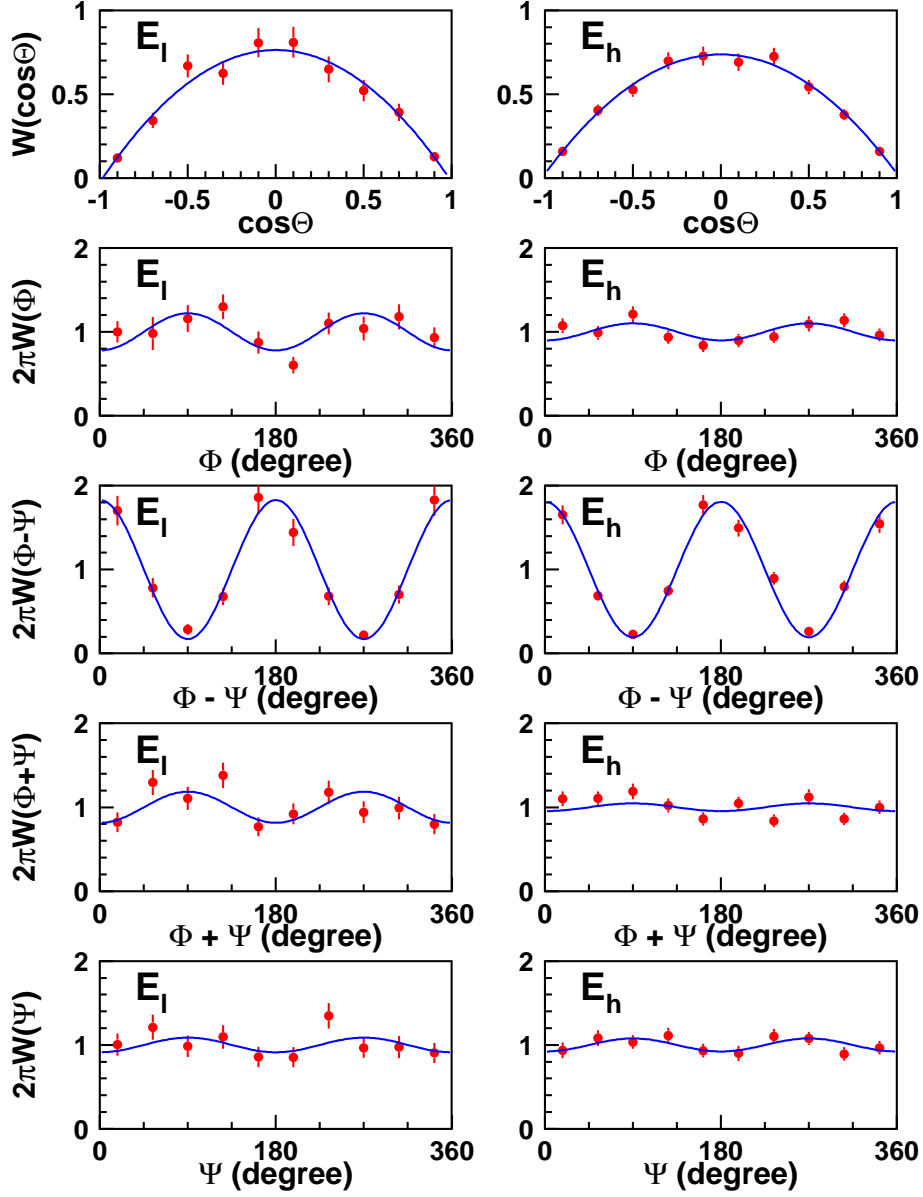
Figure K.3: Decay angular distributions $W(\cos\Theta)$, $W(\Phi)$, $W(\Phi-\Psi)$, $W(\Phi+\Psi)$ and $W(\Psi)$ for the E_l (left figures) and E_h (right figures) regions. Blue curves are the fits to the data points with Eqs. (4.1), (4.2), (4.3), (4.4) and (4.5).
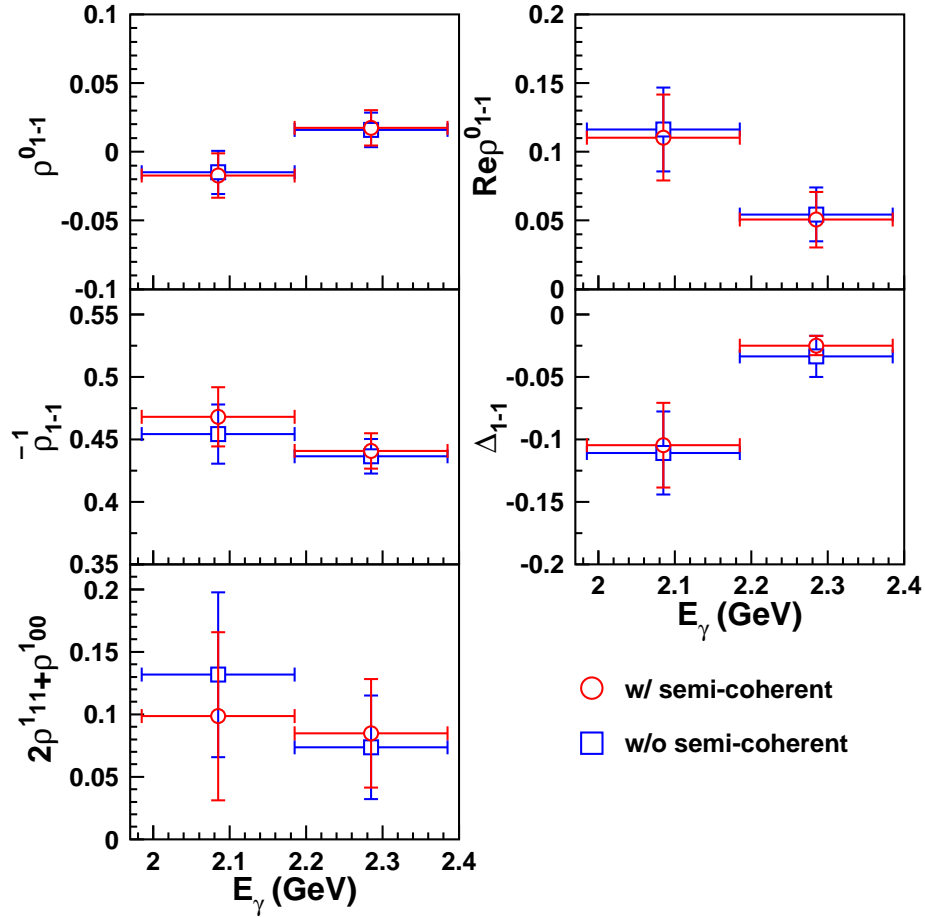
Figure K.4:   Comparison of the extracted SDMEs between those obtained with (red open circles) and without the semi-coherent process (blue open squares).

Appendix L   Normalization of photon flux

In the cross section measurement, the number of BCS photons in each energy bin was calculated as follows:

$$N_\gamma = N_\gamma^{\mathrm{cor}} \times \frac{d(\omega_\gamma \cdot \varepsilon_{\mathrm{tag}})}{dE_\gamma} \times \Delta E_\gamma \times P_{\mathit{fntag}=1} \times C_{\mathrm{digi}} \times T_{\mathrm{beam}}, \qquad (\mathrm{L.1})$$

where N_γ^{cor} is the corrected number of photons, $d(\omega_\gamma \cdot \varepsilon_{\mathrm{tag}})/dE_\gamma$ is a density distribution of the photon flux as a function of the photon energy, ΔE_γ is the bin width, $P_{\mathit{fntag}=1}$ is the probability of $\mathit{fntag} = 1$, C_{digi} is a correction for digitalized photon energies, and T_{beam} is a beam transmission from the collision point to the target ($= 0.53$).

Table L.1 summarizes the number of BCS photons in each energy bin for the cross section measurement.

Table L.1: Number of BCS photons in each energy bin for the cross section measurement.

E_γ	N_γ ($\times 10^{11}$)	Error ($\times 10^7$)
e-1	3.593	3.847
e-2	1.999	3.014
e-3	2.169	1.935
e-4	2.545	2.780
e-5	2.431	3.410
e-6	3.372	1.945

Corrected number of photons

The corrected number of photons (N_γ^{cor}) was calculated as follows:

$$N_\gamma^{\mathrm{cor}} = N_{\mathrm{scaler}} \times \eta_{\mathrm{DAQ}} \times C_{\mathrm{tag}}, \qquad (\mathrm{L.2})$$

where N_{scaler} represents the scaler counts for the tagger trigger, η_{DAQ} is the DAQ efficiency, and C_{tag} is a dead time correction for the tagger scaler counts, which depends on the filling patterns and the tagger hit rate. Each value was evaluated run by run from the scaler counts.

Density distribution of photon flux

A density distribution of the photon flux $[d(\omega_\gamma \cdot \varepsilon_{\text{tag}})/dE_\gamma]$ was obtained from the cross section for the BCS process (Fig. 2.4) and the efficiencies of the tagging system (ε_{tag}). The density distribution $d(\omega_\gamma \cdot \varepsilon_{\text{tag}})/dE_\gamma$ was normalized so that

$$\int_{E_{\text{min}}}^{E_{\text{max}}} \frac{d(\omega_\gamma \cdot \varepsilon_{\text{tag}})}{dE_\gamma} dE_\gamma = 1, \tag{L.3}$$

where E_{min} (E_{max}) is the minimum (maximum) photon energy ($E_{\text{min}} = 1.475$ GeV, $E_{\text{max}} = 2.385$ GeV).

The tagger efficiencies ε_{tag} were estimated channel by channel for TAG-SF and TAG-PL. For these estimation, a proton was required in the LEPS spectrometer by PID-FWD to select a true electron track in the tagging system. For the estimation of the TAG-SFF (SFB) efficiencies, an electron track was identified by searching for the corresponding TAG-SFB (SFF) and TAG-PL hits, whereas, for the estimation of the TAG-PL efficiencies, it was identified by searching for the corresponding TAG-SFF and TAG-SFB hits.

Since at least one layer of TAG-SFF and TAG-SFB was required to have a hit at the trigger stage, the tagger efficiency ε_{tag} is given by

$$\varepsilon_{\text{tag}} = [1 - (1 - \varepsilon_{\text{SFF}})(1 - \varepsilon_{\text{SFB}})] \times \varepsilon_{\text{PL}}, \tag{L.4}$$

ε_{SFF}, ε_{SFB} and ε_{PL} are the TAG-SFF, TAG-SFB and TAG-PL efficiencies, respectively. Figures L.1(a) and (b) show the efficiencies for TAG-SF and TAG-PL, respectively. Figure L.2 shows the resulting density distribution as a function of the photon energy.
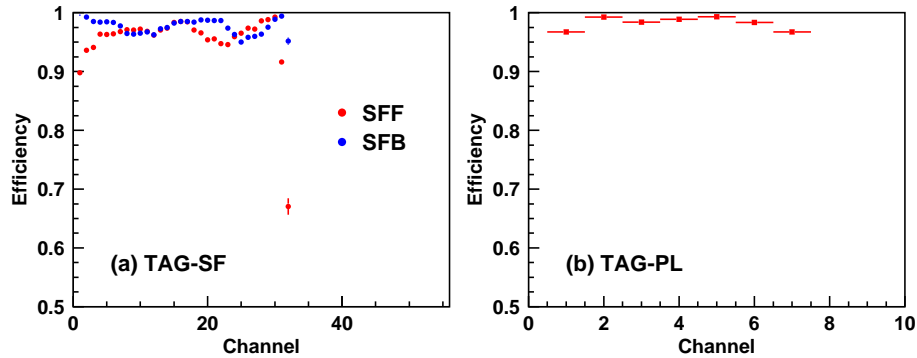
Figure L.1:   (a) Efficiencies for TAG-SFF (red) and TAG-SFB (blue), and (b) those for TAG-PL.
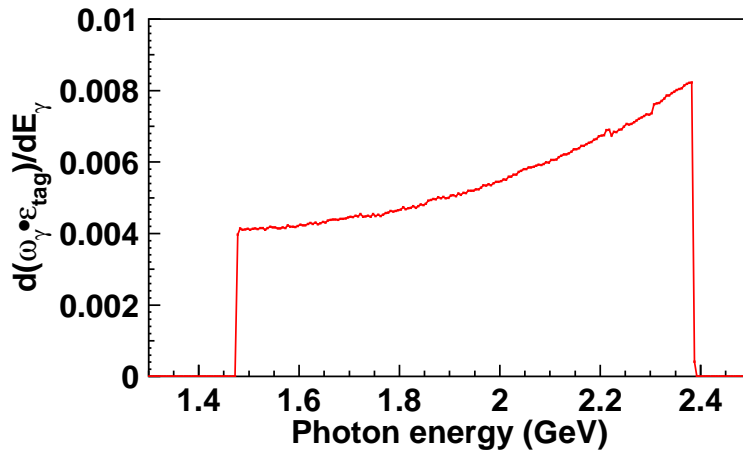
Figure L.2:   Density distribution of the photon flux as a function of the photon energy.

Probability of *fntag* = 1

The probability of *fntag* = 1 was estimated for each filling pattern. It is known that the electron tracks corresponding to low-energy BCS photons hit the side wall of the tagging system, producing electromagnetic (EM) showers, and these effects are already taken into account in the beam transmission (T_{beam}). To avoid the EM shower events, a high-momentum proton (> 2 GeV/c) was required in the LEPS spectrometer by PID-FWD. The

198

probabilities of *fntag* = 1 for each filling pattern are summarized in Table L.2.

Table L.2: Probabilities of *fntag* = 1 for each filling pattern. Values in the brackets represent an error.

Filling pattern (Run number)	Prob. of *fntag* = 1
C-mode (r41811–41871)	0.7243 (0.0019)
D-mode (r41872–41946)	0.7243 (0.0021)
E-mode (r41948–41992)	0.7400 (0.0017)
Multi-bunch (r42032–42108)	0.8734 (0.0013)
C-mode (r42110–42188)	0.7793 (0.0017)
D-mode (r42193–42282)	0.7829 (0.0024)
E-mode (r42283–42385)	0.8036 (0.0025)
A-mode (r42424–42522)	0.9075 (0.0012)

Correction for digitalized photon energy

Since the scintillation fibers of TAG-SF have a finite width, the photon energy obtained from fired TAG-SF channels is digitalized. This could make a zigzag structure in the energy dependence of cross sections. To correct this, a correction factor, C_{digi}, was introduced. Figure L.3(a) shows the distribution of the photon energy obtained by the tagger, together with that predicted from the $p(\gamma, \pi^+\pi^-)p$ reaction with Eq. (3.9). The distribution of the predicted photon energy is smooth, whereas the distribution of the tagger photon energy shows a jump around $E_\gamma \sim 2.3$ GeV due to digitalizations. Therefore, the correction factor can be obtained by the number of events in each bin for the tagger photon energy divided by that for the predicted photon energy. Figure L.3(b) shows the correction factors for each energy bin.
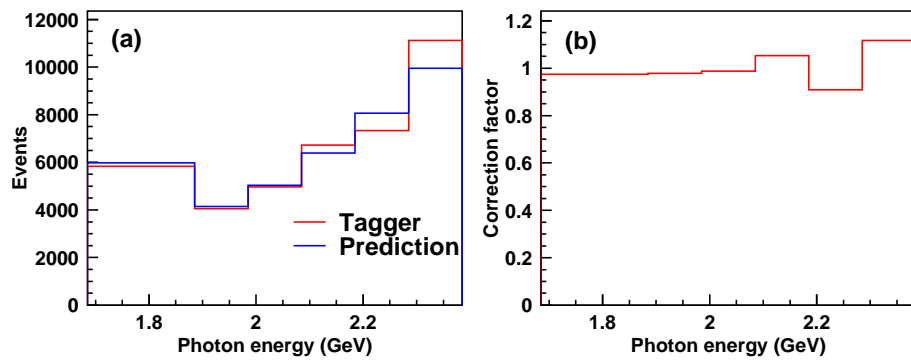
Figure L.3:   (a) Distributions of the photon energy by the tagger (red) and the predicted photon energy (blue). (b) Correction factor for digitalized photon energies for each energy bin.

Appendix M   Differential cross section with semi-coherent process

The systematic errors on the differential cross sections $d\sigma/d\tilde{t}$ due to the event contamination other than the coherent ones were estimated by considering the semi-coherent process in the $\mathrm{MM}(K^+K^-)$ fits. In this appendix, these results are presented.

Figure M.1 shows the $\mathrm{MM}(K^+K^-)$ spectra for various t bins in the e-6 bin. The fit chi-squares slightly improve by including the semi-coherent process. Figure M.2 shows the ratios of the coherent events (R_{coh}) as a function of $\tilde{t}$ for various E_γ bins. The inclusion of the semi-coherent process reduces the ratios R_{coh} at large $\tilde{t}$, whereas it does not affect so much at small $\tilde{t}$.

Figure M.3 shows $d\sigma/d\tilde{t}$ for various E_γ bins with the assumption of the semi-coherent process. Each spectra was fitted with an exponential function [Eq. (4.12)]. The fit results are summarized in Table M.1. The fit quality is reasonably good for all the E_γ bins.

Figure M.4 shows the energy dependence of the slope b in comparison with the slopes obtained without the semi-coherent process. Both the results are in agreement within the statistical errors. The averaged slope was determined to be 28.97 ± 1.11 GeV^{-2}, which is steeper than that obtained without the semi-coherent process.

The differential cross sections $d\sigma/d\tilde{t}$ were also fitted by an exponential function with a fixed slope of $b = 28.97$ GeV^{-2}, as indicated by blue dashed curves in Fig. M.3. The fit results are summarized in Table M.2. The intercepts $(d\sigma/dt)_0$ are compared with those obtained with a variable slope b in Fig. M.5. It makes no significant difference in $(d\sigma/dt)_0$ whether a fixed or variable slope is used.

Figure M.6 shows the comparison of the intercepts $(d\sigma/dt)_0$ between those obtained with and without the semi-coherent process. The systematic errors on the intercepts $(d\sigma/dt)_0$ due to the event contamination other than the coherent ones were found to be much smaller than the statistical errors.
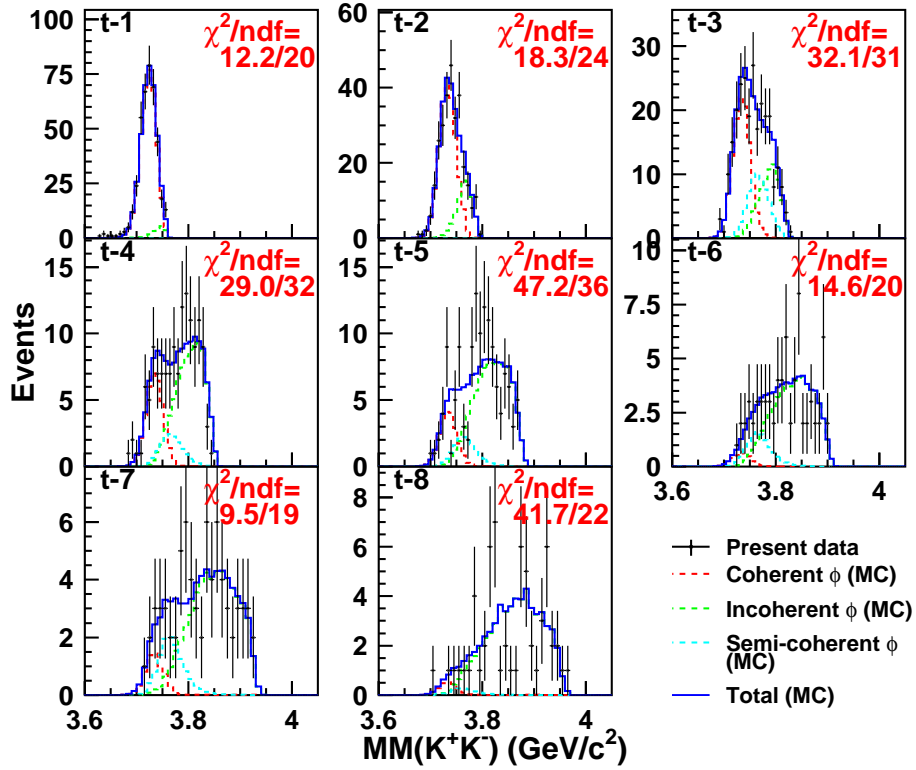
Figure M.1: MM(K^+K^-) spectra for various $\tilde{t}$ bins in the e-6 bin. Blue histograms show the results for the template fits. Red, green and cyan dashed histograms show the MC templates for the coherent, incoherent, semi-coherent production events, respectively.
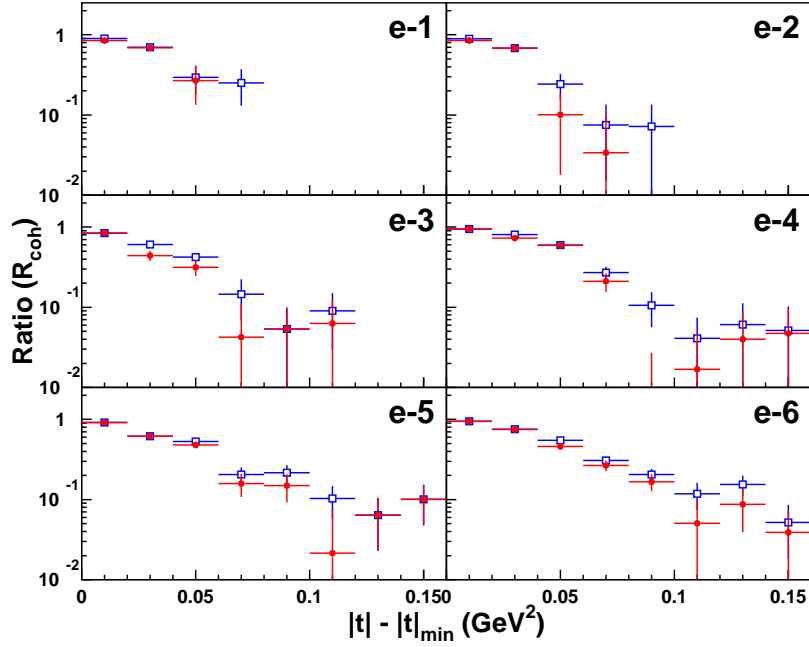
Figure M.2:   Ratios of the coherent events (R_coh) as a function of $\tilde{t}$ for various E_γ bins. Red filled circles are the results obtained with the semi-coherent process, whereas blue open circles are the results obtained without the semi-coherent process.
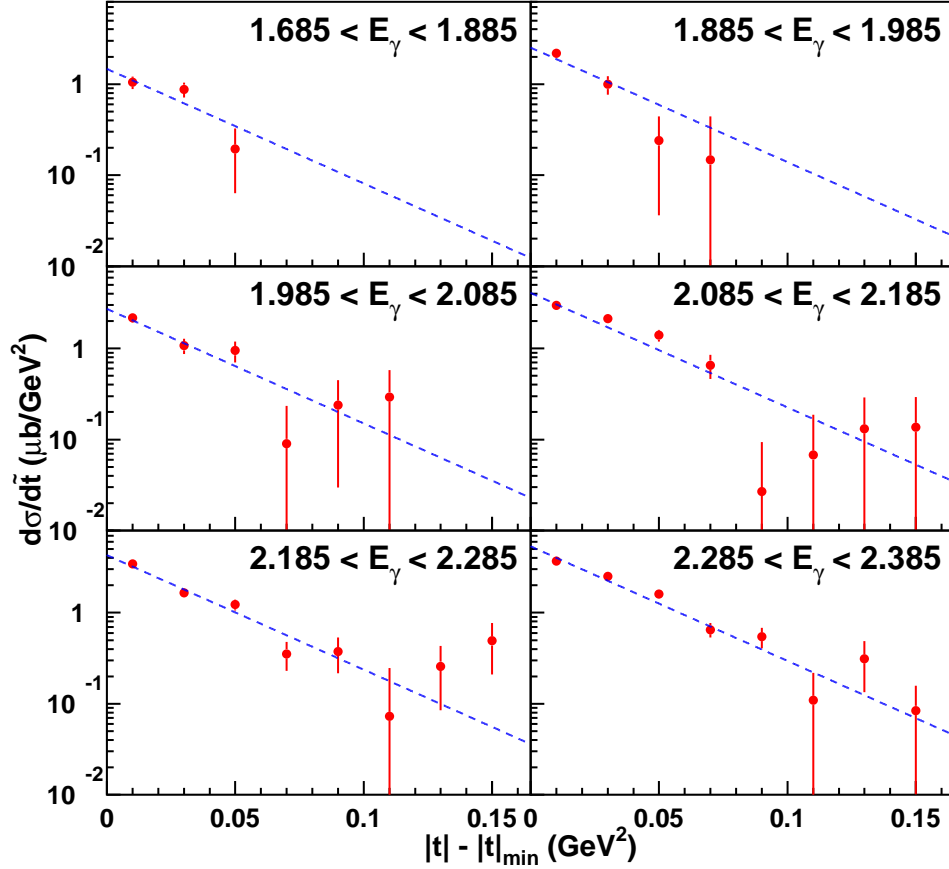
Figure M.3:   Differential cross section as a function of the momentum transfer $\tilde{t}\ (= |t| - |t|_{\min})$ for various E_γ bins. Blue dashed curves show the fit results by an exponential function [Eq. (4.12)] with a fixed slope of $b = 28.97$ GeV^{-2}.

Table M.1: Summary of the fit results on $d\sigma/d\tilde{t}$ with a variable slope.

E_γ	N_0 (μb/GeV^2)	b (GeV)	χ^2	ndf	χ^2/ndf
e-1	1.693 ± 0.280	29.73 ± 8.25	3.91	1	3.91
e-2	3.500 ± 0.589	46.16 ± 9.83	0.55	2	0.28
e-3	3.551 ± 0.409	33.72 ± 5.39	5.22	4	1.30
e-4	4.752 ± 0.337	33.05 ± 2.63	23.56	6	3.93
e-5	4.217 ± 0.331	31.29 ± 2.39	9.17	6	1.53
e-6	4.867 ± 0.264	25.88 ± 1.51	10.48	6	1.75

Table M.2: Summary of the fit results on $d\sigma/d\tilde{t}$ with a fixed slope of $b = 29.0$ GeV^{-2}.

E_γ	N_0 (μb/GeV^2)	χ^2	ndf	χ^2/ndf
e-1	1.670 ± 0.245	3.92	2	1.96
e-2	2.589 ± 0.315	4.79	3	1.60
e-3	3.219 ± 0.289	5.98	5	1.20
e-4	4.304 ± 0.288	26.75	7	3.82
e-5	3.996 ± 0.254	9.86	7	1.41
e-6	5.231 ± 0.255	14.13	7	2.02
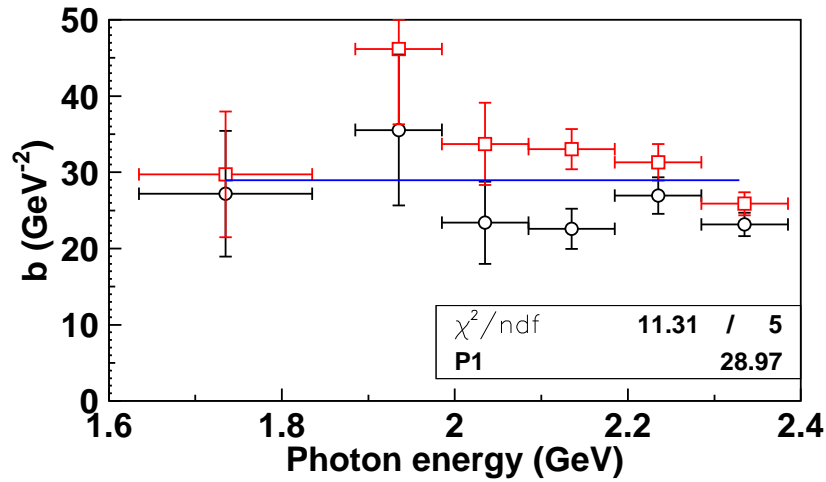
Figure M.4:   Energy dependence of the slope b. Red open squares repre-
sents the present results, whereas black open circles represents those obtained
without the semi-coherent process. A blue line represents an averaged value
of $b = 28.97 \pm 1.11$ GeV^{-2}.
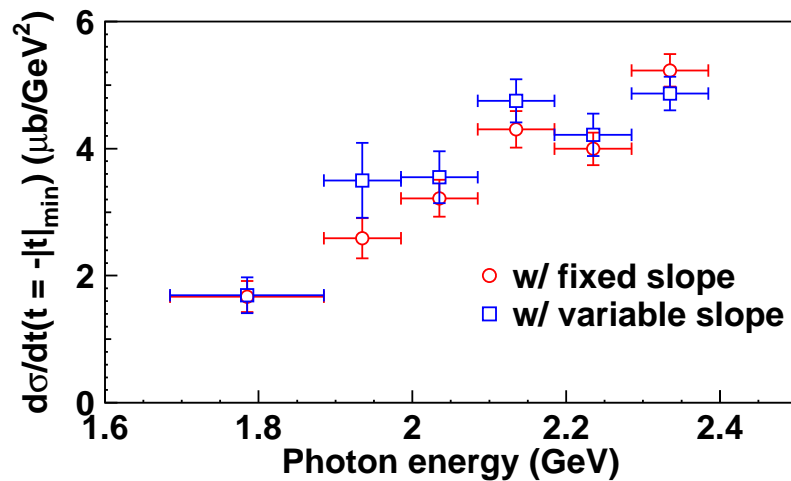
Figure M.5:   Comparison of the intercepts $(d\sigma/dt)_0$ between those obtained
with fixed (red open circles) and variable slopes (blue open squares).
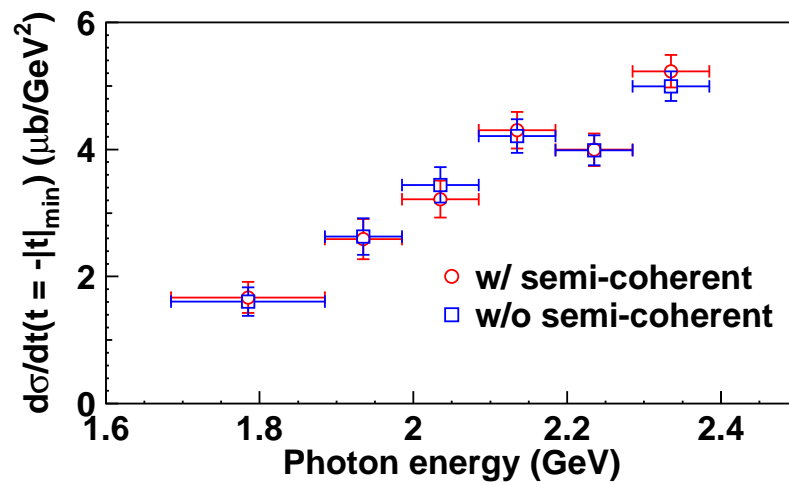
Figure M.6:   Comparison of the intercepts $(d\sigma/dt)_0$ between those obtained with (red open circles) and without the semi-coherent process (blue open squares).

Appendix N   On model-3

In this Appendix, the details of model-3 are described. For this model, we used a Pomeron and daughter Pomeron exchange model as described in Refs. [38, 47].

The amplitude for the Pomeron exchange is basically identical to that described in Sect. 1.4.2, except that the term $(s/s_\mathbb{P})^{\alpha_\mathbb{P}(t)}$ in Eq. (1.13) was replaced with $[(s - s_\text{th})/s_\mathbb{P}]^{\alpha_\mathbb{P}(t)}$. Here, s_th is a threshold parameter, which is introduced to get a better shape of the energy dependence of the forward cross section ($\theta = 0°$) near the threshold [38]. To maximize a threshold enhancement, we chose $\sqrt{s_\text{th}} = M_p + M_\phi$, where M_p and M_ϕ are the masses of protons and ϕ-mesons, respectively.

Regarding the daughter Pomeron exchange, we used basically the same formalism and parameter set as in Ref. [47]. One exception is that a strength factor C_{gl}, which governs the overall strength, was tuned so as to fit available experimental data on the forward cross section ($\theta = 0°$). Figure N.1 shows a comparison of the forward cross section ($\theta = 0°$) between model-3 and the available experimental data [64, 81, 85, 87, 122–125] when C_{gl} is set to a 5 times larger value[41] than that in Ref. [47]. By choosing the 5 times larger value, model-3 reproduces the experimental data fairly well.

---

[41]This choice is comparable to the extreme case in the appendix of Ref. [47], in which the daughter Pomeron exchange becomes dominant near the threshold.
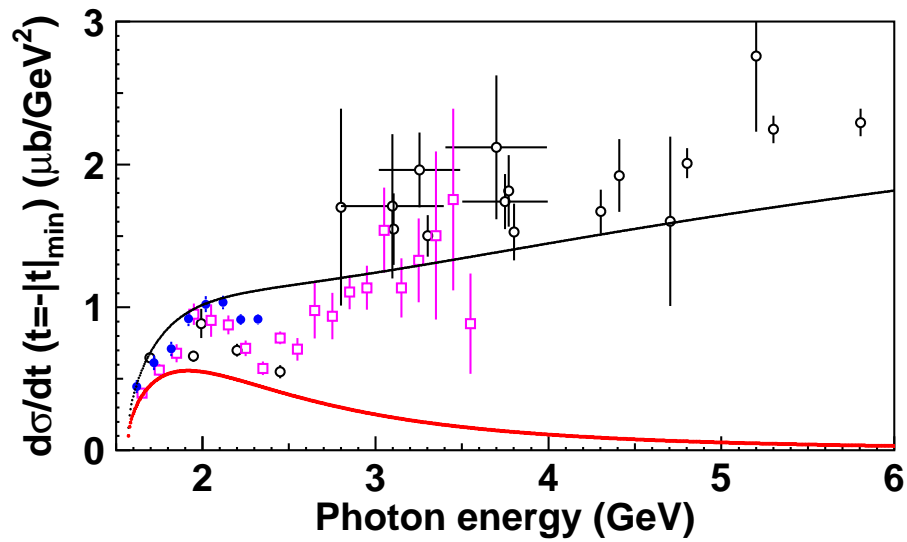
Figure N.1:   Comparison of the forward cross section ($\theta = 0°$) between model-3 (black curve) and the experimental data [64, 81, 85, 87, 122–125]. A red curve represents the contribution from the daughter Pomeron exchange [38,47]. Here, the strength factor for the daughter Pomeron exchange, C_{gl}, is set to a 5 times larger value than that in Ref. [47].